CNWRA 95-005

THERMALLY DRIVEN MOISTURE REDISTRIBUTION IN PARTIALLY SATURATED POROUS MEDIA

Prepared for

Nuclear Regulatory Commission
Contract NRC-02-93-005

Prepared by

Center for Nuclear Waste Regulatory Analyses
San Antonio, Texas

January 1995

CNWRA 95-005

THERMALLY DRIVEN MOISTURE REDISTRIBUTION IN PARTIALLY SATURATED POROUS MEDIA

Prepared for

Nuclear Regulatory Commission
Contract NRC-02-93-005

Prepared by

R.T. Green
F.T. Dodge
S.J. Svedeman
R.D. Manteufel
G. Rice
K.A. Meyer
R.G. Baca

Center for Nuclear Waste Regulatory Analyses
San Antonio, Texas

January 1995

PREVIOUS CONTRIBUTIONS

Peer-Reviewed Papers:

- Manteufel, R.D., R.T. Green, F.T. Dodge, and S.J. Svedeman. 1992. An experimental investigation of two-phase, two-component nonisothermal flow in a porous medium with a simulated fracture. HTD-216. *Heat and Mass Transfer in Porous Media*. New York, NY: American Society of Mechanical Engineers: 9–18.

- Manteufel, R.D., and R.T. Green. 1993. Observations of thermally driven liquid redistribution in a partially saturated porous medium. FED-173, HTD-265. *Multiphase Transport in Porous Media*. New York, NY: American Society of Mechanical Engineers: 93–107.

- Manteufel, R.D. 1994. *Large-Scale Buoyant Flow at an Unsaturated HLW Repository*. 94-WA, HT-39. New York, NY: American Society of Mechanical Engineers.

- Green, R.T., F.T. Dodge, and G. Rice. 1995. Prediction of thermally driven fluid flow at different scales. *Geophysical Research Letters*. In press.

Conference Papers:

- Green, R.T., R.H. Martin, S.J. Svedeman, and F.T. Dodge. 1991. Nonisothermal laboratory and numerical experimental results. *Proceedings of Workshop V: Flow and Transport Through Unsaturated Fractured Rock: Related to High-Level Radioactive Waste Disposal*. NUREG/CP-0040. Washington, DC: Nuclear Regulatory Commission.

- Green, R.T., R.D. Manteufel, and S.J. Svedeman. 1992. *An Examination of Two-Phase Flow Through Partially-Saturated Fractured Porous Media Using Numerical and Lab-Scale Experimental Results*. Presentation at Gordon Conference, New Hampshire.

- Manteufel, R.D., and M.W. Powell. 1994. Thermosyphon analysis of a repository: A simplified model for vapor flow and heat transfer. *Proceedings of the Fifth International High-Level Radioactive Waste Management Conference, Las Vegas NV*. La Grange Park, IL: American Nuclear Society: 2,207–2,216.

- Dodge, F.T., and R.T. Green. 1994. Pressure-driven gas flow in heated, partially-saturated porous media. *Proceedings of the Fifth International High-Level Radioactive Waste Management Conference, Las Vegas, NV*. La Grange Park, IL: American Nuclear Society: 2,217–2,227.

PREVIOUS CONTRIBUTIONS (Cont'd)

Meetings and Workshops:

- Green, R.T., and R.H. Martin. *Use of TOUGH Computer Code to Simulate a Laboratory-Scale Experiment*. Presented at the TOUGH Workshop, Lawrence Berkeley Laboratory, September, 1990.

- Green, R.T., F.T. Dodge, and R.D. Manteufel. Scaling of heat and fluid flow based on laboratory experiments. *Workshop IV: Flow and Transport through Unsaturated Fractured Rock: Related to High-Level Radioactive Waste Disposal*. 1993.

- NRC/DOE Technical Exchange on Near-Field Phenomena Related to Radionuclide Releases from the Engineered Barrier System, Los Alamos, New Mexico, October 14, 1993.

- NRC/DOE Technical Exchange Meeting on Field Heater Experiments associated with THMC Processes held in Las Vegas, Nevada, November 8–9, 1994.

ABSTRACT

Experimental and theoretical studies have been conducted to develop a quantitative understanding of the thermohydrologic phenomena induced by emplacement of high-level radioactive waste in an unsaturated fractured-porous media. A series of laboratory experiments were conducted in a variety of media to study the physics of thermally driven moisture redistribution. Principles of similarity theory have been applied to develop dimensionless parameters that can be used to scale the thermohydrologic behavior observed at the laboratory scale to that of field- and full-repository scale. Numerical modeling of two-phase flow phenomena was used to evaluate the scaling theories and interpret the experimental results.

Eleven laboratory-scale experiments were conducted which are categorized according to: (i) the fluid phase that is the focus of study, (ii) temperature regime, (iii) geometry, and (iv) test medium. The first seven of these experiments centered on nonisothermal liquid flow and considered sub-boiling and boiling regimes in both unconsolidated and consolidated porous media. Moisture content was measured using a gamma-ray densitometer while flow was visualized using injected dye. The other four experiments focused on pressure driven gas flow and considered boiling conditions in both unconsolidated and consolidated media. Gas and capillary pressures were measured in these experiments using pressure transducers and tensiometers, respectively.

Through the application of dimensional analysis, a set of dimensionless parameters were derived to describe the characteristic thermohydrologic behavior for the heating and cooling periods. The dimensionless parameters of key importance are the advection number $Ad_{g/l}$ for the gas (g) and liquid (l) phases and the characteristic time scale $t_{g/l}$. The advection number indicates the relative importance of the pressure and buoyancy driving forces. The characteristic time scale provides an estimate of the time for a pressure transient to be propagated over a characteristic spatial scale.

The V-TOUGH computer code was used to simulate the heating, transitional, and cooling periods for three spatial scales: (i) laboratory ($\sim$cm); (ii) field ($\sim$m); and (iii) repository ($\sim$km). Calculations of the temperature, pressure, and saturation fields were used to evaluate the proposed scaling theories.

This report summarizes studies conducted over the past two years and since the issuance of the last progress report on the Thermohydrology Research Project (Green et al., 1993). The report summarizes the experimental data, theoretical developments, and evaluation of scaling relationships.

CONTENTS

CONTENTS (Cont'd)

CONTENTS (Cont'd)

FIGURES

FIGURES (Cont'd)

FIGURES (Cont'd)

TABLES

ACKNOWLEDGMENTS

This report was prepared to document work performed by the Center for Nuclear Waste Regulatory Analyses (CNWRA) for the Nuclear Regulatory Commission (NRC) under Contract No. NRC-02-93-005. The activities reported here were performed on behalf of the NRC Office of Nuclear Regulatory Research, Division of Regulatory Applications. The report is an independent product of the CNWRA and does not necessarily reflect the views or regulatory position of the NRC.

The authors wish to express their gratitude to C. Gray for his editorial review, E. Bonano, C. Freitas, P. Lichtner, and S. Mohanty for their technical reviews, and W. Patrick for his programmatic review. The C-TOUGH code used in this study was modified from the V-TOUGH code by M. Seth.

QUALITY OF DATA, ANALYSES, AND CODES

DATA: CNWRA-generated data contained in this report meet quality assurance requirements described in the CNWRA Quality Assurance Manual. Sources for other data cited in the report should be consulted for determining the level of quality for those data.

ANALYSES AND CODES: The V-TOUGH code is controlled under the CNWRA Software Configuration Procedure. The RETC code is not currently under software configuration management. Testing is underway to bring RETC into compliance with the software configuration management procedures.

1 INTRODUCTION

1.1 OVERVIEW

It is widely recognized that the decay heat produced by high-level radioactive waste (HLW) will likely have a significant impact on both the pre- and post-closure performance of the proposed repository at Yucca Mountain (YM), in southwest Nevada. The task of delineating which aspects of that impact are favorable to isolation performance and which are adverse is an extremely challenging technical undertaking because of such factors as the hydrothermal regimes involved, heterogeneity of the geologic media, and the time and space scales involved. This difficulty has motivated both the U.S. Department of Energy (DOE) and the Nuclear Regulatory Commission (NRC) to undertake multi-year thermohydrology research programs to examine the effects of decay heat on pre- and post-closure performance of the repository. Both of these organizations are currently pursuing field and laboratory experiments, as well as numerical modeling studies, to advance the state of knowledge of the thermohydrologic phenomena relevant to the proposed geologic repository.

One of the primary objectives of the DOE repository program (U.S. Department of Energy, 1994) is to develop a thermal loading strategy that makes constructive use (Ramspott, 1991) of the thermohydrologic conditions to:

- Improve system and subsystem performance
- Protect the waste packages and other repository components from water contact
- Compensate, to the degree possible, for uncertainties in the current and future states of the repository system

Recent thermohydrologic modeling studies by DOE researchers (Buscheck and Nitao, 1992, 1993) suggest that the proper selection of the thermal loading could potentially extend the time period that the waste packages remain dry. Preliminary findings from such studies have led the DOE to consider an extended-dry concept that could: (i) extend the period of radionuclide containment in the engineered barrier system, (ii) delay the period of controlled radionuclide release (and transport), and (iii) reduce the sensitivity of total-system performance to hydrologic variability.

The NRC research program is focused on developing an adequate scientific understanding of thermohydrologic phenomena for use in reviewing the DOE repository design and site characterization program as well as in conducting total-system and subsystem performance assessments. In addition, the NRC research activities are placing emphasis on probing potentially adverse conditions that may arise as a result of thermohydrologic processes (Green et al., 1994) and associated coupled thermo-hydrologic-mechanical-chemical phenomena (Manteufel et al., 1993). One general concern is related to the possible adverse condition of rapid condensate drainage through fractures, which would result in significant moisture reflux through the repository. A prerequisite to addressing this and other important technical concerns, however, is the need to more fully understand the interrelationships among such processes as water vaporization, liquid and vapor flow, condensation, imbibition of liquid water into the tuff rock matrix, and partially saturated flow in discrete fractures.

The Thermohydrology Research Project, which was initiated in mid-1989, began with the intent of addressing a broad spectrum of generic thermohydrologic questions. While some of these questions were answered in the conduct of the study, other new and challenging ones were encountered. Initial progress made in addressing those technical questions was documented in an interim progress report (Green et al., 1993). Subsequent to that report, the laboratory scale experiments were designed to address four fundamental questions regarding thermohydrologic phenomena:

- What are the principal mechanisms controlling the redistribution of moisture?
- Under what hydrothermal conditions and time frames do individual mechanisms predominate?
- What hydrothermal regimes are associated with each driving mechanism?
- What is the temporal and spatial scale of each hydrothermal regime?

Data from a series of laboratory experiments have been compiled and utilized to test scaling theories derived using dimensional analysis. Within certain constraints, the scaling theories provide a vehicle for relating thermohydrologic behavior between laboratory, canister, and repository scale. This report presents the research results and findings obtained since issuance of the first progress report (Green et al., 1993).

1.2 REGULATORY NEED

The thermohydrologic conditions in the repository have implications regarding the two performance objectives in 10 CFR Part 60 for the engineered barrier system (EBS) stated in 10 CFR 60.113(a)(1): (i) containment requirement for the HLW packages, and (ii) radionuclide release rate limit from the EBS. How well the EBS meets the containment time performance objective greatly depends on the hydrothermal conditions because the canister corrosion processes are a direct function of the presence of liquid water. Similarly, meeting the release rate performance objective will depend on the water flow rates past failed waste packages. In addition, thermohydrologic conditions are of key importance in addressing the regulatory uncertainties associated with the performance objective for the geologic barrier. For example, 10 CFR 60.113(a)(2) defines the groundwater travel time as a performance objective for the geologic barrier. Part of this regulation introduces terms such as disturbed zone which may include consideration of thermohydrologic effects.

The DOE currently predicts (Andrews et al., 1994) that the thermohydrologic conditions associated with the extended-dry concept could potentially enhance the compliance margin with the current cumulative radionuclide release requirements set in Table 1-1 of the 1985 version of 40 CFR Part 191. The DOE studies also suggest that a favorable compliance margin may exist even if the Environmental Protection Agency (EPA) standard is amended to include a numerical limit for dose-to-man. Such compliance margins, if achievable, may indeed provide a degree of robustness that reduces the sensitivity of total-system performance to spatial or temporal variations in the subsurface hydrologic conditions.

While a number of aspects of the repository thermohydrologic environment appear beneficial to subsystem and total-system performance, detailed theoretical and experimental studies must be

performed to ensure that a quantitative understanding of thermohydrologic effects is obtained. Additional justification for studying near-field thermohydrologic phenomena is derived from the fact that the NRC must be sufficiently knowledgeable about the potential impact of the DOE thermal loading strategy to conduct effective prelicensing activities, such as commenting on: (i) the DOE Total-System Performance Assessments (TSPAs) for YM, (ii) repository and EBS designs, and (iii) thermohydrologic field and laboratory experiments.

Another regulatory purpose for the NRC thermohydrology research program is the need to support the ongoing development of the NRC License Application Review Plan (LARP) (Nuclear Regulatory Commission, 1994). More specifically, Compliance Determination Methods (CDMs) are currently being developed for the LARP that will specify the approach and acceptance criteria that the NRC will use to judge compliance with the performance objectives and other regulatory requirements. Several of these CDMs contain various Key Technical Uncertainties (KTUs) that involve considerations of thermohydrologic conditions. Some of these KTUs, for example, delineate uncertainties associated with:

- Identifying which conceptual models adequately represent isothermal and nonisothermal liquid and vapor phase movement of water through unsaturated fractured rock at YM
- Confirming experimentally the basic physical concept of groundwater flow through unsaturated fractured rock
- Modeling groundwater flow through unsaturated fractured rock caused by the lack of codes tested against field and laboratory data
- Modeling the formation of perched zones by thermally driven flow

In addition, studies of thermohydrologic processes are relevant to CDMs associated with favorable conditions (FACs) and potentially adverse conditions (PACs).

1.3 PROJECT SCOPE AND OBJECTIVES

The broad programmatic objective of the Thermohydrology Research Project is to establish an adequate scientific understanding of thermohydrologic phenomena for use in conducting independent reviews of the DOE repository design and site characterization program. A subsidiary objective is to develop the laboratory facilities, experimental methods, measurement techniques, and analytical skills to address thermohydrologic issues that may arise in the repository program. The scope of the research activities can be grouped into three categories: (i) similarity analyses, (ii) laboratory experiments, and (iii) mathematical modeling. Laboratory experiments have been pursued for the purpose of studying individual thermohydrologic mechanisms and providing data for testing mathematical models. Similarity analyses have been utilized to extend the range of applicability of data by developing scaling relationships. Mathematical modeling of heat transfer and two-phase fluid flow has been used as a tool to analyze and interpret experimental results as well as to evaluate alternate scaling theories.

A series of controlled laboratory experiments has been conducted with two prime objectives: (i) to identify and understand the key factors controlling thermally driven moisture redistribution in partially saturated, porous media, and (ii) to provide a basis for evaluating scaling laws formulated to

relate thermohydrologic processes of different spatial dimensions. Experiments have been designed in such a manner that various effects could be studied separately. The scope of these experiments has included examination of such factors as transient heating, gas pressure buildup, and liquid redistribution. These experiments have considered various thermal boundary conditions, heater configurations, and test media with contrasting hydraulic properties. Because of the inherent difficulty of conducting flow experiments under nonisothermal conditions, a number of scoping experiments were necessary in order to perfect instrumentation and measurement techniques, properly select and characterize test media, and systematically compile data on moisture and temperature fields. Results from the scoping and preliminary experiments are documented in an earlier report (Green et al., 1993). In addition to fulfilling the objective of compiling experimental data, the experience gained from these investigations has been very valuable to the NRC objective of conducting effective prelicensing interactions with DOE. For example, the investigators have actively participated in several NRC/DOE Technical Exchanges.

Numerical modeling studies (Buscheck et al., 1993; Lichtner and Walton, 1994) suggest that the thermal evolution of a geologic HLW repository can be divided into three distinct periods: (i) heating, (ii) transitional, and (iii) cooling. During the heating period, radioactive decay of the waste causes a monotonic rise in temperature that may last several hundreds of years. During this period, the rise in temperature at the heat source vaporizes liquid water which then moves away from the heat source due to gas-phase pressure gradients. Water movement occurs primarily as water vapor migrating away from the heat source resulting in the drying of rock near the waste containers. Late in the thermal regime, after temperatures at the heat source have decreased, water transport occurs essentially only in the liquid phase. This is the cooling period in the repository thermal regime. A transitional period occurs between the heating and cooling periods during which water is transported as both vapor and liquid, potentially in opposing directions. The three periods in the thermal evolution of a HLW repository form the basis of the conceptual model proposed in this document.

A similarity analysis was used in this study to characterize the heating and cooling periods. One important technical objective of the similarity analysis work was to formulate scaling theories that could be used to relate the observations of thermohydrologic behavior at the laboratory scale to that of the field scale, and ultimately to the repository scale. Techniques of similitude theory were applied to the set of governing equations relevant to heat transfer and two-phase flow for the heating and cooling periods. A set of dimensionless parameters was derived that can be used to delineate thermo-fluid regimes in the context of scaling theories.

The thrust of this research project was experimental heat transfer and fluid flow. Mathematical modeling of thermohydrologic phenomena was an integral component in the analysis of experimental results. For the most part, the basic purposes of the mathematical models has been to aid the analysis and interpretation of experimental results, to design various experiments, to test various hypotheses, and to evaluate proposed scaling theories. Simple analytical models, for example, were developed for use in describing gas pressure buildup as a function of temperature. Similarly, detailed simulations of selected laboratory experiments were made using the V-TOUGH code (Nitao, 1990) to interpret the observed patterns of moisture redistribution and temperature variation. In addition, computer simulations were performed to test the scaling relationships developed through similarity analysis.

1.4 REPORT ORGANIZATION

In addition to this introductory chapter, this report covers the following topics:

- Chapter 2, Thermohydrologic Phenomena and Scaling Theory
- Chapter 3, Description of Laboratory Experiments
- Chapter 4, Laboratory Experimental Results and Analyses
- Chapter 5, Conclusions and Recommendations

A brief overview is presented in Chapter 2 that covers the relevant conservation principles (and associated mathematical theory) applied to two-phase flow in unsaturated media and the similarity analysis theory developed for thermohydrologic regimes. In Chapter 3, the laboratory experiments designed and used to study the relation between thermohydrologic driving forces and moisture redistribution and gas buildup are described. In Chapter 4, interpretations of the experimental data and their use in evaluating scaling theories are presented. In Chapter 5, the broad conclusions drawn from this research project are listed and explained. This final chapter also presents ideas for possible further experimental research.

2 THERMOHYDROLOGIC PHENOMENA AND SCALING THEORY

2.1 MATHEMATICAL THEORY OF TWO-PHASE FLOW

A brief description of the physical mechanisms that control two-phase flow in unsaturated porous media is presented. The mathematical framework used to describe the dynamics of these mechanisms is then developed.

2.1.1 Physical Mechanisms of Two-Phase Flow

Flow of a two-component (water and air), two-phase (liquid and gas) fluid in a partially saturated, fractured, porous medium involves many diverse and coupled physical processes. In some situations, certain mechanisms are controlling, while others are relatively unimportant; in other situations, all the mechanisms may play equally important roles. Thus, in this study, the approach taken was to begin by investigating the individual processes separately and then, after an understanding was obtained, embark upon investigations of the coupled processes. These experimental and mathematical investigations were guided by conceptual models that were used to develop similitude requirements in the form of dimensionless parameters. The dimensionless parameters also provided insight into the relative importance of various physical mechanisms to the experimental and numerical cases of interest and permited laboratory and field-scale test results to be interpreted in terms of the anticipated responses of the HLW repository. As an introduction to two-phase phenomena, the theory of single phase flow in saturated media is first briefly reviewed.

2.1.1.1 Flow in Saturated Media

Flow in a fully saturated porous medium is always a one-component, single-phase (liquid or gas) flow. Conceptual models of such flows are based on well understood and plausible physical mechanisms. The fluid is conceptualized to be transported through a multitude of interconnected capillary-like channels of varying length and diameter, under the combined action of pressure difference, laminar viscous stresses, and gravity (Batchelor, 1967; Bear, 1972; Freeze and Cherry, 1979; Domenico and Schwartz, 1990). Instead of attempting to describe the geometry of the flow channels in detail, the mathematical theory of porous flow characterizes the medium as a continuum with certain parameters such as porosity ϕ and saturated permeability k. Porosity is defined as the percentage of void space in the solid matrix per unit volume. The permeability incorporates other geometric details (such as pore diameter, channel length and connectivity, etc.) of the medium; it can best be understood by its use in the relation between the flow and the net driving force:

$$\vec{V} = -\frac{k}{\mu}(\nabla p + \rho g \vec{e}_z) . \qquad (2\text{-}1)$$

In Eq. (2-1), the symbol p represents the fluid pressure, μ the fluid viscosity, ρ the fluid density, the z coordinate is positive upwards, and $\vec{e}_z$ is a unit vector in the direction of increasing elevation (opposite gravity). Equation (2-1) is Darcy's law and $\vec{V}$ is the Darcy velocity, defined as the fluid volumetric flow rate divided by the total cross-sectional area. Darcy's law is theoretically exact for creeping flows in

which fluid inertia is small, and it can be derived from the general Navier-Stokes equations for simple geometries such as bundles of capillaries or spheres. Solutes and marker particles are transported, not at a rate equal to the Darcy velocity, but with a velocity equal to the larger velocity of the fluid in the flow channels. For steady-state conditions, the mass flux of solute or marker particles past a given location is the same when computed by either the Darcy velocity or the interstitial. This is also approximately true for the slow time-varying flows of interest here. The time of first arrival of the solute or particles at a specific location does, however, depend on the interstitial velocity. In general, k, which has units of area, must be inferred from measurements of flow and pressure drop for a given porous medium. If the medium contains fractures, the inferred k is a volume-average, and probably does not represent the permeability of either the porous matrix or the fractures separately.

When a saturated porous medium is heated to temperatures below the boiling point of the liquid, buoyancy forces can induce a natural convection motion. The mathematical description of such a flow is complicated in detail, but experiments show that the flow pattern is similar to that of liquid confined in a volume of the same shape that contains no porous material (Kulacki and Emara, 1975; Wooding, 1956). Figure 2-1, for example, shows the predicted stream lines for a heated geothermal area at Wairakei, New Zealand; this is the same kind of flow pattern that would be anticipated for a heated body of fluid in a cavity. Small-scale experiments can thus be interpreted in terms of large-scale responses through the relevant Rayleigh, Prandtl, and Reynolds dimensionless numbers (Keyhani et al., 1981).

2.1.1.2 Flow in Partially Saturated Media

Compared to a saturated porous medium, flow in a porous medium that contains both liquid and gas presents a difficult challenge to model (Narasimhan, 1982; Wang and Narasimhan, 1986; Rasmussen and Evans, 1989). The flow is strongly influenced by surface forces at the interfaces between the liquid and gas phases. In addition, the phases may not be distributed as continuous bodies throughout the medium. If one of the phases is distributed as a series of isolated pockets, that phase is essentially immobile (although the discontinuities can be cleared by a high velocity flow of the continuous phase). If both phases are mobile (i.e., if they are each connected throughout), the phases must be intertwined in some complicated three-dimensional (3D) pattern; therefore, the flow of each phase is inherently 3D, as sketched in Figure 2-2. The modeling difficulties are accentuated for a fractured medium like the host rock of YM repository because the widely different permeability of the matrix and the fractures sometimes, but not always, segregates the flow of the two components—liquid through the matrix and gas through the fractures. Some of the important effects of two-component, two-phase flow in a porous medium are discussed in the following subsection.

Liquid Suction Pressure. When the liquid saturation is small, the liquid adheres to the solid surfaces of the medium by molecular forces. The effective capillary or suction pressure of these layers may be tens or even hundreds of atmospheres for sufficiently tight, low-permeability matrices, even for saturations of 50 percent or more. Figure 2-3 shows, for example, the variation of capillary pressure with liquid saturation for one of the media used in the laboratory experiments described in Section 4. These large negative pressures are not caused by the familiar kind of surface tension forces, since the required capillary diameter would be only of molecular (or smaller) dimensions. Consequently, conceptual modeling is made even more difficult by the lack of an easily measured physical property that characterizes such large suction pressures.

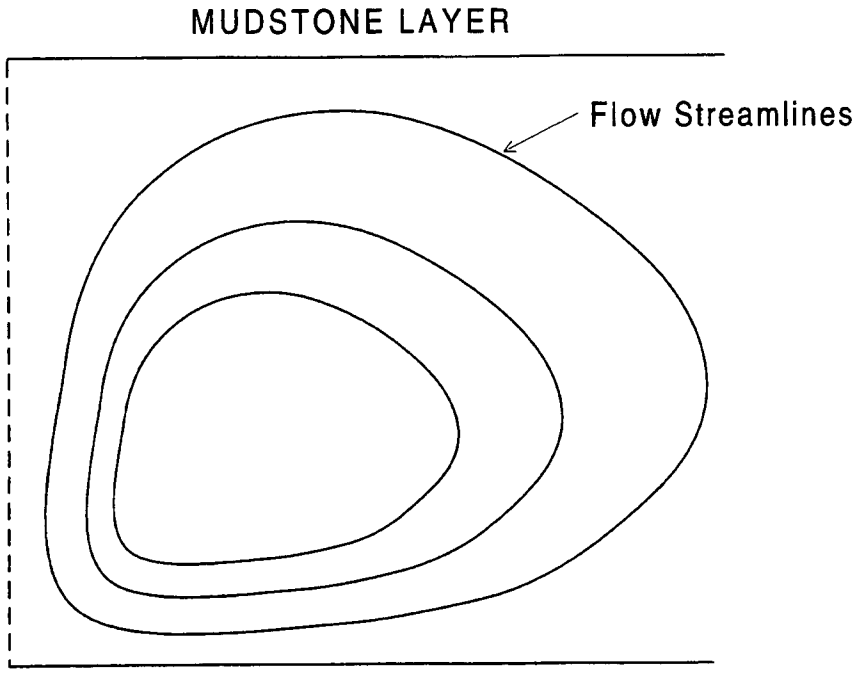

Figure 2-1. Buoyancy-induced flow streamlines in a heated, saturated porous medium

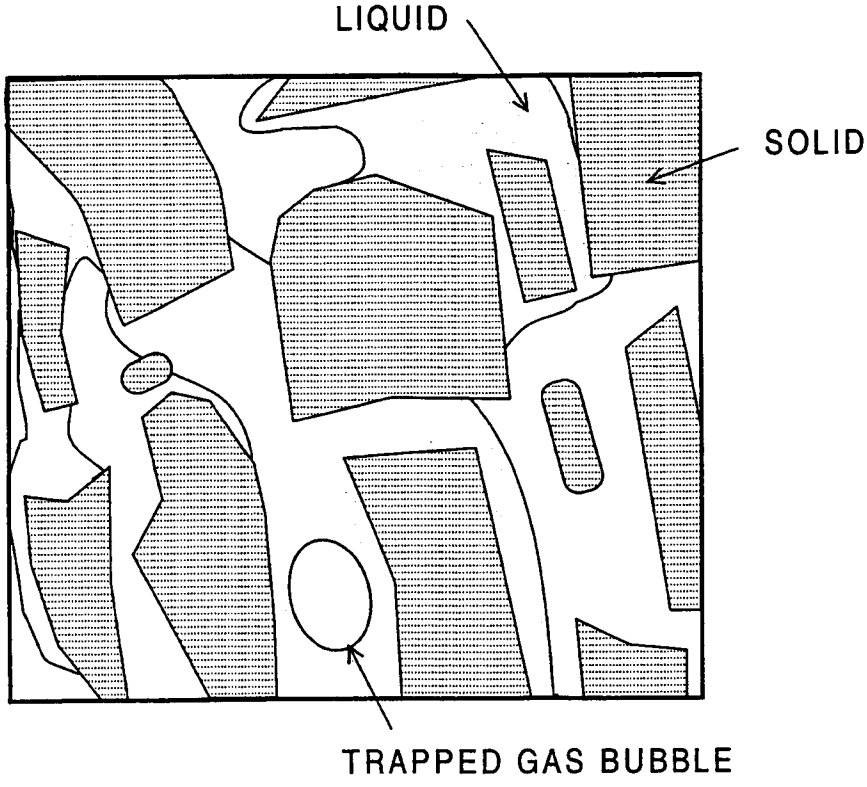

Figure 2-2. Cross-section through a partially saturated porous medium showing continuous and discontinuous bodies of liquid and gas

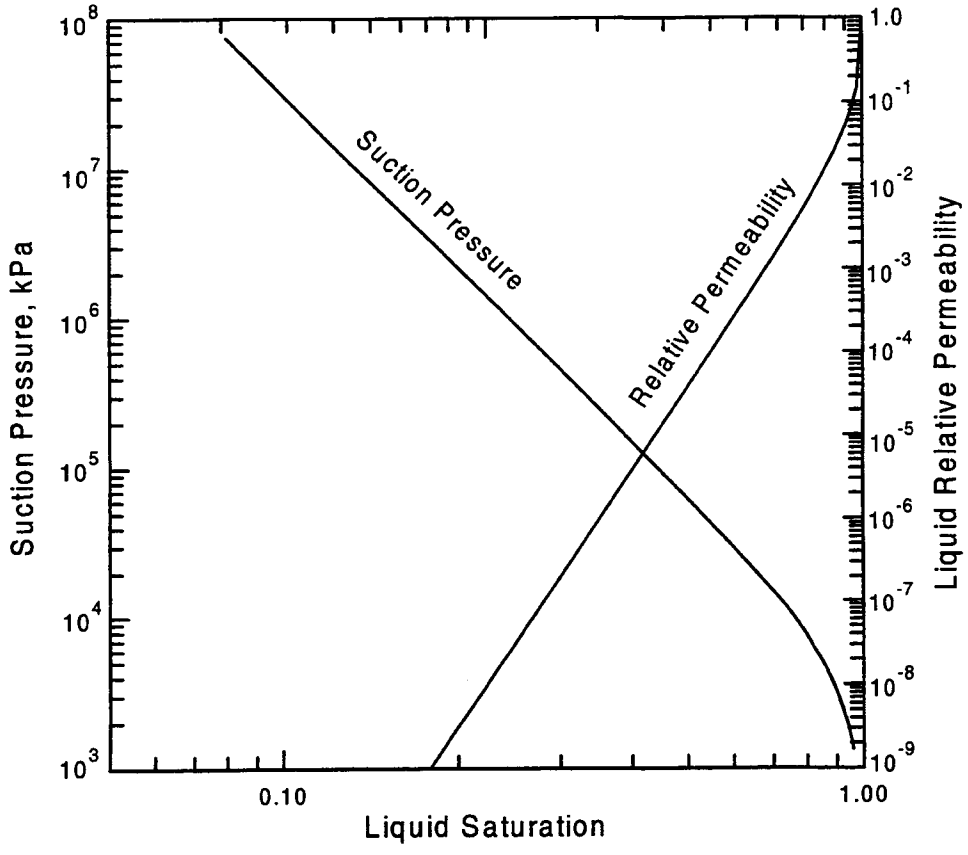

Figure 2-3. Variation of liquid suction pressure and relative permeability for the Apache Leap Test Site tuff used in laboratory cylinder experiment Test 11

Relative Permeability. When a fluid phase that does not occupy the entire pore space is mobile, the permeability of the porous medium for that phase is less than the saturated permeability k. This decrease in k is a consequence of flow channels that are only partially full and thus have a larger wetted area per unit cross-sectional area and a greater viscous friction than full channels. The effective permeability, called the relative permeability $k_{rel,i}$, is usually cited as a fraction of the saturated permeability for the component i of interest. Relative permeability, like suction pressure, depends on the saturation. For media with a pore-size distribution comparable to tuffaceous rocks, the relative permeability of the liquid component decreases by orders of magnitude when the saturation is only marginally less than 100 percent. Figure 2-3, which shows the relative permeability as a function of liquid saturation for the media used in some CNWRA laboratory experiments, demonstrates this conclusion.

As a result of the dependence of permeability on saturation, the flow in an unsaturated medium can exhibit various kinds of instabilities. For example, when water infiltrates at a boundary, the flow rate at a point depends on the saturation level at that point (because of the relative permeability), which in turn depends on the amount of water that has already infiltrated to that location. Thus, locations that receive slightly more than the average infiltration are more open to the flow and receive even more infiltration

than other locations. Consequently, preferential flow, called fingering, can occur. In fractures, nearly all of the infiltrating liquid flows in one or more distinct channels (Miller and Gardner, 1962; Glass et al., 1989a,b). It is also common that a flow distribution, for the same saturation level, is different when the saturation is increasing than when it is decreasing. This difference indicates that relative permeability can also exhibit a hysteresis effect.

Fracture-Matrix Interaction. For fractured media, the effects of saturation on suction pressures and relative permeability can dominate the flow and liquid distribution. Because the effective pore size of a fracture is much larger than that of the matrix, the suction pressures in the matrix are much greater than in the fractures. Thus, the matrix will tend to imbibe any mobile liquid out of the fractures, unless the matrix is nearly 100 percent saturated, and thus fractures remain dry. However, this liquid extraction takes time, so during transient events liquid can flow in the fractures. In addition, mineral coatings on fracture surfaces can limit the imbibition into the matrix. Similarly, the relative permeability of the fractures for gas flow is much larger than that of the matrix. This phenomenon tends to make the gas flow preferentially through the fractures rather than the matrix.

Taken together, the large suction pressures in the matrix and the high gas relative permeability of the fractures can lead to a heat pipe effect when the fluid in a fractured, porous medium is heated locally to near the boiling point of the liquid. As sketched in Figure 2-4, vapor flows away from the heated region through the fractures, condenses in cooler regions, and flows back to the heated region through the matrix (Pruess, 1985; Lichtner and Walton, 1994). These kinds of heat pipes are capable of transporting large amounts of thermal energy away from the heat source and of maintaining, under some conditions, a relatively large volume of material near the heated region at a nearly constant temperature for extended periods of time.

2.1.2 Conservation and Constitutive Equations for Flow

With the concepts just described, the mathematical model of heat and mass transport in an unsaturated, heated porous medium can be summarized as follows.

2.1.2.1 Mass Conservation for Liquid and Gas Components

As an example of the relevant conservation of mass requirements, the differential equation that describes the conservation of the gas phase of the liquid component (i.e., the vapor) is presented. The vapor stored in a small differential volume can change because of: (i) phase changes (evaporation, condensation), (ii) transport due to pressure and buoyancy gradients (Darcy's law), and (iii) diffusion caused by mass concentration gradients. These relations are expressed mathematically as:

$$\frac{\partial}{\partial t}\left(\phi \rho_g S_g w_v\right) = -\nabla\cdot\left(w_v \vec{V}_g\right) - \nabla\cdot\vec{q}_v + \dot{m}_{evap}\,, \qquad (2\text{-}2)$$

where in addition to the porosity ϕ already described, the symbols are defined as:

ρ_g = density of gas (kg/m^3)
S_g = saturation level of gas (-)
w_v = mass fraction of water vapor in the gas mixture (-)

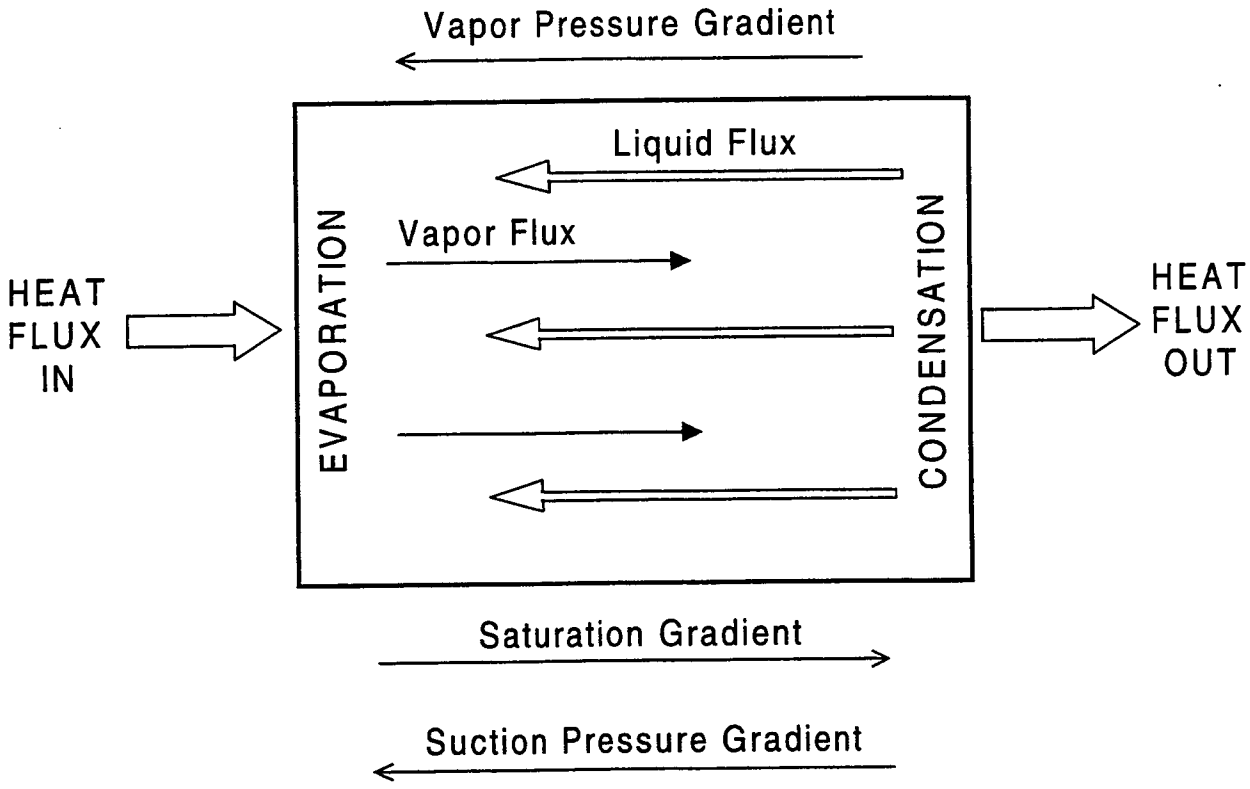

Figure 2-4. Schematic diagram of heat and mass transfer in a porous-medium heat pipe

$\vec{V}_g$ = Darcy velocity (advection) of the gas (m/s)
$\vec{q}_v$ = mass diffusion flux of the vapor through the gas mixture (kg/m^2-s)
$\dot{m}_{evap}$ = rate at which liquid water is evaporated per unit volume (kg/m^3-s)

The small effects due to diffusion of the gas through the liquid phase are neglected in this equation.

There are several equivalent ways of expressing Eq. (2-2) that involve other choices for the controlling variables. Furthermore, by combining Eq. (2-2) with the similar one for the liquid component, the mass transfer between the liquid and vapor phases (i.e., $\dot{m}_{evap}$) can be eliminated. The conservation of mass relations for the other components are similar in form to Eq. (2-2).

Inter-Phase Mass Transfer Rates. In general, an empirical transfer model is needed to evaluate the rate at which liquid and vapor are transferred between the phases $\dot{m}_{evap}$. For porous media flow, however, the need for this model is eliminated by assuming that the partial pressure of the vapor in the air-vapor mixture is equal to the saturation pressure; hence, the relative humidity of the gas is always 100 percent. This assumption, which is equivalent to an infinitely large mass transfer coefficient, is reasonable because

(i) the rates of change in porous media flow are slow compared to the mass transfer rate, and (ii) the liquid and gas phases always remain in intimate contact. There are cases of large suction pressures, as described in the following, when the assumption of 100-percent relative humidity must be modified. Even for these cases, the partial pressure of the vapor can be specified so a mass transfer model is still not needed.

2.1.2.2 Energy Conservation

The media of interest are locally heated by a thermal energy source. The flow of thermal energy affects the transport of fluid through the media and, conversely, the fluid transport may affect the energy flow. These interactions are expressed mathematically as:

$$\frac{\partial}{\partial t}\left[\phi\left(\rho_l S_l u_l + \rho_g S_g u_g\right) + (1-\phi)\rho_s u_s\right] = -\nabla\cdot\left(\rho_l h_l \vec{V}_l + \rho_g h_g \vec{V}_g\right) - \nabla\cdot K\,\nabla T + Q\,, \qquad (2\text{-}3)$$

in which the subscripts l, g, and s represent the liquid, gas, and solid matrix respectively. The new symbols are defined as:

- u = fluid internal energy per unit mass (J/kg)
- h = fluid enthalpy per unit mass (J/kg)
- K = thermal conductivity of the gas-liquid-solid combination (W/m-K)
- T = temperature (K)
- Q = heat sink/source rate of energy addition per unit volume (W/m^3)

Equation (2-3) must be supplemented by constitutive relations that describe how to evaluate, for example, u or K as a function of temperature and pressure of the pure components. These relations are described later. Note that in Eq. (2-3), the liquid, gas, and solid components are assumed to be in thermodynamic equilibrium, which is justified by the slow rate of change of the system compared to the respective thermal diffusivities for the processes of interest.

2.1.2.3 Constitutive Relations

Three kinds of constitutive relations are needed to evaluate the terms in the differential equations listed above: (i) flux laws (actually, conservation of momentum relations specialized for specific kinds of transport), (ii) material relations, and (iii) basic definitions or closure relations.

Flux Laws. The mass transport or advection fluxes of the fluids are given by Darcy's law:

$$\vec{V}_i = -\frac{k k_{rel,i}}{\mu_i}\left(\nabla p_i + \rho_i g \vec{k}\right), \qquad (2\text{-}4)$$

where the subscript i indicates the component (liquid or gas), and

$k_{rel,i}$ = is relative permeability (−)
μ_i = fluid viscosity (Pa-sec)
ρ_i = fluid density (kg/m^3)

Darcy's law can be written in an alternative form to show more explicitly the effects of heating by subtracting out the gravitational pressure gradient, and by using the Boussinesq assumption to express the density in terms of a reference density and the temperature change from the reference condition. The result is:

$$\vec{V}_i = - \frac{k k_{rel,i}}{\mu_i} \left(\nabla \tilde{p}_i - \rho_{i,o} \beta_i \Delta T g \vec{e}_z \right) , \tag{2-5}$$

where the pressure $\tilde{p}_i$ is now the nonhydrostatic or dynamic component only and

$\rho_{i,o}$ = reference density (kg/m^3)
β_i = thermal expansion coefficient of the ith component (K^{-1})

The mass flux in the gas phase due to diffusion is given in terms of the gradient of the relevant mass fraction w_i by Fick's law:

$$\vec{q}_i = - \tau \phi S_i \rho_i D \nabla w_i , \tag{2-6}$$

where the new symbols are defined as

τ = tortuosity or flow path length relative to a straight line (−)
D = binary gas diffusion coefficient (m^2/sec)

Fick's law is valid when the pore size is larger than the mean free path and the gas molecules (e.g., large partial pressure).

Material relations. The physical properties of the liquid are reasonably assumed to depend only on temperature; the relations are not presented here, since they can be obtained easily from standard references (Hirschfelder et al., 1954; van Wylen and Sonntag, 1968). Similarly, the densities of the gas-phase components are assumed to be given adequately by the ideal gas laws in terms of their mixture partial pressures. Other physical properties, such as viscosity of the pure gas-phase components, can be a function of pressure and temperature, but these relations can also be obtained from standard references. The mixture of air and water vapor is also assumed to respond as an ideal gas composed of nonreacting pure components.

The internal energy and enthalpy of the liquid and air are assumed to be linear functions of temperature over the range of interest, with the proportionality constant being the specific heats at constant volume, c_v, and constant pressure, c_p. The internal energy and enthalpy of the water vapor

differ from the internal energy and enthalpy of the liquid water by the respective latent heats of vaporization, u_{lg} and h_{lg}.

When the liquid suction pressure is sufficiently large, the partial pressure of vapor in equilibrium with the liquid water is less than the thermodynamic saturation pressure at the temperature of the liquid. This vapor pressure lowering is given by Kelvin's equation:

$$p_v = p_{sat} \exp\left(\frac{-p_c}{\rho_l R_v T} \right) . \tag{2-7}$$

The new symbols are defined as:

p_v = partial pressure of the vapor (Pa)
p_{sat} = thermodynamic saturation pressure of the pure substance (Pa)
p_c = suction (capillary pressure), a positive value (Pa)
R_v = ideal gas constant for the pure substance (J/kg-K)

One important consequence of Eq. (2-7) is that a gas mixture in regions where the suction pressure is large will have a relative humidity of less than 100 percent, since the relative humidity is equal to the ratio p_v/p_{sat}, and this ratio is less than one. Stated another way, the mixture, if put in contact with liquid that did not have a large capillary pressure, could take up more vapor from the liquid before becoming saturated.

The thermal conductivity K of the mixture of solid, liquid, and gas is a function of the saturation levels. There are several models in use to predict the thermal conductivity. A common model is:

$$K = K_s \left(S_l=0\right) + \sqrt{S_l} \left[K_s \left(S_l=1\right) - K_s\left(S_l=0\right) \right] , \tag{2-8}$$

where K_s is the conductivity of the solid-liquid mixture, for cases when the liquid saturation is either 100 percent or 0 percent, as indicated.

Models are also needed to predict the way capillary suction pressure and relative permeability vary as the saturation level changes. Again, a number of models are in use, but here one of the van Genuchten soil property models (van Genuchten, 1978) is adopted. This model relates the relative permeability of the liquid to the liquid saturation by:

$$k_{rel,l} = (S_{eff})^{\frac{1}{2}} \left[1 - \left(1 - S_{eff}^{-\frac{n}{1-n}} \right)^{\frac{n-1}{n}} \right]^2 , \tag{2-9}$$

where

n = empirically determined parameter (dimensionless)
S_{eff} = effective liquid saturation level, $(S_l - S_r)/(1 - S_r)$ (dimensionless)
S_r = minimum saturation possible (the residual saturation) (dimensionless)

Typically, the residual saturation is very small for most media. Therefore, unless it is stated otherwise, S_r is assumed to be zero here. For this condition, S_{eff} is the same as S_l. Typically, Eq. (2-9) predicts that $k_{rel,l} << 1$ for any liquid saturation slightly less than one. Equation (2-9) was used to compute the results shown in Figure 2-3.

There is no widely accepted comparable relation for the relative permeability of the gas phase. Here, it is assumed that:

$$k_{rel,g} = 1 - k_{rel,l} . \tag{2-10}$$

This assumption is commonly made (Pruess, 1987; Nitao, 1990), although different relations have also been assumed elsewhere (Rasmussen et al., 1993). The main consequence of the assumption is that $k_{rel,g}$ is approximately equal to one for any liquid saturation only slightly less than one.

The van Genuchten model is also used to relate the capillary pressure to liquid saturation:

$$p_c = \alpha^{-1} \left(S_{eff}^{-\frac{n}{n-1}} - 1 \right)^{\frac{1}{n}} , \tag{2-11}$$

where α is an empirically determined constant (Pa^{-1}). Typically, $\alpha << 1$ and n is about 2 for the media of interest here, so from Eq. (2-11), the capillary pressure is predicted to increase by orders of magnitude as the liquid saturation decreases. Equation (2-11) was used for the computations of capillary pressure shown in Figure 2-3.

Basic definitions. The closure relations are stated simply as follows. The capillary pressure is the difference between the gas and the liquid pressure:

$$p_c = p_g - p_l . \tag{2-12}$$

The total gas pressure is the sum of the partial pressures of the vapor and the air:

$$p_g = p_v + p_a . \tag{2-13}$$

The sum of the liquid and gas saturations is always unity:

$$S_l + S_g = 1 \ , \tag{2-14}$$

and the sum of the mass fractions of the gas components in the gas mixture is also always unity:

$$w_v + w_a = 1 \ . \tag{2-15}$$

2.1.2.4 Initial and Boundary Conditions

The response of a partially fractured porous medium to local heating can be dominated in the short term by initial conditions (saturation distribution, for example) existing at the start of heating, and in the long term by conditions imposed at the boundaries (zero heat flux, for example) of the region of interest. For those reasons, the initial and boundary conditions imposed on theoretical, numerical, and laboratory investigations must be chosen with the goal either of simulating the conditions in the YM repository or of eliminating the influence of the initial and boundary conditions on the investigated responses.

In the absence of detailed knowledge of the repository, reasonable assumptions for the initial state for these investigations are (i) isothermal conditions, and (ii) saturation distribution as a function of elevation equal to the equilibrium gravitational distribution. Alternatively, a linear temperature profile can be estimated using the geothermal gradient, whereas the initial saturation can be determined by solving the steady-flow equation.

Reasonable assumptions for boundary conditions depend on the problem to be investigated. Constant temperature (i.e., a heat sink or source) and constant saturation conditions (liquid sink or source) may be appropriate for some of the boundaries; for example, to simulate the water table below the heat sources in the repository. Other boundaries may be appropriately assumed to have zero heat flux (insulated) or zero flow conditions. In any case, it is important that either the boundary conditions used in laboratory, theoretical, and numerical investigations simulate the physical situation of interest, or that the boundaries be so far removed from that region that conditions at the boundaries do not affect the region over the time scale of interest.

2.1.2.5 Closure

Equations (2-1) through (2-15) complete the basic mathematical description of two-component, two-phase flow in a fractured, locally heated porous medium. These equations must be supplemented by other assumptions or models in particular cases. For example, a model is needed to determine an average permeability for a volume of solid that contains fractures when only the permeability of the fractures and the porous matrix are known individually. In addition, some of the terms in the equations may be negligible for certain cases; these cases can be determined by a dimensional or similarity analysis of the terms or effects in conjunction with conceptual models that highlight the effects. The following sections describe these kinds of similarity analyses.

2.2 SIMILARITY ANALYSIS OF THERMOHYDROLOGIC PERIODS

Scaling theories can be developed using the techniques of dimensional analysis or similitude. The dimensionless parameters needed to equate the model to the prototype can be deduced by either analysis methodology. Dimensional analysis is the procedure by which the variables are grouped together to form dimensionless terms by dimensional considerations alone. An implicit knowledge of all pertinent variables and parameters is required in dimensional analysis (Buckingham, 1914; Fox and McDonald, 1978; Corey, 1986). By contrast, similitude theory provides a general procedure by which dimensionless parameters are developed by starting with the representative mathematical equations, transforming these equations into dimensionless form. All aspects of the actual physical system and all the macroscopic phenomena need to be expressed in terms of mathematical equations for similitude analysis to be used (Bear, 1972, Baker et al., 1973; Fox and McDonald, 1978; Miller, 1980; Corey, 1986). Dimensional analysis and similitude are each a form of similarity analysis.

2.2.1 General Application of Similarity Analysis

A laboratory experiment conducted with a physical scale model of a larger system will simulate or represent exactly the response of a larger system if the scale model is geometrically, kinematically, dynamically, and constitutively similar to the large system. The definitions of these types of similarity are:

(i) Geometric Similarity—The model has the same shape and proportions as the large system for those parts of the system in which geometry affects the responses

(ii) Kinematic Similarity—The velocity at each point in the model has the same direction as that in the large system, and the magnitude of the model velocities is a constant multiple of the larger system velocities

(iii) Dynamic Similarity—The forces, torques, and accelerations at each point in the model have the same direction as those in the large system, and their magnitudes are a constant multiple of those in the large system

(iv) Constitutive Similarity—The constitutive properties of the model materials (e.g., the relation between relative permeability and saturation) have the same functional relationship as the large system materials

When the conditions for all four similarities are fulfilled, the response of the model is identical to that of the large system, at homologous locations and homologous times. The ratio between the time required for an event to occur in the model to the time required for the same event to occur in the large system is the time scale factor. A geometric scale factor can be similarly defined, in general, as can scale factors for any physical property or physical phenomenon. It is worth stating that similarity does not apply only to linear systems; nonlinear phenomena can also be duplicated.

Many kinds of requirements are placed on a physical scale model to obtain all four kinds of similarity. These requirements can be determined by a similitude analysis, which develops a set of dimensionless parameters starting from the mathematical equations that describe the desired responses, or by a dimensional analysis, which develops the set of dimensionless parameters more formally by listing

all the pertinent variables and parameters, and then arranging them into dimensionless groups by algebraic methods. In principle, both methods are equally valid and will lead to the same conclusions.

As would be most clearly evident from the dimensionless form of the mathematical equations describing the system response, all four kinds of similarity are satisfied when the dimensionless groups have the same numerical value for the model and the large system. It is common, however, that various kinds of practical implementation difficulties arise when the dimensionless groups of parameters for the model and large system are equated and the consequences of the equality examined. In some cases, for example, two different scale factors are required for the same parameter. In other cases, a physical property must take on a value that is not realizable; for example, the surface tension of the model liquid must be larger than that of any known liquid, or the geometric size of some feature must be smaller than is practical or can be fabricated. When this condition occurs, the model can still be used to investigate some limited part of the general response, but conceptual and analytical mathematical models are needed to help interpret the model responses.

These kinds of physical models with only partial equality of all dimensionless groups are required to investigate thermohydrologic responses of the repository because of the small value of the geometric scale factor for laboratory models and the multiplicity of phenomena that affect the responses of interest. Hence, simplified and conceptual analyses must be an important part of the investigations.

As discussed in Section 1.3, the thermohydrologic responses of the repository can be considered in three different periods that follow each other in time (with some overlapping). Conceptual models of the thermohydrologic responses for each period have been developed and are described in the following sections.

2.2.2 Conceptual Model for the Heating Period

In the heating period, the rate at which heat is released has a dominant influence on thermohydrologic responses. Large heating rates can lead to a so-called hot or dry repository, while smaller heating rates lead to a cool or moist repository. A conceptual analytical model is needed to distinguish between conditions that lead to a hot or to a cool repository so that laboratory and numerical investigations can focus on the relevant parameters.

The DOE G-Tunnel heater tests (Zimmerman et al., 1986; Ramirez et al., 1991) and numerical simulations and laboratory tests conducted here indicate that one of the distinguishing features of the heating regime is whether large pressure gradients develop in the gas phase. If they do, the repository will tend to become of the dry type, because the large gas flow produced by the pressure gradients transports significant amounts of water, in the form of vapor, away from the heated region. Since the source of this water is the liquid water initially in the porous matrix, the repository tends to dry out. Consequently, the focus of the conceptual model for the heating regime is the occurrence of significant gas-phase pressure gradients.

The conceptual model is a generalization of the situation in which buoyancy is the only important force driving the flow. For that situation, gas-phase pressure gradients are of the same magnitude as buoyancy body forces, and an overall circulation of fluid is produced. For this kind of circulatory flow pattern, Darcy's law can be expressed in the following dimensionless form (Green et al., 1993):

$$\hat{V}_g = -\hat{\nabla}\hat{p}_g + \theta\vec{e}_z \ , \tag{2-16}$$

where the caret (^) indicates a dimensionless quantity, $\theta = \Delta T/\Delta T_0$ is the dimensionless temperature change, and ΔT_0 is a maximum or characteristic temperature charge of the heated region. The nonhydrostatic gas pressure has been made dimensionless by the characteristic nonhydrostatic pressure magnitude:

$$p \sim \rho_{g,o} g L \beta_g \Delta T_o \ , \tag{2-17}$$

in which $\rho_{g,o}$ is the characteristic, or representative, gas density of the flow, ΔT_O is the characteristic or representative temperature increase of the flow, and L is the characteristic length scale of the flow.

Similarly, the characteristic, representative velocity of the flow is:

$$V_g \sim \frac{k k_{rel,g}}{\mu_g}\left(\rho_{g,o} g \beta_g \Delta T_o\right) \ , \tag{2-18}$$

With these definitions, it can be seen that all quantities in Eq. (2-16) are of order one. It should be noted that, because of the small numerical value of β_g, the characteristic nonhydrostatic pressure is much less than the hydrostatic pressure. Hence, buoyancy-induced velocities in porous media are relatively small.

The ratio of the characteristic pressure of the model system to that of the large system is the pressure scale factor of the flow. The velocity scale factor is defined in a similar way. The time scale of the flow is equal to the ratio of the length scale to the velocity scale. These scale factors can be used to interpret, or scale up, measurements from a scale model to a larger system. When there are more than two forces driving the flow, more than one velocity scale can be defined; to make the various velocity scales equal, or consistent, imposes additional restrictions on a physical scale model, such as the need to use a more viscous gas for the model or to have smaller temperature increases.

Pressure, velocity, and time scales expressed in terms of heating rates or temperature increases of a more general form than Eqs. (2-17) and (2-18) are needed to determine when large pressure gradients might occur. Just as for the buoyancy flow described above, the analysis starts from Darcy's law.

2.2.2.1 Control Volume Analysis of a Heated Partially Saturated Region

Consider an imaginary control volume around a heater that encompasses the region of high gas pressures, as shown in Figure 2-5. For this conceptual model, a two-dimensional (2D) geometry (i.e., a line heat source) is considered but, as becomes apparent, the same analysis would hold for area heaters and 3D geometries, except for some numerical factors of order unity. The spatial extent of the control volume is somewhat indeterminate, so it will be specified by a characteristic length, L, that can be the same as the control volume radius r_o.

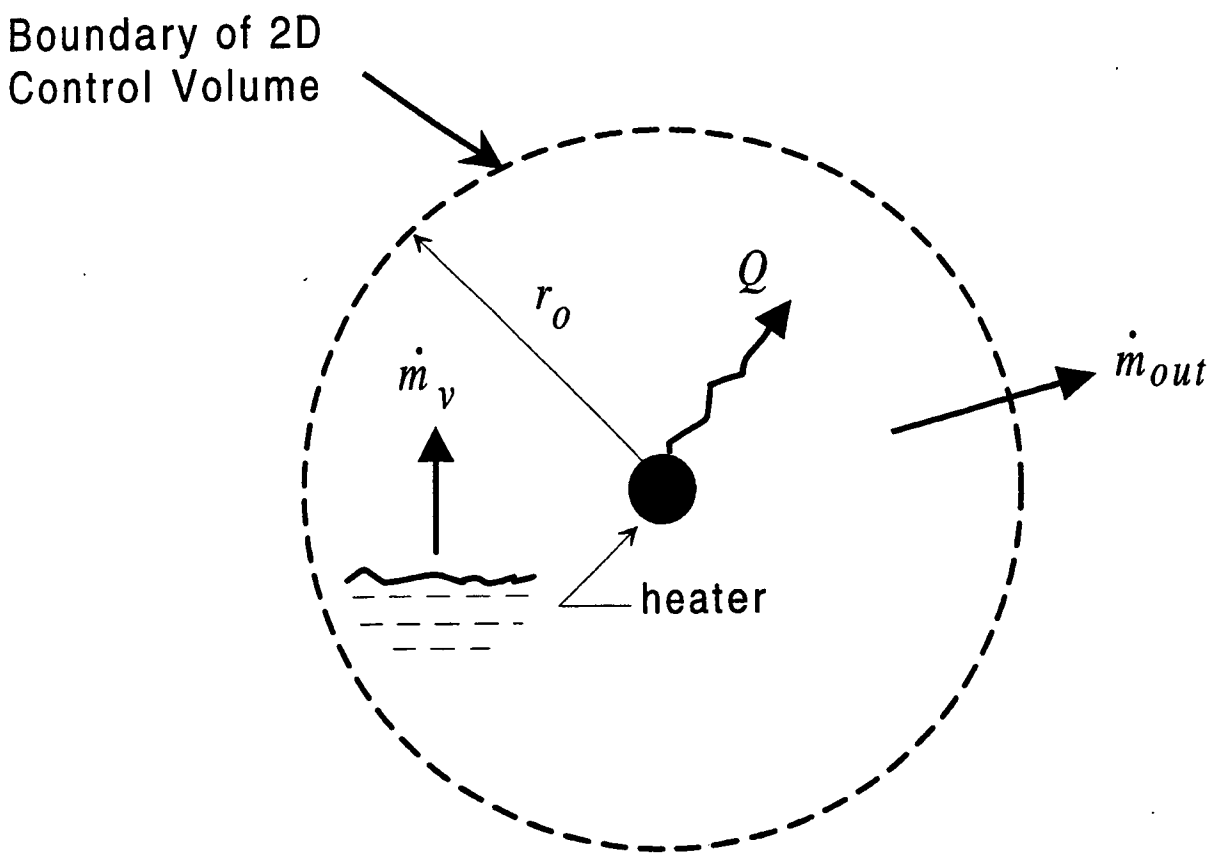

Figure 2-5. Sketch of control volume used for the conceptual model of pressure-driven gas flow during the heating phase

Gas Flow at the Control Volume Boundary. The advective component of the gas flow out of the control volume, driven by the pressure gradient, is given by a simplified form of Darcy's law:

$$\dot{m}_{out} = -(2\pi r_o)\frac{k k_{rel,g}}{\mu_g}\left(\rho_g \frac{dp_g}{dr}\right)_{r_o}, \qquad (2\text{-}19)$$

where the pressure gradient is evaluated near the boundary of the control volume.

Ideal Gas Law in the Control Volume. The flow out of the control volume is related to the thermodynamics of the mass of gas M_g contained in the control volume through the ideal gas law. This law can be expressed as:

$$\bar{V}_g \left(\frac{dp_g}{dt} \right) + p_g \left(\frac{d\bar{V}_g}{dt} \right) = M_g R_g \frac{dT}{dt} + R_g T \frac{dM_g}{dt} , \qquad (2\text{-}20)$$

where $\bar{V}_g = \phi S_g \bar{V}$ is the volume of that part of the control volume $\bar{V}$ containing gas, and p_g and T are characteristic or lumped averages of the control volume pressure and temperature. For the purposes of this conceptual model, the volume of gas in the control volume is considered to be constant over the time period of interest (i.e., the change in S_g is neglected) since the pressure derivative on the left hand side of Eq. (2-20) is typically much larger than the volume derivative.

Conservation of Mass. The rate at which the mass of gas in the control volume changes is related to the rate of vapor generation, $\dot{m}_v$, and the outflow rate $\dot{m}_{out}$:

$$\frac{dM_g}{dt} = \dot{m}_v - \dot{m}_{out} . \qquad (2\text{-}21)$$

Equations (2-20) and (2-21) are combined to give:

$$\dot{m}_{out} = \dot{m}_v + \frac{M_g}{T} \frac{dT}{dt} - \frac{M_g}{p_g} \frac{dp_g}{dt} . \qquad (2\text{-}22)$$

Vapor Generation Rate. The rate at which vapor is generated inside the control volume is computed by assuming, as discussed previously, that the relative humidity remains at 100 percent, which means that the partial pressure of the vapor is the saturation pressure. Vapor pressure lowering may change this relation slightly but this effect is neglected during the heating regime (although not during the cooling regime). Thus, from the ideal gas law for the vapor, it is found that:

$$\dot{m}_v = \frac{\bar{V}_v}{R_v T} \frac{dp_v}{dt} - \frac{M_v}{T} \frac{dT}{dt} , \qquad (2\text{-}23)$$

where M_v is the mass of vapor in the control volume and $\bar{V}_v$ is its partial volume. Since the vapor pressure is the saturation pressure, which is related to other thermodynamic variables by the Clapeyron equation, Eq. (2-23) can also be rewritten in the form:

$$\dot{m}_v = \frac{\bar{V}_v}{R_v T} \left(\frac{\rho_v h_{fg}}{T} \right) \frac{dT}{dt} - \frac{M_v}{T} \frac{dT}{dt} . \qquad (2\text{-}24)$$

Mass Flow Rate at Control Volume Boundary. Equations (2-22), (2-23), and (2-24) are now combined to give an expression for the mass flow rate at the control volume boundary. This expression is:

$$\dot{m}_{out} = \frac{M_v}{T}\left(\frac{h_{fg}}{R_v T}\right)\frac{dT}{dt} + \left(\frac{M_g - M_v}{T}\right)\frac{dT}{dt} - \frac{M_g}{p_g}\frac{dp_g}{dt} \quad . \tag{2-25}$$

The factor $M_g - M_v$ is the mass of air M_{air} in the control volume. Now M_g, M_v, and M_{air} are of the same order of magnitude, as are the quantities $(dT/dt)/T$ and $(dp_g/dt)/p_g$. However, the quantity $h_{fg}/R_v T$ has a numerical magnitude of about 20. Thus, to a good approximation, Eq. (2-25) can be replaced by:

$$\dot{m}_{out} \approx \frac{M_v}{T}\left(\frac{h_{fg}}{R_v T}\right)\frac{dT}{dt} \quad . \tag{2-26}$$

This relation simply expresses the conclusion that most of the flow out of the control volume is composed of the vapor generated by heating the initial mass of liquid in the matrix.

Characteristic Pressure Gradient. Equation (2-26) is substituted into Darcy's law, Eq. (2-19), to yield an expression for the nonhydrostatic pressure gradient at the control volume boundary:

$$\left(\rho_g \frac{dp_g}{dr}\right)_{r_o} = -\frac{\mu_g M_v}{2\pi r_o k k_{rel,g} T}\left(\frac{h_{fg}}{R_v T}\right)\frac{dT}{dt} = -\frac{\phi S_v \mu_g \rho_v r_o}{2 k k_{rel,g} T}\left(\frac{h_{fg}}{R_v T}\right)\frac{dT}{dt} \quad . \tag{2-27}$$

This expression can be used to define a characteristic pressure gradient in terms of other representative quantities after a characteristic or maximum temperature change is determined from the heating rate.

By making the realistic assumption that the maximum temperature occurs before any substantial fraction of the energy addition rate Q (per unit length of the heater, i.e., W/m) is conducted to distant parts of the medium, the temperature increase in Eq. (2-27) can be approximated by an energy balance on the control volume:

$$\frac{dT}{dt} \approx \frac{Q}{\pi r_o^2 \rho_s C_s} \quad . \tag{2-28}$$

It has been assumed that the temperature distribution is governed primarily by heat conduction (Green et al., 1993) and that the thermal properties of the solid medium are representative of the properties of the solid-liquid-gas mixture. Alternatively, dT/dt can be expressed in terms of a maximum or characteristic temperature change ΔT_o and the time duration required to obtain this value, which is roughly the thermal diffusion time scale L^2/α_s. This alternative gives the estimate:

$$\frac{dT}{dt} \approx \frac{\alpha_s \Delta T_o}{L^2}\,, \tag{2-29}$$

where α_s is the thermal diffusivity of the solid. Equations (2-28) and (2-29) are order-of-magnitude equivalent, although the expression based on Q is more convenient to use to establish heating rates for laboratory and numerical investigations when the heating rate of the larger system is known. The expression involving ΔT_o is perhaps more convenient to use to interpret the results of these investigations. Both forms will be carried along in the subsequent discussions.

With these expressions for dT/dt, a characteristic pressure gradient can be defined:

$$\frac{dp_g}{dL} \sim \frac{\phi S_{vo} \mu_{go} \alpha_s Q}{k k_{rel,go} K L T_{avg}} \left(\frac{\rho_{vo}}{\rho_{go}}\right)\left(\frac{h_{fg,o}}{R_v T_{avg}}\right) \approx \frac{\phi S_{vo} \mu_{go} \alpha_s \Delta T_o}{k k_{rel,go} L T_{avg}} \left(\frac{\rho_{vo}}{\rho_{go}}\right)\left(\frac{h_{fg,o}}{R_v T_{avg}}\right)\,, \tag{2-30}$$

where K is the thermal conductivity of the solid material.

Dimensionless Darcy's law and Characteristic Gas Velocity. With this expression for a characteristic pressure, the full Darcy's law can be rewritten in dimensionless form as:

$$\hat{V}_g = -\left(\frac{\mu_{go}}{\mu_g}\right)\left(\frac{k_{rel,g}}{k_{rel,go}}\right)\left(\hat{\nabla}\hat{p}_g - \frac{\beta_g/\beta_{go}\,\theta}{Ad_g}\bar{k}\right)\,. \tag{2-31}$$

The dimensionless group Ad_g, which is called the gas Advection Number, will be discussed below.

The gas velocity in Eq. (2-31) has been made dimensionless by a characteristic velocity equal to:

$$V_g \sim \frac{\phi S_{vo} \alpha_s Q}{L K_s T_{avg}} \left(\frac{\rho_{vo}}{\rho_{go}}\right)\left(\frac{h_{fg,o}}{R_v T_{avg}}\right) \approx \frac{\phi S_{vo} \alpha_s \Delta T_o}{L T_{avg}} \left(\frac{\rho_{vo}}{\rho_{go}}\right)\left(\frac{h_{fg,o}}{R_v T_{avg}}\right)\,. \tag{2-32}$$

The ratios of viscosity, relative permeability, and thermal expansion coefficient in Eq. (2-31) are all of order of magnitude unity and could be neglected if desired. The dimensionless pressure gradient and the dimensionless buoyancy θ are also of order unity. Consequently, the relative importance of pressure gradients and buoyancy with respect to vapor transport depends solely on the magnitude of the dimensionless number Ad_g in Eq. (2-31).

2.2.2.2 Gas Advection Number

The dimensionless Darcy's law, Eq. (2-31) introduced a new dimensionless number that will be named the gas Advection Number, Ad_g. The magnitude of Ad_g determines when the heating rate is

large enough to cause the advection gas velocity to be larger than the buoyancy-induced gas velocity. The gas Advection Number is defined in terms of the relevant parameters by:

$$Ad_g = \frac{\phi S_{vo} \alpha_s \mu_{go} Q}{k k_{rel,go} L \rho_{go} g \beta_{go} K_s \Delta T_o T_{avg}} \left(\frac{\rho_{vo}}{\rho_{go}}\right)\left(\frac{h_{fg,o}}{R_v T_{avg}}\right)$$

$$\approx \frac{\phi S_{vo} \alpha_s \mu_{go}}{k k_{rel,go} L \rho_{go} g \beta_{go} T_{avg}} \left(\frac{\rho_{vo}}{\rho_{go}}\right)\left(\frac{h_{fg,o}}{R_v T_{avg}}\right) . \qquad (2\text{-}33)$$

where the two alternative forms result from using either Eqs. (2-28) or (2-29) to evaluate the characteristic pressure.

The gas Advection Number is physically the ratio of nonbuoyancy pressure gradient to buoyancy body-force gradient. Thus, when $Ad_g >> 1$, gas flow is controlled by pressure gradients induced by a large heating rate. Conversely, when $Ad_g << 1$, gas flow is controlled by buoyancy. When $Ad_g \approx 1$, pressure gradients and buoyancy are comparable in their effects and Eq. (2-31) is then the same as Eq. (2-16). It should be noted, however, that for $Ad_g \leq 1$, the characteristic gas velocity is quite small.

Some of the more important factors that determine the magnitude of Ad_g are:

- Permeability k—smaller values (tighter porous media) lead to larger values of Ad_g
- Matrix thermal diffusivity α_s—larger values (equivalent to a more rapid increase in temperature) lead to larger values of Ad_g

Note that the heating rate Q has no direct, or first order, effect on Ad_g. It does, however, strongly influence the velocity, pressure, and buoyancy responses and, of course, the rate of vaporization.

2.2.2.3 Characteristic Time Scale

According to this conceptual model, the time duration over which large pressure gradients will be created in the gas phase of the flow is roughly the same as the duration needed to obtain a steady-state temperature duration, that is, the time scale of this phenomenon is the thermal diffusivity characteristic time:

$$t \sim \frac{L^2}{\alpha_s} . \qquad (2\text{-}34)$$

This expression for the time scale assumes that the heating duration is at least equal to L^2/α_s. If it is of shorter duration, the maximum pressures will occur near the end of the heating period. The time scale given by Eq. (2-34) depends on both the geometric size L of the heated region and the thermal characteristics α_s of the heated material.

After the gas pressure obtains its maximum value represented by the characteristic pressure, the pressure will slowly decay. The decay time cannot be predicted by this conceptual model, although, if the heating persists, it will be as least as long as the time L^2/α_s required for the pressure to increase to its maximum.

2.2.3 Transitional Period

Eventually, the temperature of the heated volume approaches a near steady-state and the gas pressure thereafter begins to decrease. The advective gas flow thus decreases in magnitude, although the gas flow is still away from the heat source. As the pressure continues to decrease, the capillary pressure gradient becomes larger than the gas pressure gradient, and liquid water begins to flow back toward the heated region. The net flow of water (vapor away from the heated region, liquid toward the heated region) remains near zero for an extended period of time. When the vapor flow has decreased sufficiently, however, there is a net flow of water back toward the heated region. This point represents the initiation of the cooling period.

A separate conceptual model is not developed specifically for the transitional period, since the models developed for the heating and cooling periods could be adapted to the transitional period, if necessary.

2.2.4 Conceptual Model for the Cooling Period

In the cooling period, the heat generation rate is negligible compared to the heating period, and the temperature distribution gradually equalizes throughout the medium. As a result, the water initially driven away from the vicinity of the heating source by heating moves back toward this dried-out region as both liquid and vapor. The primary thermohydrologic concern for this phase is the time required to complete this rewetting as a function of the medium geometry, physical properties, and initial heating rate. Just as for the heating period, a conceptual model of the rewetting is desirable to (i) delineate the dominant phenomena, and (ii) ensure that laboratory and field experiments are designed and interpreted correctly with respect to repository behavior.

2.2.4.1 Rewetting by Liquid Transport

The liquid saturation level near the heating source decreases significantly during the heating period. The resulting saturation gradients in the medium lead to corresponding capillary pressure gradients directed toward the heating source. After the impressed gas pressure gradient caused by the heating diminishes sufficiently (i.e., after the heating rate has diminished sufficiently), these capillary gradients will produce a return transport of liquid water to the dried-out region. The first part in the development of a conceptual model for the cooling period is thus to estimate the capillary pressure gradients.

Pressure Gradients. For this conceptual model, the liquid pressure is expressed as the sum of the gas pressure impressed on the liquid and the pressure difference between the gas and the liquid:

$$p_l = p_g + p_{lg} \tag{2-35}$$

The pressure difference p_{lg} is the negative of the capillary pressure p_c (where the negative sign is used so that p_c itself is a positive value). Further, to ensure that only gradients that create motion are considered, p_c is written relative to the equilibrium pressure $p_{c,\rho}$ that balances the gravitational gradient. Hence:

$$p_{lg} = - p_c + p_{c,\rho} + \left(\rho_{l,\rho} g z - p_{c,\rho}\right) - \rho_{l,\rho} g z \ . \tag{2-36}$$

The sum in parentheses in Eq. (2-36) is equal to zero, and the sum of the first two terms is defined as $-\Delta p_c$, which is the nonhydrostatic component of capillary pressure.

The nonhydrostatic capillary pressure is a function of pore size d, liquid saturation S_l, and liquid surface tension σ (or some other surface property such as adhesion), and whether the liquid wets the medium. Since water wets the media of interest here, the gradient of nonhydrostatic pressure can be expressed in the general form:

$$\nabla\left(\Delta p_c\right) = \frac{\partial \Delta p_c}{\partial S_l} \nabla S_l + \frac{\partial \Delta p_c}{\partial d} \nabla d + \frac{\partial \Delta p_c}{\partial \sigma} \frac{d\sigma}{dT} \nabla T \ , \tag{2-37}$$

where the gradient of σ has been written in a way to show explicitly its dependence on temperature T. For the conceptual model, the equivalent continuum model is adopted, so the variation with d is neglected. Further, although surface tension gradients may not be totally unimportant during rewetting, they are neglected here for simplicity. Thus, Eq. (2-37) is expressed here simply as:

$$\nabla\left(\Delta p_c\right) = \frac{d\Delta p_c}{dS_l} \nabla S_l \ . \tag{2-38}$$

Since $d\Delta p_c / dS_l < 0$, Eq. (2-38) demonstrates that Δp_c increases in the direction in which the saturation decreases and roughly in proportion to it.

Darcy's law. With these definitions and simplifications, Darcy's law for the liquid transport is expressed as:

$$\vec{V}_l = -\frac{k k_{rel,l}}{\mu_l} \left(\nabla p_g - \frac{d\Delta p_c}{dS_l} \nabla S_l - \rho_{l,\rho} g \vec{k} + \rho_l g \vec{k} \right) . \tag{2-39}$$

As explained in Section 2.1.2, the net gravitational gradient is expressed in terms of the temperature change ΔT from ambient and the liquid expansion coefficient β_l, with the result that:

$$\vec{V}_l = -\frac{k k_{rel,l}}{\mu_l}\left(\nabla p_g - \frac{d\Delta p_c}{dS_l}\nabla S_l - \rho_{l,o}\beta_l g \Delta T \vec{k}\right). \tag{2-40}$$

Characteristic Liquid Pressure and Velocity. The increase in gas pressure caused by heating is the initial driving force for fluid transport, so p_g is used to make all pressures dimensionless. While this choice is physically sensible, it has the consequence that not all the dimensionless variables in Darcy's law for liquid transport will be of an order of unity. Using Eqs. (2-30) and (2-38), Eq. (2-40) gives the dimensionless form of Darcy's law for rewetting:

$$\hat{V}_l = -\frac{\mu_{l,o} k_{rel,l}}{\mu_l k_{rel,lo}}\left[\hat{\nabla}\hat{p}_g - \frac{d\Delta\hat{p}_c}{dS_l}\nabla S_l - \frac{(\beta_l/\beta_{l,o})\theta}{Ad_l} g\vec{k}\right]. \tag{2-41}$$

The liquid velocity has been made dimensionless by the quantity:

$$V_l = \left(\frac{\mu_{go}}{\mu_{lo}}\right)\left(\frac{k_{rel,lo}}{k_{rel,go}}\right)V_g, \tag{2-42}$$

where V_g is the characteristic gas velocity defined by Eq. (2-32). Note, however, that since the dimensionless capillary pressure gradient is significantly greater than unity during rewetting, the characteristic liquid rewetting velocity is significantly greater than that given by Eq. (2-42). In fact, from Eq. (2-42), the characteristic liquid velocity during the cooling period is given by:

$$V_l \sim \left(\frac{\mu_{go}}{\mu_{lo}}\right)\left(\frac{k_{rel,lo}}{k_{rel,go}}\right)\left(\frac{d\Delta\bar{p}_c}{dS_l}\right)\left(\frac{\Delta S_l}{L}\right)V_g. \tag{2-43}$$

The liquid Advection Number Ad_l is defined in terms of the gas Advection Number, Ad_g (as given in Eq. (2-33):

$$Ad_l = \left(\frac{\rho_{go}}{\rho_{lo}}\right)\left(\frac{\beta_{go}}{\beta_{lo}}\right)Ad_g. \tag{2-44}$$

Ad_l is considerably smaller than Ad_g, thus indicating that buoyancy effects may be more evident in the liquid flow pattern during cooling than in the gas flow pattern during heating.

Rewetting Times. The characteristic liquid velocity is used to estimate the time for the volume near the heating source to regain its original liquid saturation level when only liquid-phase transport is active. If the characteristic decrease in liquid saturation during the heating period is ΔS_l, the mass of liquid ΔM_l that must be replaced during rewetting is about $\bar{V}\phi\rho_{lo}\Delta S_l$, where $\bar{V}$ is the affected volume (roughly equivalent to the control volume introduced in Section 2.2.1) and ϕ is the medium porosity. The

rewetting mass flow rate is roughly $A\rho_{lo}V_l$ where A is the area bounding the volume $\bar{V}$, and V_l is the characteristic liquid velocity. Thus, from Eq. (2-43), the time required to rewet the dried-out zone from liquid flow alone is:

$$t_l = \left[\frac{(\mu_{lo}/\mu_{go})(k_{rel,go}/k_{rel,lo})(\rho_{lo}/\rho_{go})(R_v T_{avg}/h_{fg})(T_{avg}/\Delta T_o)}{S_{wo}(\Delta\hat{p}_c/\Delta S_l)}\right]\left(\frac{L^2}{\alpha_s}\right). \qquad (2\text{-}45)$$

Note that the formal dependence on saturation decrease ΔS_l cancels out of Eq. (2-45). However, a representative value ΔS_l must be known to compute an appropriate value for $k_{rel,lo}$ and $\Delta\hat{p}_c/\Delta S_l$. The factor L^2/α_s in Eq. (2-45) is the time scale over which the initial heating, gas pressure increase, and drying occurs. Thus, Eq. (2-45) shows that during the cooling period, the rewetting time is proportional to the drying time of the heating period, although the proportionality constant may be much larger than one or less than one, depending on the physical properties of the medium and the decrease in S_l during the heating.

The saturation decrease ΔS_l needed to estimate both $k_{rel,lo}$ and the representative capillary pressure gradient can be estimated in principle by using the relations derived in Section 2.2.2 for the heating period. However, the estimate is likely to be fairly crude because the conceptual model is capable of making predictions only to within an order of magnitude, and the total range of ΔS_l is typically only one order of magnitude. Thus, a more reasonable approach is to assume that ΔS_l is about 0.5, which is the approach taken here.

Rewetting Time Similitude. Equation (2-45) represents the similarity relation that can be used to interpret or scale up laboratory and field tests.

2.2.4.2 Rewetting by Vapor Diffusion

Diffusion of vapor can also contribute to rewetting the dried-out region. The diffusion is driven by the vapor partial pressure gradient created by the vapor pressure lowering in zones of low liquid saturation as explained in Section 2.1. This kind of vapor pressure gradient has also been called a relative humidity gradient.

Vapor Mass Flux. For Fickian diffusion, the vapor flux is given by:

$$\vec{q}_v = \tau\phi S_v \rho_v D \nabla w_v , \qquad (2\text{-}46)$$

where D is the binary diffusion coefficient of air and water vapor, τ is the tortuosity of the porous medium, and w_v is the mass fraction of water vapor in the gas mixture. The mass fraction w_v can be determined in terms of the partial pressure p_v of the vapor as follows:

$$w_v = \frac{M_v}{M_g} = \frac{M_v}{M_v + M_a} = \frac{M_v}{M_v + 1.61 M_v (p_a/p_v)} = \frac{p_v}{p_g + 0.61 p_a} , \qquad (2\text{-}47)$$

where the ideal gas law has been used, and the numerical factor 1.61 is the ratio of the gas constants for water vapor and air.

During the rewetting period, the total gas pressure p_g remains approximately constant and equal to ambient throughout the region of interest. Thus, a vapor pressure gradient is accompanied by an approximately equal air partial pressure gradient in the opposite direction. Consequently, the gradient of vapor mass fraction can be found from Eq. (2-47) to be:

$$\nabla w_v = \left[\frac{p_g + 1.22 p_a}{(p_g + 0.61 p_a)^2}\right] \nabla p_v \approx \left(\frac{1}{2 p_v}\right) \nabla p_v \ . \tag{2-48}$$

(The last approximation follows from the assumption that the partial pressures of air and vapor in the mixture are roughly the same. If the partial air pressure is much larger than the vapor pressure, the numerical factor is 0.85 rather than 0.5, and if it is much smaller than the vapor pressure, the factor is 1. In either case, the difference is negligible in a conceptual model.)

Rewetting Times. The mass flow of vapor into the affected region is given by the product of the mass flux and the flow area. The time required for this flow to increase the liquid saturation to its initial level is thus about:

$$t_g = \left(\frac{\rho_{lo}}{\rho_{wo}}\right)\left(\frac{\Delta S_l}{\tau S_v}\right)\left(\frac{p_v}{\Delta p_v}\right)\frac{L^2}{D} \ , \tag{2-49}$$

where Δp_v is the magnitude of the vapor pressure difference. This relation can be compared to the liquid-flow rewetting time estimate by noting that D has a value that is approximately 30 times larger than the thermal diffusion coefficient α_s. Thus:

$$t_g \approx 0.03 \left(\frac{\rho_{lo}}{\rho_{wo}}\right)\left(\frac{\Delta S_l}{\tau S_v}\right)\left(\frac{p_v}{\Delta p_v}\right)\frac{L^2}{\alpha_s} \ . \tag{2-50}$$

This relationship will be used in the next chapter in a proposed scaling theory.

Rewetting Time Similitude. Although the contribution of vapor diffusion to rewetting is less important than liquid water flow in most cases, Eqs. (2-49) and (2-50) provide a similarity relation to interpret laboratory and field tests for those cases in which vapor mass diffusion should be considered.

3 DESCRIPTION OF LABORATORY EXPERIMENTS

Laboratory-scale experiments were conducted to study the thermally induced redistribution of moisture in porous media. For the purpose of identifying the various experiments, they are designated as Tests 1 through 11. Results from the laboratory-scale experiments are intended to be used in addressing basic technical concerns regarding thermohydrologic phenomena and in formulating scaling theories. This section provides information on the experimental groups, instrumentation and sensors,and the hydraulic and thermal characterization methods. Also included is a summary of the properties of the test media used in the laboratory experiments. Additional information on these topics can be found in: (i) the report by Green et al. (1993) which describes Test 1 in great detail; and (ii) Manteufel et al. (1992) and Manteufel and Green (1993), which summarize Tests 1 and 2, and semi-annual CNWRA progress reports.

3.1 THERMOHYDROLOGIC ISSUES AND CONSIDERATIONS

A series of laboratory experiments has been performed in an attempt to replicate and characterize the three distinct thermal periods: heating, transitional, and cooling. To study thermohydrologic phenomena at the laboratory scale, the experiments were designed in a manner that would permit addressing the following basic technical questions:

- What are the principal mechanisms controlling the redistribution of moisture?
- Under what thermohydrologic conditions and time frames do individual mechanisms predominate?
- What hydrothermal regimes are associated with each driving mechanism?
- What is the temporal and spatial scale of each hydrothermal regime?

The data described here were used in the interpretation of the laboratory experiments and in evaluating scaling theories. The interpretations and evaluations are presented in Section 4.

3.2 DESCRIPTION OF EXPERIMENTAL GROUPS

Eleven laboratory-scale experiments were conducted and are designated as Tests 1 through 11. The experiments are categorized according to: (i) the fluid phase that is the focus of the study, (ii) temperature regime, (iii) geometry, and (iv) test medium. Two groups of experiments were designed to address the four basic technical questions regarding coupled thermal and hydrologic flow processes. In addition, they were designed to provide the data necessary for testing various scaling theories proposed in Section 2. The first group, referred to as the liquid flow experiments, was designed to study the flow patterns in the liquid phase. The second group, designated as the gas flow experiments, focused on the dynamics of the gas phase and the buildup of gas pressure. The critical question addressed in both groups is how to relate the fluid flow regimes to system variables; that is, pressure, temperature, heat source, and media properties. Of particular interest are the rates and directions of liquid and vapor flow and their time histories during the heating and cooling periods. The laboratory-scale experiments are summarized in Table 3-1.

Table 3-1. Summary of laboratory-scale thermohydrology experiments

Test Number	Group	Temperature Regime	Geometry	Medium
1	Liquid flow	Sub-boiling	1D rectangular	Silica beads
2	Liquid flow	Sub-boiling	1D rectangular	≤ 149 μm tabular alumina
3	Liquid flow	Sub-boiling	2D rectangular	≥ 44 μm and ≤ 149 μm tabular alumina
4	Liquid flow	Sub-boiling	2D rectangular	≥ 44 μm and ≤ 149 μm tabular alumina
5	Liquid flow	Boiling	2D rectangular	≥ 44 μm and ≤ 149 μm tabular alumina
6	Liquid flow	Boiling	2D rectangular	Ceramic
7	Liquid flow	Boiling	2D rectangular	Cement slurry (C3)
8	Gas flow	Boiling	1D radial	≤ 250 μm tabular alumina
9	Gas flow	Boiling	1D radial	Cement slurry (C4)
10	Gas flow	Boiling	1D radial	Cement slurry (C6)
11	Gas flow	Boiling	1D radial	Tuff

Both groups of laboratory experiments followed the basic strategy of beginning with homogeneous test media and idealized hydrothermal conditions, and then progressing to more complex media and hydrothermal conditions that would better represent the repository setting. The absence of heterogeneous hydraulic characteristics in the initial experiments was desired to allow direct observation of thermohydrologic phenomena and to simplify interpretation of results. It was expected that the knowledge gained in the idealized setting would be helpful in designing and instrumenting the more complex experiments, as well as in interpreting those experimental results. This approach would allow each subsequent experiment to build upon the knowledge gained in previous experiments and to focus on specific experimental design modifications.

3.2.1 Liquid Flow Redistribution Experiments

To investigate thermally driven moisture redistribution in partially saturated porous media seven experiments were conducted. These tests can be divided into two subcategories according to geometry, the first subcategory with Tests 1 and 2 and the second with Tests 3 through 7. The two subcategories

had slightly different objectives. The primary objective of the first sub-category was to observe the redistribution of moisture through partially saturated porous media in response to a one-dimensional (1D) horizontal thermal gradient. The geometry of the two tests in this sub-category was intentionally simple and uniform media were used (with the exception of the simulated fracture in Tests 1 and 8) to permit observation of heat and mass transfer in the absence of complex boundary conditions and heterogeneities. It is important to note than even though these tests were designed to be 1D, apparent 2D, or even 3D flow features were observed in the actual experiments. A similar statement can be made with regard to the 2D and 1D radial experiments. Nonetheless, the experiments are referred to as 1D because their primary design was limited to 1D.

Theoretical development conducted simultaneously with Tests 1 and 2 identified a need for experimental data to test the proposed scaling theories. Therefore, the objective of the second sub-category of tests was altered to provide observable and quantifiable experimental results for evaluating heat and mass transfer mechanisms predicted for different geometries and possibly to assess the proposed scaling laws. This development necessitated a modification in the technical objective of Tests 3 through 7 from the objective of earlier experiments. Whereas Tests 1 and 2 were essentially 1D, the heat source in Tests 3 through 7 was designed to be a point source, rendering these tests into a 2D configuration. The second category of tests was 2D due to the off-centered location of the point heat source. This change in the geometry of the experimental design was made to provide a database more appropriate for evaluating the scaling theories under development. It was anticipated that information on fluid flow derived from this category of tests would not only aid in evaluating the scaling relationships, but also contribute to the basic investigation of heat and mass transfer mechanisms. Further development of the proposed scaling theories eventually necessitated an additional change in the objective of the experiments. This change resulted in the gas pressure buildup experiments.

The geometric configuration of all seven liquid flow redistribution tests was similar but not identical. Differences among the experiments included instrumentation, type of medium, and heat source. Detailed descriptions of the configurations, design, and instrumentation are summarized in Table 3-2. In all the liquid flow redistribution tests, an upright rectangular cell filled with uniform porous media was heated to induce moisture redistribution. All seven rectangular test cells were of similar construction. The right and left vertical side boundaries were constructed of anodized aluminum through which water was circulated to maintain their respective temperatures constant. The top, bottom, front, and back were constructed of clear plexiglass to permit direct visual observation of fluid flow. Temperature and matric potential were measured directly with thermistors and tensiometers, respectively. Moisture content was measured indirectly with a horizontally oriented gamma-ray densitometer.

The direction of liquid fluid flow was visually illustrated using injected dye to provide optical contrast and photographed. The dye was injected at two locations in Tests 1 and 2 (one each on the right and left sides of the test cell) and at five locations in Tests 3 and 4 (one above, below, right, and left of the heater and one located horizontal to the heater but near the left test cell boundary). No more than 0.1 ml of dye was used per injection to minimize any potential fluid movement resulting from a local increase in saturation. A red food color dye was used in all experiments. The dye ports in all these tests extended through most of the test medium from the back of the test cell so that the dye was introduced into the medium at a point very close to the front plexiglass wall of the test cell. Two dye ports were installed in the Test 7 cell through the front plexiglass wall of the cell into the cement slurry late in the duration of the experiment. However, this proved to be ineffective, possibly due to the low permeability of the cement as the dye became too faint for viewing prior to any flow movement becoming apparent.

Table 3-2. Summary of laboratory-scale experimental configuration, thermal design, and instrumentation

Test Number	Saturation	Test Geometry (cm)	Thermal Conditions	Instrumentation		Saturation Measurements (Densitometer Measurements)	Dye Injection
				Temperature Sensor	Pressure Sensor		
1	0.65	20.3×15.2× 5.7 fracture	right 60 °C for 98 days left 20 °C	3 internal 2 external	2 tensiometers	4 rows of 6	2 ports
2	0.50	20.3×15.2× 5.7	right 90 °C for 80 days left 20 °C	8 internal 2 external	6 tensiometers	4 rows of 6	2 ports
3	0.70	15.2×15.2×6.6	right, left 20 °C internal heater at 60 °C for 89 days, 90 °C for 58 days	6 internal 2 external	6 tensiometers	8 rows of 12	5 ports
4	0.70	15.2×15.2×6.6 fracture	right, left 20 °C internal heater at 60 °C for 90 days, 90 °C for 84 days	6 internal 2 external	6 tensiometers	8 rows of 12	5 ports
5	0.585	15.2×15.2×6.6	right, left 20 °C internal heater ramped to 122 °C in 30 days, 30 days at 122 °C	2 external	None	8 rows of 12	None
6	0.80 and 0.50	15.2×15.2×5.5	right, left 20 °C 8 days at 58 °C, 3 days at 90 °C, 7 days at 120 °C, 4 days at 20 °C, 5 days at 95 °C, 11 days at 124 °C, 4 days at 178 °C	2 external	None	4 rows of 12 6 rows of 11 7 rows of 17	None

Table 3-2 (Cont'd). Summary of laboratory-scale experimental configuration, thermal design, and instrumentation

Test Number	Saturation	Test Geometry (cm)	Thermal Conditions	Instrumentation		Saturation Measurements (Densitometer Measurements)	Dye Injection
				Temperature Sensor	Pressure Sensor		
7	0.50	15.2×15.2×6.6	right, left 20 °C 25 days at 144–160 °C	2 external	None	4 rows of 12 6 rows of 11 7 rows of 17	2 ports added late
8	0.50	11.4 tall, 30.5 cm diameter cylinder	side wall at 20 °C 120 °C for 4 hr	1 at heater 1 at side wall	1 at heater 2 at side wall	None	None
9	0.47	11.4 tall, 30.5 cm diameter cylinder	side wall at 20 °C 8 days at 193 °C	1 at heater 1 at side wall	1 at heater 2 at side wall	2 radial lines of 34	None
10	0.50	11.4 tall, 30.5 cm diameter cylinder	side wall at 20 °C 7 days at 215–240 °C	1 at heater 1 at side wall	1 at heater 2 at side wall	1 radial line of 34	None
11	0.30	11.4 tall, 30.5 cm diameter cylinder	side wall at 20 °C 7 days at 162 °C	1 at heater 1 at side wall	1 at heater 2 at side wall	1 radial line of 34	None

A generalized schematic of the test cell for Tests 1 and 2 is illustrated in Figures 3-1, and for Tests 3 through 7 in Figure 3-2.

The densitometer used in the liquid flow redistribution tests, identified as the x-z densitometer, was configured to measure density contrasts in an x-z oriented plane. Saturation was calculated from measured density contrast measurements along several horizontally oriented traverses in each experiment. The number of traverses and measurements per traverse varied with the tests. Evenly spaced densitometer measurements were collected in most traverses. More closely spaced densitometer measurements near the heater were collected in Tests 6 and 7. The calculated saturation values represented an average saturation through the short dimension of the rectangular enclosure at the point at which the densitometer measurement was recorded. Although variations in saturation along the short dimension were not detectable with this experimental configuration, the relatively short vertical dimension (5.5 or 6.5 cm) of the test medium tends to minimize any importance this variation might have. Therefore, either a vertically oriented 2D saturation distribution or a vertically or horizontally oriented 1D profile of saturation was constructed from the x-z densitometer measurements.

3.2.2 Gas Pressure Buildup Experiments

Continued development and refinement of the scaling theories identified specific heat and mass transfer mechanisms for experimentation. In particular, identification of the buildup of gas pressure as a key indicator in the scaling analysis led to the design of the last set of laboratory-scale experiments. These experiments, identified as Tests 8 through 11, were designed to permit the observation of gas pressure buildup and the associated concurrent redistribution of moisture. The fundamental objective of the gas pressure buildup tests was to provide a database for evaluation of the proposed scaling relationships and to contribute to the continued investigation of heat and mass transfer mechanisms.

In the gas-pressure buildup tests, an upright cylindrical configuration was used to provide a medium in which the buildup of gas pressure in an intact matrix could be monitored. The cylinders were 11.5 cm tall and had a diameter of 30.5 cm. Instrumentation in the gas pressure buildup tests was limited to a thermocouple and pressure transducer incorporated into a axially centered, vertically oriented electric cartridge heater and a thermocouple, pressure transducer and manometer inserted into the outside wall of the test cell (Figure 3-3). Intrusive instrumentation was minimized in the gas pressure buildup tests to ensure that the test medium was intact and that new gas pathways were not inadvertently introduced via the instrumentation. Additionally, great care was exercised to prevent gas flow along the two horizontal ends of the cylinders by covering the consolidated test medium ends (of Tests 9 through 11) with silicon cement prior to enclosure within the plexiglass end plates.

The densitometer used in the gas buildup tests, identified as the x-y densitometer, was configured to measure density contrasts in an x-y oriented plane. Saturation was calculated from measured density contrast measurements along one or two radially oriented traverses in each experiment. The calculated saturation values represented an average saturation for the vertical span of the cylinder at the point at which the densitometer measurement was recorded. Although vertical variations in saturation were not detectable with this experimental configuration, the relatively short vertical dimension (11.4 cm) and the cylindrical shape of the test medium tended to minimize any impact this variation might cause. Therefore, a horizontally oriented 1D radial distribution of saturation was obtained from the x-y densitometer measurements. The number of radial traverses and measurements per traverse varied with the tests. Traverses in two radial directions separated by 90° were measured in Test 9, but this

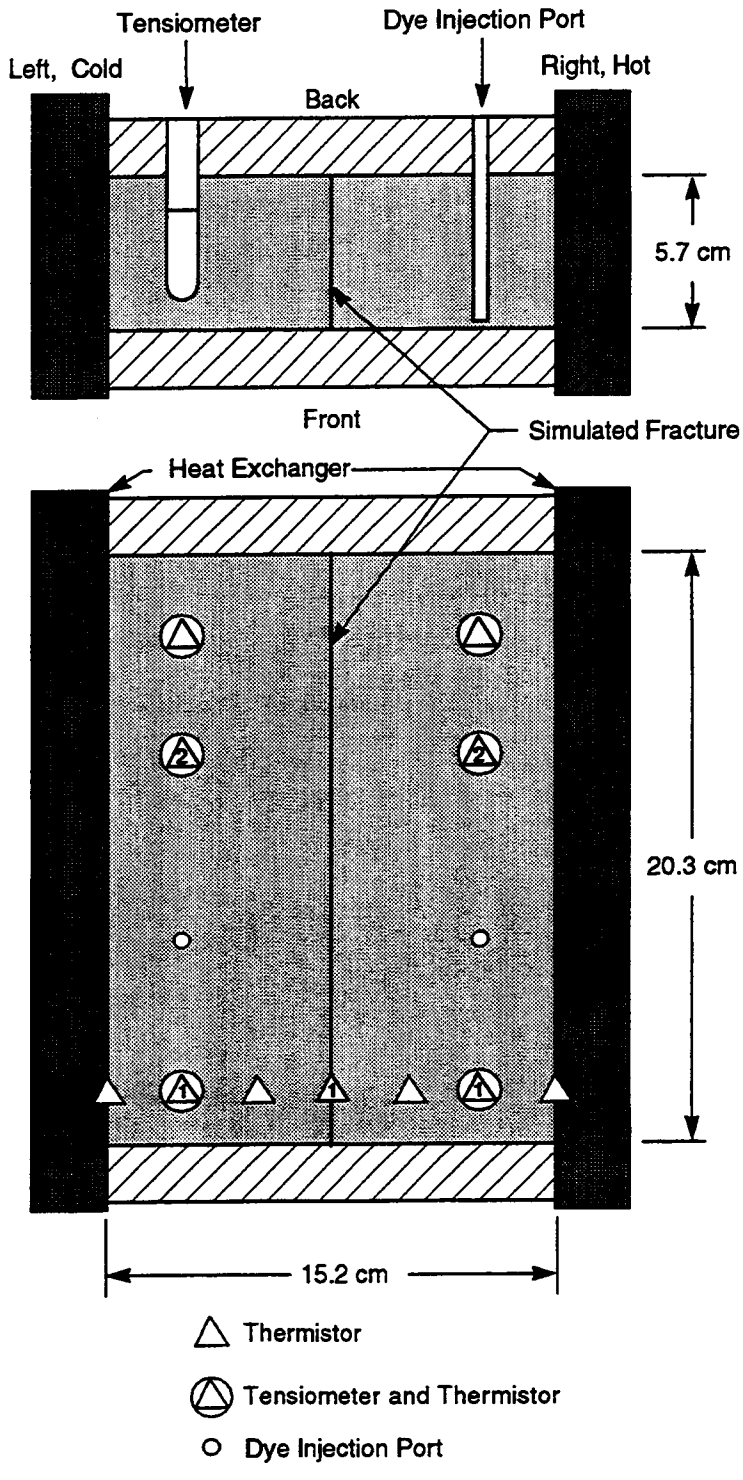

Figure 3-1. Experimental cell for Tests 1 and 2. Internal thermistors for Test 1 are denoted with a 1. All thermistors, except the internal thermistor along the midline, were used in Test 2. Tensiometers only at location 2 were used in Test 1. Tensiometers were used at all six locations in Test 2.

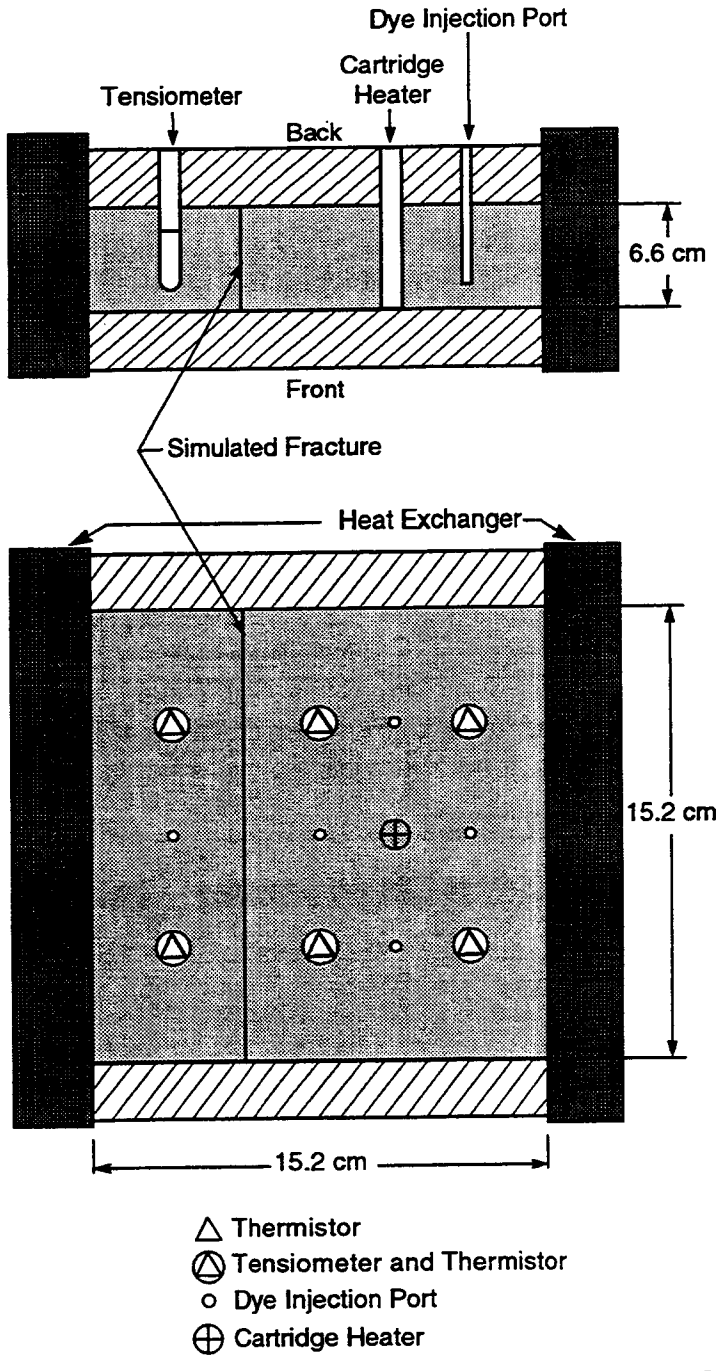

Figure 3-2. Experimental cell for Tests 3 through 7. Thickness of Test 6 was 5.5 cm. Tensiometers are numbered 1 through 6 from left to right and top to bottom.

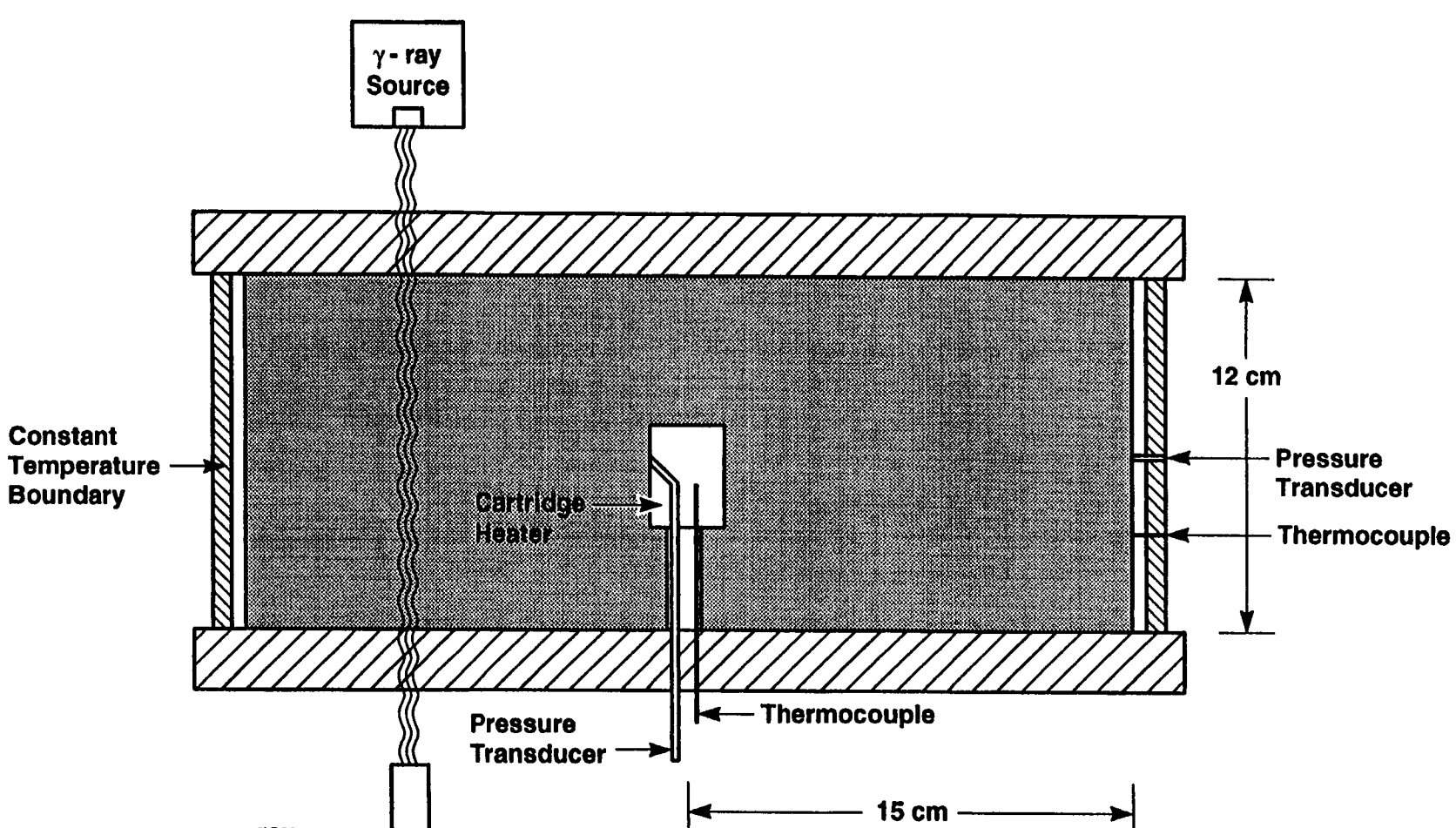

Figure 3-3. Experiment cell for Tests 8 through 11

configuration was reduced to a single radial traverse in Tests 10 and 11 to increase the frequency of the saturation profile measurements, since each profile required 1.5 to 2.0 hr of measurement. Although some detailed saturation information may have been lost by the relatively long measurement times, no feasible alternative was possible. Measurement times were required to be 1.5 to 2.0 hr to provide the desired accuracy.

Three different types of media were used in the gas pressure buildup tests; tabular alumina, cement slurry mixture, and tuff. The first two of these media were selected to provide a uniform test medium of sufficiently low permeability to accommodate the objectives of the gas pressure buildup tests. Tabular alumina was used in the first experiment in this group. This experiment, Test 8, was conducted as a scoping experiment to evaluate the feasibility of the gas pressure buildup experiments. However, the relatively high permeability of the alumina powder (5.5×10^{-14} m^2) rendered it inadequate for experiments in which gas pressure gradients were of interest. Tests 9 and 10 had cement slurry mixtures as their media material. The permeability of the cement slurries proved to be adequately low, and a sufficiently uniform cement slurry mixture was attained after several attempts; however, this medium also proved to be unsatisfactory. Although the cement slurry mixtures were allowed to cure at room temperature for a period in excess of 30 days, additional curing of the cement slurry mixture appeared to continue throughout the course of the experiment. Unfortunately, a continued decrease in the permeability was also experienced with curing. This phenomenon was noted and measured during saturated hydraulic conductivity measurements of the cement slurry mixtures. Although uniformity of the test medium was impacted, a stable medium of sufficiently low permeability was obtained through the use of an intact piece of tuff from the Apache Leap Test Site (ALTS) for the final gas pressure buildup test.

3.3 DESCRIPTION OF INSTRUMENTATION AND SENSORS

To monitor the laboratory-scale experiments, instrumentation was used to measure the changes in: (i) temperature, (ii) moisture content, (iii) capillary pressure head, (iv) gas pressure, (v) tracer movement, and (vi) heater power. The specific instrumentation selections were based on a detailed review of various intrusive and nonintrusive sensing techniques; this review is documented in Green et al. (1993). A description of the instrumentation and sensors used in the series of laboratory experiments is presented in the following sections.

3.3.1 Temperature Sensors

Thermistors were used to measure the temperature of the heater plates and the media in Tests 1 through 7. In order to reduce the effects of sensor intrusion on the flow field, small-diameter temperature sensors (1 mm) were used in Tests 8 through 11. The specific temperature sensors used in the experiments are listed in Table 3-3.

3.3.2 Gas Pressure Sensors

Gas pressure sensors were used in Tests 8 through 11 to measure the gas pressure at the heater and in the media container. The pressure sensors were model 142PC05D, manufactured by Micro Switch Corporation. The sensor measurement range was from 0 to 5 psig (0 to 0.34 bar) with a measurement uncertainty of ± 1.0 percent of full-scale output. The locations of the pressure taps for these tests are shown in Figure 3-3.

Table 3-3. Temperature sensors used in experiments

Manufacturer	Model	Accuracy
YSI Incorporated	Thermistor: #031-46031-4-RPM-120-ST	±0.5 °C
YSI Incorporated	Thermistor: #030-44006-4-RPM-120-ST	±0.5 °C
OMEGA Engineering Co.	Thermocouple: TMTSS-020U-6	±1.0 °C

3.3.3 Tensiometers

Tensiometers were used in Tests 1 through 5 to measure the capillary pressure head. A schematic of the tensiometer design is shown in Figure 3-4. The tensiometer consisted of a porous ceramic cup that was bonded to a plastic tube. The ceramic cup was inserted into the medium before the test medium was placed in the respective test cell. The tensiometers were filled with water prior to initiation of the experiment. After injection of the water, a pressure sensor was attached to the end of the tensiometer. Water would flow between the tensiometer and the medium (through the porous cup) until pressure in the tensiometer equaled the capillary pressure in the medium. When this equalization occurred, hydraulic equilibrium through the porous cup was assumed to exist.

The tensiometer porous cups were 9.5 mm in diameter and 28 mm long. The Soil Moisture Equipment Corporation Model 652X07-B1M3 cups were used as one-bar high-flow cups. The pressure sensors, manufactured by Micro Switch Corporation, were Model 140PC05G with a pressure range from 0 to 5 psi vacuum (0 to −3.5 m of water) with an accuracy of ±1.0 percent of the full scale output. For Tests 7 and 8, temperature sensors were placed inside the tensiometers to provide additional temperature measurements without further disturbing the medium by introducing additional sensor intrusions into the medium.

3.3.4 Moisture Content Measurements

The gamma-ray densitometry methodology (Nichols and Heaviside, 1988, Gilboy, 1984) was selected to provide saturation measurements of the test medium because: (i) the technique is nonintrusive and does not disrupt the flow in the test medium, (ii) measurements can generally be conducted within an acceptable period of time, and (iii) the accuracy of the measurement technique is acceptable for most applications in this project. The standard method for calculating water saturation level from the densitometer reading requires detailed information about material and fluid properties in order to account for the attenuation of all components of the system (e.g., cell walls, dry medium, and water). Saturation is calculated from the total count rate using the exponential expression (Gardner, 1986):

$$I/I_o = e^{-\left[X\left(\mu_m \rho_m + \mu_w \rho_w \phi S\right) + 2X'\mu_c \rho_c\right]} \qquad (3\text{-}1)$$

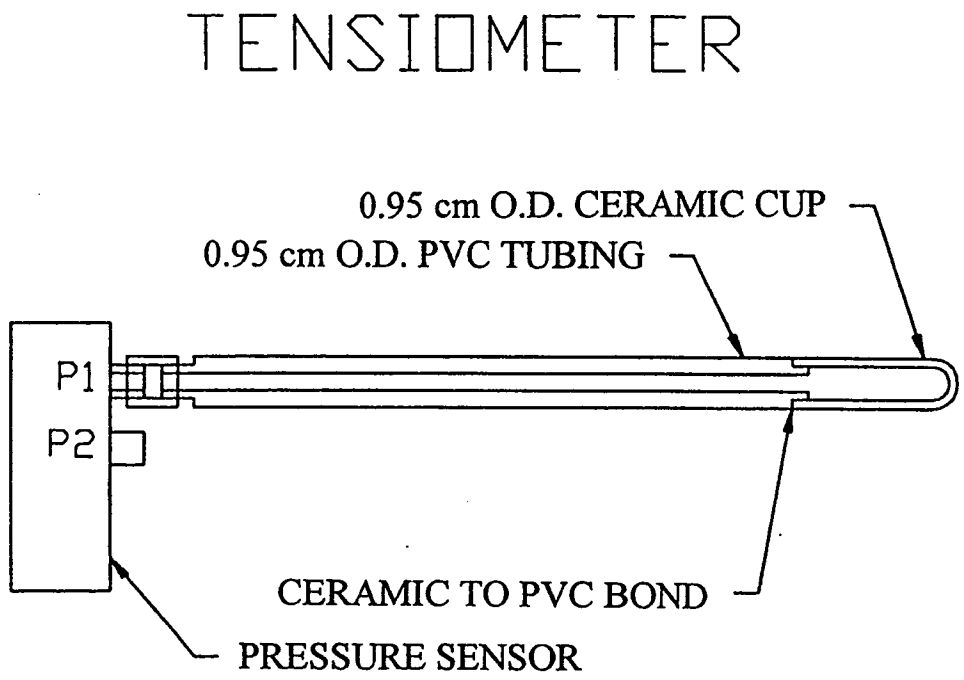

Figure 3-4. Schematic of the tensiometer

where

I = gamma ray intensity, detector
I_o = gamma ray intensity, source
X = medium thickness
X' = cell wall thickness
μ_m = attenuation coefficient of medium
μ_w = attenuation coefficient of water
μ_c = attenuation coefficient of cell
ρ_m = density of the medium
ρ_c = density of the cell
ϕ = porosity
S = liquid saturation in media ($0 \leq S \leq 1$)

In the thermohydrology experiments, ideally the only parameter in the attenuation expression that would change is the local water content, θ, (or saturation if porosity is known). If the container wall thickness and the medium thickness remain constant, changes in the measured count rate (I) would be entirely attributed to a change in local saturation. Equation (3-1) could then be used to determine changes in the local saturation by recording changes in the gamma beam intensity. It was possible that the density of either the silica beads (Test 1) or the cement mixtures (Tests 7, 9, and 10) varied during the experiment. However, the consistency of densitometer measurements of the silica beads and, particularly, the cement mixture throughout the duration of each experiment, suggests that matrix density remained constant at

least in terms of γ-ray attenuation. Thus, measured changes in densitometer counts are wholly attributed to changes in saturation. Densitometer measurements would not detect pore water that chemically bonded to the cement during additional curing of the mixture. In this circumstance, a reduction in available pore water would not be detectable with a densitometer. The amount of water chemically taken into the matrix, if any, was not quantified during testing. A listing of the equipment used in the densitometer measurements is given in Table 3-4.

Differences in the objectives of the distinct laboratory experiments required the use of two differently oriented densitometers. Both of these densitometers were mounted on traversing systems that simultaneously moved the detector and radiation source to scan the test containers. The densitometers were constructed with traversing systems that moved in two orthogonal directions in accordance with an automated data acquisition system (DAS). Tests 1 through 7 were vertically oriented, 2D experiments. Flow and moisture redistribution in the x-z plane were of interest in these experiments and flow in the y-direction was neglected. A densitometer that measured attenuation over the x-z plane (by integrating attenuation in the y-direction) was used in these experiments. The radiation source was placed on one side of the test container, and the radiation detector was placed on the other side.

Tests 1 through 7 were conducted using the x-z densitometer with a 500 mCi ^{137}Cs radiation source equipped with a scintillation-type detector. The energy level of the ^{137}Cs source is 662 KeV. Tests 8 through 11, however, had different objectives and a correspondingly different geometric configuration. These four experiments had a cylindrical geometry with a vertically oriented axis. The densitometer used in these experiments traversed in the x-y plane and integrated attenuation in the z-direction. The x-y densitometer was equipped with a 300 mCi ^{137}Cs radiation source and a pulse height analyzer. In practice, either a single or double radial traverse was measured in these experiments to take advantage of the radial symmetry and assumed matrix homogeneity of the experiment. The first of these two densitometers is referred to as the x-z densitometer and the second as the x-y (or r) densitometer, for identification purposes.

In conducting Tests 1 through 6 and Test 8, an adaptation of the standard method was used to calculate the water saturation levels. By taking densitometer readings for the fully saturated and completely dry test container, it was possible to eliminate the attenuation of the container and solid media. Thus, Eq. (3-1) results in the Beer-Lambert law (Moore, 1963):

$$S = \frac{\ln\left(\frac{I_d}{I}\right)}{\ln\left(\frac{I_d}{I_w}\right)}, \qquad (3\text{-}2)$$

where

I_d = gamma beam intensity through container and dry media
I_w = gamma beam intensity through container and saturated media
I = gamma beam intensity at unknown saturation level

Table 3-4. Gamma-ray densitometer components

Test Numbers	Gamma Source	Detector	Traverse Direction
1-7	500 mCi Cs 137 (662 keV) 3.2 mm dia. collimator	Ludlum Instruments Model 44-14 NaI Detector Model 2200-1 Scaler/Ratemeter	x and z
8-11	300 mCi Cs 137 (662 keV) 3.0 mm dia. collimator	Canberra Nuclear Products Model 802-3 NaI Detector Model 35+ Multichannel Analyzer	x and y

With this equation, the attenuation coefficients, media porosity, container thickness, and media thickness are eliminated, and a direct measure of the saturation level is obtained.

For Tests 7 and 9 through 11, another variation of the standard method was used to calculate saturation level. A densitometer measurement for a medium at a known saturation can provide sufficient information to determine the saturation change associated with a different densitometer reading at the same location provided saturation is the only property changed. Given this information, all other unknowns in the attenuation equation [Eq. (3-1)] can be summed and cumulatively determined. After this cumulative unknown has been determined, saturation can then be determined from densitometer measurements made at the identical location but at different saturation values. This technique was used to calculate saturation from densitometer measurements in tests in which the initial saturation was known. Average initial saturation was known for all experiments; however, saturation was vertically variable through test media with a relatively high saturation. Thus, saturation at each measurement point was not well defined even though average saturation was known. Media with relatively low permeability tended to have a more uniform saturation distribution. Thus, determination of saturation with this technique was better suited to test media with low permeability (i.e., Tests 7, 9, 10, and 11).

Attenuation measurements were made on aluminum standards prior to and subsequent to each traverse to normalize measurements made over a period of time. The aluminum standards were maintained constant throughout the course of the experiments; thus, attenuation of gamma rays through these standards was assumed to remain constant. Measurement of attenuation before and after each traverse allows normalization of the attenuation measurements to remove those transient effects that impact the measurements, both during each traverse and throughout the duration of the experiment. Normalizing each measurement to the aluminum standards allows quantitative comparison of attenuation measurements that reflect changes in test container density (from which saturation can be calculated or inferred) rather than transient effects not related to the objective of an experiment. All densitometer data were normalized to the aluminum standards prior to use in these analyses.

Gamma-ray production from a radioactive source is not constant with time but instead follows a Poisson distribution. Consequently, there will be fluctuation in the count rate measured at the detector. An average count rate with mean N will have a standard deviation of $\sqrt{N}$. As an example, the typical

count for Test 11 was about 200,000 counts (over a 1/m count period). The standard deviation due to the random emission nature of the gamma source was $\sqrt{200{,}000}$ or about 450 counts. In accordance with the second saturation determination method discussed above, a 1-percent decrease in saturation corresponded to an increase of about 585 counts. Therefore, the accuracy of saturation calculations was about 1 percent in Test 11. Similar calculations for the other tests also indicate an accuracy in saturation calculations of about 1 percent.

3.3.5 Liquid Flow Measurements

In order to study the relationship between thermhydrologic phenomena and solute transport in partially saturated media, various methods of monitoring the liquid flow patterns were reviewed (Green et al., 1993). Based on this review, a dye tracer method was selected. This method of tracking the liquid movement was used in Tests 1, 2, 3, 4, and 6. In conducting the tracer test, a very small amount of liquid dye was injected into the test media, which was enclosed in transparent walls. Photographs were taken periodically to capture the dye patterns representing the flow features. The time-lapse photographs provided a flow visualization that captured the general flow directions and solute-spreading patterns.

3.3.6 Heater Control and Measurement

All experimental tests incorporated heating of the porous media to create a range of hydrothermal conditions. For Tests 1 through 4, heat was supplied by circulating water from a constant-temperature bath (Neslabs EX-251HT and Neslabs Model EN-850 cooler) through the heater placed in contact with the porous media. The heat source was changed to electric resistance heaters for Tests 5 through 11 to provide temperatures in excess of 100 °C and to allow for measurement of heater power. The heater power was set using a Variac, and was measured using an Ohio Semitronics Model GW5-001X5 watt meter.

3.4 HYDRAULIC AND THERMAL CHARACTERIZATION OF TEST MEDIA

In conducting the sequence of thermohydrology experiments, both unconsolidated and consolidated media were used. The unconsolidated media consisted of silica and tabular alumina, while the consolidated media consisted of an industrial ceramic, cement, and tuff. In the early series of laboratory-scale experiments, unconsolidated media were used because of their uniform properties. This series of experiments was followed by experiments with consolidated media, which were progressively more representative of the geologic media at the proposed repository site. Silica beads were used as the initial test medium in the first laboratory experiment, which was designated as Test 1. Next, the test series referred to as Tests 2 through 5, and later Test 8, was conducted with tabular alumina. This test series was followed by Tests 7, 9, and 10, which used cement slurries as the test medium. The final test, Test 11, used a tuff rock sample from the ALTS in Arizona.

Physical, thermal, and hydraulic properties of the test media, for the most part, were obtained through direct laboratory measurement. In some cases, estimates of these properties for certain test media were obtained from the literature. Laboratory measurements were performed at CNWRA laboratories for (i) bulk density, (ii) effective porosity, (iii) saturated liquid permeability, and (iv) water retention and relative permeability curves. Thermal conductivity measurements for consolidated media samples were obtained with the assistance of the Southern Methodist University (SMU). Thermal conductivity values

for the unconsolidated media and other property values of media samples, for which no other measurement values were available, were taken from the literature or estimated using analytical methods.

Measuring the properties of the test media became a challenging task, particularly for the high-temperature conditions of the laboratory experiments. This section provides a detailed description of the test media used, the characterization methodologies, and summaries of the characterization data compiled for the test media.

3.4.1 Description of Test Media

Several unconsolidated and consolidated media were used in the conduct of the laboratory-scale thermohydrology experiments. The unconsolidated media used in the experiments included silica beads (Test 1) and three different sieve fractions of tabular alumina (Tests 2 through 5 and Test 8). Three general types of consolidated media were used consisting of ceramic, cement slurry mixtures, and tuff.

The silica-glass coated beads used in Test 1 were obtained from FERRO Corp., Cataphote Division. The beads are Class IV, annealed unispheres of soda-lime glass with manufacturer's specifications of ≤ 15 percent irregular shaped particles. Two separate fractions of factory-sieved beads (one from 28 to 53 μm and the other from 74 to 105 μm) were combined to create the bead mixture used in Test 1. The resulting 50/50-percent by volume bead mixture had a bimodal size distribution.

The tabular alumina samples used in Tests 2 through 5 (and later Test 8) were manufactured by ALCOA, Inc., and are described as massive sintered alumina, thoroughly shrunk and consisting of coarse well-developed alpha alumina crystals (ALCOA Chemical, 1969). Chemical analysis indicates that the tabular alumina contains 99.7 percent Al_2O_3, 0.16 percent Na_2O, 0.06 percent Fe_2O_3, and 0.04 percent of SiO_2 and CaO. Three different sieve fractions of tabular alumina were used in the experiments. The sieve fractions are defined in terms of mesh sizes. Mesh size for the tabular alumina used in the experiments included 60, 100, and 325, which translate to grain sizes of ≤ 250, ≤ 149, and ≤ 44 μm, respectively. The 100-mesh tabular alumina was used in Test 2. Tests 3, 4, and 5 also used 100 mesh tabular alumina, however, only after the alumina was wet-sieved with a 325 mesh to eliminate the fines. The 60 mesh tabular alumina was used in Test 8, a scoping experiment for the gas-flow experiments.

An industrial ceramic, from Refractron Technologies, was used in Test 6. The ceramic consisted of 90 percent Al_2O_3 and 10 percent aluminum silicate. Cement slurry mixtures were used in Test 7 (cement slurry C4), Test 9 (cement slurry C3), and Test 10 (cement slurry C6). Cement slurry C3 consisted of cement and water. C4 and C6 were of similar composition and contained additives in addition to water and cement. The mixture used in these two tests consisted of type 1 portland cement, barite powder, bentonite powder, water, Draceon, Vynsol resin (for air entrainment), and ivory soap. The Test 10 sample differed in preparation from Test 7 in that it was vibrated as it was poured into the test enclosure. All cement slurry mixtures were cured at room temperature for a minimum of 30 days prior to use in the experiments.

The cylindrically shaped tuff sample, which was used in Test 11, was prepared from a larger 0.46-m-diameter core sample. This tuff sample was collected from an abandoned road tunnel located approximately 2 km west of the ALTS (Hsiung et al., 1994). The 0.11-m-tall 0.30-m-diameter cylinder used in Test 11 was cored and cut from the larger core sample extracted from the road tunnel.

3.4.2 Characterization Methodologies

Laboratory characterization methodologies for soils were directly applicable to the silica bead and tabular alumina media. Characterization methodologies for consolidated media, which are typically adapted from soil characterization procedures, were used to measure the ceramic, cement slurry mixtures, and the ALTS tuff. A brief description of the characterization methodologies is summarized in this section. A more detailed description of the characterization methodologies is presented in Green et al. (1994), with the exception of the thermal conductivity measurement methodology. The measurement methodology used for the consolidated media is described in Blackwell and Spafford (1987). A detailed description of techniques used to determine thermal conductivity for unconsolidated media is contained here.

Standard testing procedures were used to determine the intrinsic media properties; namely, bulk density, effective porosity, and thermal conductivity. Bulk density of the unconsolidated and consolidated media was measured using a standard testing procedure described in Rasmussen et al. (1990), in which bulk density is defined as the dry mass (g) of a sample divided by the sample volume (cm^3). Two methods were used to determine the effective porosity: (i) the gravimetric method, and (ii) the pycnometric method. The gravimetric method is described in Rasmussen et al. (1990) and the pycnometric method was adapted from that described in Gardner (1986). Saturated and dry thermal conductivities of the consolidated test media were measured using the divided bar method. Thermal conductivities of the unconsolidated tabular alumina and the silica beads were taken from the manufacturer's data sheets and calculated using analytical methods (Woodside and Messmer, 1961). Saturated permeability was measured for both unconsolidated and consolidated media using a constant head permeameter following the procedure described in American Society for Testing and Materials (ASTM) 5084-90.

Moisture retention data were obtained using three different methodologies, each for a different range of matric potentials. Saturation/matric potential data at low matric potentials (i.e., up to 15 bar), or relatively wet conditions, were measured with a porous plate extractor following ASTM D3152-72 and ASTM D2325-68 procedures. Retention curve data for samples with matric potentials from about 2 to 15 bar were measured with the centrifuge methodology adapted from Flint and Flint (1990). Samples at the dry end of the curve, with matric potentials as low as 10 bar to greater than 1,000 bar, were measured using an Aqualab CX-2 water activity meter (Gee et al., 1992). In all three methods, the percent saturation was determined gravimetrically. The measured matric potential/saturation relationship for each test medium was used to fit a moisture retention curve for that medium. Relative permeability curves were estimated using the van Genuchten-Mualem theory (van Genuchten, 1978).

3.4.3 Summary of Test Media Properties

Measurements of the material, thermal, and hydraulic properties of the unconsolidated and consolidated test media were obtained. The specific properties measured for each test medium included: (i) bulk density, (ii) effective porosity, (iii) saturated liquid permeability, (iv) thermal conductivity, and (v) water retention and relative permeability curves. These properties were measured at the laboratory, SMU, or estimated from the available technical literature. The compiled data are summarized and discussed in the following sections.

3.4.3.1 Bulk Density

Bulk density measurements for the unconsolidated test media were conducted on samples collected from the same supply as the test media. In the case of the consolidated media, such as the cement slurry, additional samples of the medium were prepared at the same time the test medium was constructed, then retained for property characterization. Problems were encountered in obtaining accurate bulk density measurements for the unconsolidated media. The problem is believed to have been due to inconsistency in packing which resulted in variations of bulk density as large as 18 percent. Bulk density measurement of the silica beads was also affected by bead degradation, that is, dissolution and precipitation of silica. Bulk density measurements listed in Table 3-5 were taken for pre-experiment media samples.

Difficulties with packing were not encountered during bulk density measurement of the consolidated media, although the bulk density of the cement slurry mixtures may have been altered by the continued curing they experienced during testing. Bulk density measurement of the cement slurry mixtures was conducted on pre-test samples prior to any alteration that might have resulted from the conduct of the experiments. The effect of continued curing on bulk density measurements was not further evaluated.

3.4.3.2 Effective Porosity

Porosity data for the test media were obtained using standard measurement methods. Sample preparation for effective porosity measurements was similar to that for the bulk density measurements. As in bulk density measurements, problems were encountered with maintaining packing consistency of the unconsolidated media, degradation of the silica beads, and continued curing of the cement slurry mixtures. Packing inconsistencies resulted in porosity measurements that varied by about 20 percent. Effective porosity measurements of the test media are summarized in Table 3-6. The mean, maximum, and minimum effective porosity values are also given in the table.

3.4.3.3 Saturated Liquid Permeability

Saturated permeability was measured for each test medium using the standard constant head test. Permeability measurements for the tabular alumina, ceramic, and the tuff were successful and appeared to remain constant throughout the duration of their respective measurements. However, some problems were encountered in performing the measurements for the silica beads and cement slurries. For example, the permeability of silica beads varied during the conduct of the experiments. SEM photographs of the silica beads taken after the execution of Test 1 indicated degradation of the medium and changes in the permeability value. Water flow through the cement slurry mixture samples was not constant during the constant-head permeability test. This transient effect, in addition to growth of calcite minerals on the end plates of the testing apparatus, indicated that the cement may not have been fully cured and that mineralogical changes occurred during testing.

Consequently, the saturated permeability data presented here are for the test media prior to actual conduct of the laboratory experiment. Whether these pre-test values are sufficiently representative of the actual test medium permeability under the conditions of the experiments, is uncertain at this time. Saturated permeabilities measured on pre-test samples are summarized in Table 3-7.

Table 3-5. Bulk density measurements of the test media

Bulk Density (g/cm^3)				
Test Number	Test Medium	Mean	Maximum	Minimum
1	Silica beads	1.53	1.59	1.45
2	≤149 μm tabular alumina	2.35	2.48	2.15
3	≥44 μm and ≤149 μm tabular alumina	2.00	2.09	1.93
4	≥44 μm and ≤149 μm tabular alumina	2.00	2.09	1.93
5	≥44 μm and ≤149 μm tabular alumina	2.00	2.09	1.93
6	Ceramic	1.68	1.73	1.64
7	Cement slurry (C3)	1.60	1.63	1.56
8	≤249 μm tabular alumina	2.34	2.55	2.22
9	Cement slurry (C4)	1.57	1.67	1.49
10	Cement slurry (C6)	1.82	n/a	n/a
11	Tuff	2.44	2.49	2.42

3.4.3.4 Thermal Conductivity

Although the thermal conductivities of different geologic media are, in general, relatively similar, they can vary significantly with water saturation level. Media exposed to heat sources will experience wide variability in saturation levels. This dependence on saturation level appears to be greater for high porosity earth materials than for low porosity materials (Woodside and Messmer, 1961). In case of low-porosity tuff, for example, the ratio of wet to dry thermal conductivity has been found to be about 2 (Ashworth, 1992).

Thermal conductivity values for the test media used in this study were compiled through a combination of: (i) direct measurements, (ii) analytical methods, and (iii) published values. Thermal conductivity values for dry unconsolidated media (silica beads and tabular alumina) were calculated using published values, and values for the consolidated media (ceramic, cement slurry, and tuff) were determined by direct measurement. Where available, published thermal conductivity values for the test media were compared with the calculated or measured values. Dry thermal conductivity values estimated for the test media are summarized in Table 3-8.

For the silica beads, thermal conductivity values were taken from Woodside and Messmer (1961). These values are assumed to represent the pre-test silica beads, and the effect of bead degradation on thermal conductivity was not measured. Similarly, the thermal conductivity of the tabular alumina was

Table 3-6. Effective porosity measurements of the test media

Porosity				
Test Number	Test Medium	Mean	Maximum	Minimum
1	Silica beads	0.38	0.43	0.34
2	≤149 μm tabular alumina	0.31	0.39	0.27
3	≥44 μm and ≤149 μm tabular alumina	0.41	0.48	0.37
4	≥44 μm and ≤149 μm tabular alumina	0.41	0.48	0.37
5	≥44 μm and ≤149 μm tabular alumina	0.41	0.48	0.37
6	Ceramic	0.42	0.44	0.41
7	Cement slurry (C3)	0.50	0.52	0.48
8	≤250 μm tabular alumina	0.32	0.34	0.30
9	Cement slurry (C4)	0.36	0.39	0.30
10	Cement slurry (C6)	0.45	n/a	n/a
11	Tuff	0.06	0.07	0.05

not measured; they were assigned dry thermal conductivity values obtained from the manufacturer's specification sheet. The thermal conductivity value of 2.6 W/m-K corresponded to a porosity of 26 percent, a porosity similar to the 27-percent porosity for the un-sieved tabular alumina used in Test 2, but less than the 37-percent porosity of the sieved tabular alumina used in Tests 3, 4, and 5. There was uncertainty in the assignment of thermal conductivity values for wet tabular alumina, particularly because thermal conductivity can change significantly with saturation.

For three different sand samples, Woodside and Messmer (1961) report wet to dry thermal conductivity ratios of about 10. Similarly, for glass beads, they report a ratio of about 4. The porosity of the sands was 19 to 59 percent, and the glass beads 38 percent in their study. Based on these observations, the thermal conductivity for wet tabular alumina was estimated to range from about 3 to 5 W/m-K. Although these values are high, they are significantly less than the measured thermal conductivity of 18 W/m-K for a 99.5-percent Al_2O_3 ceramic, with porosity less than 1 percent (ALCOA Chemicals, 1969). The relatively lower wet thermal conductivity was estimated to account for the porosity of 27 to 37 percent.

Dry and wet thermal conductivity values for the consolidated samples [ceramic, cement (C3), cement (C4), and the tuff] were measured at the SMU Geothermal Laboratory using the divided bar thermal conductivity technique (Blackwell and Spafford, 1987). Cement (C6) was assigned the same values as cement (C4), since both cement slurry mixtures had the same composition.

Table 3-7. Saturated liquid permeability measurements of the test media

Test Number	Test Medium	Permeability (m^2)
1	Silica beads	6.23×10^{-13}
2	$\leq$149 μm tabular alumina	2.95×10^{-14}
3	$\geq$44 μm and $\leq$149 μm tabular alumina	8.04×10^{-13}
4	$\geq$44 μm and $\leq$149 μm tabular alumina	8.04×10^{-13}
5	$\geq$44 μm and $\leq$149 μm tabular alumina	8.04×10^{-13}
6	Ceramic	3.75×10^{-13}
7	Cement slurry (C3)	n/a
8	$\leq$ 250 μm tabular alumina	5.5×10^{-14}
9	Cement slurry (C4)	2.06×10^{-18}
10	Cement slurry (C6)	n/a
11	Tuff	5.0×10^{-17}

A number of candidate relationships exist for calculating thermal conductivity as a function of water saturation. First, however, an appropriate relationship relating solid- and liquid-phase fractions to an effective thermal conductivity must be considered. For a parallel model of the matrix and fluid-filled pore space of the medium, Domenico and Schwartz (1990) give a linear relationship between the matrix and fluid components, namely:

$$K_e = \phi K_f + (1-\phi)K_s \,, \tag{3-3}$$

where K is effective thermal conductivity, ϕ is porosity, and the subscripts *e*, *f*, and *s* denote effective, fluid and solid, respectively. Likewise, Woodside and Messmer (1961) propose a series model

$$K_e = \frac{K_s K_f}{\phi K_s + (1-\phi)K_f} \,. \tag{3-4}$$

Table 3-8. Summary of dry and wet thermal conductivities for silica

Test Number	Medium	Porosity	Thermal Conductivity-Dry (W/m-K)	Thermal Conductivity-Wet (W/m-K)
1	Silica beads	0.38	0.2	0.9
2	≤149 μm tabular alumina	0.31	2.6	3-5
3	≥44 μm and ≤149 μm tabular alumina	0.41	2.6	3-5
4	≥44 μm and ≤149 μm tabular alumina	0.41	2.6	3-5
5	≥44 μm and ≤149 μm tabular alumina	0.41	2.6	3-5
6	Ceramic	0.42	2.194	3.4091
7	Cement slurry (C3)	0.50	0.502	1.0207
8	≤250 μm tabular alumina	0.32	2.6	3-5
9	Cement slurry (C4)	0.36	0.728	0.9746
10	Cement slurry (C6)	0.45	0.728	0.9746
11	Tuff	0.06	1.744	1.9091

A tortuosity term can be added to Eq. (3-3) to accommodate the parallel model for the nonparallel structure encountered in porous media (Slattery, 1972). This added term yields

$$K_e = \phi K_f + (1 - \phi) K_s - K_s K^* , \qquad (3\text{-}5)$$

where K^* represents a reduction in free transport because of the tortuosity of porous media.

These three relationships can be used to calculate fully saturated (wet) and fully unsaturated (dry) thermal conductivity values by assigning either water or air values, respectively, as the fluid thermal conductivities. However, these expressions do not define variations in thermal conductivity values as a function of saturation. The heat and mass transfer simulator V-TOUGH (Pruess, 1987; Nitao, 1990) provides two models that represent the thermal conductivity/saturation relationship—either a linear model or a relationship weighted by the square root of saturation (Somerton et al., 1973, 1974). The linear model is:

$$K(S) = K_d + S(K_w - K_d), \quad (3\text{-}6)$$

and the weighted model is

$$K(S) = K_d + \left[\sqrt{S}(K_w - K_d)\right], \quad (3\text{-}7)$$

where the subscripts d and w denote dry and wet, respectively. Dry or wet thermal conductivities calculated with either Eqs. (3-3), (3-4), or (3-5) could be incorporated into Eqs. (3-6) or (3-7).

Thermal conductivity measurements by Woodside and Messmer (1961) indicate that a linear relationship may not be appropriate for selected geologic porous media (e.g., various sand samples). Consistent with this observation, data reported by Ashworth (1992) for tuff samples from the ALTS indicated a plateau/jump feature in thermal conductivity near mid-saturation. Several alternative models were proposed by Ashworth to explain this departure from linearity. However, since this departure from a linear thermal conductivity/saturation relationship is not significant, the assumption of linearity for the tuff samples has been used in these analyses.

By contrast, a linear thermal conductivity/saturation relationship for unconsolidated media is difficult to support. First, the difference between wet and dry thermal conductivity is greater for unconsolidated media than for consolidated media. This difference is attributed to the greater porosity and the diminished matrix skeletal connectivity in unconsolidated media as compared to consolidated media, particularly low porosity consolidated media. Second, there is not an extensive database of thermal conductivity/saturation measurements for the unconsolidated media used in this investigation. Thus, the presence of significant nonlinear features may go undetected. Third, thermal conductivity in unconsolidated media is sensitive to packing. Methods and degree of packing can have a profound effect on grain-to-grain connectivity and, consequently, on the funicularity of water and the resultant thermal conductivity of unconsolidated sample. Nonetheless, a linear thermal conductivity/saturation model was assumed for the unconsolidated media.

3.4.3.5 Water Retention and Relative Permeability Curves

Unsaturated hydraulic properties consisting of the water retention and relative permeability curves were determined for each test media. Water retention curves have been determined for all test media using saturation and matric potential data measured with porous plate extractors, centrifuge, and a water activity meter. Each set of saturation-matric potential data was fitted using the RETC computer code (van Genuchten, 1985) which calculates the fitting parameters for the van Genuchten (1978) soil properties models. The curves produced with these soil property models are shown in Figures 3-5a through 3-5f). The water retention curves are plotted with their respective data set. Values for the van Genuchten fitting parameters, α, n, and θ_r, are summarized in Table 3-9 for each test medium. The relative permeability curves were estimated using the Mualem theory, which uses the van Genuchten parameters and the relationship of $m=1-1/n$. Goodness of fit was determined by visual observation. The highly nonlinear saturation-matric potential relationships of media with narrow pore-size distributions resulted in less than desirable curve fitting. However, these representative models were the best possible and were used in subsequent analyses.

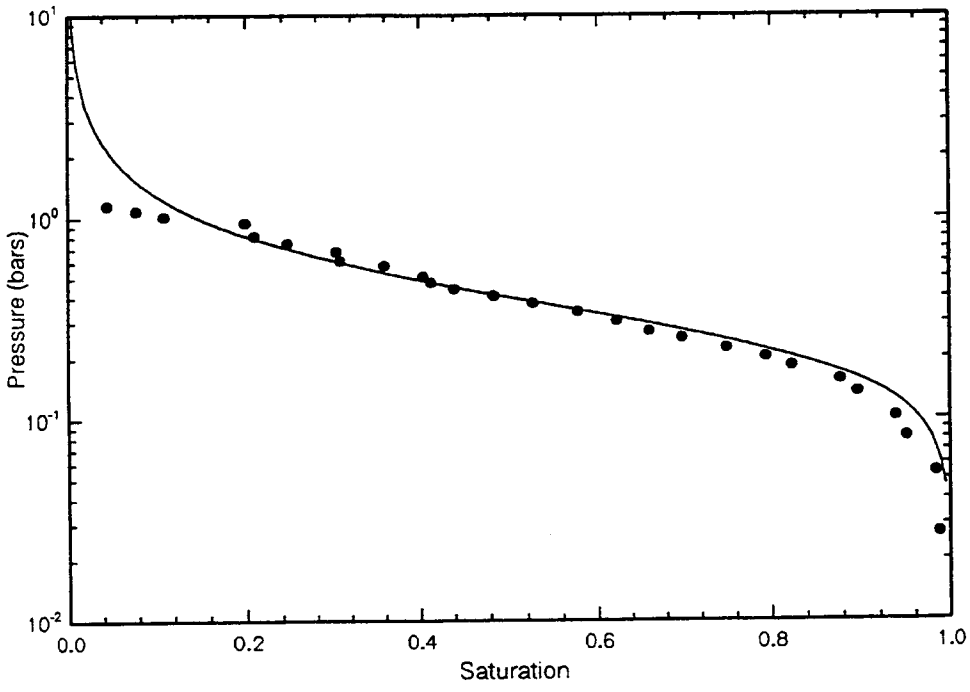

(a)

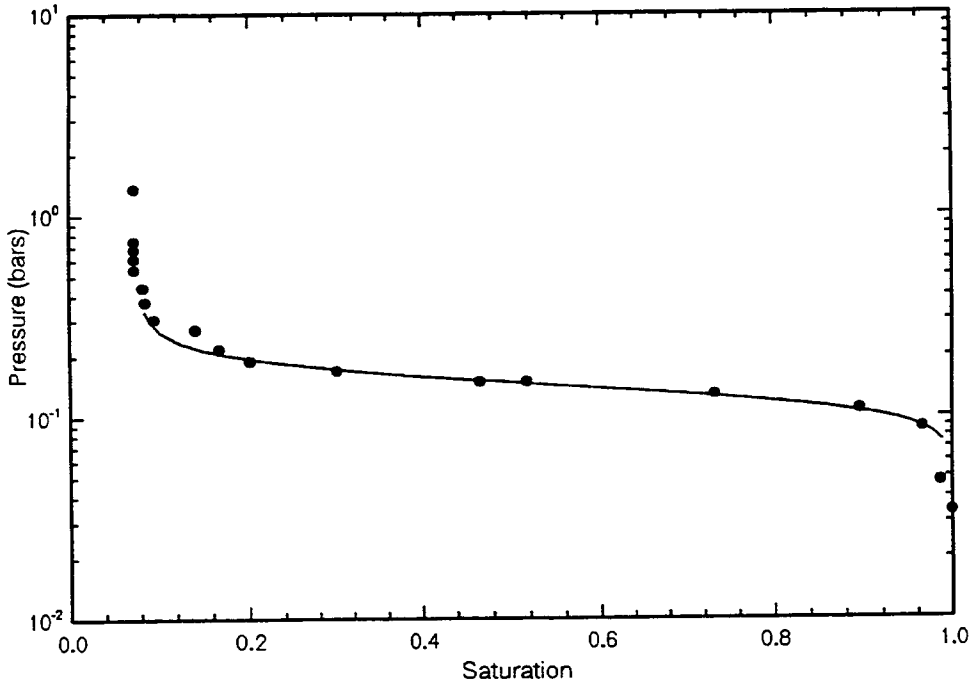

(b)

Figure 3-5. Water retention curves for test media: (a) silica beads (b) ≤149 μm tabular alumina

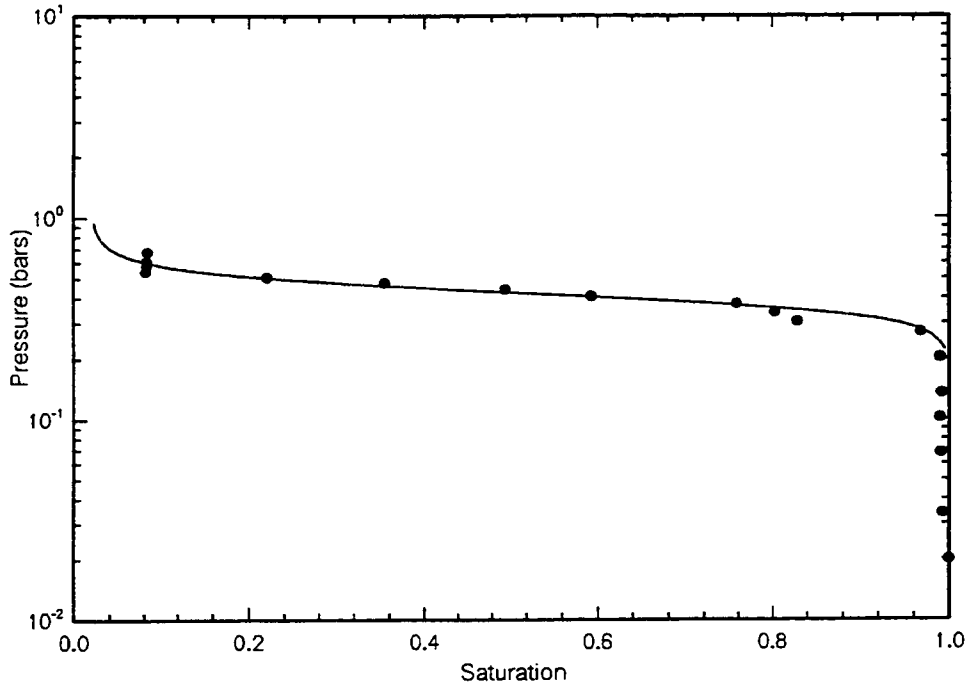

(c)

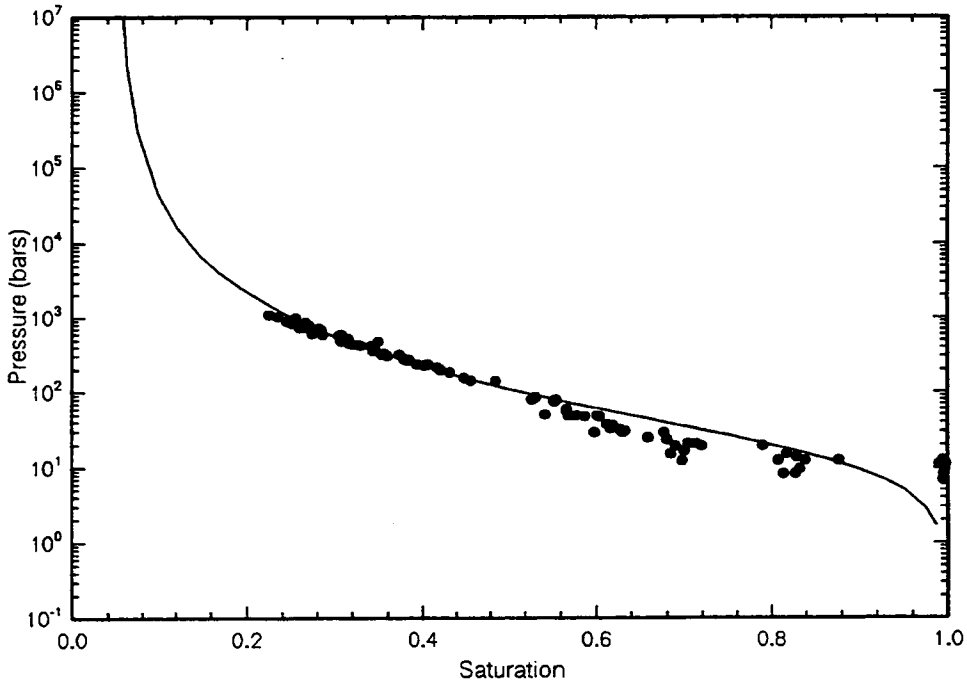

(d)

Figure 3-5 (Cont'd). Water retention curves for test media: (c) ≥44 μm and ≤149 μm tabular alumina, and (d) ceramic

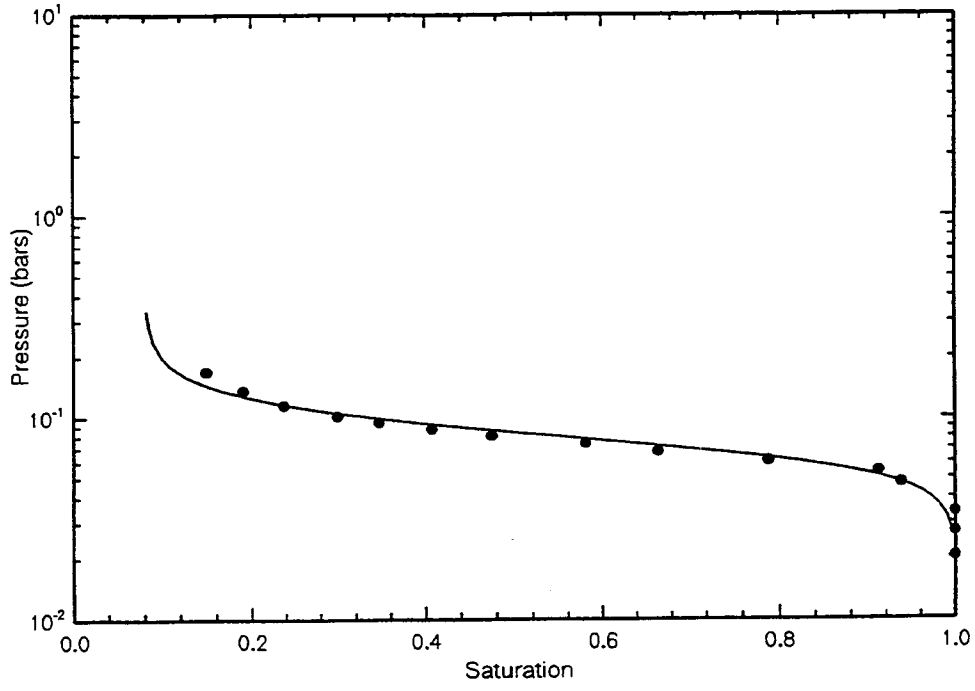

(e)

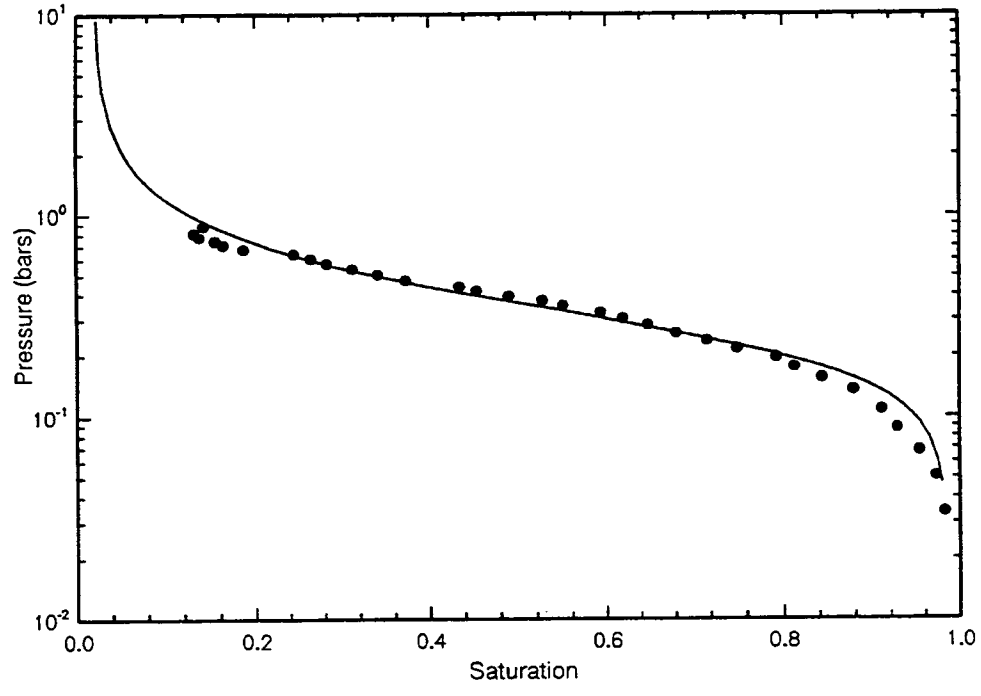

(f)

Figure 3-5 (Cont'd). Water retention curves for test media: (e) cement slurry (C3), and (f) ≤249 μm tabular alumina

Table 3-9. van Genuchten α and n parameter values for the test media

Unsaturated Hydraulic Parameters				
Test Number	Test Medium	van Genuchten α ($\times 10^5$ Pa^{-1})	van Genuchten n	Residual Saturation
1	Silica beads	7.19	6.81	0.08
2	$\leq$149 μm tabular alumina	3.58	2.70	0.02
3	$\geq$44 μm and $\leq$149 μm tabular alumina	13.10	5.00	0.08
4	$\geq$44 μm and $\leq$149 μm tabular alumina	13.10	5.00	0.08
5	$\geq$44 μm and $\leq$149 μm tabular alumina	13.10	5.00	0.08
6	Ceramic	2.42	8.23	0.02
7	Cement slurry (C3)	0.0636	1.373	0.05
8	$\leq$249 μm tabular alumina	—	—	—
9	Cement slurry (C4)	—	—	—
10	Cement slurry (C6)	—	—	—
11	Tuff	—	—	—

4 LABORATORY EXPERIMENTAL RESULTS AND ANALYSES

This chapter summarizes the results of the laboratory-scale experiments conducted in this study. These results provided the necessary information to satisfy the two objectives of the study:

- Investigate fluid flow formation near a heat source, particularly in the region of vaporization and condensation
- Evaluate the temporal and spatial scales of gas pressure formation

Of the 11 experiments conducted in this study, the first 7 provided the physical basis for evaluating the heat and mass transfer mechanisms affecting redistribution of thermally driven moisture through partially saturated porous media. The other four, Tests 8 through 11, provided information for evaluating the proposed scaling laws; in addition, these gas pressure buildup tests also contributed to the evaluation of heat and mass transfer mechanisms.

Analyses of the results from the laboratory-scale experiments were strengthened by using results from previous field-scale experiments to gain a better understanding of thermally driven moisture redistribution. These field-scale heater tests are described by Patrick (1986), Zimmerman et al. (1986), and Ramirez et al. (1991). The results from field-scale heater tests provided stronger support for both understanding the heat and mass transfer mechanisms and the proposed scaling laws. The soundness of the interpretation of the heat and mass transfer mechanisms and of the proposed scaling laws was further tested by conducting numerical analyses of the laboratory-scale experiments, field-scale heater tests, and the repository system.

Analyses were performed using experiments and numerical simulations designed to isolate specific heat and mass transfer mechanisms identified as important in earlier theoretical studies and reviews of previous laboratory- and field-scale experiments. Numerical analyses were conducted using either V-TOUGH (Pruess, 1987; Nitao, 1990) or a modified version of V-TOUGH, referred to as C-TOUGH. Modifications to V-TOUGH that resulted in C-TOUGH include new pre- and post-processors and a new iterative solver. Comparisons between results from V-TOUGH and C-TOUGH indicate that both codes generate practically identical numerical predictions. C-TOUGH was used in most numerical analyses reported in this document because of the added ease provided by the modified pre- and post-processors, and because of the increased numerical efficiency.

Analyses of (i) heat and mass transfer mechanisms, and (ii) the proposed scaling laws are presented in the following two subsections.

4.1 HEAT AND MASS TRANSFER MECHANISMS

Results from the laboratory-scale experiments, field-scale heater tests, and numerical analyses contribute to the understanding of heat and mass transfer mechanisms instrumental in thermally driven moisture redistribution in partially saturated porous media. The first issue addressed in these analyses is the identification of the driving mechanisms responsible for moisture redistribution at a geologic HLW repository. Results of experiments conducted under both sub-boiling ($T < 100$ °C) and boiling conditions ($T > 100$ °C) were used to identify the contribution of water transport as both vapor and liquid to moisture

redistribution observed in laboratory- and field-scale experiments. Some unresolved questions, however, were identified. These questions include (i) the contribution of each phase to heat and mass transfer, (ii) the duration of their respective contributions, and (iii) the spatial scale at which each phase of transport operates. Practical limitations were encountered in attempting to resolve these issues. For example, liquid flow could be directly monitored using dyes injected into the flow field of some experiments; however, vapor phase flowlines could only be inferred. Similar difficulties were encountered when attempting to measure the quantity of water transported as vapor or as liquid. Again, liquid quantities could be at least estimated using measured values for saturation, permeability, and pressure gradients; however, vapor transport quantities could only be indirectly inferred. The indirect inference for vapor transport is a source of uncertainty.

Results from the laboratory-scale experiments conducted in this investigation and heat and mass transfer experiments at field-scale conducted previously demonstrate that a broad range of liquid and vapor redistribution phenomena can take place. Important aspects of these phenomena include (i) transport of water as either gas or liquid, (ii) mass flow rates and velocities, and (iii) the direction or flow regime in which each fluid phase is transported. As indicated in the development of the transport equations and substantiated by experimental and analytical results, the nature of the fluid flow fields is primarily dependent on the hydraulic properties and thermal conductivity of the medium, strength of the heat source, and saturation level of the medium. These properties, as well as other factors, were monitored and controlled during each experiment. The sensitivity of the flow fields to these properties was assessed by varying their values in both laboratory and numerical experiments. Numerical simulations of experiments were also conducted in this evaluation to assess the sensitivity of flow fields to changes in these property values. The effect of enhanced vapor diffusion was not considered in these analyses, although results by Lichtner and Walton (1994) indicated this effect could be significant.

4.1.1 Liquid Flow Redistribution Experiment Results

Liquid flow redistribution was the focus of experiments conducted under sub-boiling conditions in four of the experiments (Tests 1 through 4), and under boiling conditions in three experiments (Tests 5 through 7). As discussed in Chapter 3, the type of test medium, boundary conditions, and heat source were among the conditions varied in these experiments. In the sub-boiling tests (Tests 1 through 4), experiments designed to examine liquid flow regimes caused by a heat source were studied for both 1D and 2D geometries. The direction of liquid flow in the test cells was monitored by observing the movement of dyes injected at strategic locations. The state of the liquid phase was monitored using temperature, densitometer, and matric pressure measurements. An analysis and discussion of results from the 1D and 2D liquid flow redistribution experiments are presented in the following subsections.

4.1.1.1 One-Dimensional Experiments

Two experiments (Tests 1 and 2) were conducted in a 1D geometry as part of the liquid flow redistribution experiments. These two related experiments provided an opportunity to observe thermally driven moisture redistribution through partially saturated porous media. The objective of these experiments was two-fold: (i) to understand basic mechanisms of heat and mass transfer in a 1D geometry, and (ii) to help guide the design of more realistic and insightful experiments. To accomplish this goal, the 1D experiments were designed to avoid complications arising from media heterogeneities and complex boundary conditions. Some complications, but not all, were successfully avoided in the execution of these experiments. Nonetheless, lessons learned from Tests 1 and 2 contributed to the design

of subsequent experiments whose results responded more directly to issues of thermally driven moisture redistribution through naturally occurring porous media. This subsection contains a summary of the analyses of heat and mass transfer observed in the two experiments and results that were used to define more clearly the objectives and design of subsequent experiments.

The design and objectives of the 1D experiments were predicated on results of an earlier series of separate effects and scoping experiments conducted as part of the Thermohydrology Research Project. Results from the separate effects and scoping experiments are summarized in Green et al. (1993). Preliminary results of Test 1 are contained in this earlier report. (Note: Test 1 in this report was identified as Test 6 in Green et al. (1993) and Test 2 was conducted after the earlier document was published.) As discussed, Test 2 was designed and conducted to address uncertainties raised in Test 1 results. These uncertainties may have resulted from the inclusion of the artificial fracture in Test 1. Results and discussions of Test 1 and 2 have been published in Manteufel et al. (1992) and Manteufel and Green, (1993). These results are summarized here, with complementary numerical analyses.

The experimental designs of Tests 1 and 2 were similar, with the exceptions that Test 1 contained a simulated fracture, Test 2 included a higher degree of instrumentation, and the silica bead test medium used in Test 1 was replaced with tabular alumina in Test 2. The silica bead test medium was not used in subsequent experiments because the silica exhibited significant degradation during the conduct of the experiment. Degradation included the dissolution and precipitation of silica as indicated in an SEM photograph of the post-test beads (Figure 4-1). Silica bead degradation has been attributed to the aggressive effect of the slightly acidic (pH ~ 5) deionized water used in the experiment. Consequently, the silica bead retention curve reported in Section 3.4 did not represent the saturation/matrix potential relationship of the silica beads over the entire duration of Test 1. Additionally, measurement of a representative value for permeability of the silica beads was not possible. Although difficulties were encountered with the media in Test 1, quantitative assessments of the tests have been made and are reported here.

Several distinct manifestations of moisture redistribution were observed near the heated boundary in the 1D liquid flow redistribution experiments. The best defined and most pertinent of these manifestations was the way in which thermally driven flow redistributed the water in the porous media. Vaporization, vapor diffusion, condensation, and liquid advection were observed to be the primary driving mechanisms which, when coupled with hydraulic properties of the media, dictate the liquid redistribution. In the tests, it was observed that liquid can accumulate in a narrow zone near the heat source (Test 1) or lead to a gradual saturation gradient in the media (Test 2). In both tests, a dryout zone was observed.

The formation of the dryout zone/moisture buildup zone has potentially important implications. Moisture that remains close to the heat source rather than moving to a greater distance before condensing would have a greater hydraulic potential and shorter distance back to the heat source than moisture uniformly condensed at a greater distance. Therefore, the source mechanism(s) for this dryout zone/moisture buildup zone should be identified. This moisture redistribution mechanism is evaluated by analyzing Test 1, which exhibited a defined, narrow moisture buildup zone, and Test 2, which exhibited liquid redistribution over a broad area.

An analysis was conducted to ascertain the physical mechanism(s) that could have caused the accumulation of moisture immediately on the cool side of the dryout zone prominently observed in Test 1, but to a lesser degree in Test 2. Therefore, properties exhibited by Test 1 but not Test 2 are potential

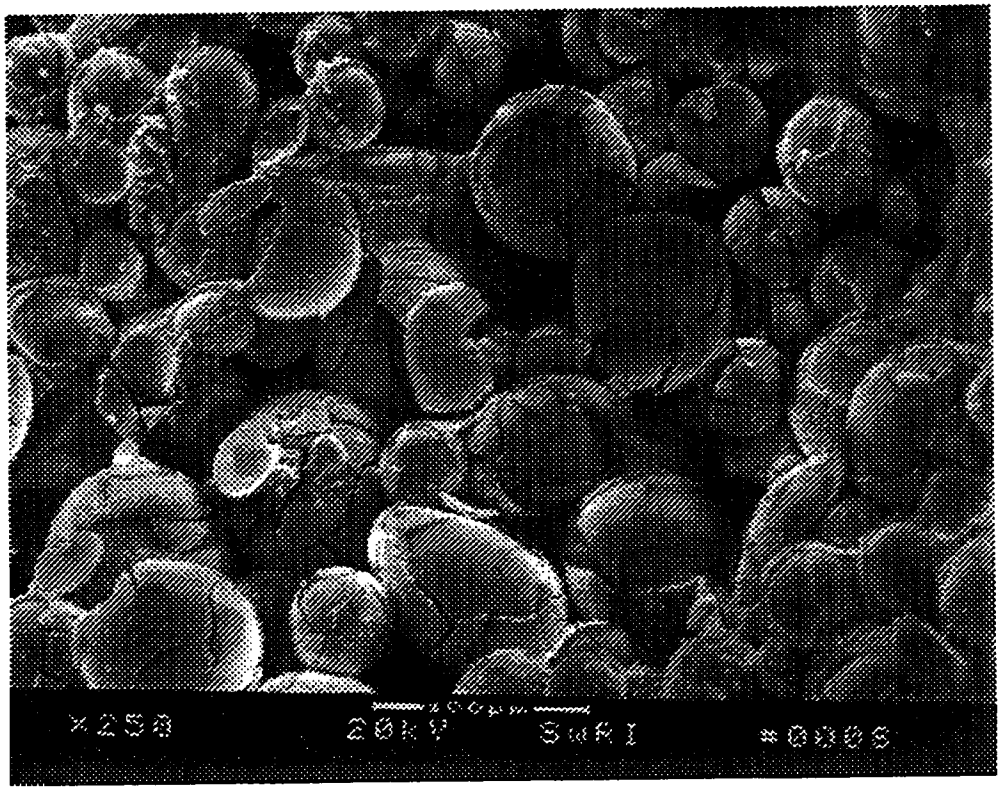

Figure 4-1. Scanning electron microscope photograph of the post-test silica beads used in Test 1

candidates for instigating the formation of a prominent dryout/moisture buildup zone. Possible sources for the discrepancies in moisture redistribution between Tests 1 and 2 include differences in media properties (i.e., thermal conductivity, permeability, retention curves, etc.) between the silica beads and the tabular alumina, and the increased temperature gradient in Test 2. Also possible is that the tabular alumina had higher suction pressures which resulted in a higher capability to advect liquid that dissipated the condensate buildup. As mentioned, additional complications were encountered when attempting to interpret the results because of the degradation of the silica beads used in Test 1.

Experimental Results. A combination of experimentally measured and observed results was used in the analysis of the 1D series of experiments. Test variables measured in the 1D liquid flow redistribution experiments that were used in the analyses included:

- Temperature distributions measured using internal and external thermistors
- Liquid flow pathlines measured using injected dyes
- Liquid saturation determined using a gamma-ray densitometer

- Matric potential measured using internal tensiometers

Horizontal temperature profiles for Test 1 (from 20 °C on the left to 60 °C on the right) and Test 2 (from 20 °C on the left to 90 °C on the right) are illustrated in Figure 4-2. Although approximately steady-state temperature regimes were established after initiation of heating in both Tests 1 and 2, the temperature distributions varied slightly throughout the duration of the experiments. This temperature variation for Test 2 is illustrated in Figure 4-3. The time-varying behavior becomes more pronounced by the end of the experiment. The temperature gradient was higher near the right heated side, indicating some heat loss through the uninsulated plexiglass front and back walls. Greater heat loss would be experienced near the heated boundary where the side wall heat loss temperature gradient was greatest. An explanation for the time-varying temperature is that the thermal conductivity was moisture-dependent and the saturation profile was changing during the test. As illustrated in Table 3-8, the thermal conductivities of the silica beads and the tabular alumina vary from dry (0.2 W/m-K for the silica beads and 2.6 W/m-K for the tabular alumina) to wet (0.9 W/m-K for the silica beads and 3.5 W/m-K for the tabular alumina). The potential of these two candidate physical mechanisms to cause a nonlinear temperature gradient was numerically evaluated.

Movement of liquid through the test media in Tests 1 and 2 was illustrated using neutrally-buoyant inert dye injected into the test container at two locations about a third of the distance from the bottom boundary. The two dye injection ports successfully illustrated the flow patterns at the points of injection, one near the heated boundary and the other near the cool boundary. A sequence of ten photographs for each test illustrates the movement of dye over a duration of 6 days for Test 1 and 8 hr for Test 2 (Figures 4-4 and 4-5). The dye flow patterns in each test exhibited similarities and differences. Dye injected at the left injection port in both tests exhibited mostly diffusion-driven flow, except for some downward late-time dye movement as shown in the photograph sequence of Test 1. The lateral rate of diffusion of the dye was measured at 3×10^{-8} m/s in Test 1 and 8×10^{-8} m/s in Test 2. Since the same dye was used in both tests and the saturation was not greatly different, the different rates of diffusion are attributed to the different media types.

The major difference in the dye flow patterns of the two tests was exhibited at the injection port near the heated boundary. The dye injected in Test 1 moved downward and, eventually, away from the heated boundary. The expansion of a dryout zone in the lower portion of the test container was well defined by the dye. The dryout zone expanded to a distance of 3.5 cm at the bottom of the Test 1 container at a rate of almost 3×10^{-8} m/s. Less dye movement near the heated boundary was illustrated in Test 2 than in Test 1. Additionally, the dryout zone observed in Test 2 was less extensive than the dryout zone in Test 1, even though the temperature of the heated boundary in Test 2 was greater than Test 1. One final important observation is that the movement of dye from the right injection port in Test 2 was directly toward the heated boundary, while in Test 1, the movement of dye was oblique to the boundary. The rate of the near heater advection-driven flow was downward at 2×10^{-7} m/s in Test 1 and laterally at 1×10^{-6} m/s in Test 2. Similar to the measured rates of diffusion-driven dye movement, the advection-driven flow in Test 2 was a factor of two to five times more rapid than advection-driven flow in Test 1.

Potential reasons for higher flow rates in Test 2 than in Test 1 include differences in the permeability of the test media and the higher boundary temperature in Test 2. The pre-test silica bead matrix actually had a higher measured permeability than the tabular alumina. However, degradation of the silica beads undoubtedly altered the hydraulic properties of the test medium in Test 1. Inspection of the SEM photograph of the silica beads in Figure 4-1 suggests that a significant portion of the inter-beads

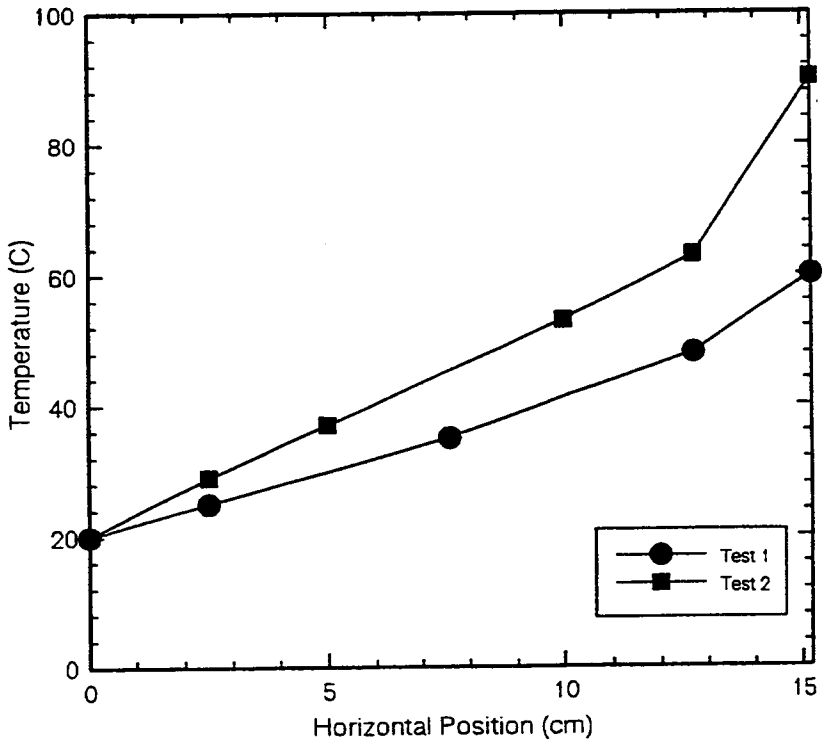

Figure 4-2. Horizontal temperature profiles for Tests 1 (60 °C) and 2 (90 °C)

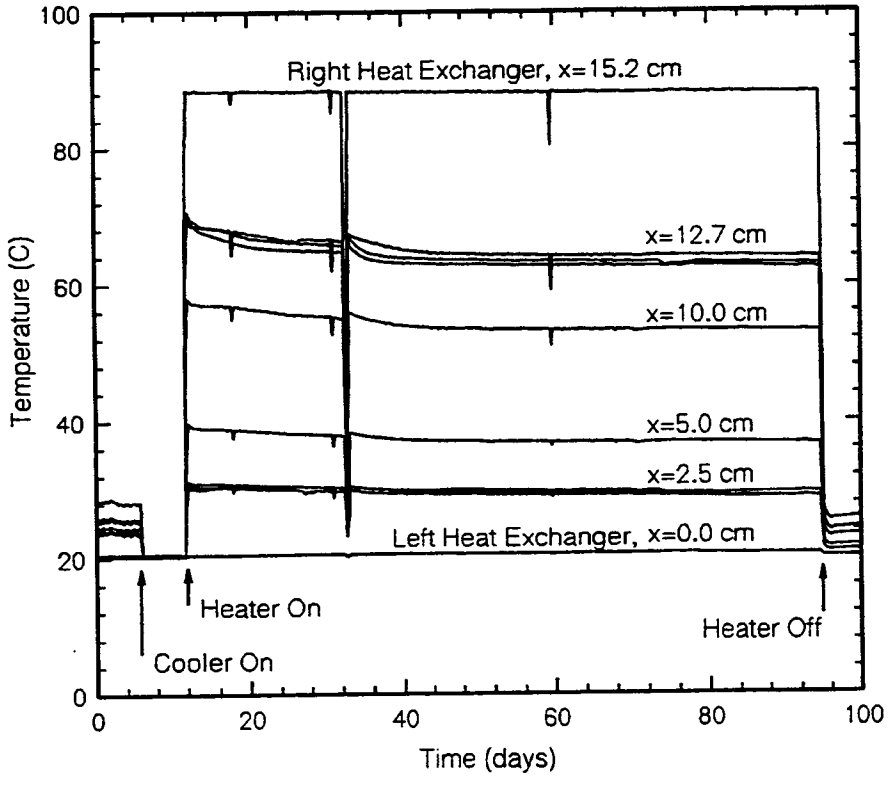

Figure 4-3. Transient temperature variations for Test 2

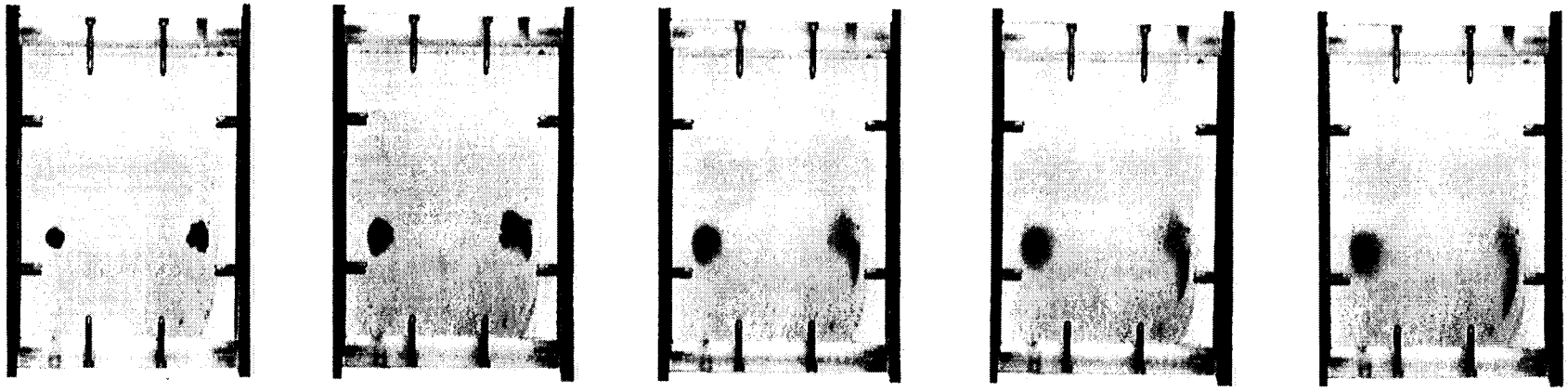

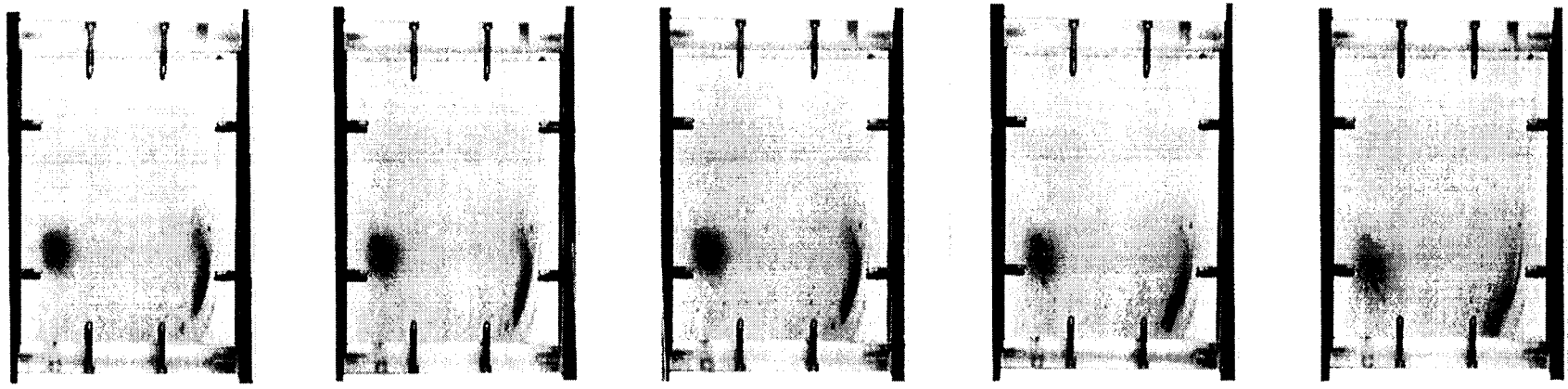

Figure 4-4. Series of photographs over a 6-day period for Test 1 using injected dye to help illustrate the dryout zone/moisture buildup zone phenomenon

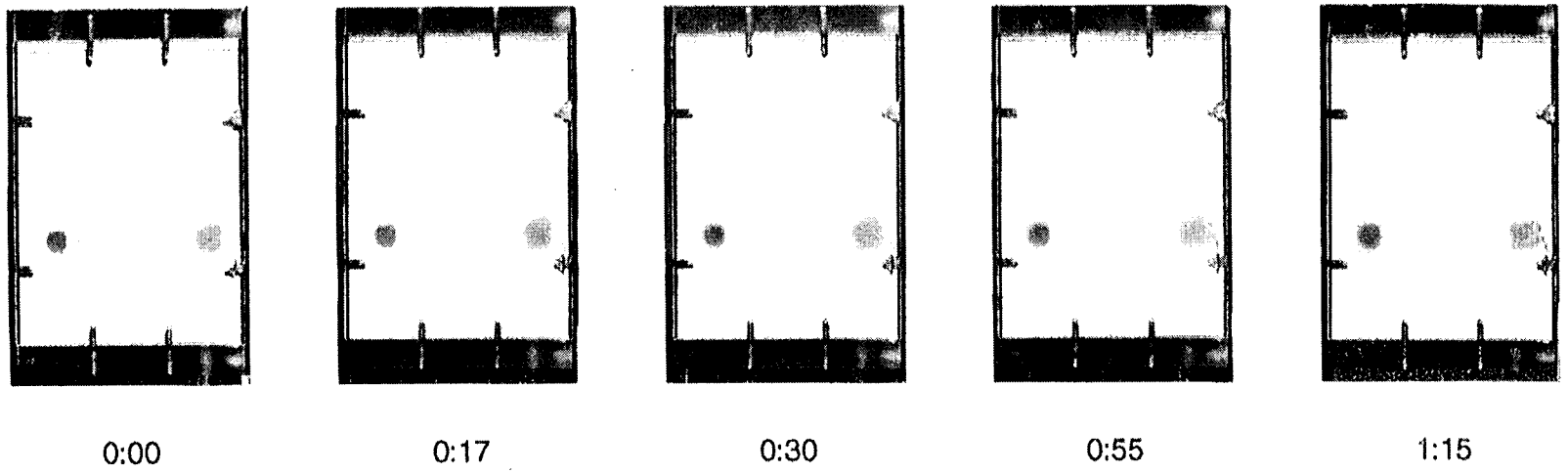

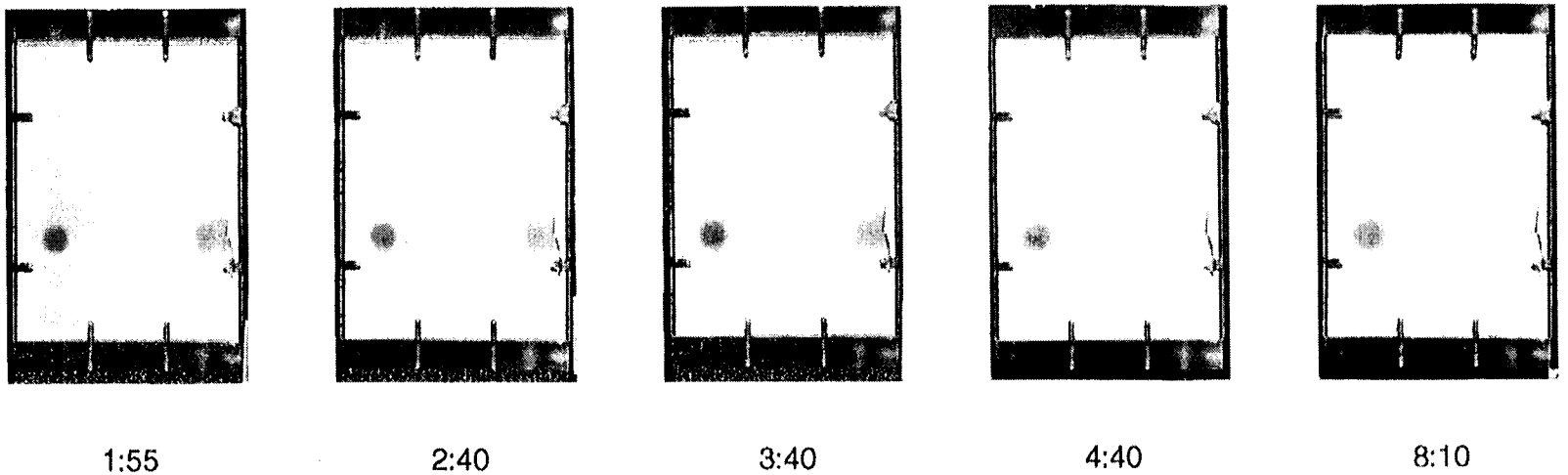

Figure 4-5. Series of photographs over an 8-hr period for Test 2 using injected dye to help illustrate the movement of liquid

pore space was filled with precipitate by the end of the experiment. The permeability of the silica beads evidently changed; although the permeability during or after the test was not measured.

Evidence of actual moisture redistribution was provided using gamma-ray densitometer measurements periodically recorded throughout Tests 1 and 2. Saturation was calculated using densitometer measurements of the test media at zero and full saturation in both tests. In Test 1, saturation profiles determined at three times (days 75, 99, and 113) are illustrated in Figure 4-6. The heater was turned on at day 6 and off at day 105. Although the number of calculated saturation values in both tests is sparse due to the relatively few number of densitometer measurements (four rows of six measurements), trends are observed in the saturation plots. The plotted results are for densitometer measurements that were averaged over a full day to increase accuracy. Inspection of the four horizontal profiles in each figure illustrates the growing size of the dryout zone located at the base of the test container during this time in the experiment (Figure 4-6). Due to an absence of densitometer measurements close to the heated boundary, no evidence of the dryout zone is seen in the top three profiles. The estimated extent of the dryout zone has been indicated in Figure 4-6. However, the formation of a band of high saturation located immediately to the cool side of the dryout zone is well illustrated. These trends indicate that the bulk of water that vaporized near the heated boundary in Test 1 condensed in a narrow band nearly parallel to the heater. These data provide the best evidence of the formation of a dryout/moisture buildup zone.

Saturation profiles at these different locations late in the experiment in Test 2 are presented in Figure 4-7. A greater density of data was collected along these horizontal transects to better define the possible formation of a dryout/moisture buildup zone. The three illustrated profiles from Test 2 are along similarly located transects in Test 1 (i.e., the lower three transects in Test 1). A narrow zone of apparent moisture build-up was detected at 2 to 3 cm from the heated boundary. The subtle 0.02 to 0.04 increase in saturation in Test 2 was significantly less than the more prominent but less well-defined 0.10 to 0.20 saturation buildup in Test 1. An additional important observation is that the average saturation along the left side of the test medium in Test 2 uniformly increased above the pre-test saturation of 0.50 to about 0.60 to 0.65. The area of greatest saturation increase occurred near the cool boundary in Test 2 and not next to the dryout zone as in Test 1.

Matric pressure measured using tensiometers provided an independent means to verify densitometer-determined saturations for Test 1. Matric pressure measurements for Test 1 are presented in Figure 4-8. Matric pressure measurements for Test 2, were less conclusive because of problems encountered by frequent dryout of the tensiometers. Measurements at one location near the cool boundary are presented in Figure 4-9, for example. In Test 1, the matric pressures for the tensiometer closest to the heated boundary from pre-heat pressures of about 8 kPa increased to pressures of 13 kPa after 80 days of heating. Matrix suction near the cool boundary remained constant for the duration of the test.

The measured matric pressure/saturation relationship for the pre-test silica beads is illustrated in Figure 3-5a. Matric pressures of 8 and 13 kPa equate to saturations of 0.98 and 0.10, according to the van Genuchten retention curve that was fitted to the measured matric pressure/saturation data. Two uncertainties were encountered in the calculation of saturations from the retention curve. First, the measured retention curve is representative of the pre-test silica beads. Second, because of the relatively narrow pore-size distribution of the beads, the retention curve is highly nonlinear, and thus minor changes in matric pressure result in large changes in saturation. Therefore, there is not a high level of accuracy in saturation calculated from matric pressure measurements in Test 1. Nonetheless, evidence of dryout at the location of the right tensiometer is conclusive, corroborating the densitometer-calculated saturations.

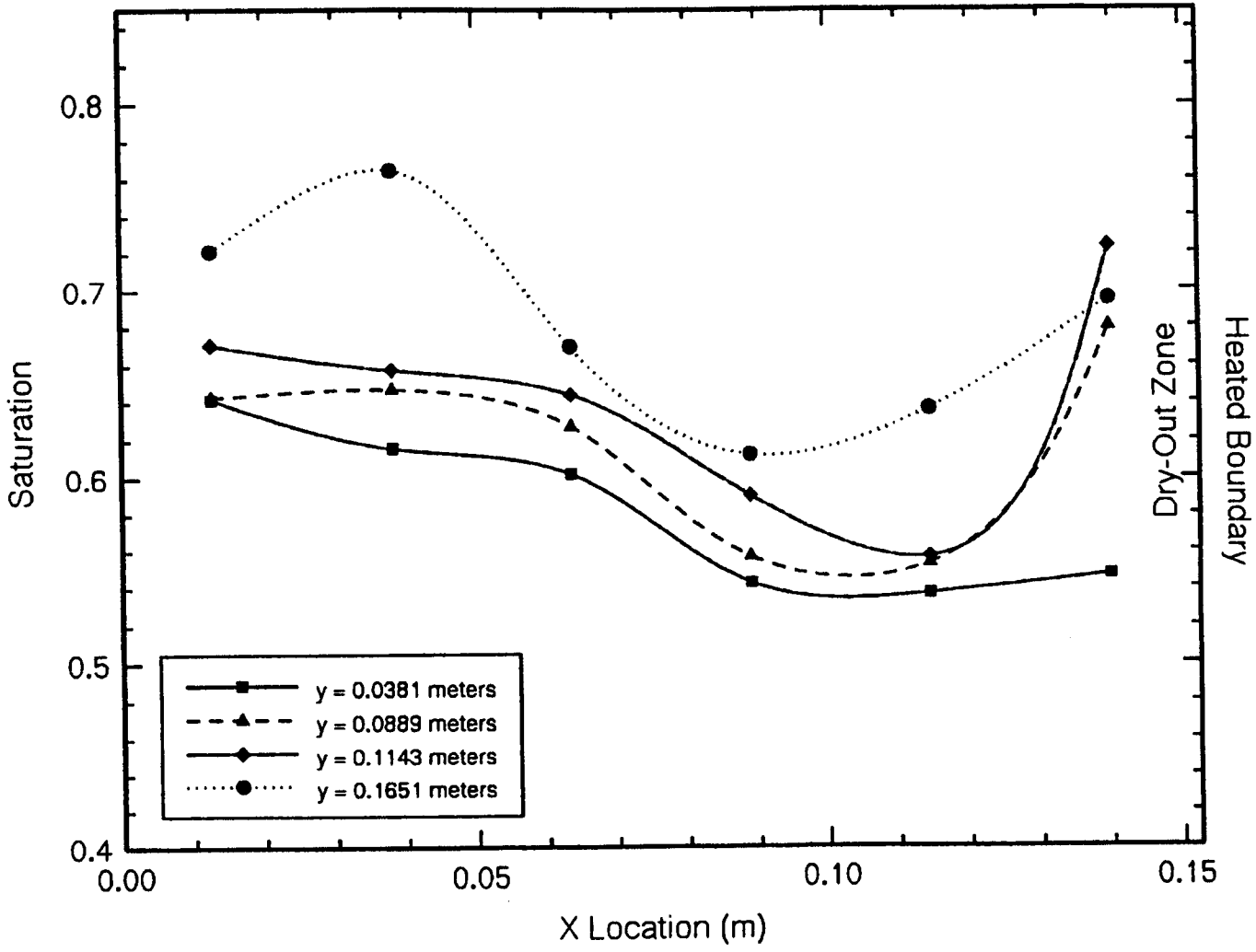

Figure 4-6. Horizontal densitometer-determined saturation profiles for Test 1 at day (a) 75

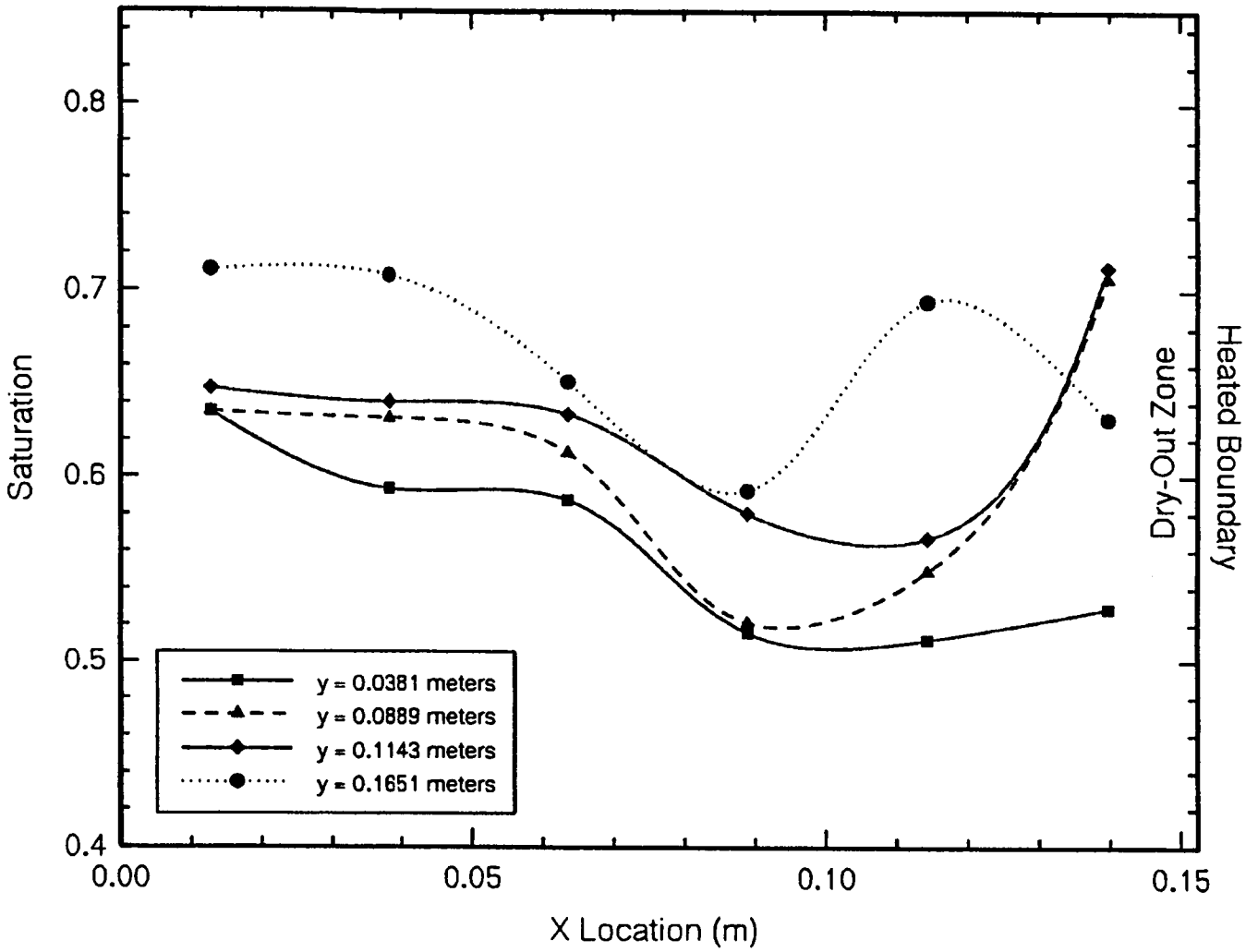

Figure 4-6 (Cont'd). Horizontal densitometer-determined saturation profiles for Test 1 at day (b) 99

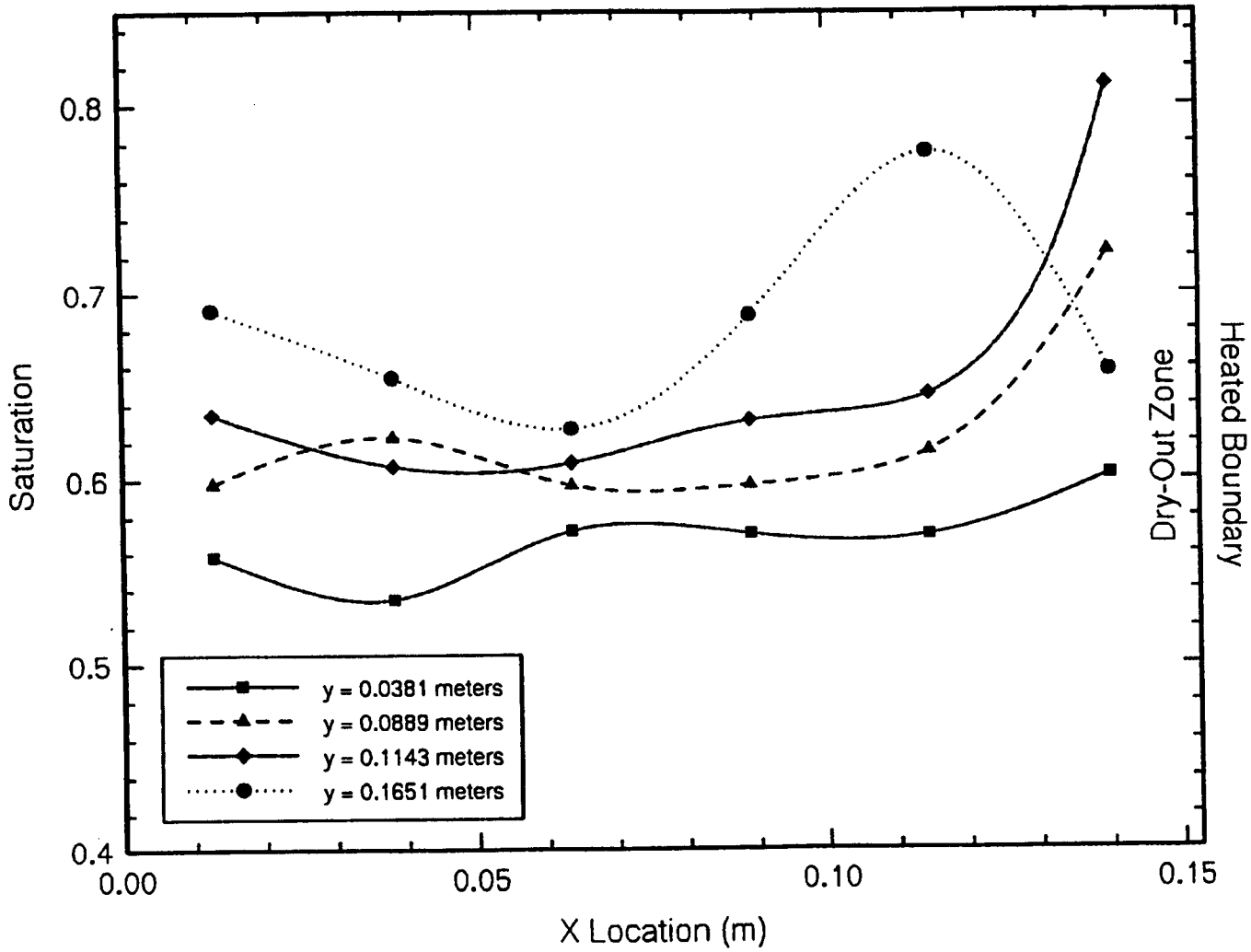

Figure 4-6 (Cont'd). Horizontal densitometer-determined saturation profiles for Test 1 at day (c) 113

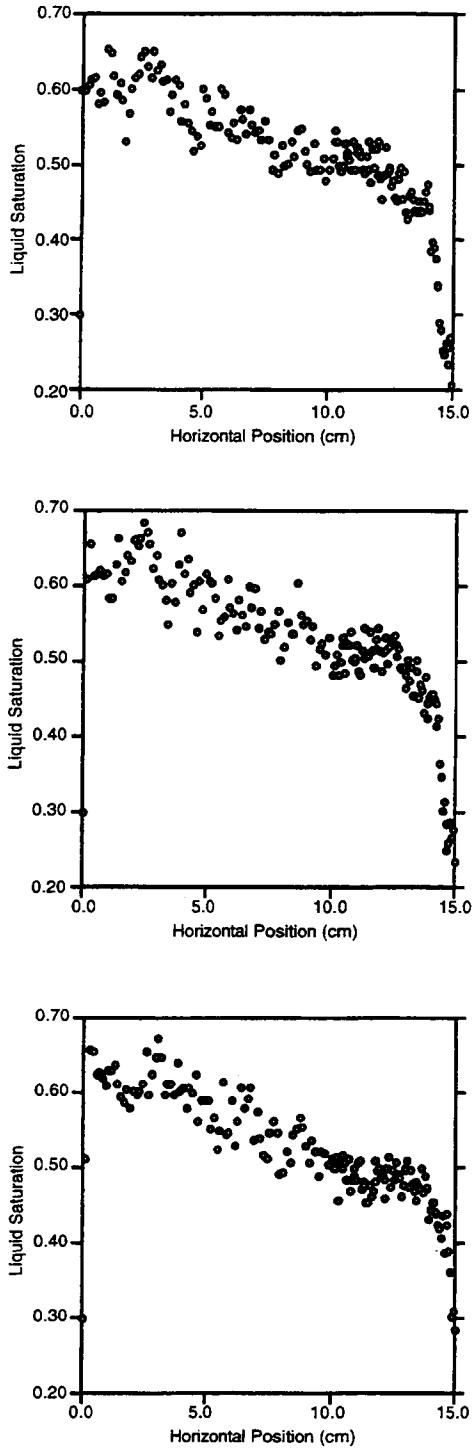

Figure 4-7. Horizontal densitometer-determined saturation in Test 2 located at (a) 8.9 cm, (b) 11.4 cm, and (c) 16.5 cm from top of container

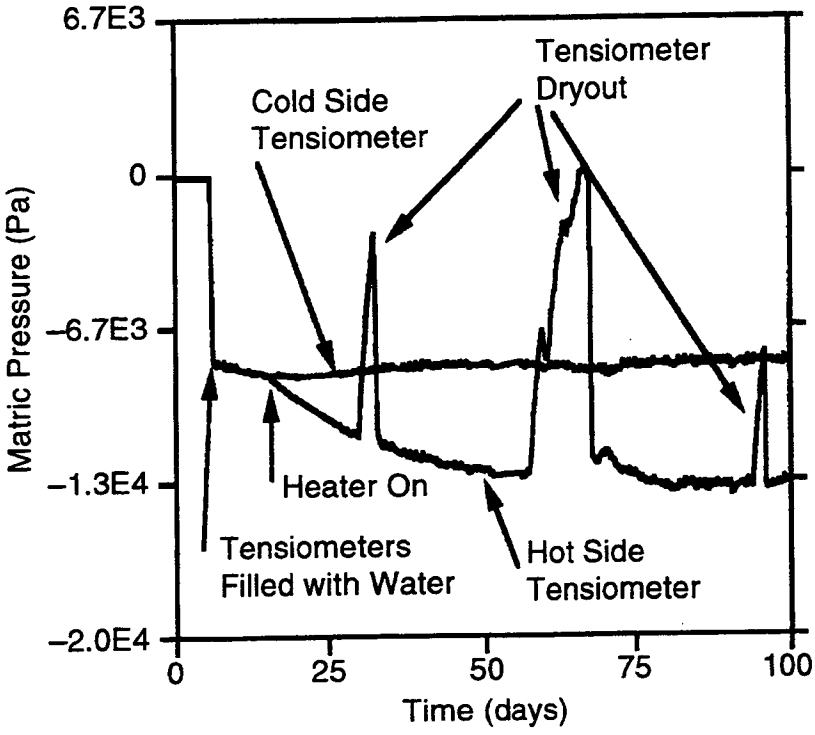

Figure 4-8. Tensiometer measurements from Test 1

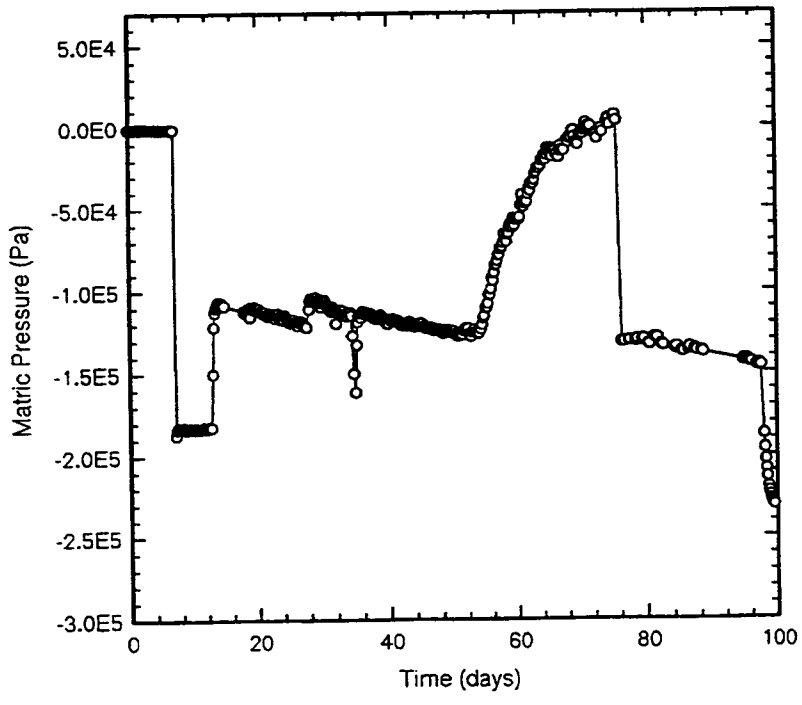

Figure 4-9. Tensiometer measurements from near the cool boundary in Test 2

The tensiometer measurement from Test 2 (located near the cell base at the cool boundary) indicated matric pressures were about 12 kPa until day 56, at which time the matric pressure decreased to zero. At 80 days, the heater was turned off and the matric pressure returned to about 12 to 14 Kpa. A corresponding saturation was determined from Figure 3-5b to be about 0.90 for a matric pressure of 12 to 14 Kpa. This tensiometer measurement indicated that water condensed away from the dryout zone during heating, then decreased back to 0.90 soon after heating ceased. This observation confirms conclusions drawn from densitometer measurements.

Numerical Analysis. Thermally driven redistribution of moisture in Tests 1 and 2 was numerically modeled using V-TOUGH. The prime objective of the numerical analysis was to ascertain the source mechanism for the dryout/moisture buildup phenomenon observed in Test 1 and weakly observed in Test 2. Rigorous analysis of Test 1 results using numerical simulations was hampered by the apparent alteration in the hydraulic properties of the silica beads throughout the conduct of the experiment. Nonetheless, results of Test 1 were numerically analyzed to evaluate the mechanisms associated with the formation of a dryout/moisture buildup zone. A secondary objective was to assess the ability of V-TOUGH to replicate the thermally driven moisture redistribution exhibited in the 1D group of experiments.

Assessment of the 1D group of experiments identified four media parameters that are potentially responsible for the formation of the dryout/moisture buildup zones well defined in Test 1 and weakly defined in Test 2. The four media properties are:

- Spatial and moisture-dependent variations in thermal conductivity
- van Genuchten α parameter (inverse of air-entry value)
- Liquid permeability
- Chemical effects associated with silica degradation

The potential for chemical degradation of the silica beads to lead to the formation of a dryout/moisture buildup zone was not directly evaluated. However, degradation was indirectly evaluated in terms of how the degradation potentially affected permeability and the van Genuchten α parameter.

A 1D numerical model was configured to span the horizontal distance from the cool to the hot boundaries. The numerical model used in this evaluation was 1D, since the geometric configuration and the heat and mass transfer mechanisms in both Tests 1 and 2 appeared to be essentially 1D. The basecase models for Tests 1 and 2 were assigned the property values presented in Section 3.4. The silica beads in the basecase were assigned the pre-test permeability of 6.23×10^{-13} m^2. These values are summarized in Table 4-1. Several numerical grids were assessed in this analysis. The finite element grid size was decreased until no difference in numerical results was observed.

The basecase models for Tests 1 and 2 were numerically simulated to evaluate the appropriateness of the conceptual model and assigned parameter values. Temperature and saturation profiles predicted by the basecase models are illustrated in Figures 4-10 and 4-11 for Tests 1 and 2. The basecase temperature and saturation profiles are not in agreement with the observed results for either Test 1 or Test 2. Three model input parameters were varied in a set of sensitivity analyses to resolve the differences between the model and experimental results. Permeability, as determined by the

Table 4-1. Summary of numerical parameters used in 1D numerical analyses for Tests 1 and 2

Parameter	Test 1	Test 2
Bulk Density (g/cm^3)	1.53	2.35
Permeability (m^2)	6.23×10^{-13}	2.95×10^{-14}
Porosity	0.38	0.41
Saturation	0.65	0.50
van Genuchten n	2.70	5.00
van Genuchten α (Pa^{-1})	7.19×10^{-5}	3.58×10^{-5}
Thermal Conductivity - Dry (W/m-K)	0.2	2.6
Thermal Conductivity - Wet (W/m-K)	0.9	3.5

van Genuchten α parameter, and thermal conductivity were varied either separately or together in the model to better replicate Tests 1 and 2. Thermal conductivity was first varied to attain agreement in the temperature regime. After the temperature was adequately replicated, agreement in saturation was attempted by variation of the two hydraulic parameters.

Spatial and moisture-dependent variations in thermal conductivity values were evaluated for their effects on saturation and temperature. The thermal conductivity values of the test media used in Tests 1 and 2 exhibit relatively large variations between zero and full saturation. Values for the dry and wet thermal conductivity assigned to the silica beads changed by a factor of 4.5. The tabular alumina had values that varied by as much as a factor of two. Thermal conductivity varied linearly with saturation in the representation incorporated in V-TOUGH. The effect of a moisture-dependent thermal conductivity was not apparent in the basecases, however, saturation varied by less than 0.02 in Test 1 and by 0.12 in Test 2. This effect is expected to be more prominent in models that predicted large variations in saturation.

Thermal conductivity was adjusted to be spatially variable in addition to being moisture-dependent. Spatially variable thermal conductivity was incorporated into the model as a means to accommodate 3D heat loss through the plexiglass front and back sidewalls. A piece-wise linear thermal conductivity model was used for both the dry and wet conductivities. Thermal conductivities assigned to the three segments of each piece-wise approximation were normalized relative to the segment closest the cool boundary. The lengths of the three segments are 7.5, 5.2, and 2.5 cm from left to right. The assigned thermal conductivity values are summarized in Table 4-2.

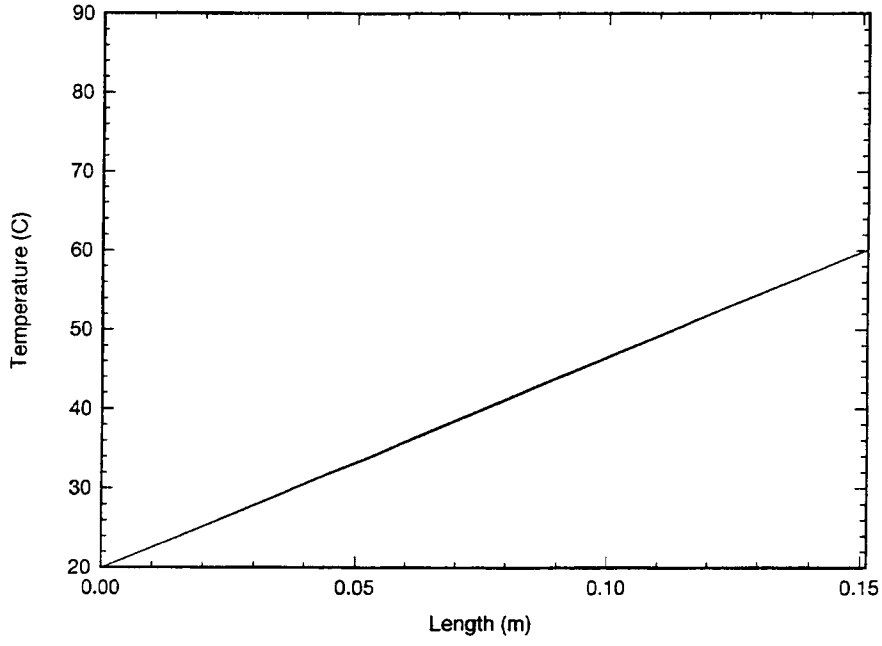

(a)

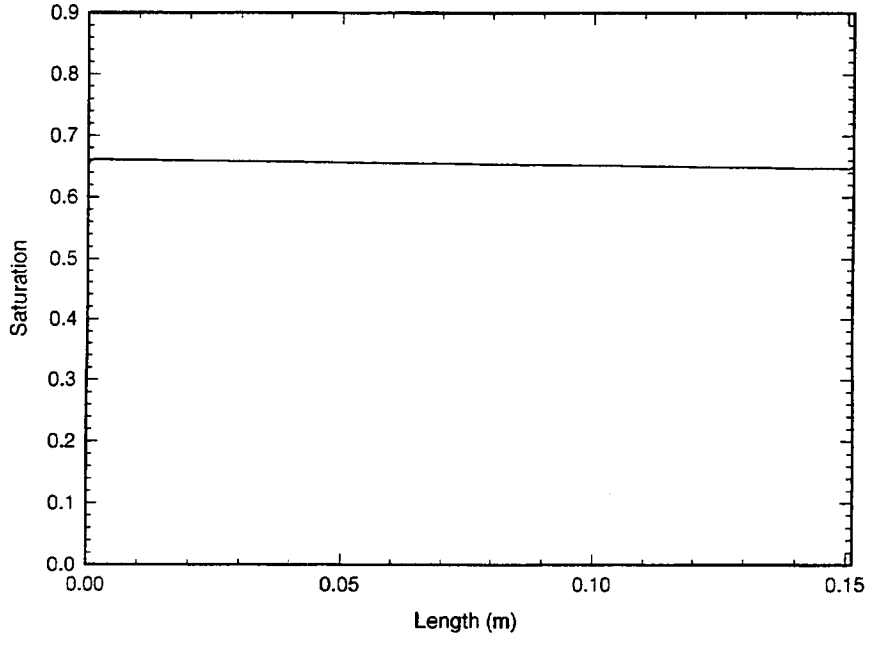

(b)

Figure 4-10. Profile predicted for the basecase properties for Test 1 (a) horizontal temperature, and (b) saturation

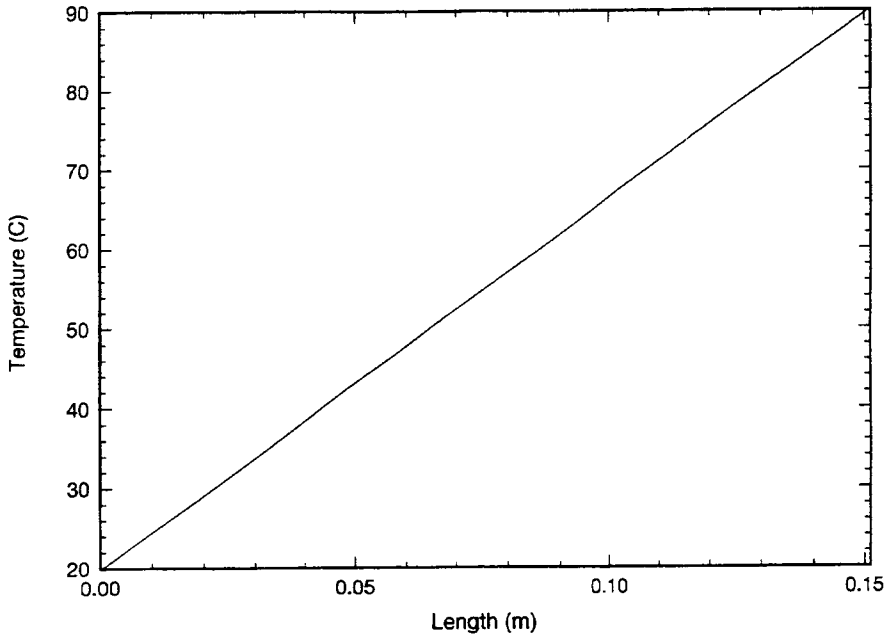

(a)

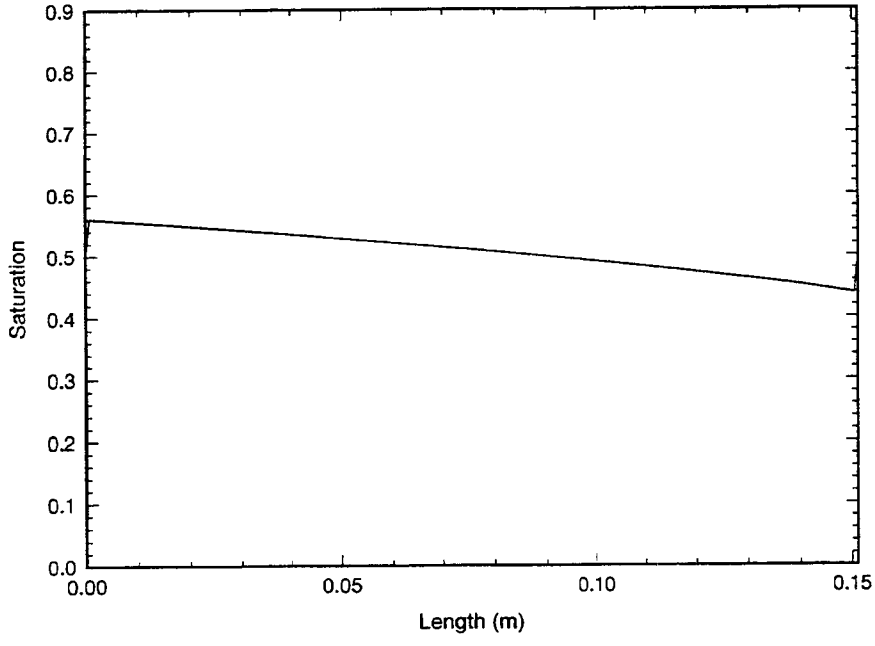

(b)

Figure 4-11. Profile predicted for the basecase properties for Test 2 (a) horizontal temperature, and (b) saturation

Table 4-2. Spatially variable thermal conductivity used in 1D numerical analyses for Tests 1 and 2 where the cool boundary is at x=0 cm and the hot boundary is at x=15.2 cm

	Segment	Test 1	Test 2
Thermal Conductivity - Dry (W/m-K)	0<x<7.5 cm	0.20	2.60
	7.5<x<13.7 cm	0.15	1.98
	12.7<x<15.2 cm	0.11	0.88
Thermal Conductivity - Wet (W/m-K)	0<x<7.5 cm	0.90	4.00
	7.5<x<13.7 cm	0.68	3.00
	12.7<x<15.2 cm	0.31	1.36

The simulated temperature profiles for both Tests 1 and 2 were reasonably replicated using the linear piece-wise approximation for thermal conductivity (Figure 4-12). Minor variation was introduced into the model saturation values, however, the simulated saturation profiles do not adequately replicate any of the basic features of the experimentally observed saturation profiles (Figure 4-13).

The permeability of each of the models was adjusted to attain better model/experiment agreement. A significant reduction in the permeability assigned to Test 1 was justified by the degradation experienced by the silica beads. Packing inconsistency in the tabular alumina was the rationale for incorporating minor changes in the permeability of the test medium of Test 2. The permeability of the silica beads was reduced in the calculation by three orders of magnitude to 6.23×10^{-16} m^2. Likewise, the assigned permeability of the tabular alumina was reduced by a factor of 10 to 2.95×10^{-15} m^2. The final assigned values for permeability for Tests 1 and 2 are now in relative agreement with the measured flow velocities which indicated a higher permeability for the tabular alumina than for the silica beads. Temperature and saturation profiles for these adjusted models are illustrated in Figures 4-14 and 4-15. Both the temperature and saturation profiles for this Test 2 model are reasonably close to the experimental results. The Test 1 model, however, does not replicate the significant (i.e., 0.10 to 0.20) moisture buildup exhibited in Test 1.

As a final modification from the basecase values, the van Genuchten α parameter was increased by a factor of 10 to 7.19×10^{-4} Pa^{-1} in the Test 1 model. Reasonable agreement between the model and experimental results was attained with this modification. The magnitude of the moisture buildup feature grew to 0.10 to 0.20, values similar to those observed near the base of the Test 1 container, and the temperature regime demonstrated the same transient behavior observed during Test 2. Modification of the model by decreasing the permeability and increasing the α parameter from the pre-test property measurements was justified by changes in pore structure resulting from silica bead degradation. Typically, a decrease in permeability is associated with a decrease in α (Wang, 1992). However, models in which α was decreased provided predictions that did not agree with the experimental results. Thus, agreement between the numerical/experimental results was achieved by altering α in a manner contrary to standard practice, but justified by the significant changes experienced by the medium during the test.

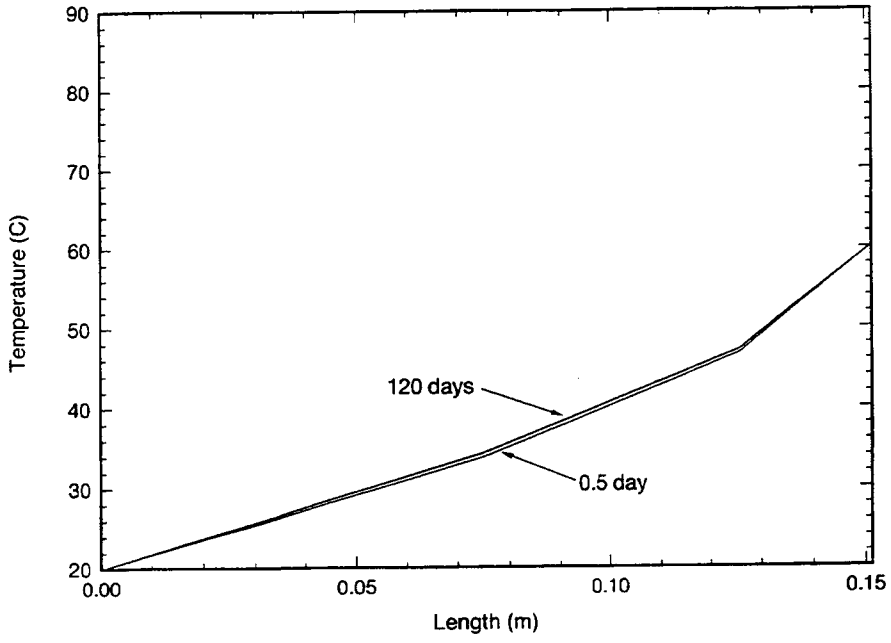

(a)

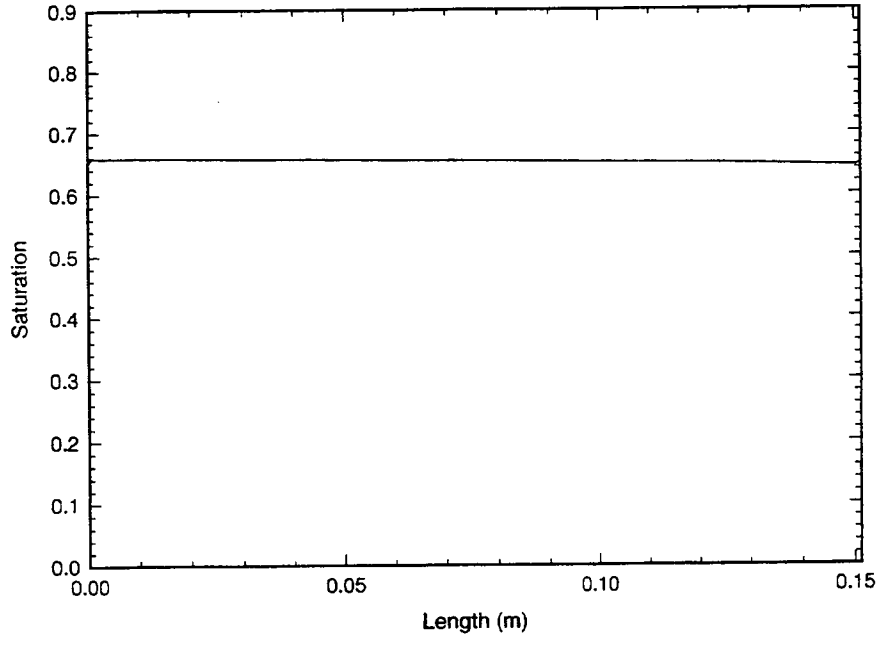

(b)

Figure 4-12. Profile predicted for the basecase properties but with spatially variable thermal conductivity for Test 1 (a) horizontal temperature, and (b) saturation

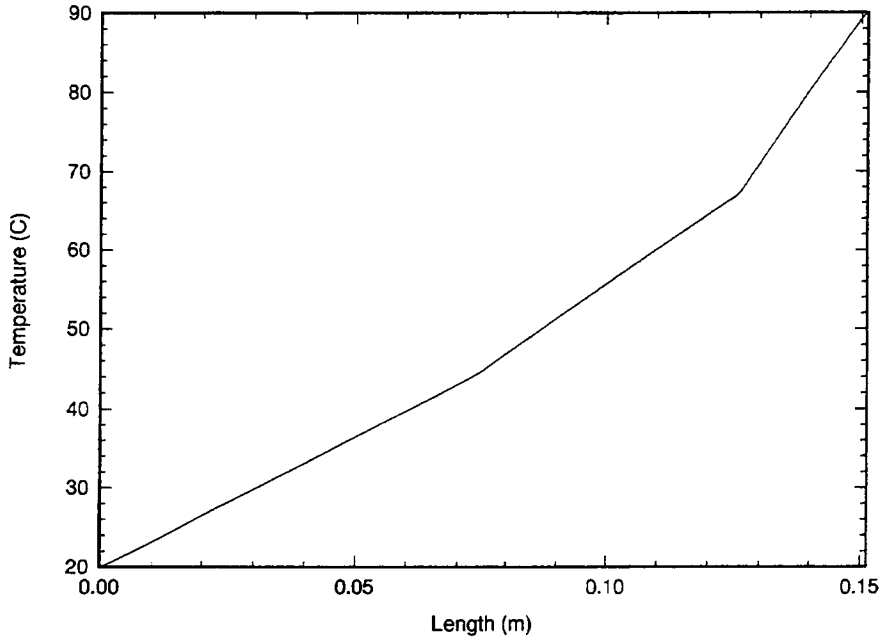

(a)

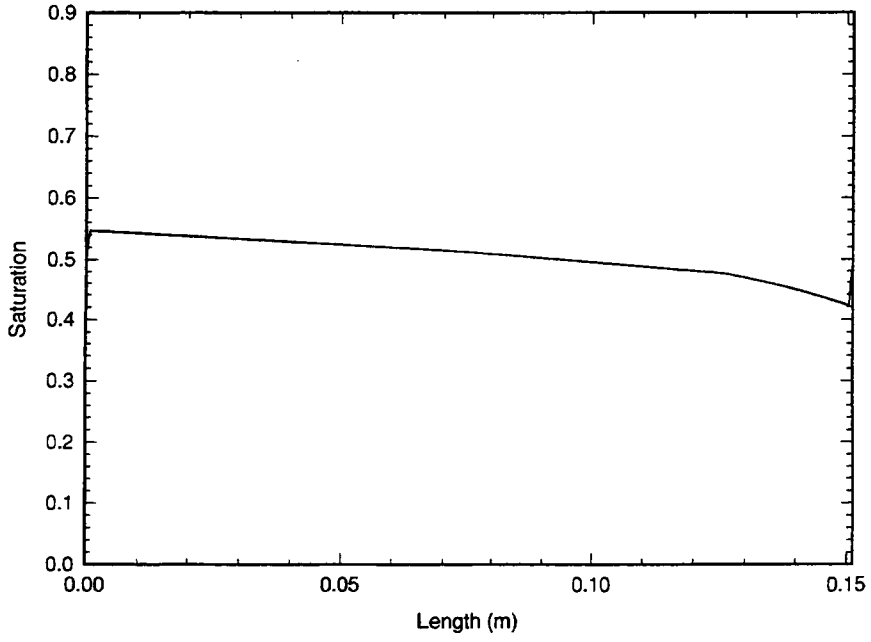

(b)

Figure 4-13. Profile predicted for the basecase properties but with spatially variable thermal conductivity for Test 2 (a) horizontal temperature, and (b) saturation

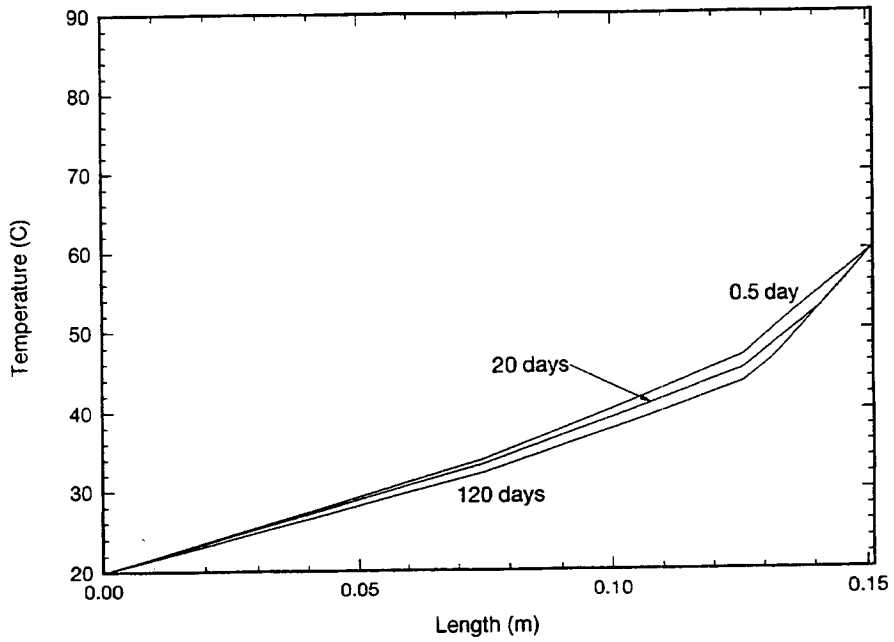

(a)

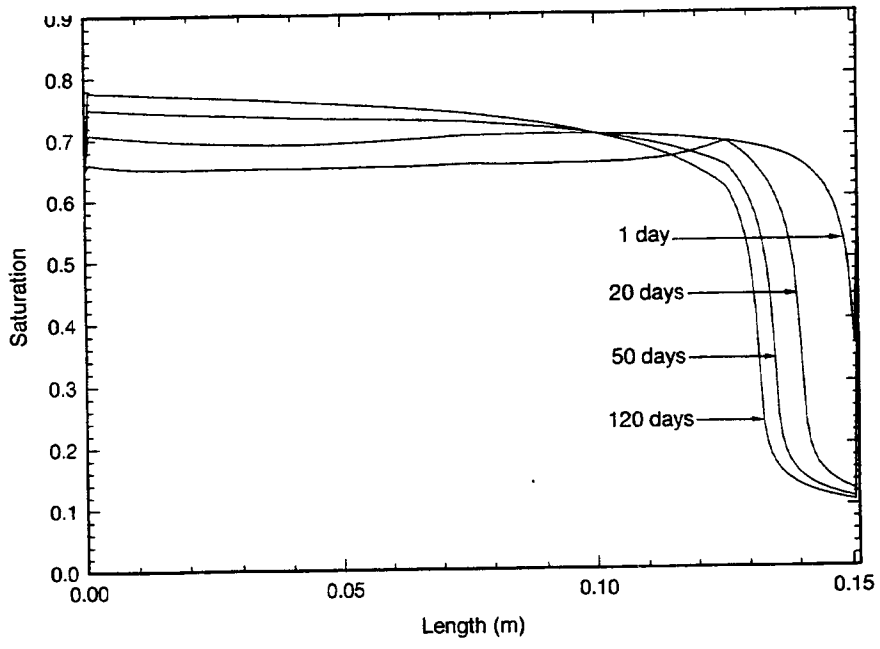

(b)

Figure 4-14. Profile predicted for the basecase properties but with spatially variable thermal conductivity and lower permeability for Test 1 (a) horizontal temperature, and (b) saturation

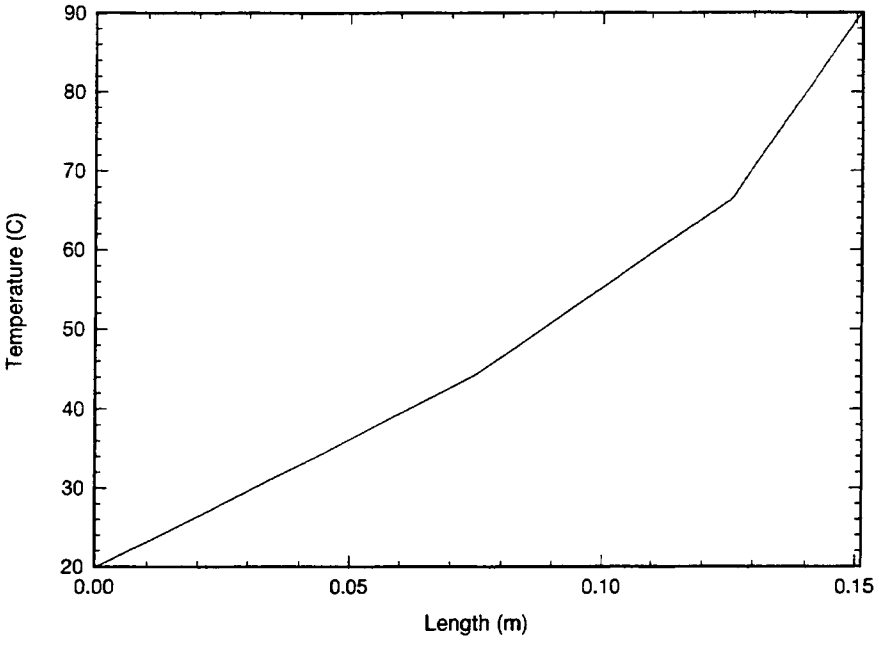

(a)

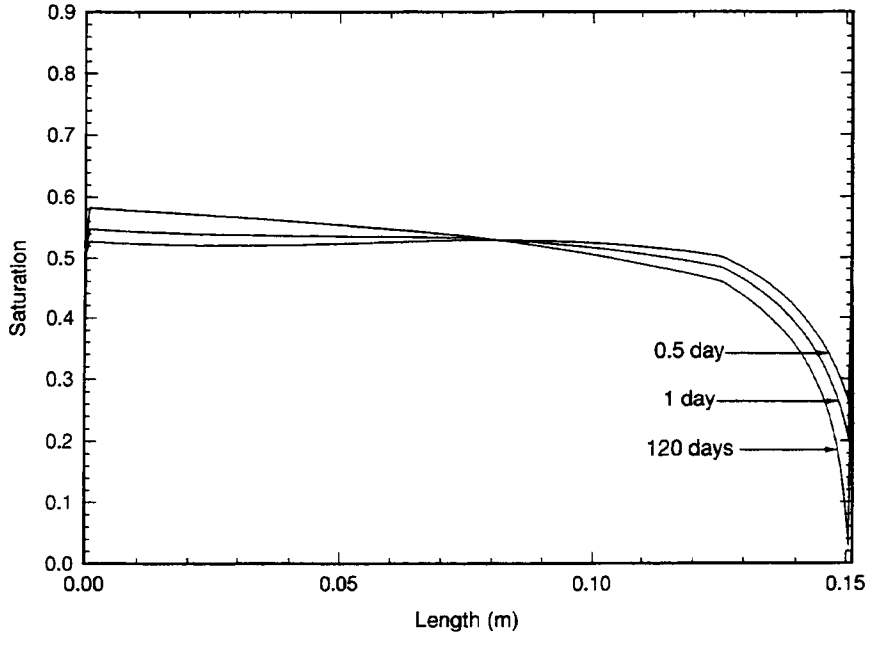

(b)

Figure 4-15. Profile predicted for the basecase properties but with spatially variable thermal conductivity and lower permeability for Test 2 (a) horizontal temperature, and (b) saturation

Conclusions. Results from the 1D liquid flow moisture redistribution experiment and analyses are summarized in the following:

- Laboratory-scale experiments exhibited thermally driven moisture redistribution in two distinct vaporization and condensation models:

  (i) Model 1—condensate building up over a narrow zone proximal to a heat source (Test 1)

  (ii) Model 2—condensate building up over a broad area at some distance from a heat source (Test 2)

- Permeabilities less than about 1×10^{-13} to 1×10^{-14} m^2 are required before prominent saturation gradients can be developed, otherwise the returning liquid flow exceeds the outward vapor flow

- Incorporation of saturation-dependent thermal conductivity into the numerical model adequately matched temperature measurements recorded in the experiments

- Agreement between numerical/experimental results was achieved by decreasing the permeability in both 1D models, and increasing the van Genuchten α parameter for Test 1

- Test results indicated that the 1D group of experiments were not wholly 1D as evidenced by the oblique movement of dye in Test 1

Results from the 1D group of experiments and analyses provided the following conclusions that contribute to understanding the fundamental basis of thermally driven moisture redistribution through partially saturated porous media. Two fundamentally different condensation models have been identified:

- Media with low permeability and a large van Genuchten α parameter (small air-entry value) will be more likely to experience a relatively narrow moisture buildup zone on the cool side of the dryout zone

- Media with a low permeability and a low van Genuchten α parameter (large air-entry value) will tend to exhibit condensation over a broad area beyond the zone of dryout

The importance of these two condensation models is that moisture that condenses in a narrow zone near the dryout zone will have a larger hydraulic gradient and a shorter travel path back to the heater after temperatures have decreased than moisture that condenses over a broad area at a distance from the heat source

4.1.1.2 Two-Dimensional Experiments

Results from a series of five related experiments (Tests 3 through 7) were used to examine mechanisms of heat and mass transfer in a 2D geometry. The experimental results used in the evaluation were drawn from several different experiments because no single experiment provided all the necessary information for the analysis. The evolution in experimental design over the duration of this investigation provided different types of test results. For example, early tests were equipped with ports for injected

dyes to illustrate flow patterns and contained internal instrumentation for measurement of temperature and suction pressure. Later tests had less internal instrumentation but used consolidated media with lower permeabilities, which closely resembled natural rock. As the understanding of heat and mass transfer mechanisms and of the physical state of the flow field improved based on the results of earlier tests, the introduction of dyes into the flow field and the use of internal instrumentation became less necessary. Thus, the introduction of dyes and inclusion of potentially intrusive instrumentation was avoided in the later tests.

Experimental Results and Analysis. Several distinctive features indicative of heat and mass transfer mechanisms were observed in the liquid flow fields. These features were mainly due to the redistribution of moisture in the vicinity of the heater. Prominent among these features was the downward movement of liquid from above the heater, a zone of rapid upward liquid movement toward the heater from below, and a dryout or capture zone along the sides of the heater.

A combination of experimental results was used to identify, describe, and examine these features. A key observation was that the moisture redistribution features were consistent throughout all five related experiments, even though there were differences among the experiments with respect to material properties and thermal conditions. The principal components used in evaluation of the moisture redistribution features were:

- Dye patterns observed in Test 3
- Densitometer-determined saturation measurements from Test 3
- Comparison of experimental and numerical simulation results for Test 3
- Densitometer-determined saturation measurements from Tests 6 and 7

Results from Test 3 were selected for emphasis in the analysis of the 2D experiments for several reasons. Test 4 results were dismissed due to the uncertain effect the simulated fracture may have had on thermally driven moisture redistribution. Interpretation of Test 5 results did not substantively contribute to the analysis. Tests 6 and 7 were conducted under boiling conditions in consolidated media. Detailed analysis of the heat and mass transfer mechanisms under boiling conditions was prevented by the complex two-phase flow phenomena observed near the heater. Therefore, the well documented results from Test 3 provided the strongest evidence in the analysis of the 2D experiments. Following are descriptions of the data and the analyses used to examine these features.

The formation of the moisture redistribution features near the heater was best illustrated by the movement of dye in Test 3. A neutrally buoyant inert dye was introduced into the medium within 5 mm of the front face of the test cell. Dye was injected into the medium at different times during the tests at different combinations of the five ports: the top, bottom, and far left ports; the two side and the far left ports; or all five. Movement of the dye was easily observed through the clear plexiglass front face of the test enclosures. Two sequences of photographs illustrate essentially all flow components of moisture redistribution observed in the experiments. One sequence was taken when the heat source was set at 60 °C, and the second sequence was taken with the heater at 90 °C. The first sequence contains five photographs from Test 3 over a period of 4 days starting 26 days after the initiation of heating at 60 °C (Figure 4-16). The second series of photographs was taken over a 4-day interval, 120 days after the start of heating, and 23 days after the heater temperature was increased from 60 to 90 °C (Figure 4-17).

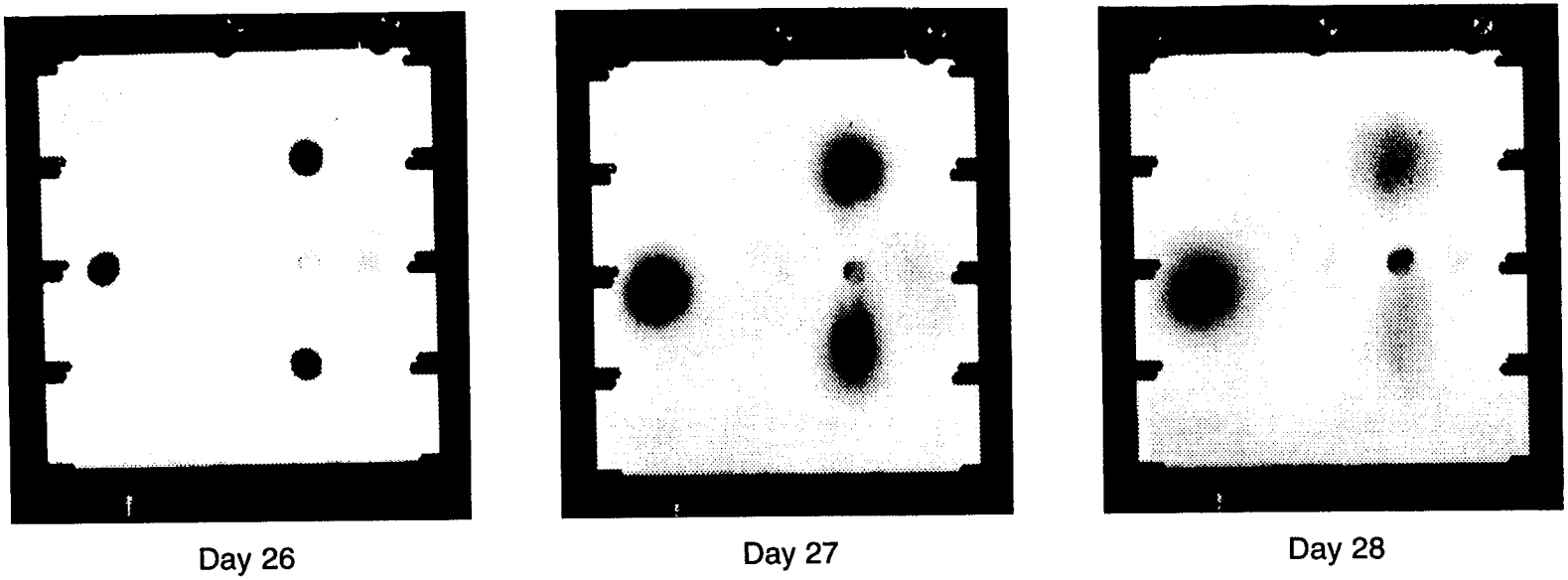

Figure 4-16. Sequence of photographs illustrating dye movement viewed through plexiglass side wall of Test 3 with a heater temperature of 60 °C. The 4-day sequence was taken at days 26 to 30 of the experiment. Heater can be located by black dot at days 27, 28, and 29.

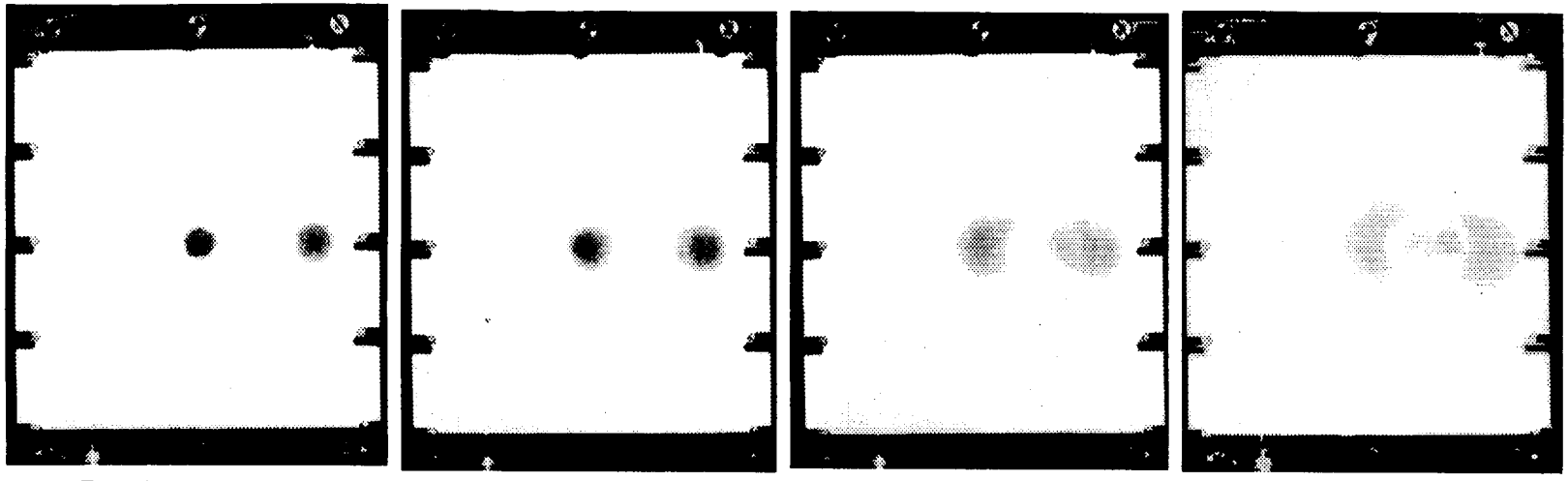

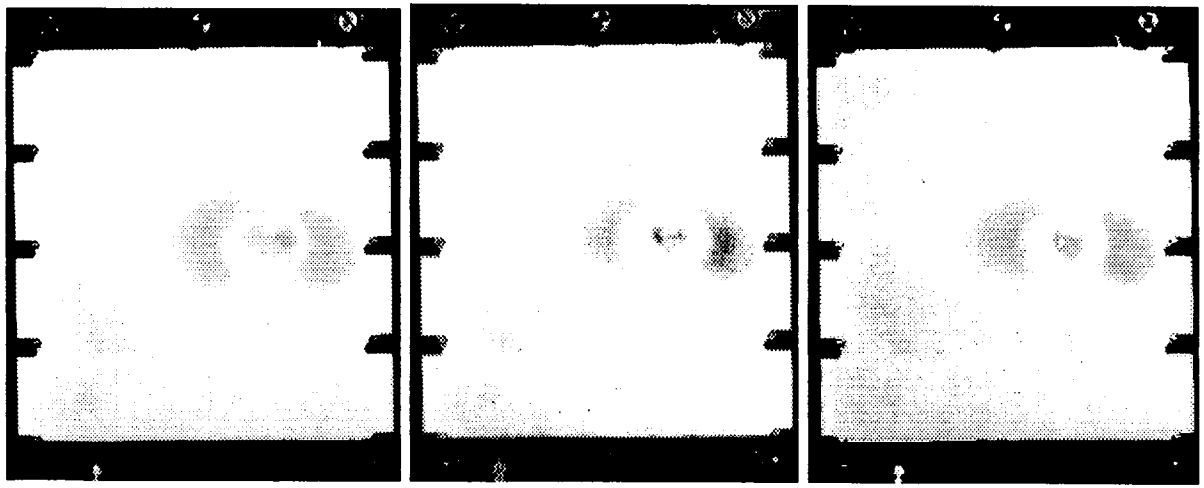

Figure 4-17. Sequence of photographs illustrating dye movement viewed through plexiglass side wall of Test 3 23 days after the heater temperature was increased to 90 °C. The 4-day sequence was taken at days 120 to 123 of the experiment. Heater location is illustrated by faint dot in last four photographs.

The coupled stagnation/rapid flow and dryout/capture zone formation are illustrated in the first sequence of photographs (Figure 4-16). Dye injected at the port located 3 cm directly below the heater tended to move relatively quickly toward the heater. The upward flow rate of the advection-driven fluid from below the heater was measured at 1×10^{-6} m/s from the dye movement documented in the photographs. Dye injected at the port located 3 cm above the heater, however, tended to spread uniformly away from the point of injection at a relatively slow speed. This slow movement appeared to be diffusion-driven. The rate of lateral diffusion was measured to be 7×10^{-8} m/s, more than an order of magnitude slower than advection. The lateral component of the diffusion-driven dye was measured to avoid possible buoyancy effects from affecting the measurement. Because of the apparent lack of advective movement, the area located more than 2 cm above the heater is believed to be a stagnation zone. Downward movement of dye below the stagnation region was observed in Test 3 at both 60 and 90 °C after the dye had diffused to a point closer to the heater. Upon reaching a point sufficiently below the point of injection (within about 1.5 cm of the heater), the dye exhibited a downward rate of movement that was in excess of that due to diffusion alone.

The relatively slow downward movement of dye at the far left injection port was the only flow feature observed away from the near-heater area. Flow in this area consisted of both vapor diffusion and advection. The measured flow velocity of the dye was 1×10^{-7} m/s, a rate slightly greater than that measured for lateral diffusion alone and an order of magnitude lower than advection-driven flow near the heater.

As shown in the second sequence of photographs (Figure 4-17), dye at the right and left of the heater indicated inconsistent flow features. Initially, dye injected at both the right and left of the heater moved toward the left by a combination of advection and diffusion (7.3 hr after injection, photograph 3 in Figure 4-17). Dye from the right injection port appeared to actually reach the heater. This particular flow feature was not generally observed during the experiments. An excessive volume of injected dye is one possible cause for dye from the right injection port reaching the heater. The most common behavior of flow in this region is illustrated in photographs 4 through 7 in Figure 4-17, which indicate the formation of either a dryout or capture zone extending about 1.5 cm to the right and left of the heater.

An additional feature in the flow field of Test 3 was noted on several occasions when dye was injected at either the top and bottom, or the right and left pairs of injection ports. After the injected dye had migrated away from the points of injection (by either advection or diffusion), two additional small, yet distinct, plumes of dye appeared at the upper left and the upper right edges of the heater. These secondary plumes extended less than 0.5 cm from the heater and were very distinct, suggesting that the dye had concentrated at these two points. The small secondary plumes resulting from dye injected at the side ports are illustrated in the photograph in Figure 4-17. This dye could have moved directly toward the heater from the different points of injection before concentrating near the heater, the dye may have traveled through the interior of the medium possibly indicating a 3D flow mechanism, or the dye may be an indication of the formation of secondary circulation cells near the heater. Unfortunately, the actual pathway was not discernable during testing.

Additional evidence of a possible 3D flow mechanism was illustrated by the arrival of dye at the back plexiglass wall near the bottom edge of the heater cartridge in Test 3. This was observed one day after the heater temperature was increased to 90 °C. The possibility of 3D flow is suggested because this dye had originally been introduced within 5 mm of the front plexiglass wall. After arriving at the bottom edge of the heater near the back wall, the dye moved downward toward the base of the test cell.

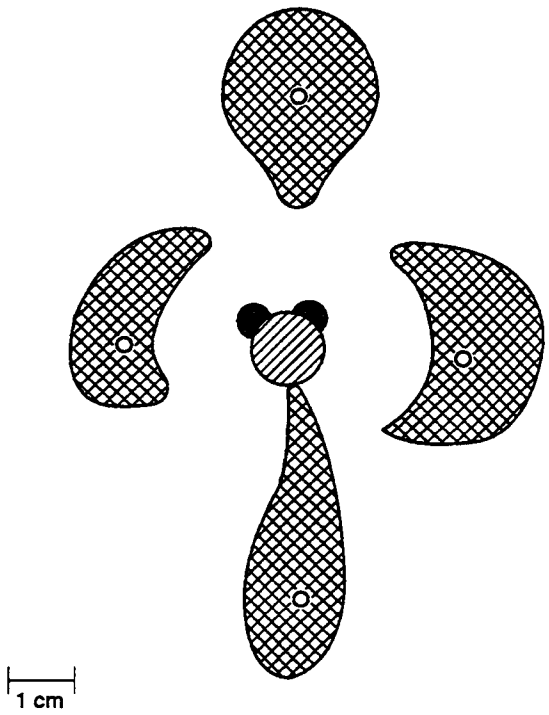

Figure 4-18. Graphical illustration of the major near-heater flow features in the 2D experiments determined using dye movement from Test 3. Heater is indicated by slanted pattern, primary dye plumes by cross-hatch pattern, secondary plumes by solid pattern, and dye injection ports by open circles.

The movement of dye upward at the front of the cell, coupled with downward movement at the back of the cell, suggested that liquid circulation may have formed in the region below the heater. One caveat in this interpretation is that dye arrival at the back of the test cell was periodic and not observed in all tests. It is not known if 3D circulatory flow was present below the heater throughout the experiment or if it was simply a spurious anomaly at the time the heater temperature was increased. Therefore, there is limited evidence that liquid flow in the 2D experiments included a 3D component. It is believed that this evidence is insufficient to suggest that 3D flow components were present, and thus negates the consideration of the experimental results as 2D.

Flow features observed near the heater in experiments under both sub-boiling and boiling conditions may have been different at microscopic levels; however, the major flow features deduced from saturation measurements under both sets of conditions were similar. The major flow features in the 2D experiments, as indicated by dye movement observed in Test 3, are illustrated in the drawing in Figure 4-18. The major flow components of the Test 3 experiments in this summary illustration are:

- Relatively rapid upward flow from below the heater.
- A stagnation zone more than 1.5 to 2.0 cm above the heater.
- Downward flow below the stagnation zone above the heater.

- Stagnation zones to the far (i.e., more than about 1.5 cm) right and left of the heater.
- Two secondary, small (less than 0.5 cm) plumes located at the upper right and left edges of the heater.
- Capture or dryout zones located between the right and left stagnation zones and the heater (referred to here as the lateral capture/dryout zones).
- Possible inactive or dead zones separating the major plumes to right, left, top, and bottom of the heater. These zones may be either no-flow areas separating zones of inward and outward flow on opposing sides or areas of flow not observed due to an absence of dye.

The fluid redistribution mechanisms associated with the last three of these features are not well understood. Two hypotheses, A and B, are proposed to explain these near-heater flow features. The capture/dryout zone acts as a dryout zone in Hypothesis A and as a capture zone in Hypothesis B. Schematics of these hypotheses are illustrated in Figures 4-19 and 4-20.

Hypothesis A. The dryout zone is analogous to the dryout zone phenomenon observed and documented in the 1D experiments. In this interpretation, fluid flows toward the heater and is vaporized. The vapor is then transported away as vapor from the heat source to a point where it condenses at lower temperatures. Water vapor could condense in a narrow band immediately outside the dryout zone (i.e., similar to Test 1) or more evenly over a wider region beyond the dryout zone (i.e., similar to Test 2). In this hypothesis, dye injected to the right and left of the heater is the probable source of the secondary dye plumes because the dye is injected at points near the outer limits of the dryout zone. Minimal dye from above and below the heater reaches the heater because of the greater distance traveled and the vaporization of liquid as it approaches the heat source.

Hypothesis B. Water is circulated as liquid within the capture zone near the heater. Liquid flow to the heater from above and below continues as liquid away from the heater in the lateral directions. Dye injected at the top and bottom ports is the probable source of the secondary dye plumes in this hypothesis. Liquid flow in the capture zone at the locations of the secondary plumes of dye is outward, however, liquid flow away from the heater is limited at the furthest outward extent of the secondary dye plumes.

The direction of flow, in either the lateral dryout/capture zone or the dead zones separating the four major plumes, is not easily discerned from observing the dye movement. Saturation profiles and contour plots calculated from densitometer readings measured in experiments for the tabular alumina (Test 3 at 60 and 90 °C), the relatively highly permeable ceramic (Test 6), and the low-permeability cement slurry mixture (Test 7) are used to help interpret the flow features identified with injected dyes. Saturation values calculated from densitometer measurements from each of the four case studies are graphically presented for two horizontal profiles (one 0.6 cm above the center of the heater and one 0.6 cm below the center of the heater), and one vertical profile through the center of the heater, and as a contour plot. These saturation plots are illustrated as Figures 4-21, 4-22, and 4-23 for Test 3 at 60 °C; Figures 4-24, 4-25, and 4-26 for Test 3 at 90 °C; Figures 4-27, 4-28, and 4-29 for Test 6; and Figures 4-30, 4-31, and 4-32 for Test 7; saturation measured at six different times during Test 7 is also included.

The saturation profiles (Figures 4-21, 4-22, 4-24, and 4-25) and contour plots (Figures 4-23 and 4-26) for the two Test 3 tabular alumina case studies exhibit significantly less resolution than those for

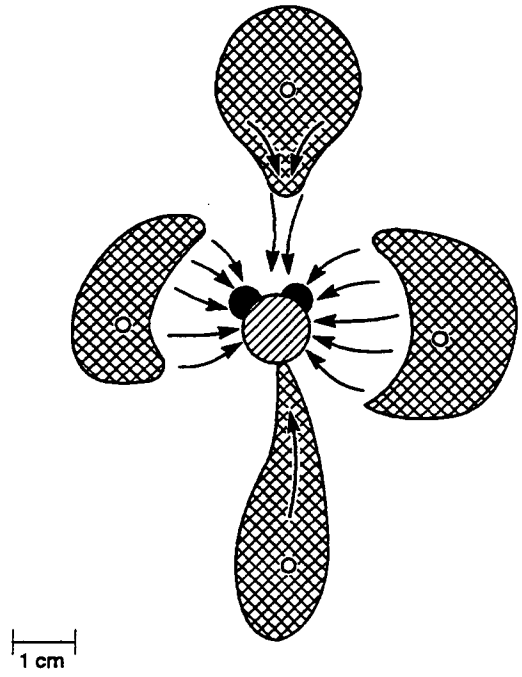

Figure 4-19. Hypothesis A. Lateral capture/dryout zones result from inward movement and vaporization of liquid water. Dye injected at right and left is the source of the secondary dye plumes. Heater is indicated by slanted pattern, primary dye plumes by cross-hatch pattern, secondary plumes by solid pattern, and dye injection ports by open circles.

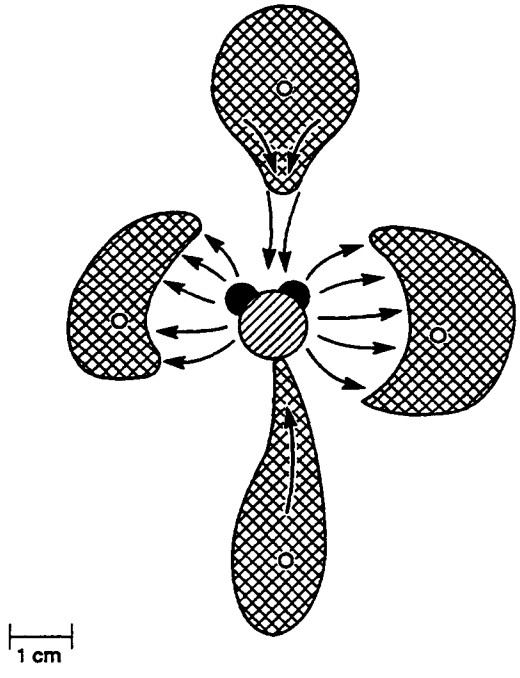

Figure 4-20. Hypothesis B. Lateral capture/dryout zones result from outward movement of liquid water. Dye injected at top and bottom is the source of the secondary dye plumes. Heater is indicated by slanted pattern, primary dye plumes by cross-hatch pattern, secondary plumes by solid pattern, and dye injection ports by open circles.

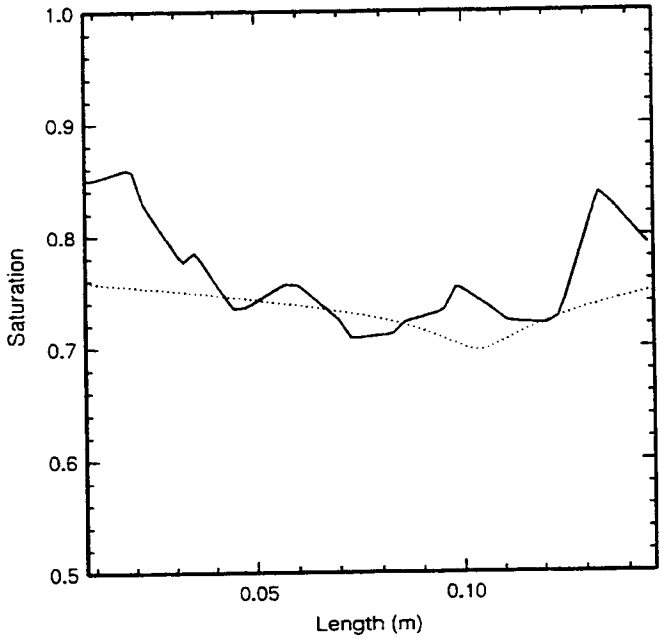

(a)

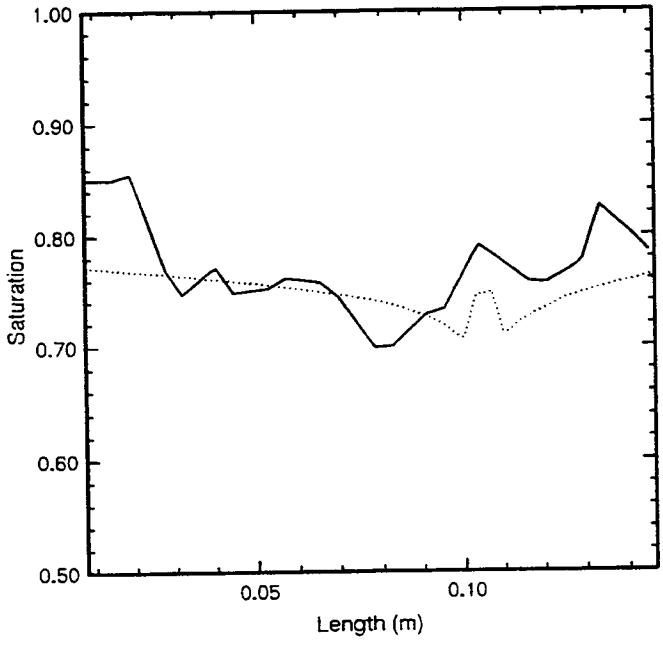

(b)

Figure 4-21. Test 3: solid line is saturation calculated from densitometer measurements along a horizontal profile located (a) 0.6 cm above the center of the heater at 60 °C, and (b) 0.6 cm below the center of the heater. Dotted line is the numerically predicted saturation.

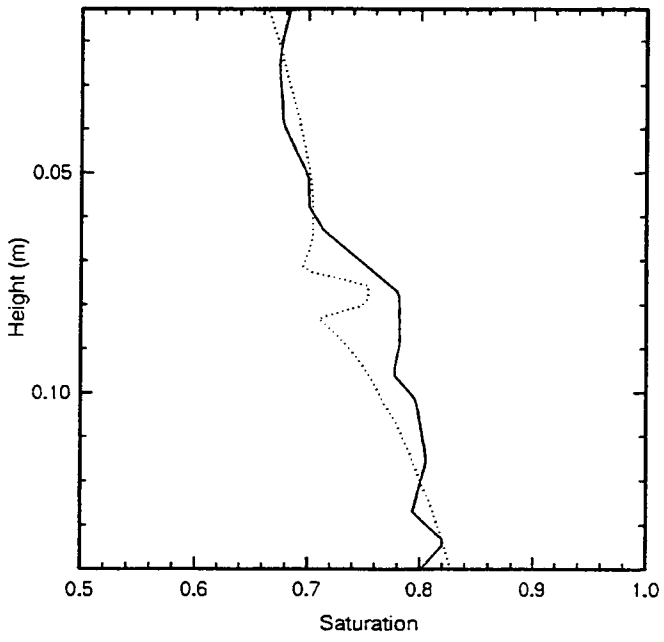

Figure 4-22. Solid line is saturation calculated from densitometer measurements along a vertical profile through the center of the heater for Test 3 at 60 °C. Dotted line is the numerically predicted saturation.

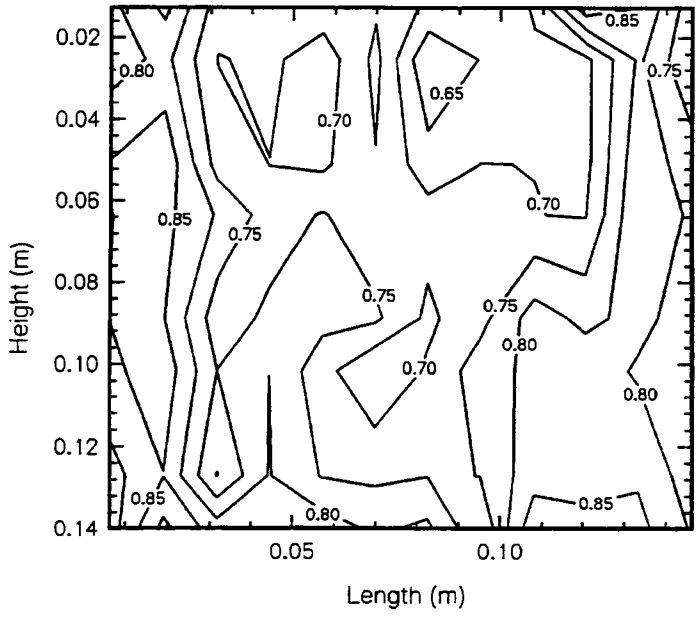

Figure 4-23. Saturation contours calculated from densitometer measurements for Test 3 at 60 °C

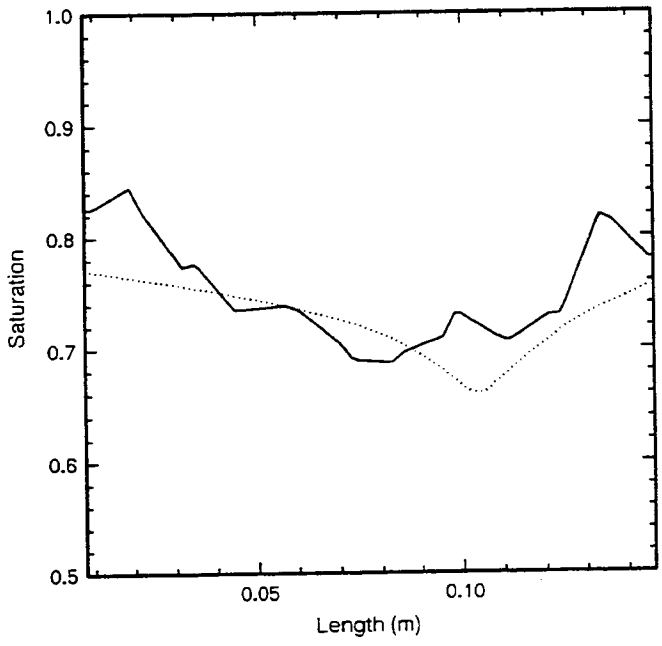

(a)

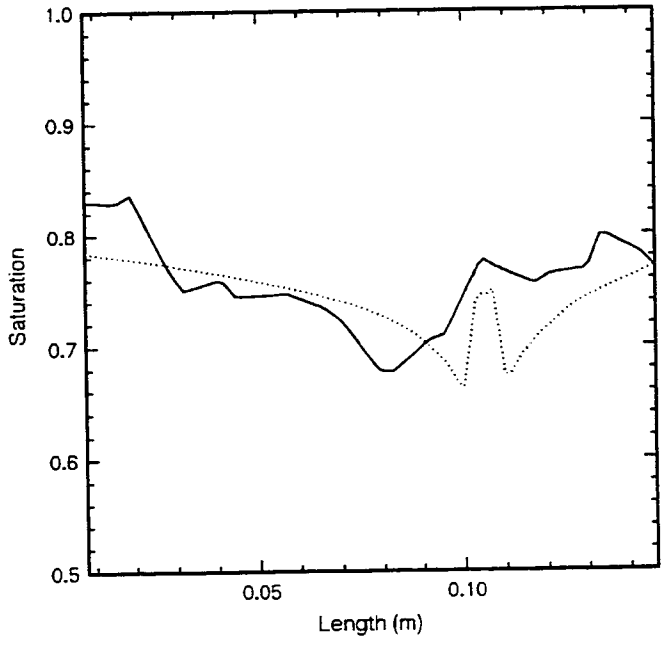

(b)

Figure 4-24. Test 3: solid line is saturation calculated from densitometer measurements along a horizontal profile located (a) 0.6 cm above the center of the heater at 90 °C, and (b) 0.6 cm below the center of the heater. Dotted line is the numerically predicted saturation.

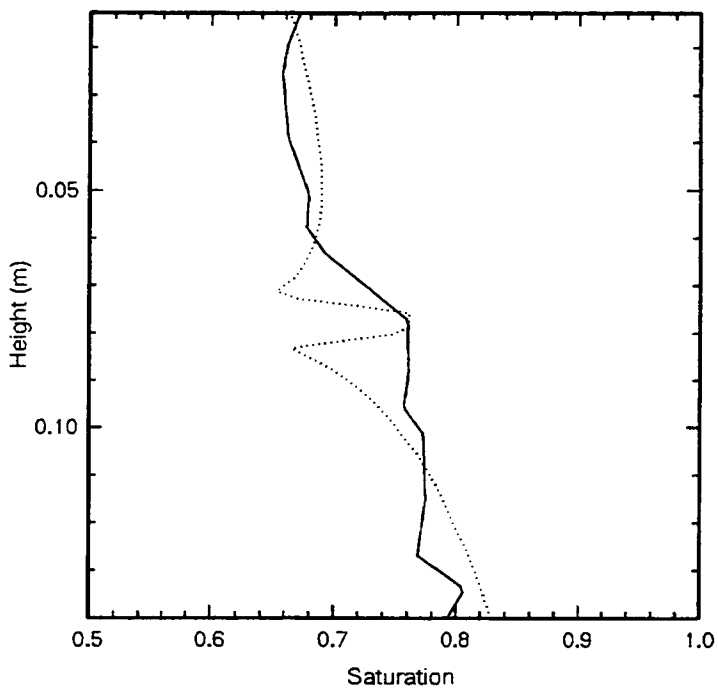

Figure 4-25. Solid line is saturation calculated from densitometer measurements along a vertical profile through the center of the heater for Test 3 at 90 °C. Dotted line is the numerically predicted saturation.

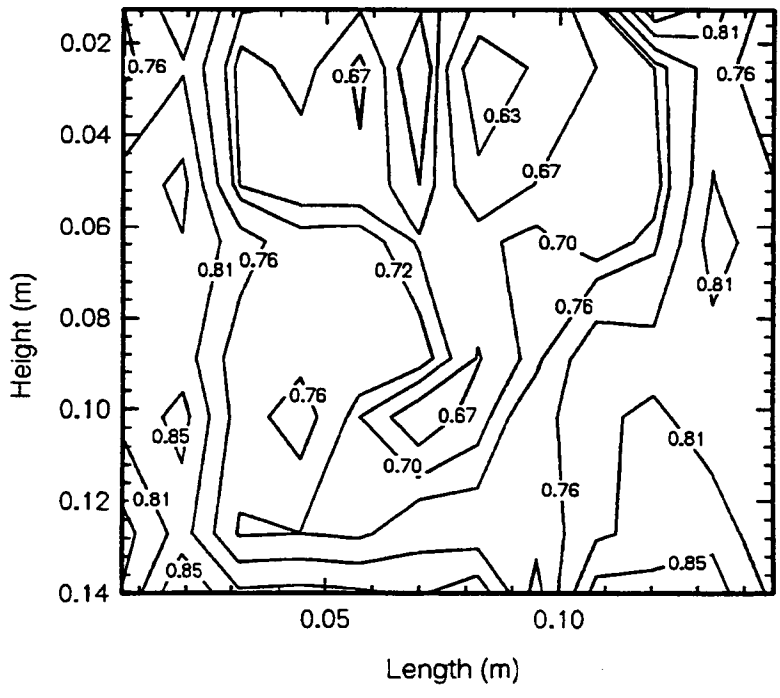

Figure 4-26. Saturation contours calculated from densitometer measurements for Test 3 at 90 °C

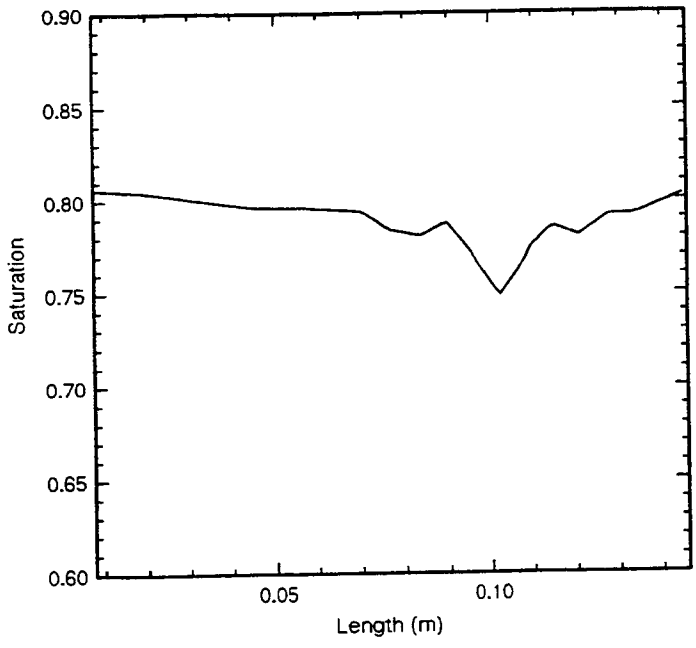

(a)

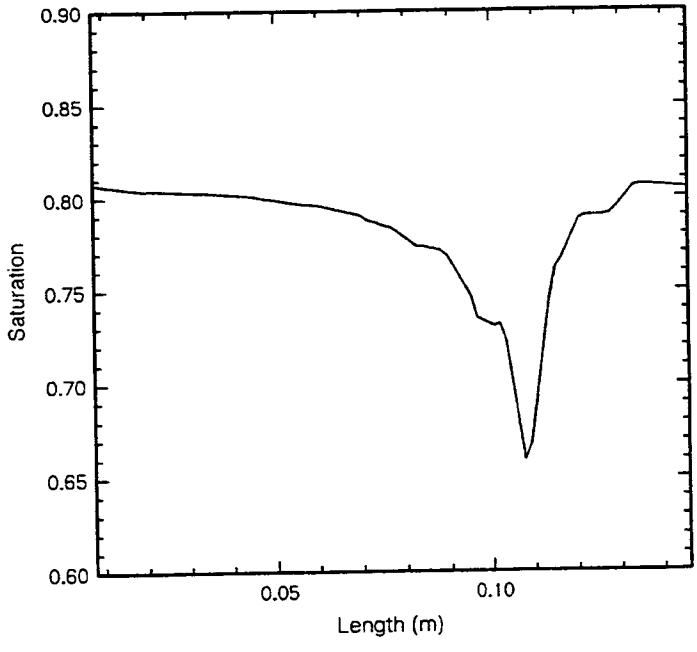

(b)

Figure 4-27. Test 6: saturation calculated from densitometer measurements along a horizontal profile located (a) 0.6 cm above the center of the heater for the ceramic, and (b) 0.6 cm below the center of the heater

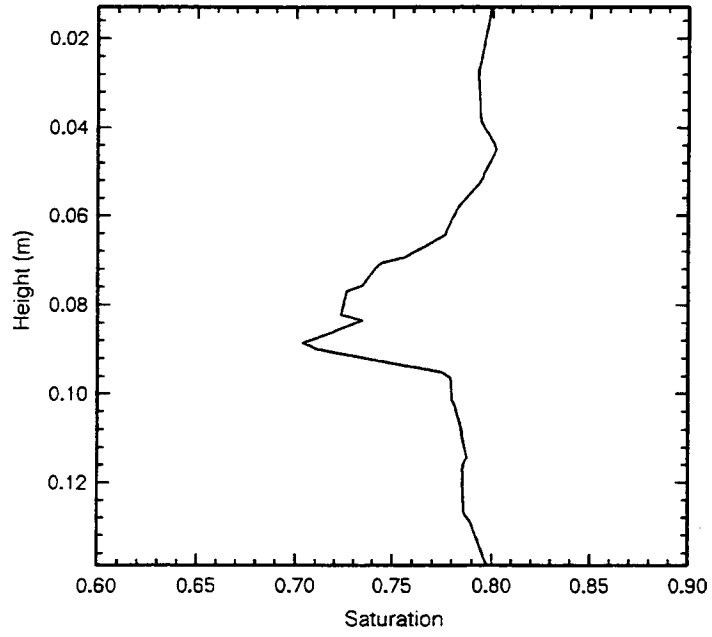

Figure 4-28. Saturation calculated from densitometer measurements along a vertical profile through the center of the heater for the ceramic in Test 6

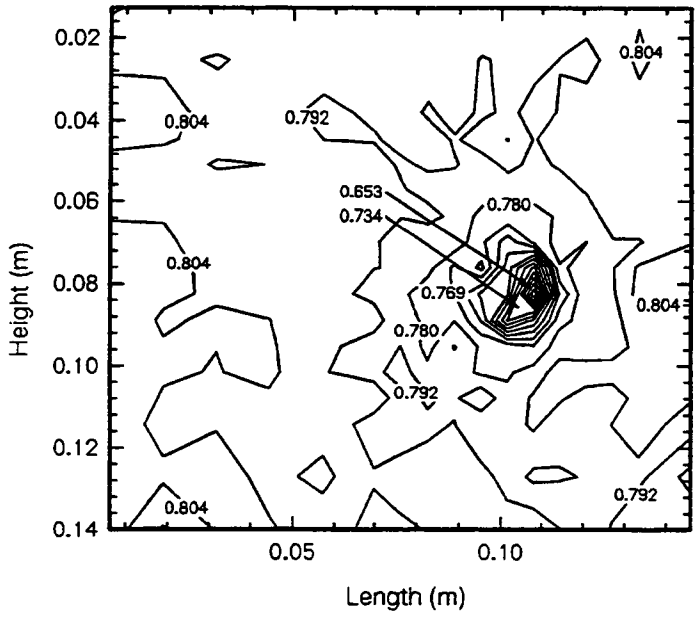

Figure 4-29. Saturation calculated from densitometer measurement contours for the ceramic in Test 6

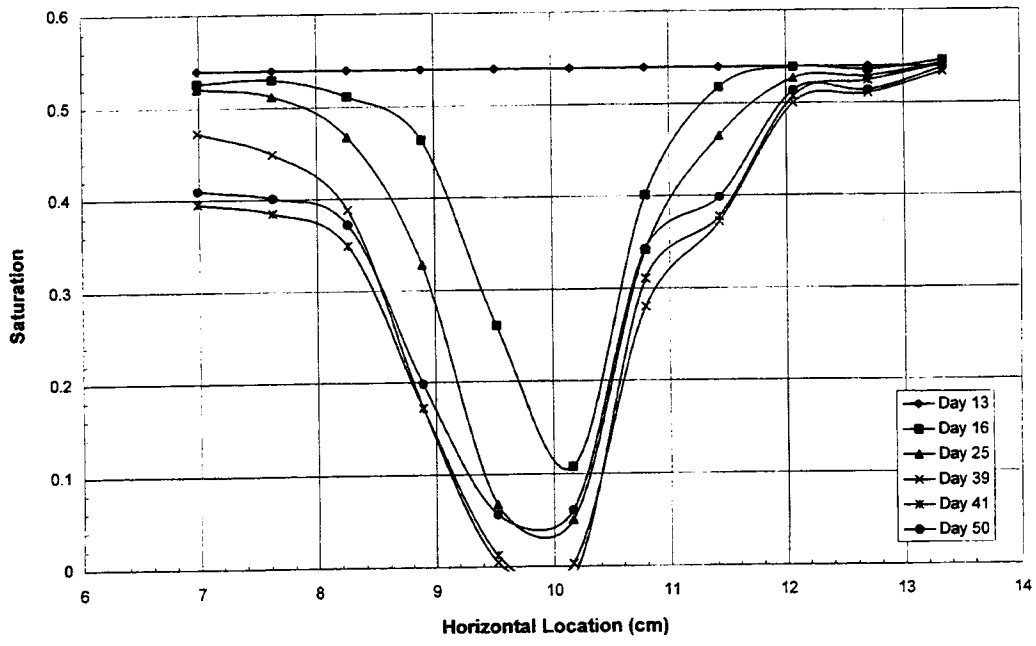

(a)

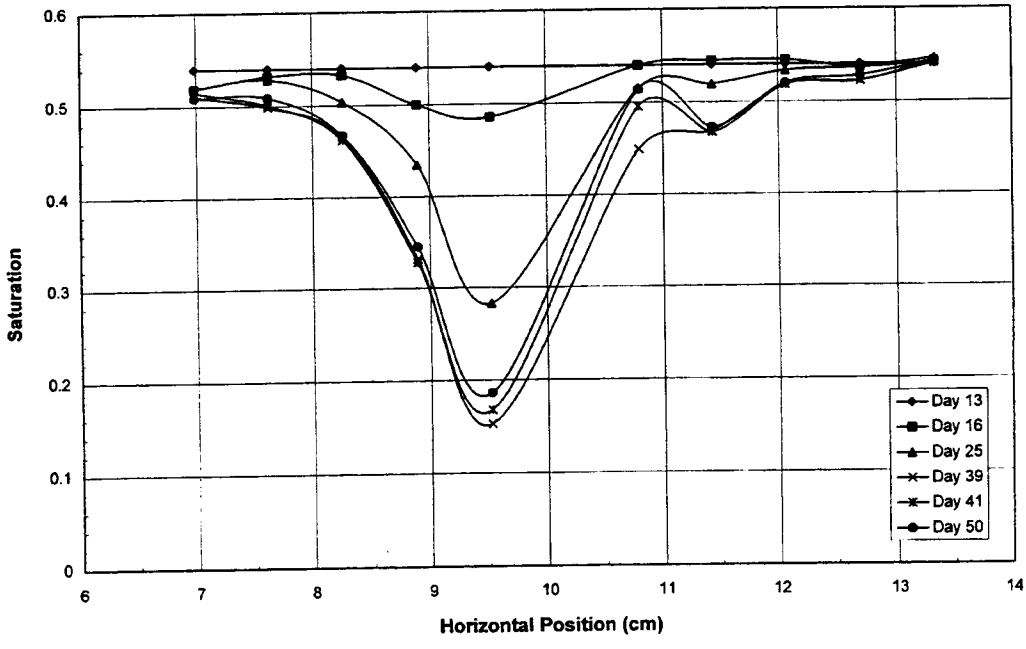

(b)

Figure 4-30. Test 7: saturation calculated from densitometer measurements at six times along a horizontal profile located (a) 0.6 cm above the center of the heater for the cement slurry mixture, and (b) 0.6 cm below the center of the heater

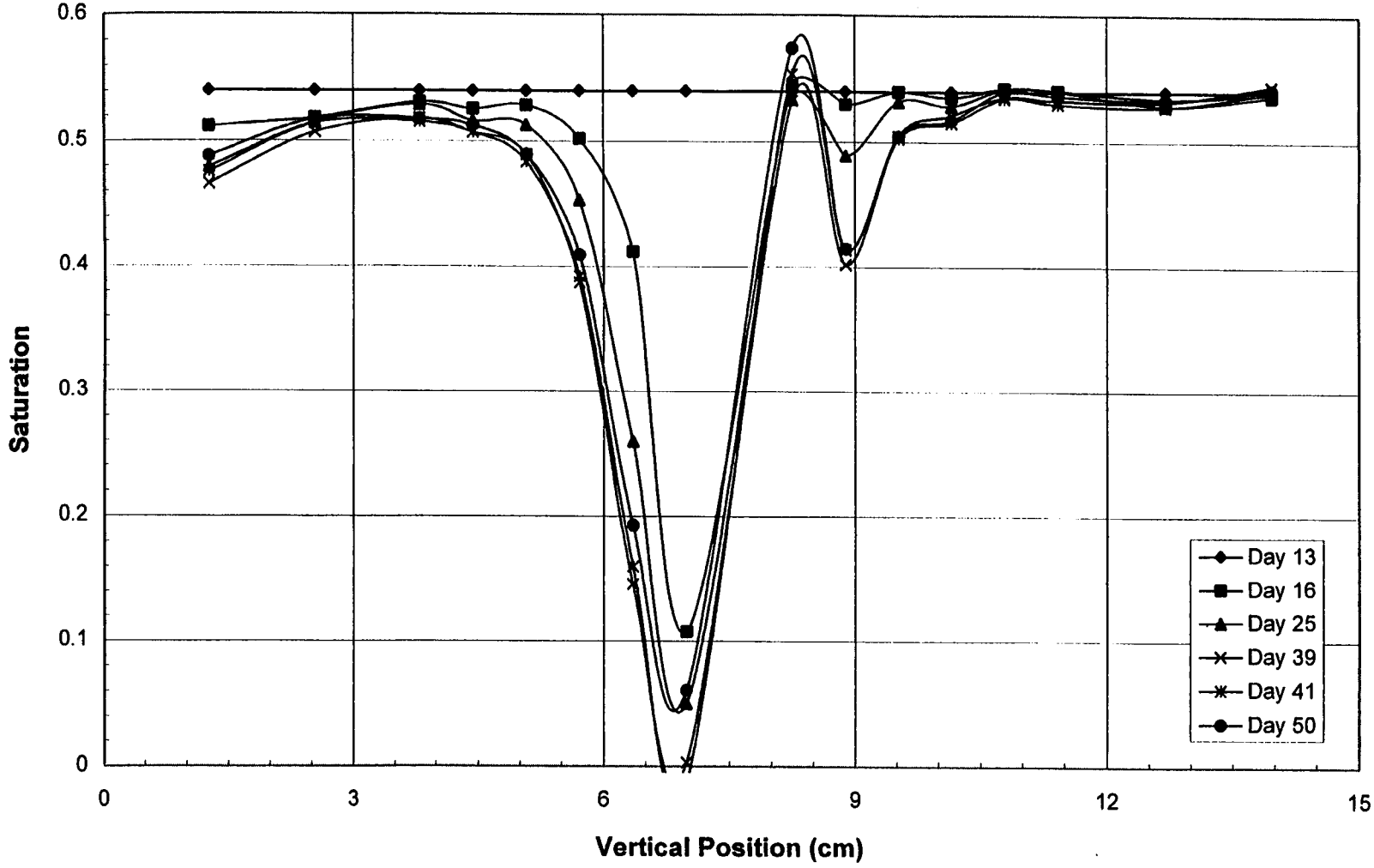

Figure 4-31. Saturation calculated from densitometer measurements at six times along a vertical profile through the center of the heater for the cement slurry mixture in Test 7

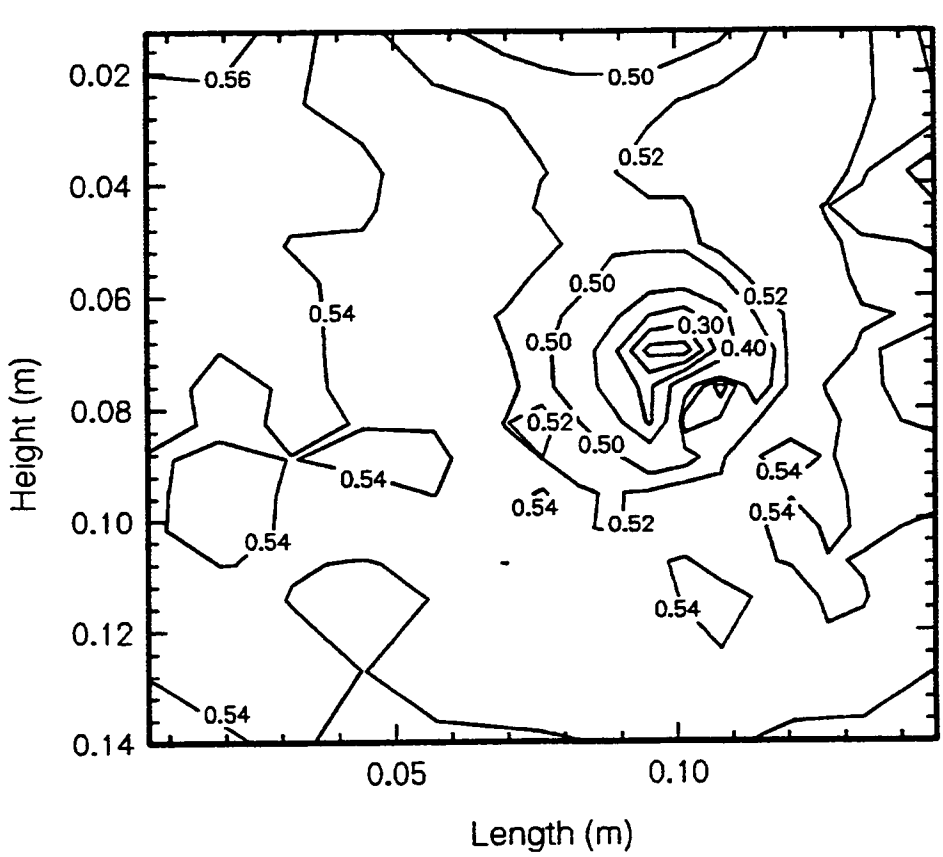

Figure 4-32. Saturation calculated from densitometer measurement contours for the cement slurry mixture in Test 7

the ceramic in Test 6 (Figures 4-27, 4-28, and 4-29) and the cement slurry mixture in Test 7 (Figures 4-30, 4-31, and 4-32). Lack of resolution in the Test 3 data is attributed to difficulties associated with packing, preparing a uniform test medium, and a spatial density of densitometer data. The horizontal and vertical saturation profiles for Test 3 reflect the general trend of lower saturation near the heater but do not provide adequate detail for analysis. No identifiable trends in moisture redistribution are exhibited in the saturation contour plots for Test 3 at 60 and 90 °C. Implied decreases in saturation, such as the 0.60 to 0.65 valley in the upper central portion of the Test 3 contour plot (Figure 4-23), are attributed to a decrease in density resulting from an inconsistency in packing of the granular material.

Saturation plots for the ceramic and the cement slurry mixture provided significantly better accuracy than those for the tabular alumina. This improved accuracy is attributed to the uniformity of the media and the higher heater temperatures. The boiling temperatures of Tests 6 and 7 created larger density gradients, which provided better accuracy for the saturation calculations. A distinct desaturation anomaly is visible in the saturation contour plot for Test 6 (Figure 4-29) and Test 7 (Figure 4-32). The relatively high permeability ceramic in Test 6 was desaturated only to a minimum of 0.65 from an initial saturation of 0.80, as compared to the low-permeability cement in Test 7, which was completely desaturated near the heater. Also plotted are saturation contours for the ceramic with an initial saturation of 55 percent and heated to over 170 °C (Figure 4-33). Return flow of liquid in the ceramic toward the

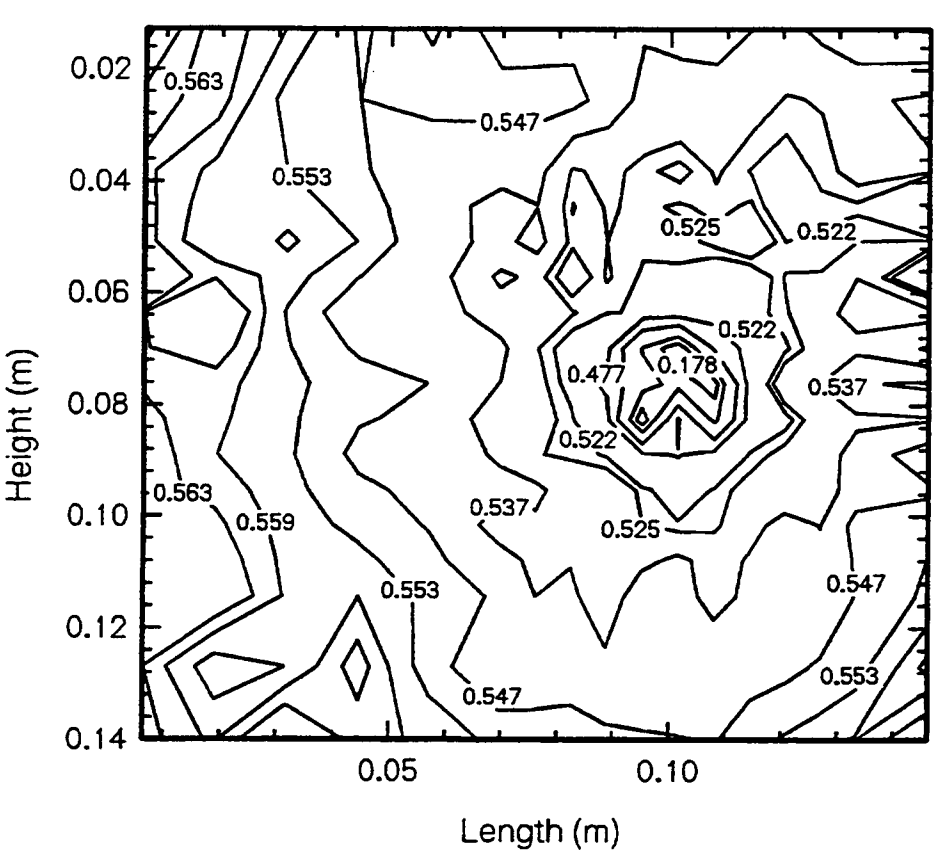

Figure 4-33. Saturation contours calculated from densitometer measurements for ceramic in Test 6 at 170 °C

heater was sufficiently rapid to keep the heater from complete dryout (at least at the locations of measurement) even though the heater temperature exceeded 170 °C.

The horizontal saturation profiles of all four cases indicate the same basic trend of desaturation near the heater. There is no compelling evidence in either the saturation profiles or the contour plots of a moisture buildup zone at the edge of the dryout zone. It appears that moisture vaporized at the heater did not condense in a narrow band immediately outside of the dryout zone, but instead was transported away from the heater before condensing uniformly over the total area between the dryout zone and the test container edges. Although minor anomalies in the saturation profiles could arguably be interpreted as evidence of the presence of a moisture buildup zone (i.e., the best example is to the right of the heater in Test 7), there was no evidence of a prominent dryout/moisture buildup zone in any of the 2D experiments.

The rates and times for resaturation of the media after the cessation of heating during Test 7 were estimated using saturation measurements made at different times. Times for resaturation were estimated from the two horizontal profiles and the one vertical profile by calculating the rate of resaturation from saturation measurements soon after the heater was turned off and from saturation measurements at the end of the experiment. The estimated times for resaturation calculated from the upper horizontal, lower horizontal, and vertical profiles were 250, 100, and 80 days. The rates of resaturation

(defined as the rate at which a particular level of saturation moves) were calculated to be 1×10^{-9} to 1×10^{-8} m/s in the horizontal direction, 1×10^{-8} m/s in the downward direction, and negligible resaturation from below the heater.

Numerical Simulations. The computer code V-TOUGH was used to simulate liquid redistribution resulting from the point heat source in the 2D liquid flow experiments. Results from Test 3 at 60 and 90 °C were selected for analysis by numerical simulation. The numerical analyses were conducted to: (i) identify whether Hypothesis A or B is most likely to represent the source mechanisms for moisture redistribution in the near-heater region, and (ii) evaluate the ability of V-TOUGH to replicate the liquid flow regimes observed in the 2D experiments. The near heater, secondary flow features were not replicated in the numerical model. Flow features similar to these have been shown to be numerically unstable and not suitable to modeling (Bonano and Davis, 1980). Additional analysis of grid resolution that could aid in interpreting the secondary features. Model results are only used to assess the primary flow features observed in the experiments.

The numerical model was constructed to replicate Test 3. The same numerical values of experimental properties and thermal conditions measured for Test 3 were used in the numerical simulations. The vertical and horizontal dimensions of the numerical model are the same as Test 3, and the boundary conditions for the numerical simulations approximate those of the laboratory-scale experiments. The vertical and horizontal boundaries are prescribed as no fluid flow. The assigned values for experimental parameters are taken from Tables 3-2 and 3-5 through 3-9. A porosity of 0.41 and a permeability of 8.04×10^{-13} m^2 were assigned to the tabular alumina. The van Genuchten values in the retention curve were 1.31×10^{-4} Pa^{-1} for α and 5.00 for n. Saturation was originally measured to be 0.70, however, densitometer measurements and review of the laboratory procedure indicated that the actual saturation for Test 3 was probably closer to 0.75. Therefore, a saturation of 0.75 was used in the simulation.

The right and left vertical boundaries of the numerical model were maintained at 20 °C. The top and bottom boundaries were adiabatic. The heat source was modeled as an impermeable 0.75×0.75 cm square. The power input into the water-circulating bayonet heater of Test 3 could not be measured and was not known. The numerical model values for heat load for the two temperatures of Test 3 were adjusted to achieve an acceptable comparison between the experimentally observed and numerically predicted temperature at the heater. This calibration process was used to accommodate, at least in part, the 3D heat loss experienced through the plexiglass side walls during the tests. Differences between predicted and experimental temperatures (measured at the heat source and at other locations) at steady-state are a function of the property values assigned to the medium, particularly thermal conductivity, in addition to the strength of the heat source. The transient formation of the temperature regime depends on the specific heat of the medium. However, since the thermal regime was established relatively quickly in these tests, the experimental results are relatively insensitive to minor variations in the values of the specific heat. Therefore, specific heat was not examined in detail.

Values assigned to thermal conductivity, however, can significantly affect the outcome of model predictions. Difficulty in directly measuring the thermal conductivity of tabular alumina was due to variations in packing and the nonuniform distribution of moisture in tested samples. Therefore, published thermal conductivity values for tabular alumina were assigned to the Test 3 medium in the numerical simulations. The assigned dry and wet thermal conductivities were 2.6 and 4.0 W/m, respectively, for tabular alumina.

The cumulative effect of the values assigned to the heat source load and the thermal properties of the medium can be estimated by comparing the measured temperature distribution with that predicted in the simulation. The simulated steady-state temperature distributions for Test 3 with the heater set at 60 and 90 °C are illustrated in Figures 4-34 and 4-35, respectively. Also presented in these figures are the temperatures recorded by the six internal thermistors. As illustrated in these figures, the numerical model was successful in replicating the temperatures observed during Test 3 at 60 °C. The temperature distribution predicted for the 90 °C heater agreed with four of the six internal thermistors (i.e., the difference between measured and predicted temperatures were within ± 1 °C). However, the temperature recorded at the two thermistors located midway on the horizontal scale differed by as much as 4 °C from the predicted values. This difference is attributed to possible inappropriate property values assigned to the medium. Higher temperatures near the heat source is an indication of higher conductivities than those assigned to the numerical model. A nonlinear thermal conductivity-saturation model that predicted higher conductivities at lower saturations could resolve this discrepancy. Regardless of the source of the difference in the temperature regimes, it suggests that temperatures in the test enclosures may not be as well replicated at higher temperatures as at the lower temperatures. In particular, the presence of the secondary plumes provides evidence of secondary circulation flows above the heater. Nonetheless, predicted temperature distributions for Test 3 at 60 °C and for most measurement locations at 90 °C were sufficiently similar to observed temperatures that no adjustment in assigned thermal conductivity values was required. The final heat loads were determined by adjusting the heat load until the predicted temperature at the heater matched either 60 or 90 °C. The heat loads for Test 3 at 60 and 90 °C were assigned values of 13.2 and 22.8 W, respectively.

Simulated capillary pressure distributions and point suction pressure measurements were compared for Test 3 at 60 and 90 °C. The predicted capillary pressures for the 60 and 90 °C simulations are illustrated in Figures 4-36 and 4-37, respectively. The simulated capillary pressure contour plots are essentially smooth, except for a small variation near the heater. This variation results from the relatively flat moisture retention curve measured for the tabular alumina in which matric pressure is insensitive to changes in saturation from 60 to 80 percent. Suction pressures measured at five tensiometers for the entire duration of Test 3 are presented in Figures 4-38 and 4-39. All five tensiometers indicate an increase in matric pressure throughout the experiment. Tensiometers 1, 3, 5, and 6 had an increase in matric pressure of about 3 Kpa and tensiometer 4 had an increase of about 6 kPa. Tensiometer 4 is located in the lower left corner of the test cell, farthest from the heater. Moisture redistribution within the test cell does not appear to adequately explain the increase in matric pressure at all measurement points. Saturation distributions determined from densitometer measurements indicate a net increase in saturation in the lower left corner of the test cell. It is important to note that the temperature in Test 3 was set at 60 °C from day 8 until day 97, then increased to 90 °C until day 155. The effect of temperature on the matric pressure/saturation relationship in the retention curve was not examined. It is possible that the retention curve determined at 20 °C for tabular alumina is not valid at higher temperatures. The full implications of discrepancies in tensiometer values are not clear.

The densitometer-determined saturation distribution in Test 3 with the heater temperature set at 60 °C was compared with liquid saturation predictions made with the numerical model. Comparisons of numerically predicted saturation along horizontal transects located 0.6 cm above and below the heat source are illustrated with the measured data at 60 °C in Figure 4-21 and at 90 °C in Figure 4-24. Vertical transects through the heater comparing measured and predicted saturation are illustrated in Figures 4-22 and 4-25. As illustrated in the horizontal profiles, there is general agreement in the trend of desaturation near the heater. The lack of resolution in the observed data for Test 3 limits in-depth analysis. The predicted decrease in saturation at the heater location in the vertical profiles is not exhibited

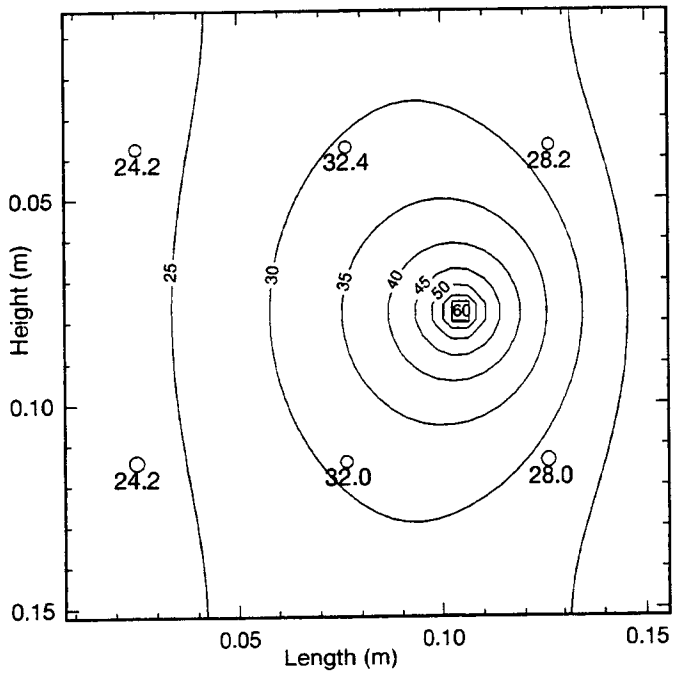

Figure 4-34. Temperature distribution for Test 3 with a 60 °C heat source. Contour lines are from the numerical simulation and point measurements are from the laboratory experiment.

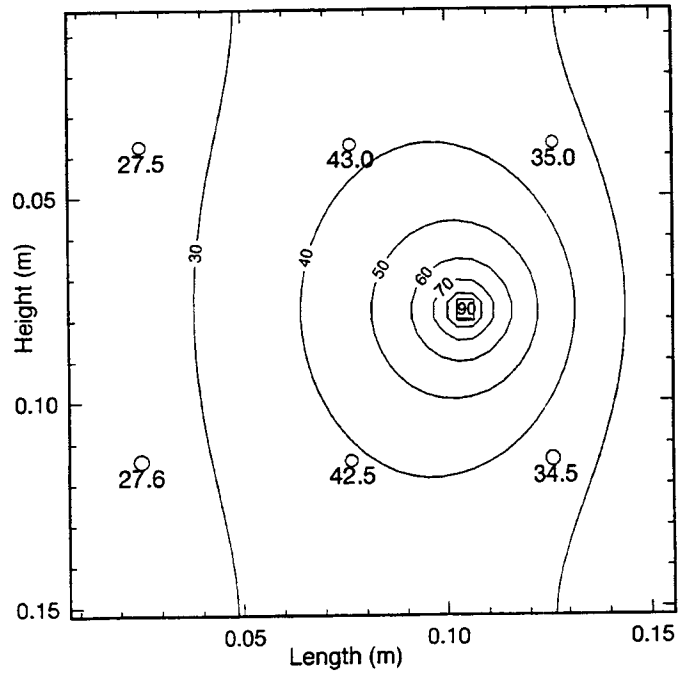

Figure 4-35. Temperature distribution for Test 3 with a 90 °C heat source. Contour lines are from numerical simulation and point measurements are from the laboratory experiment.

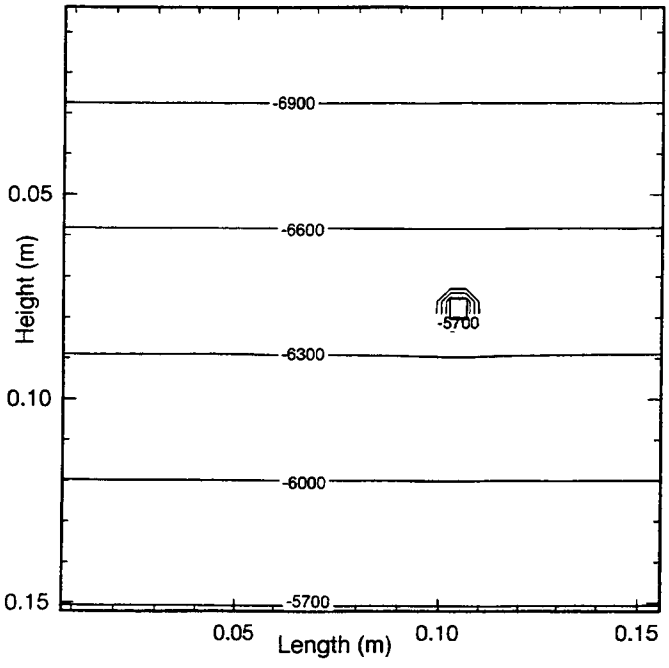

Figure 4-36. Numerically predicted capillary pressure distribution for Test 3 with a 60 °C heat source

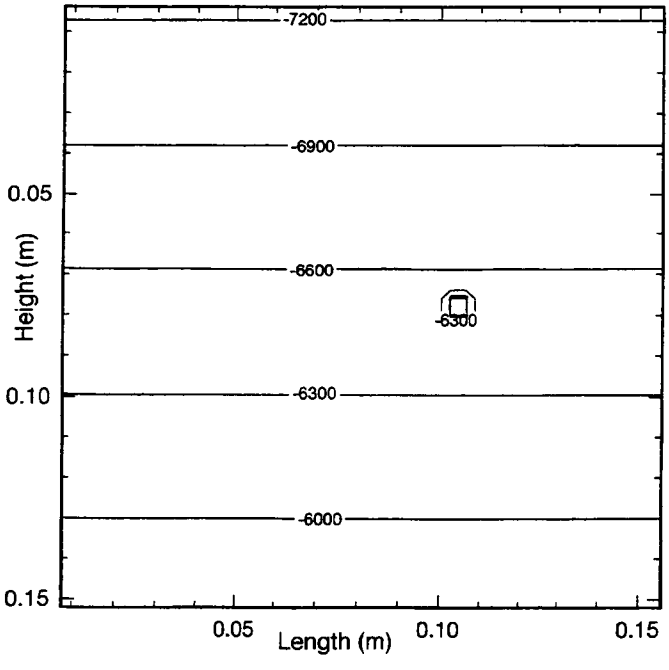

Figure 4-37. Numerically predicted capillary pressure distribution for Test 3 with a 90 °C heat source

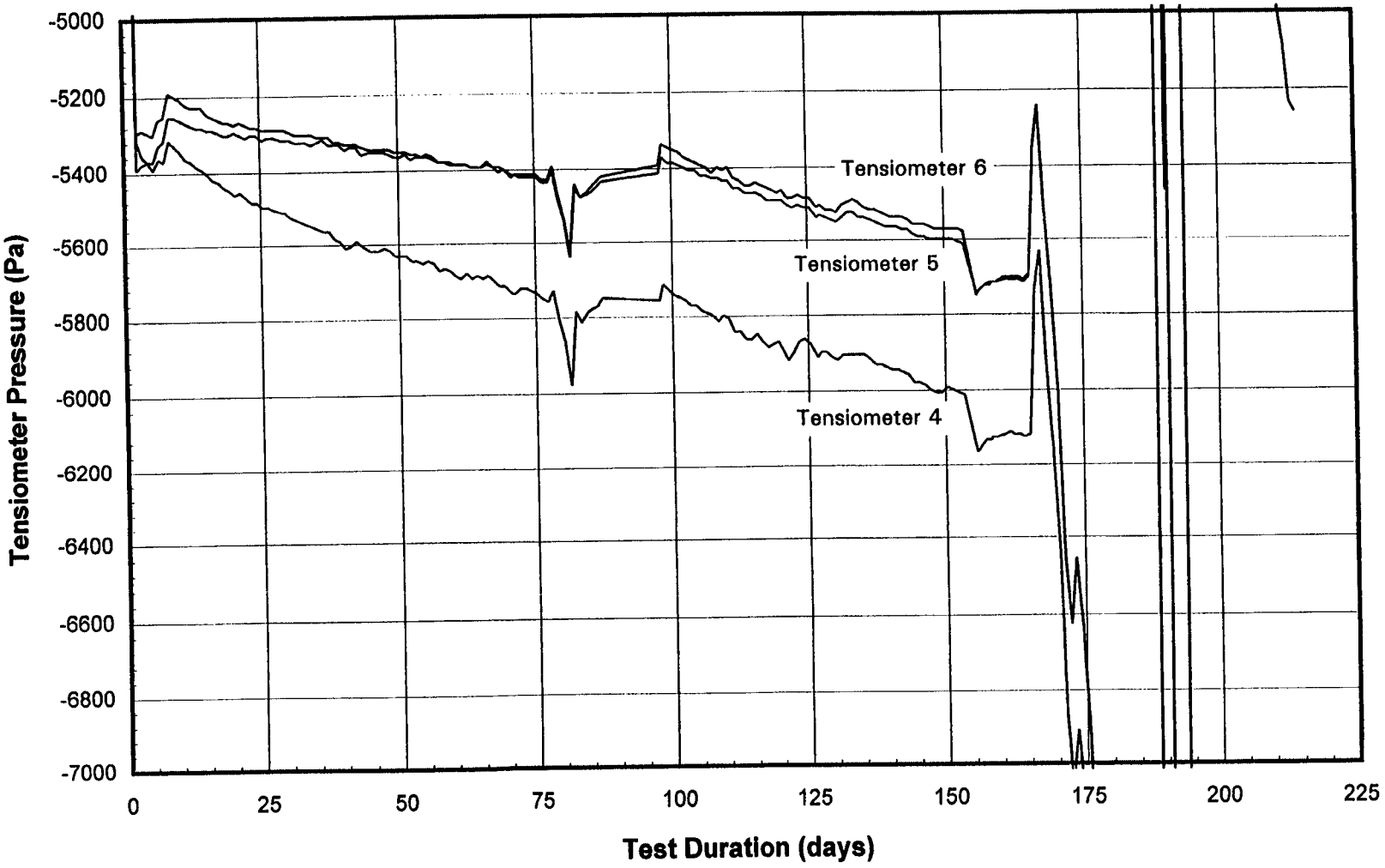

Figure 4-38. Test 3 tensiometer matric pressure measurements at locations 4, 5, and 6. Temperature of Test 3 was 60 °C from days 8 to 97 and 90 °C from days 97 to 155 (see Figure 3-2 for tensiometer locations).

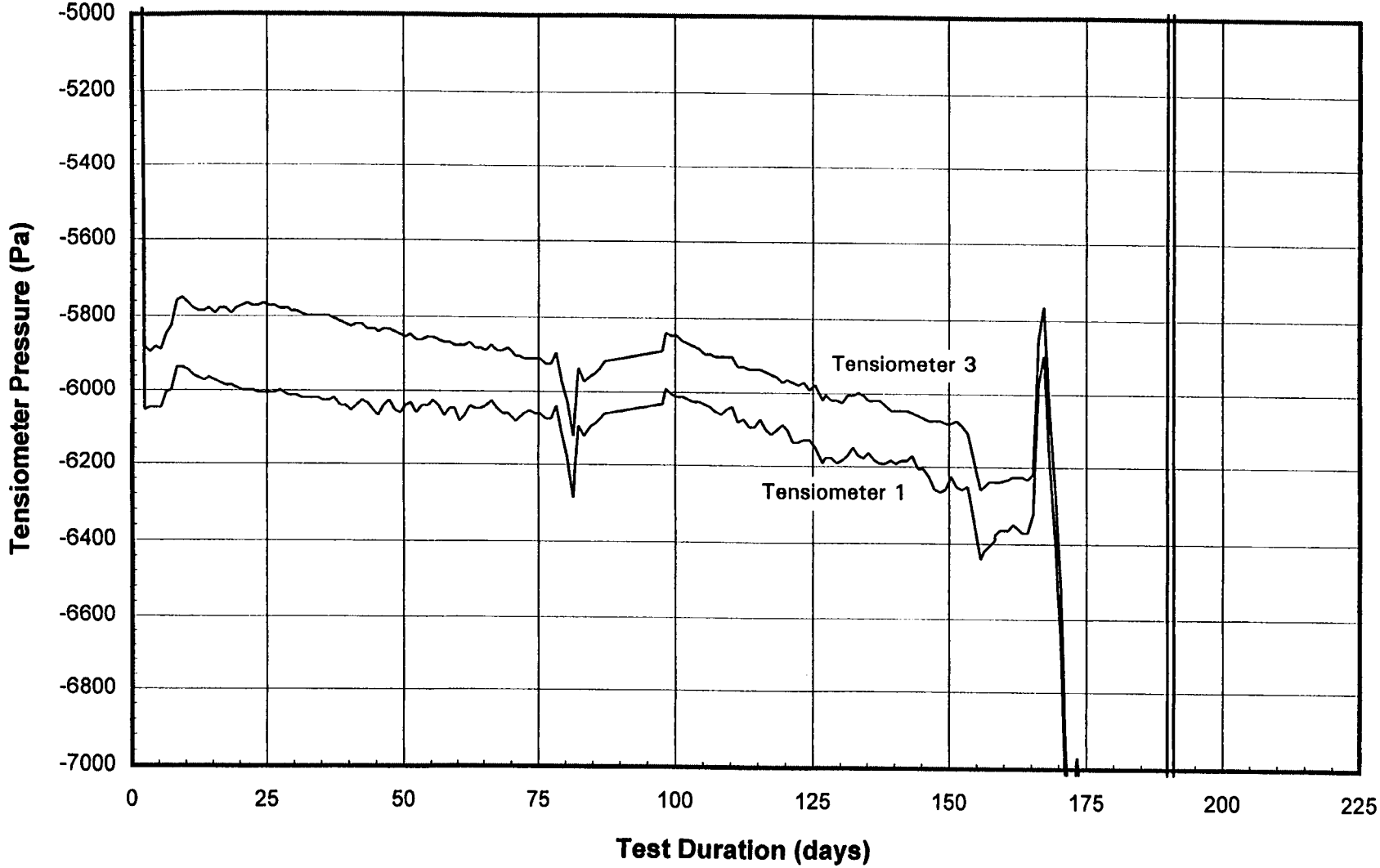

Figure 4-39. Test 3 tensiometer matric pressure measurements at locations 1 and 3. Temperature of Test 3 was 60 °C from days 8 to 97 and 90 °C from days 97 to 155 (see Figure 3-2 for tensiometer locations).

in the data. A marked increase in saturation below the heater horizon is noted in both the predicted and measured data, however, the predicted saturation increase above the heater was not observed in Test 3 data.

The vertical saturation gradient predicted in the numerical simulations of Test 3 (Figures 4-40 and 4-41) is not evident in the contour plots constructed from measured data of any of the four test cases (Figures 4-23, 4-26, 4-29, and 4-32). This is mostly due to the assumption of uniform saturation throughout the test medium that was made in the densitometer data reduction method. Any vertical saturation gradient present at the time the baseline densitometer measurements were made was eliminated from all remaining measurements. This data reduction technique might have removed vertical saturation gradients in tests with permeable media (i.e., tabular alumina and ceramic) because the rapid gravity-driven equilibration had probably occurred prior to densitometer measurements. Gravity-driven moisture redistribution in media with low permeability (i.e., cement slurry mixtures) required longer times, thus densitometer measurements prior to equilibrium would not have missed this vertical gradient. Nonetheless, a vertical saturation gradient cannot be discerned in the Test 7 profile (Figure 4-32).

An additional comparison of the flow regime observed in the experiments and the numerically predicted flow regime is effected by comparing the flow patterns of the injected dyes to streamlines predicted for steady-state liquid flow velocity. Instantaneous streamlines were introduced into liquid flow velocity plots at the approximate locations of the four dye injection ports located near the heater in Test 3. Instantaneous streamlines are injected into a flow field assumed to be steady as compared to standard streamlines, which are injected into flow fields as they evolve. Although the streamlines do not incorporate diffusion flow mechanisms, they do indicate the pathway of advection-driven liquid flow in the simulations. This comparison for Test 3 at 60 and 90 °C is illustrated in Figures 4-42 and 4-43.

The flow fields simulated with the instantaneous streamlines indicate two major features, the formation of a clockwise circulation cell located to the right of the heater and a counter-clockwise rotating circulation cell to the left of the heater, and several smaller features near the heater. Within each circulation cell is a well-defined zone of stagnation. Stagnation in these zones is indicated by the relatively short velocity vectors. These stagnation zones could be indicative of the formation of secondary circulation flows above the heat source, which could be caused by high temperature gradients. Instantaneous streamlines introduced into the simulated flow fields at the locations of the right and left dye injection ports are sufficiently within these cells that their trajectories remain, for the most part, within the cells and their respective stagnation zones (Figure 4-42).

Instantaneous streamlines were also introduced into the flow field at the dye injection points located above and below the heater. A streamline from the injection port below the heater moved directly upward in both the 60 and 90 °C simulations. This same upward flow feature was observed in the experiments using the injected dye (Figures 4-16, 4-17, and 4-18). The downward movement of dye in the region immediately above the heater was also captured by the streamlines in the numerical model only at 90 °C. Streamlines from above and below the heater are in the upward direction for the 60 °C simulation. A zone of downward movement above the heater in the 90 °C numerical simulation extended to a distance of 0.5 cm. This does not compare well with the observed results for Test 3 at both 60 and 90 °C that show this zone extending to as much as 1.5 to 2.0 cm above the heater.

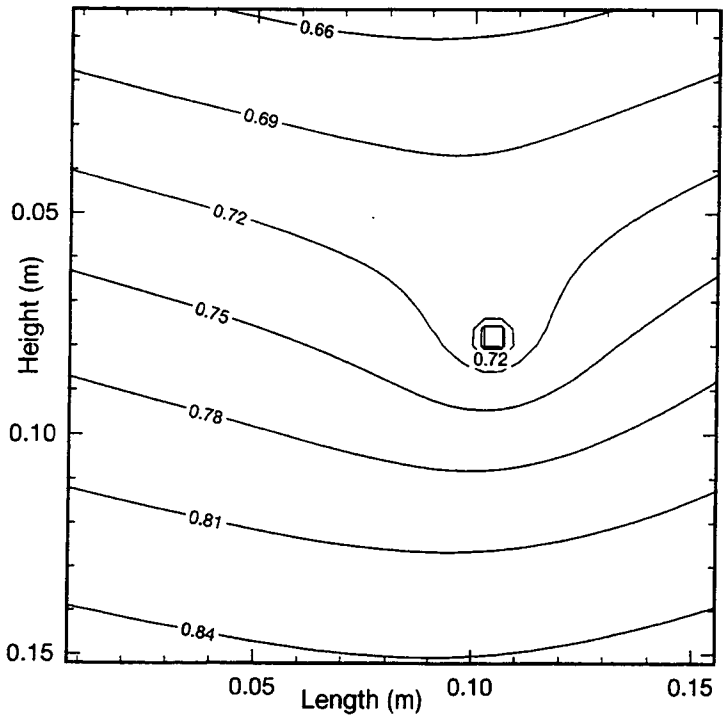

Figure 4-40. Predicted saturation contour plot for Test 3 at 60 °C

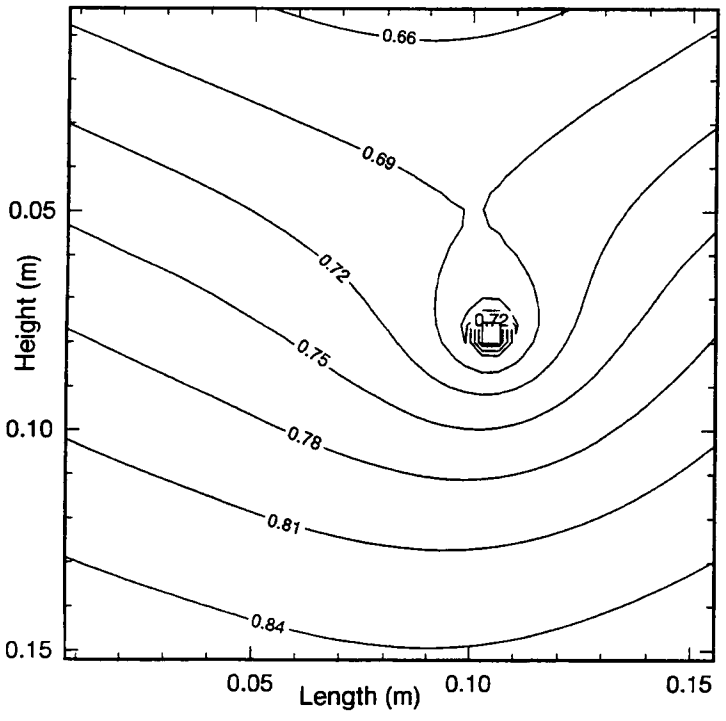

Figure 4-41. Predicted saturation contour plot for Test 3 at 90 °C

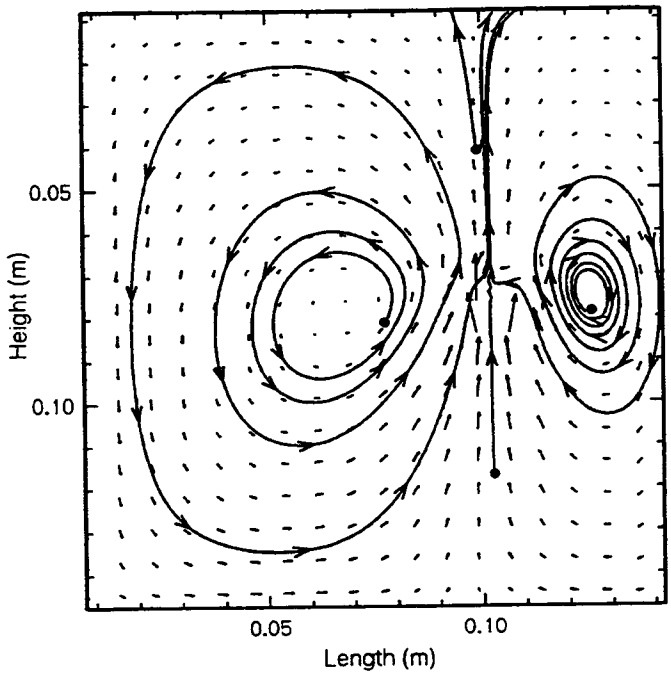

Figure 4-42. Instantaneous streamlines introduced into the simulated liquid flow velocity field at 60 °C at the dye injection ports located right, left, above, and below the heater

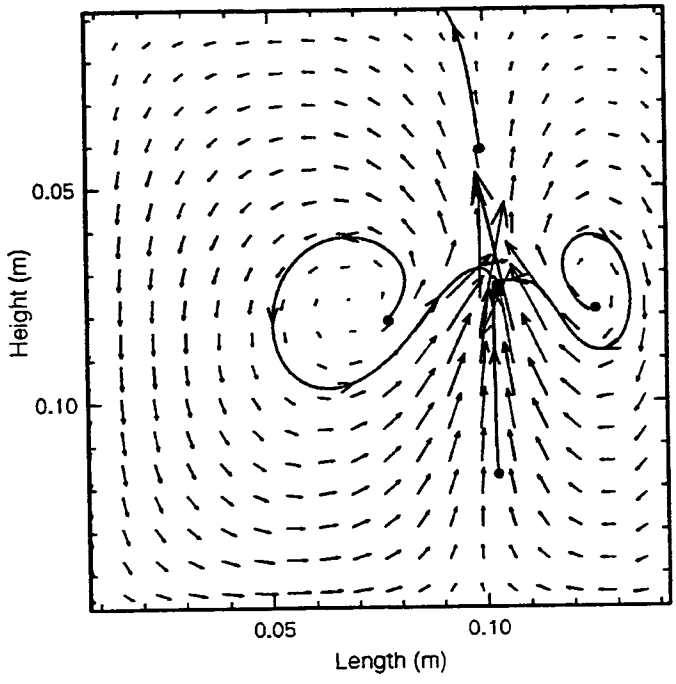

Figure 4-43. Instantaneous streamlines introduced into the simulated liquid flow velocity field at 90 °C at the dye injection ports located right, left, above, and below the heater

Conclusions of 2D Experimental Result and Analysis. Conclusions drawn from analyses of the 2D experiments can be summarized as follow:

- The conceptual and numerical models were successful in predicting the major flow features observed in the series of 2D experiments.

- Flow features near the heater in Test 3 were not predicted well by the numerical model. This may be attributed to an inadequate conceptual model of near-heater heat and mass transfer mechanisms since the precise nature of several flow features could not be determined.

- Formation of a dryout/moisture buildup zone was not observed in any of the 2D experiments. Thermally driven water vapor tended to condense uniformly throughout the test containers and not near the dryout zone. All test media had measured van Genuchten α parameters of less than 1.5×10^{-4} Pa^{-1}. Test 1, which exhibited a moisture buildup zone, had an adjusted van Genuchten value of 7×10^{-4} Pa^{-1}.

- Experimental evidence and numerical analyses were insufficient to resolve which two hypotheses describe fluid flow patterns near the heater.

- The permeability of the test media significantly influences the level of saturation near a heat source at temperatures exceeding boiling. Complete dryout was not detected in media with permeability greater than 1×10^{-13} m^2 even at temperatures in excess of 170 °C.

- Temperature-sensitive matric pressure/saturation relationships may affect local saturation which, in turn, influences fluid flow regimes.

- The cement in Test 7 had estimated resaturation times of 80 to 250 days and resaturation rates of 1×10^{-8} to 1×10^{-9} m/s. The resaturation rates during the cooling period were at least an order-of-magnitude slower than the advection flow rates (i.e., 1×10^{-7} m/s) measured during the heating period.

Results from the 2D group of experiments and analyses provided the following conclusions that contributed to resolving the fundamental basis of thermally driven moisture redistribution through partially saturated porous media.

- Temperatures as high as 170 °C were apparently not sufficient to completely dry out media with permeabilities greater than 1×10^{-13} m^2. This permeability value may be size dependant. A similar limitation may also be present at the canister scale, but with a different quantitative value.

- Fluid flow fields near a heat source may be more complex than indicated by numerical simulation. In particular, the physically observed downward movement of liquid from above the heat source was not well replicated in the numerical model. If present at the canister or repository scales, this downward flow of water could provide a source of water at the canister during the heating period of the repository. Coupling this matrix phenomenon with gravity-driven refluxing down fractures could lead to a potentially adverse scenario.

- Condensation buildup in a narrow zone near the heat source was not observed in media with a van Genuchten α parameter less than 1.5×10^{-4} Pa^{-1}.

- Resaturation rates measured during the cooling period were at least an order-of-magnitude slower than drying rates measured during the heating period for media tested.

4.1.2 Gas Pressure Buildup Experiment Results

A series of four related experiments (Tests 8 through 11) was designed and conducted to monitor the buildup of gas pressure and the redistribution of moisture in a porous medium in a controlled laboratory environment. This series of tests is referred to as the gas pressure buildup tests. One of the primary objectives of this research project was the formulation and investigation of scaling laws that would allow a complete examination of heat and mass transfer mechanisms operating at a variety of scales—from the laboratory (10^{-1} to 10^{0} m), to the field (10^{0} to 10^{1} m), to the repository (up to 10^{2} m). These experiments were designed and conducted to provide the requisite data for testing the proposed scaling laws. Results from these experiments are also useful in the investigation of those mechanisms that contribute to thermally driven moisture redistribution in partially saturated porous media and in this subsection the use of these results for this latter purpose is discussed.

The design of the experiments and instrumentation remained essentially constant during the conduct of this group of tests. Only the test medium was changed in order to evaluate different media in an attempt to select a test medium in which a gas pressure gradient could be created and that was suitable for meaningful measurement of the test variables. Tabular alumina was used as the test medium in the first experiment of this group, Test 8; however, the formation of a gas gradient was not attained due to the high permeability of this test medium. The next two experiments, Tests 9 and 10, were conducted using cement slurry mixtures as the test medium. A gas pressure gradient measurable within the confines of the test container was successfully attained in Test 9. Test 10 failed in this sense due to fracturing of the consolidated block within the first 20 min of heating the cylinder. Test 11 used tuff from the ALTS as the test medium; a gas pressure gradient was also successfully attained in this experiment. Because only Tests 9 and 11 successfully provided a medium with a measurable gas pressure gradient, only the results of these two experiments will be discussed here. Of these two experiments, results from Test 11 are discussed in greater detail because the test medium of this experiment was more relevant to the objectives of the investigation and because the experiment was the last and best controlled experiment of the series.

4.1.2.1 Experimental Results

The gas pressure buildup experiments were conducted in cylindrically shaped containers. Because of the cylindrical geometry of the test cell and the uniform boundary conditions at the cylinder wall, these experiments are considered to be essentially 1D in the radial dimension even though some 2D flow behavior was not avoidable. Descriptions of the experiments are included in Section 3.2, and a schematic of the test container is shown in Figure 3-3. Test variables measured in the gas pressure buildup experiments and used in the analyses included:

- Heater power recorded intermittently during the experiments

- Temperature measured at the heater and at the outer edge of the test medium

- Pressure measured at the heater using a pressure transducer and at the outer edge of the test medium using both a pressure transducer and a water manometer

- Saturation profile calculated from densitometer measurements in the radial direction from the center to the edge of the cylinder

The temporal evolution of heater power measured as input into the electrical cartridge heater, temperature at the heater, and the gas pressure difference between the pressure recorded at the heater and the gas pressure measured at the outside edge of the cylinder during Tests 9 and 11 are shown in Figures 4-44, 4-45, and 4-46, respectively. Although the experiment ran for longer periods (32 days in Test 9 and 76 days in Test 11), only measurements for days 10 to 21 for Test 9 and for days 4 to 12 for Test 11 are presented in these figures. After this juncture in the experiments, the heater power was turned off, and the temperature and pressure at the heater quickly (i.e., within several hours) returned to pretest ambient conditions.

As shown in Figure 4-43, the heater power was ramped up more gradually in Test 11 than in Test 9. This allowed easier characterization of the power input during analysis, particularly modeling. As expected, the heater temperature rise in Test 11 was not as abrupt as in Test 9.

Gas Pressure Observations. Gas pressure difference measured during Test 9 exhibited a monotonic rise to about 20 kPa over a 8.5 hr period, followed by a rapid decrease to about 5 kPa. Conceptually, the pressure decrease occurred when the gas pressure was sufficiently high to force an open pathway through previously saturated pores. After the pressure returned to ambient, only one other gas pressure increase was observed during Test 9. However, possible gas pressure increases may have been missed during an absence in continuous data recovery from days 12 to 18 in the test. It is believed that a gas pathway was open that allowed pressure flow from the heat source to the outer boundary for the last three days of the heating period of Test 9.

During Test 11, the gas pressure difference increased monotonically to about 17 kPa within a 4.5-hr period of time. Then there was rapid pressure decrease that reduced the pressure to about 5 kPa, after which the gas-pressure difference exhibited a series of increases and decreases until the heater was turned off after 7 days of heating. In this case, it seems that after gas pressure was initially decreased, the largest pores in the gas pathway refilled with water, thereby closing off that gas pathway. On two occasions the gas pressure rapidly decreased to approximately zero followed by fairly rapid increases to 5 kPa and 7 kPa. However, no discernable periodicity in the gas pressure buildup and decrease phenomenon was detected during the heating periods of Tests 9 and 11.

The level to which the buildup of thermally driven gas pressure can be expected is a function of the nature of the gas pathway. The mechanistic response of the gas pathway is believed to be a function of the pore structure and size, degree of saturation, and rate of heating. Stated simply, the rate of heating has to be sufficiently rapid and the gas pathways must be sufficiently restricted for gas pressure to build up. Additionally, the length of the gas pathway affects the time at which pressure builds up and decreases occur. For a small-scale system, such as the cylinder test, the size of the pores available for gas flow has greater significance than the relatively short length of the pathway on the determination of when gas discharge occurs. Gas pressure could conceivably increase until the air-entry pressure of the minimum equivalent pore diameter of the initial gas pathway is exceeded. The initial gas pathway is that pathway which has the largest minimum equivalent pore diameter. The initial gas pathway will be the first continuous gas pathway to connect the pressurized portion of the test medium with the constant pressure

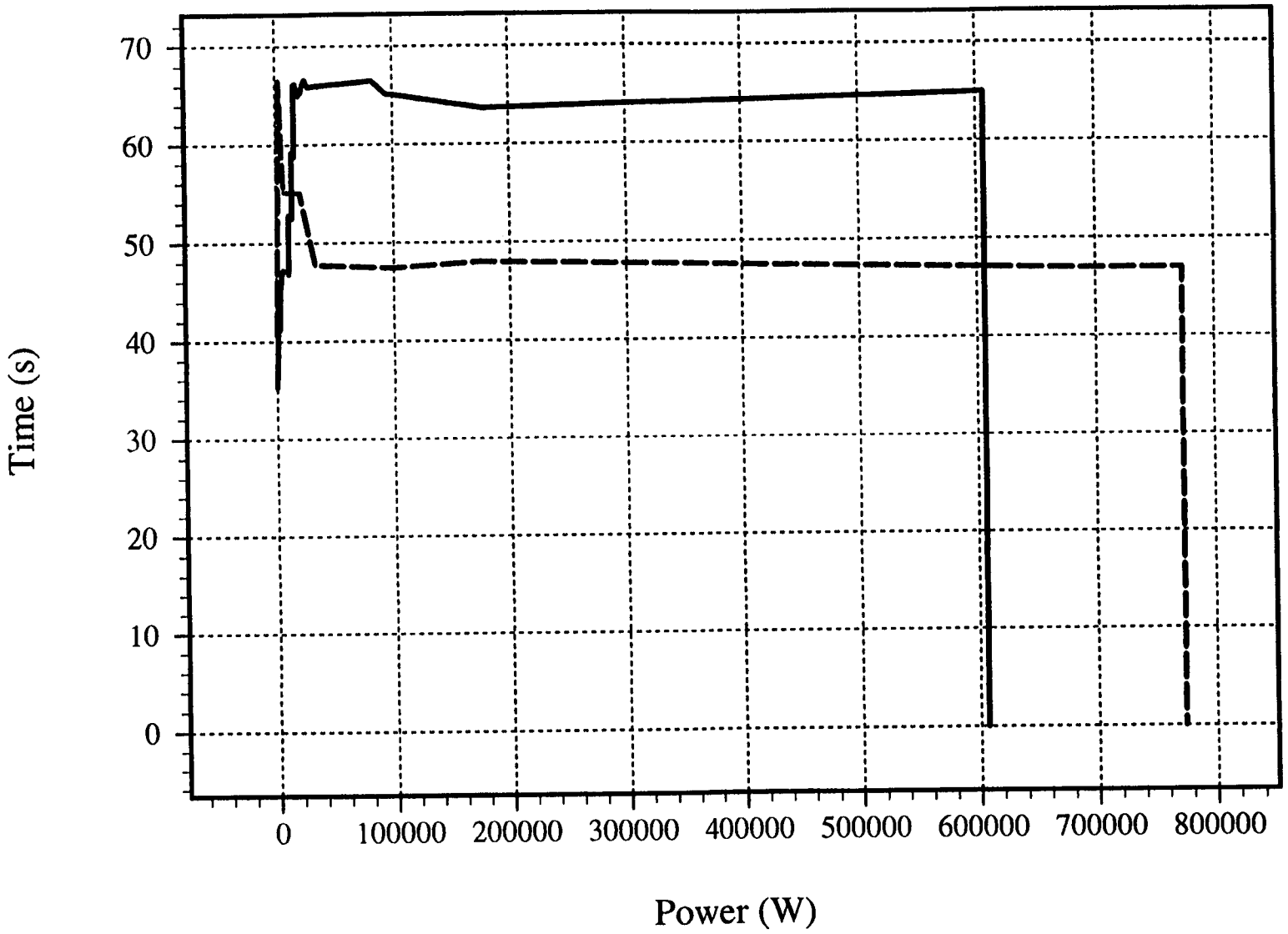

Figure 4-44. Heater power as input to the electric cartridge heaters of the cement slurry mixture cylinder in Test 9 (dotted line) and the Apache Leap Test Site tuff cylinder in Test 11 (solid line)

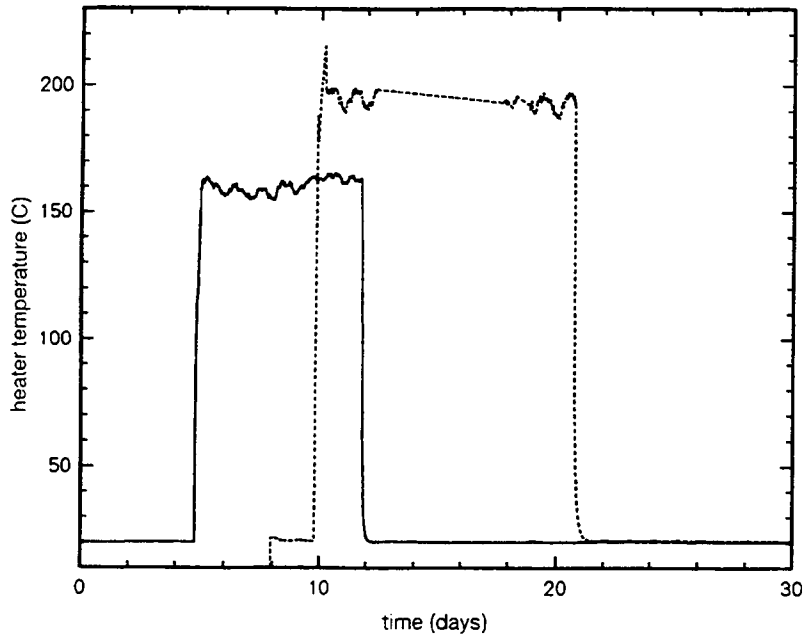

Figure 4-45. Temperature (°C) measured at the electric cartridge heaters in the cement slurry mixture cylinder in Test 9 (dotted line) and the Apache Leap Test Site tuff cylinder in Test 11 (solid line)

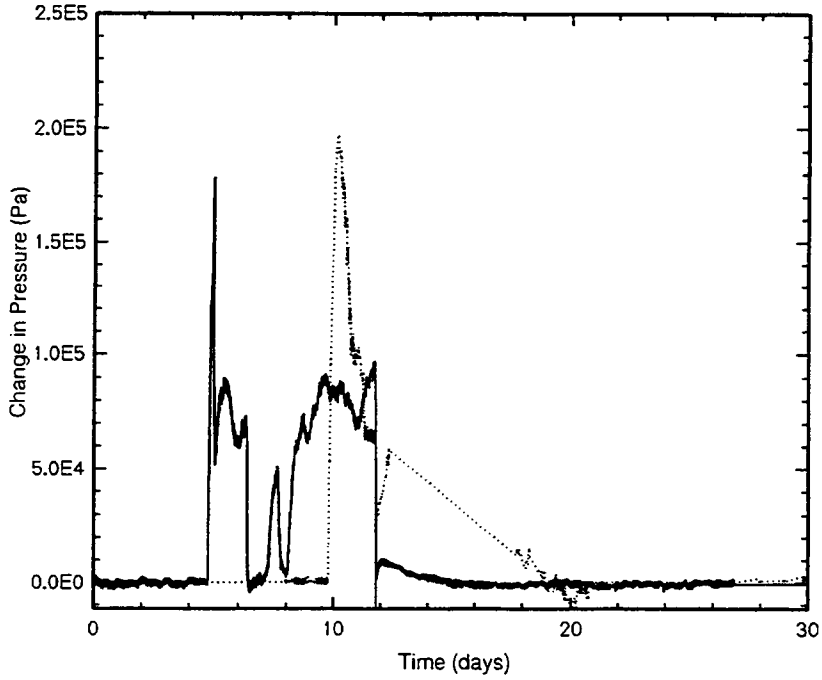

Figure 4-46. Gas pressure difference (Pa) measured between the electric cartridge heaters and the outside edge of the cement slurry mixture cylinder in Test 9 (dotted line) and the Apache Leap Test Site tuff cylinder in Test 11 (solid line)

boundary. The pathway forms when segmented or entrained air coalesces into a continuous pathway. The air-entry pressure, P_{cap}, is defined as

$$P_{cap} = \frac{2\gamma}{r}, \tag{4-1}$$

where γ is surface tension of the liquid and r is the radius of the pore. The gas pressure difference at the time of gas discharge was 20 kPa in the cement slurry mixture of Test 9 and 17 kPa in the ALTS tuff of Test 11. If these pressures are assumed to be the air-entry values of the media, than the corresponding equivalent pore radii were 7 and 8 μm, respectively. The pore-size distribution of the cement slurry mixture is not known but published values for the pore-size distribution (Rasmussen et al., 1990) indicate that the largest equivalent pore radii measured in tuff samples from ALTS are about 10–20 μm. The air-entry pressures for this range of equivalent pore radii are about 15 to 7 kPa. Therefore, the discharge pressure measured in Test 11 met or exceeded the air-entry pressure of the ALTS tuff. Additional gas pathways, perhaps longer and more tortuous but with larger minimum equivalent pore diameters, may have developed subsequent to the initial gas discharge. This would allow gas to discharge at lower gas pressure differences after the initial gas pathway was opened. The subsequent gas discharge events observed in Test 11 occurred at equivalent pore-size radii of 20 to 30 μm, somewhat larger than the minimum equivalent pore radius of the initial gas pathway.

The periodic gas discharge phenomenon observed in Tests 9 and 11 has also been observed at the field scale. A field-scale heater experiment conducted by Lawrence Livermore National Laboratory (LLNL) at the G-Tunnel facility monitored similar gas pressure buildup responses at all three locations at which gas pressure was monitored (Ramirez, 1991). The three gas measurement locations, identified as P1, P2, and P3, were located in fractured welded tuff at distances of 0.8, 2.0, and 1.0 m from the center of a 3,300 W heater. Gas pressures measured at the three measurement locations during the 9-month G-Tunnel experiment have been reproduced from Ramirez (1991) in Figure 4-47 for comparison with gas pressures measured during Tests 9 and 11. Although the pressure responses at each of the three locations exhibited distinctively different characteristics, features of gas pressure responses measured in the laboratory-scale experiments exhibited remarkable similarity to those observed in the field-scale experiment. In particular, a rapid increase in gas pressure was observed after the onset of heating at P1. The absence of the gas pressure spike at P2 and possibly P3 was attributed to mechanical failure in the instrumentation. Periodic discharge of pressure at P2 was observed for about 37 days into the test, after which the recorded pressure remained close to the pre-test ambient pressure of 11.7 psia (about 80 kPa). The return to ambient pressure after 37 days at P2 is also exhibited in pressure responses recorded during Tests 9 and 11. All three responses are indications that a gas pathway remained open allowing gas pressure to be discharged for the remainder of their respective tests. Behavior analogous to the long gradual gas pressure buildup past the duration of the heating period at P3 and subsequent to the initial pressure spike at P1 was not observed in the relatively short-term laboratory experiments.

Periodic discharge phenomena analogous to that observed in Test 11 were also reported by Persoff et al. (1992) and Ransohoff and Radke (1988). A significant difference among the case studies is that the discharge events observed in Test 11 occurred in porous media whereas in the previous studies the discharge phenomenon applied to fractures.

Saturation Observations. Radial profiles indicating saturation in Test 9 and relative change in saturation in Test 11 have been calculated from the densitometer measurements. Absolute saturation levels could not be calculated for the tuff used in Test 11 from densitometer measurements due to difficulties attributed

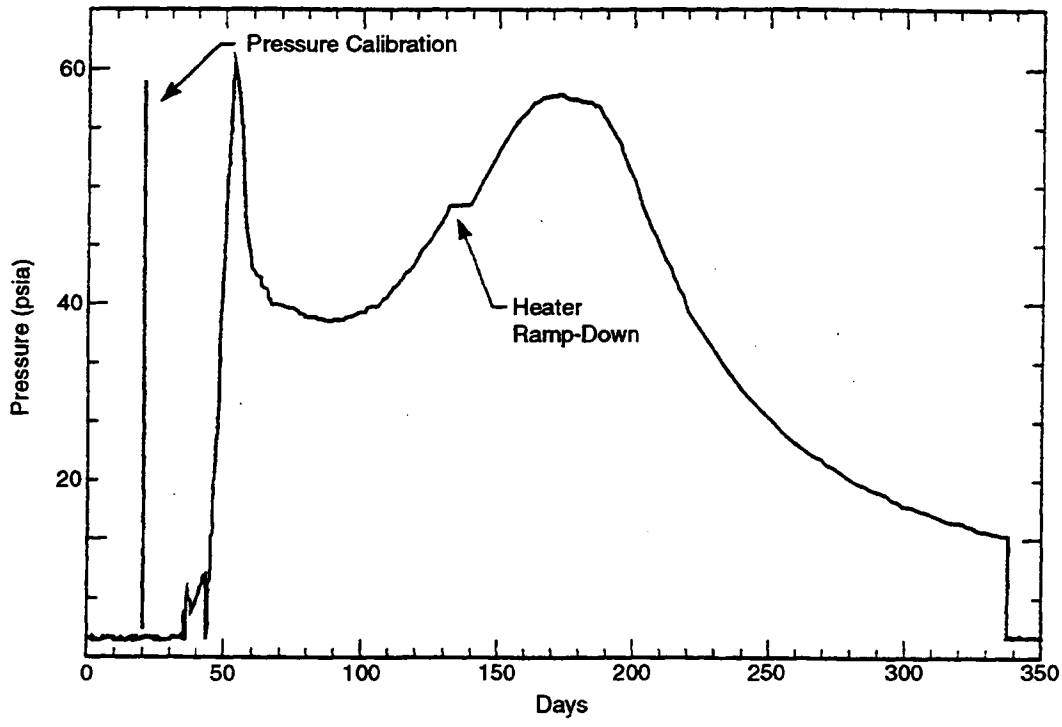

(a)

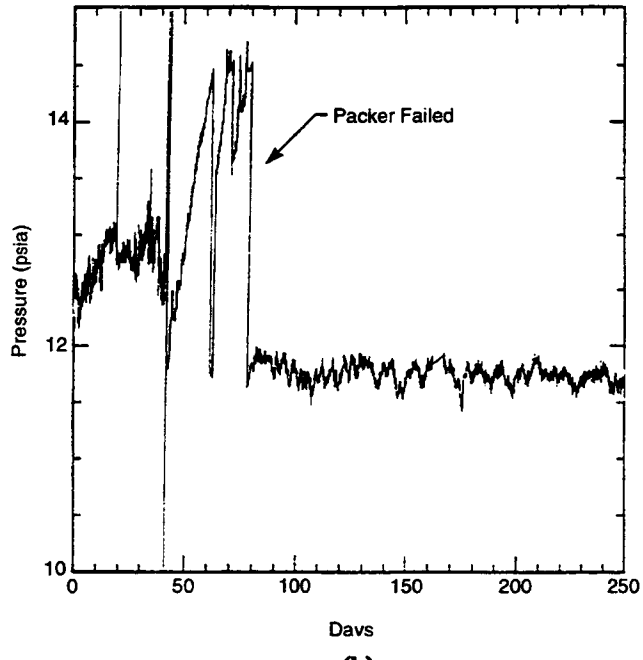

(b)

Figure 4-47. Gas pressure measurement from Lawrence Livermore National Laboratory for (a) P1, (b) P2 (after Ramirez, 1991)

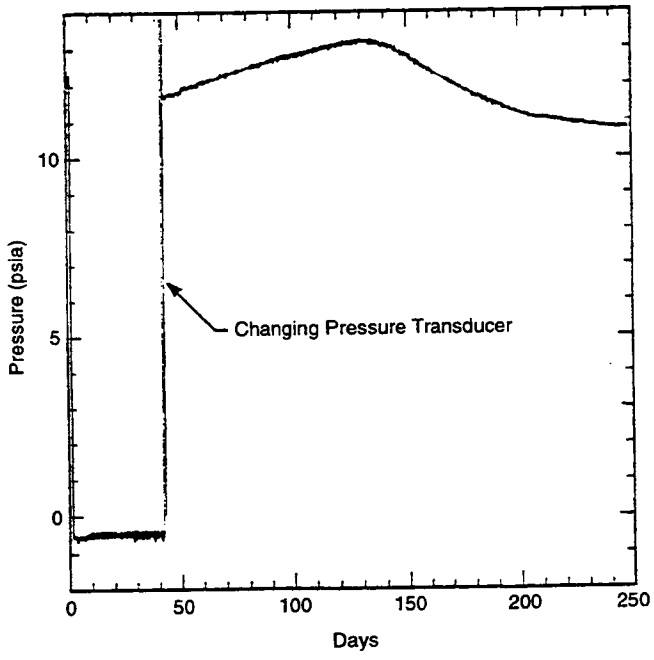

(c)

Figure 4-47 (Cont'd). Gas pressure measurement from Lawrence Livermore National Laboratory for (c) P3 (after Ramirez, 1991)

to heterogeneities, low porosity, and low permeability. The cement slurry mixture medium used in Test 9 provided a more uniform, less heterogeneous medium than the tuff in Test 11. Radial profiles of saturation for Test 9 were calculated using saturation values directly measured on media samples collected from the cylinder at the end of the test. The measured saturation values were 0.66 on a sample collected near the heater (i.e., within the near-heater zone visibly discolored by moisture movement), 0.89 to 0.92 at the radial mid-point, and 0.96 to 0.97 at the outer edge of the cylinder. The average pretest saturation (prior to the moisture redistribution effects from heating and discounting the possible effect of curing during the test) was back-estimated to be 0.90. Saturation was calculated from the densitometer measurements using this 0.90-estimate of saturation. This value is significantly greater than the 0.47 measurement made on a separate sample prepared from the same cement slurry mixture. The difference is attributed to two possible causes. The sample on which the original saturation measurement was made may have inadvertently lost moisture after preparation and prior to measurement. The second possible reason is the likely continuation of chemical alteration effects, such as curing, experienced by the cement slurry mixture but not by the sample tested for saturation.

The calculated saturation values along two radial profiles (one in the x-direction and one in the y-direction separated by 90°) at several times during Test 9 are presented in Figures 4-48 and 4-49. The heater was turned on at day 10 and off at day 21. Most notable is the uniformity in saturation values provided by the cement slurry mixture. The high level of heterogeneity observed in the unconsolidated media in the 1D and 2D experiments was successfully avoided through the use of a synthetic consolidated medium in Test 9. An inspection of the reduced data suggests that densitometer readings at the exact location of the heater and beyond the outside edge of the test medium exceeded the limit of possible

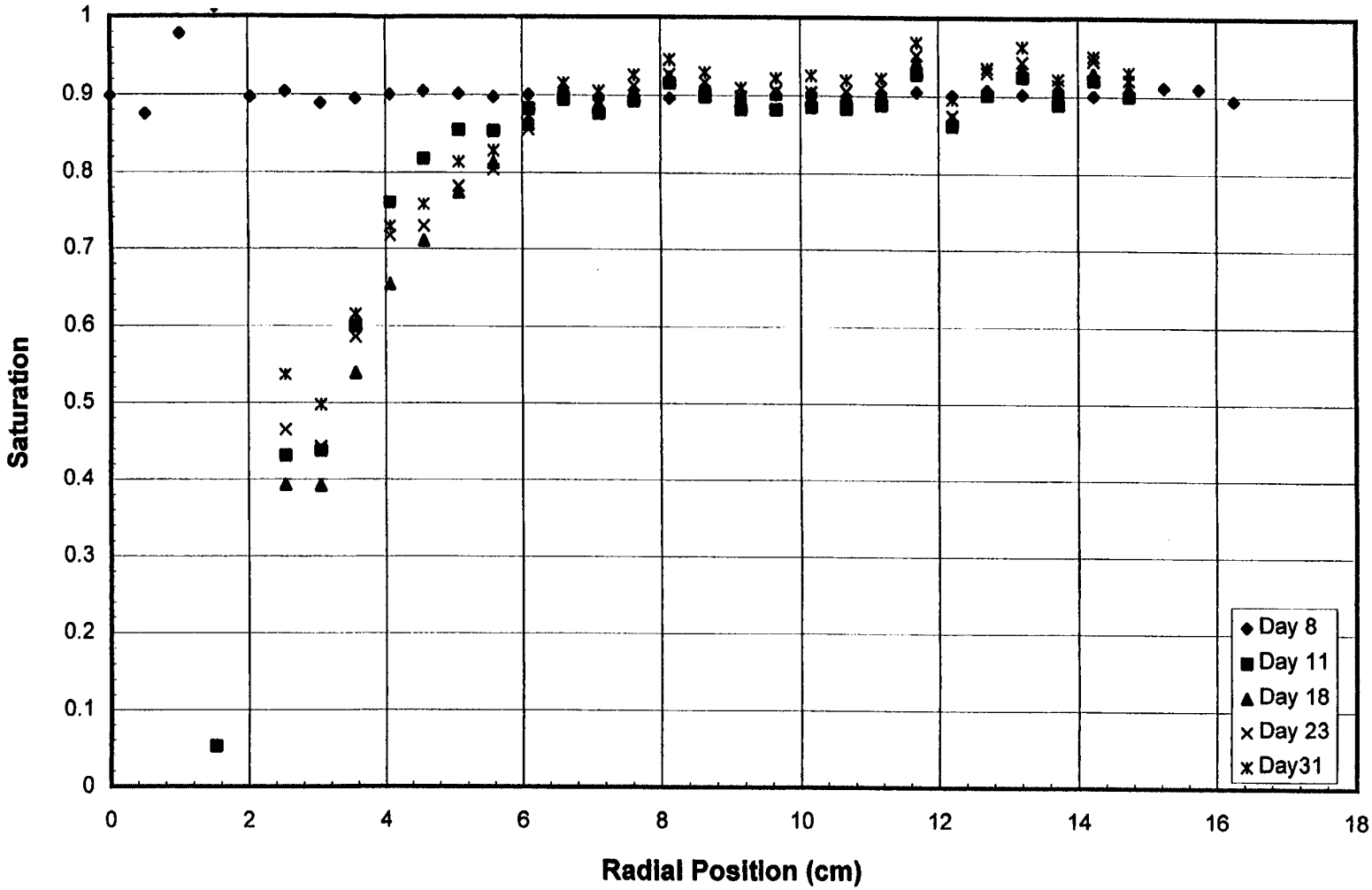

Figure 4-48. Radial saturation profile in the x-direction for the cement slurry mixture cylinder in Test 9 at days 8, 11, 18, 23, and 31

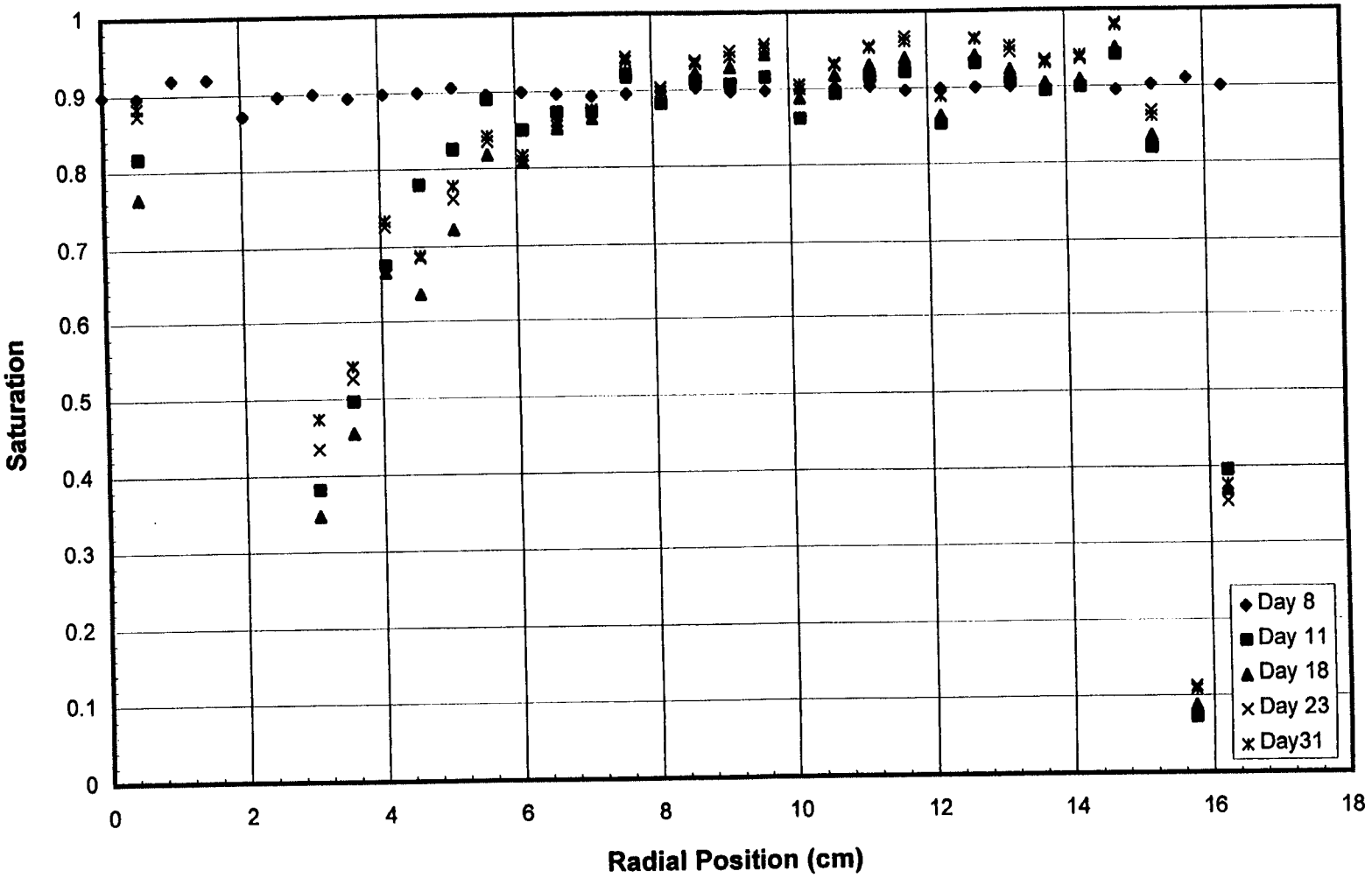

Figure 4-49. Radial saturation profile in the y-direction for the cement slurry mixture cylinder in Test 9 at days 8, 11, 18, 23, and 31

saturations (i.e., greater than 1.0 or less than 0.0). This suggested that the base saturation value of 0.90 may be in error; however, since these unrealistic values occur outside the regions of interest, they were dismissed and have not been included in these figures. Furthermore, the good agreement between the directly measured saturation values and the calculated ones for Test 9 indicate the baseline saturation estimate was reasonable.

Several features in the moisture redistribution of the Test 9 test cylinder are noticeable in the saturation plots shown in Figures 4-48 and 4-49. First, the effect of dryout extended to a maximum distance of about 5 cm beyond the edge of the heater. Although it is difficult to ascertain, it appears that the medium was completely desaturated next to the heater. Second, a relatively uniform increase in saturation was noticed from the edge of the dryout zone to the outer boundary of the test cell. This observation is in agreement with most of the 2D experimental results and analyses discussed in Subsection 4.1.1.2 that indicated condensation over a relatively wide area as opposed to in a narrow zone immediately on the cool side of the dryout zone observed in Test 1. The densitometer measurements were also in contrast with the appearance of a narrow zone of discoloration that was visibly observed when the cement cylinder was dismantled to obtain samples for saturation measurement. Third, resaturation at a distance of 3 cm from the heater was observed at the end of Test 9. The observed rate of resaturation in the x-direction profile exceeded that in the y-direction profile. Resaturation along the x-profile measured at about 0.01 per day in the region that had been totally desaturated during heating, and at about 0.005 per day in the region that had been desaturated to about 0.40 to 0.50. The rate of resaturation front was measured at 3×10^{-7} m/s. Therefore, if the rate of resaturation remained constant, complete resaturation would have been expected to occur in approximately 100 days. Resaturation in the y-direction profile was measured at 0.0025 per day in an area with 0.40 to 0.50 saturation. Full saturation would be attained in 200 days if resaturation continued at this same rate. The rate of saturation front along the y-direction profile varied from negligible to about 3×10^{-7} m/s.

Saturation could not be calculated from the Test 11 densitometer measurements due to difficulties created by heterogeneities, low permeability, and low porosity. Although considerable effort was made to insure the tuff cylinder was prepared uniformly (i.e., evenly cut with a ground surface), heterogeneities within the rock are readily apparent in variations of the total-count densitometer measurements. The low permeability of the tuff prohibited complete saturation and drying of the test medium to allow for baseline densitometer measurements. Questions regarding the initial saturation of the tuff cylinder did not allow calculation of saturation using densitometer measurements conducted at a known saturation. The effectiveness of the densitometer to detect density changes was further eroded by the low porosity of the tuff. Even large changes in a medium with such a small porosity result in relatively small changes in densitometer measurements. Total counts ranged from 61,000 near the center of the cylinder to over 64,000 at the outer edge and this does not provide sufficient resolution for estimating the saturation reliably. Taking the resolution in the measurements as the square root of the total counts indicates a cutoff of about 250 counts. Consequently, only relative qualitative changes in saturation could be inferred from the densitometer measurements. Total counts and change in counts (the difference in total counts since day 3) for the 30 measurements taken at an interval of 0.5 cm are presented for Test 11 in Figures 4-50 and 4-51. As illustrated in Figure 4-49, only densitometer measurement changes within 3 to 4 cm of the center of the cylinder are sufficiently above background noise to be considered significant.

Only one prominent feature was detected from the densitometer measurements for Test 11. A significant increase in counts was detected near the heater of the cylinder. The significance of this measurement cannot be completely ascertained because it was too close to the edge of the heater. An

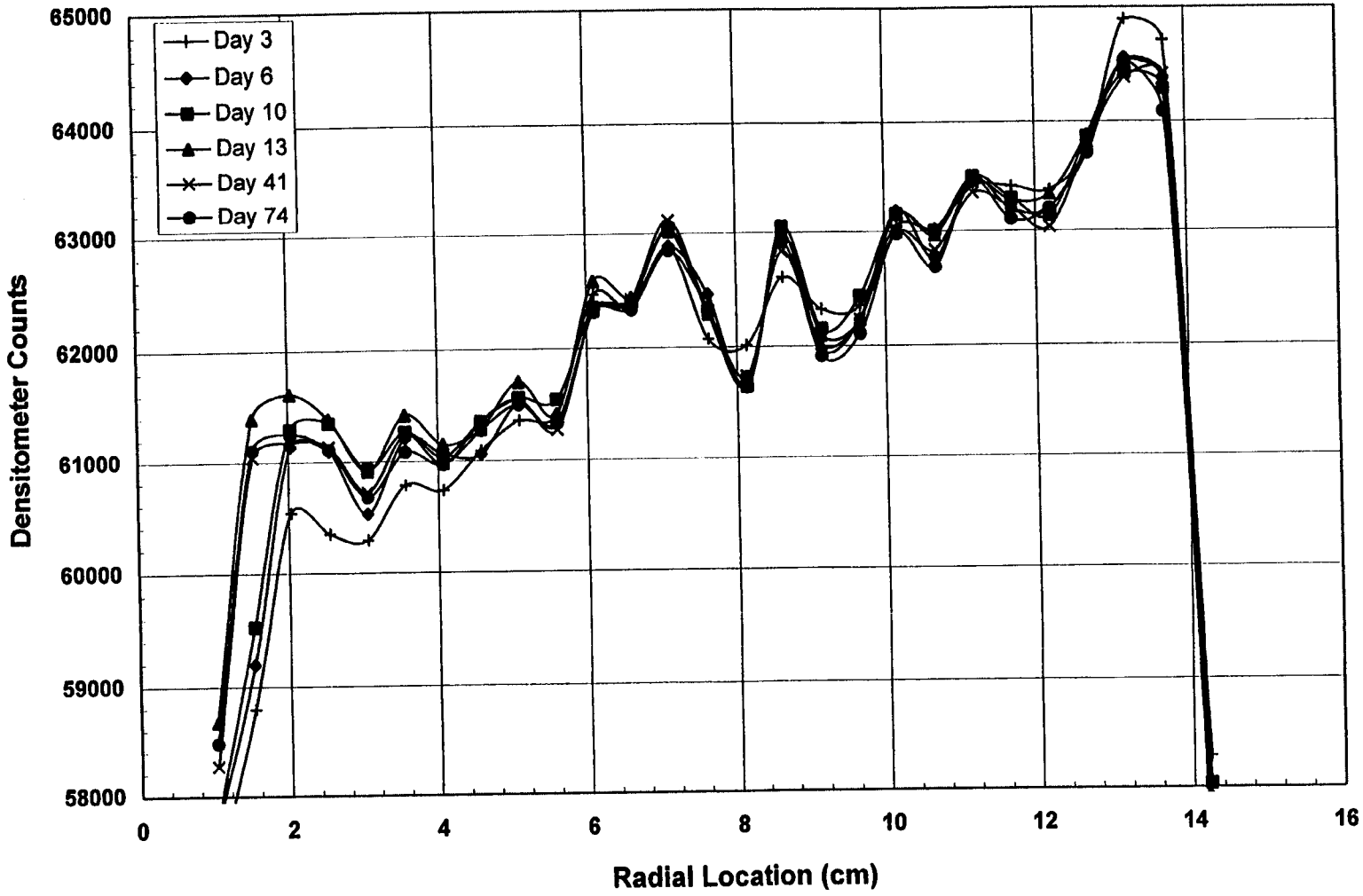

Figure 4-50. Radial profile of total densitometer counts for Apache Leap Test Site tuff cylinder in Test 11. Data presented are for days 6, 10, 13, 25, 41, and 74.

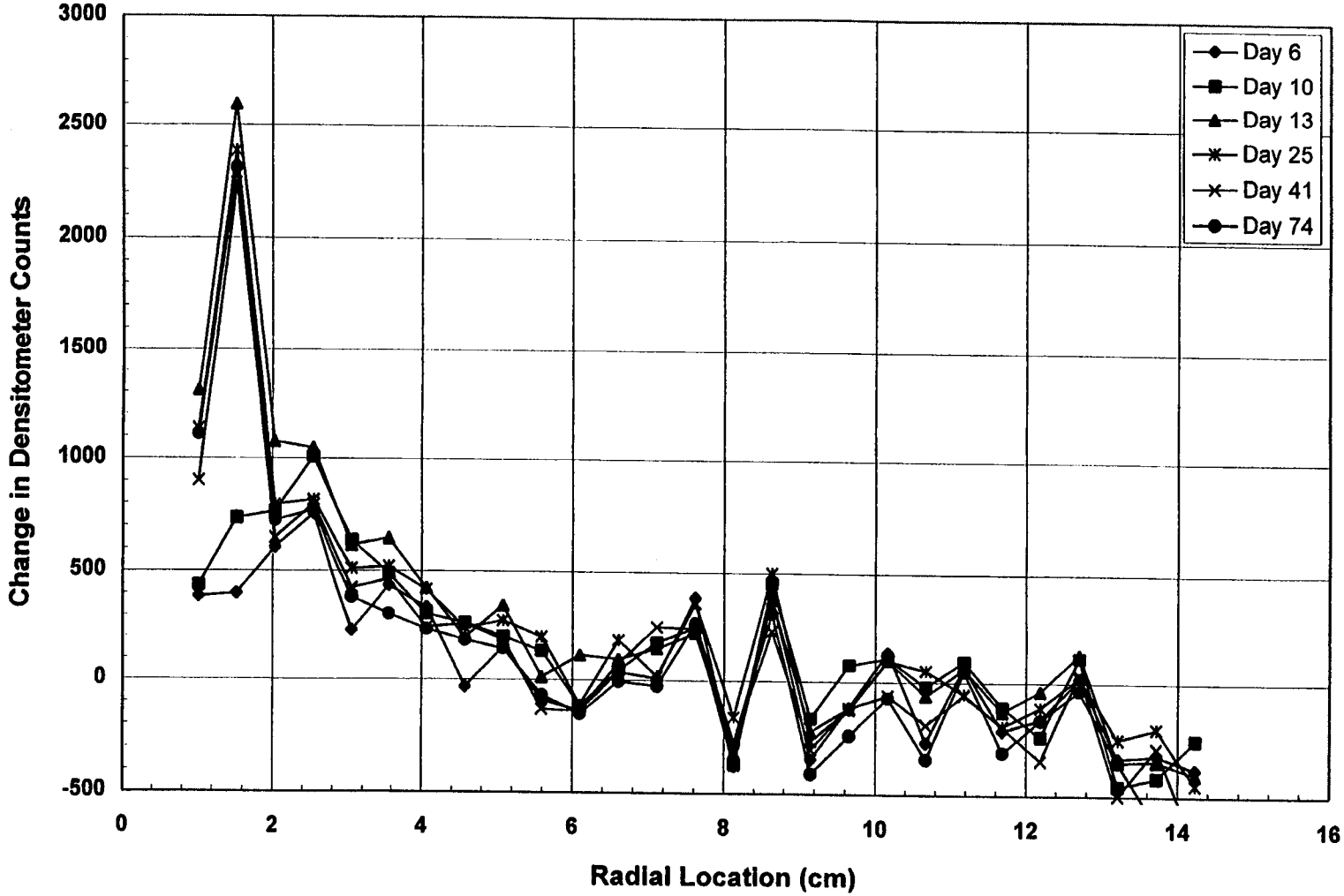

Figure 4-51. Radial profile of change in densitometer counts from initiation of experiment for Apache Leap Test Site tuff cylinder in Test 11. Data presented are for days 6, 10, 13, 25, 41, and 74.

approximation of resaturation was calculated using relative changes in densitometer counts measured at three times during the experiment: baseline counts prior to initiation of heating, at a time soon after heating was terminated (day 13), and at the end of the experiment (day 74). Resaturation rates were estimated at the four densitometer measurement points closest to the heater. Densitometer measurements at these four locations appeared to be above the calculated background noise level (i.e., 250 counts). During the 61 days following shutoff of the heater, the resaturation percentages of the near-heater or dryout zone were 13, 76, 87, and 59, calculated from the measurement locations closest to the heater to the farthest. This is equivalent to resaturation times of 470, 80, 70, and 103 days, which are in agreement with the results from Test 9.

4.1.2.2 Numerical Simulation

The thermally driven redistribution of moisture in Test 11 was simulated using the C-TOUGH code. The tuff cylinder was modeled in cylindrical coordinates with dimensions similar to those of the test cylinder. All boundaries in the model were specified as no fluid-flow boundaries. The heater was characterized as a 5-cm-long, 1-cm radius test cylinder set at a depth of 4 and 3 cm for the top and bottom of the cylinder, respectively (Figure 3-3). No rigorous assessment of grid size was conducted in the analysis. The outer cylinder boundary was maintained at 22 °C, and the upper and lower boundaries were assigned thermal conductivities of 0.4 W/m-K to allow for heat loss through the plexiglass base and top. The boundary layer thermal conductivities were adjusted to allow boundary temperatures to rise to about 40 to 50 °C, the same temperature as estimated for Test 11. As illustrated in Figure 4-43, the heater power was ramped up to about 64 W over a period of about 4.5 hr. Preliminary numerical simulations identified a discrepancy between the amount of power registering at the Variac and the temperatures experienced by the test medium. A significant amount of energy was apparently lost from the test cell because simulated temperatures exceeded 300 °C, much greater than the 165 °C measured during Test 11. Significant energy loss is attributed to the minor air gap between the cartridge heater and the borehole wall and heat conduction from the heater stem to the test container. Insertion of a heat conducting material (i.e., films, gels, etc.) in the borehole-heater air gap to prohibit energy losses was not possible because the gas pressure was measured in the air gap. The heater could not be emplaced within the test cell in Test 11, as in previous tests. For example, the cement slurry was poured around the heaters in Tests 9 and 10. Consequently, the heater stem extended along the entire length of the heater borehole in Test 11. The effective heater power input into the tuff was subsequently determined by adjusting the model heater power until the observed and predicted temperatures matched. The adjusted heater power was determined to be approximately 35 W. Back calculation of heater power was deemed appropriate because the dry and wet thermal conductivity values of the test medium were accurately measured.

Model values for porosity, permeability, saturation, and thermal conductivity were measured on samples taken from the same over-sized rock core as the Test 11 cylinder. These measured values were 0.07 for porosity, 5×10^{-17} m^2 for permeability, and 0.30 for saturation. Dry and wet thermal conductivity were measured as 1.74 and 1.90 W/m-K, respectively. The van Genuchten parameter values of 2.24×10^{-6} Pa^{-1} for α and 1.26 for n were selected from published measurements (Rasmussen et al., 1990) on an ALTS sample with porosity of 0.14. This sample had a measured permeability value of about 1×10^{-16} m^2. This published value for α may be excessively high for Test 11 in light of the higher permeability value associated with this ALTS sample than that measured for the cylinder. Wang (1992) derived a relationship between α and permeability for three different types of media, one of which was tuff from the ALTS. Wang estimated that a two order-of-magnitude change in permeability caused a one

order-of-magnitude change in α. Relying on the relationship presented by Wang (1992), it was decided that a measured permeability of 5×10^{-11} m^2 correlated to an α of 2.24×10^{-7} Pa^{-1}.

Initial numerical simulations estimated the saturation of the test medium to be greater than the 0.30 measured from the rock samples. Several factors may have influenced the saturation of the initial oversized core and the cylinder used in Test 11. The rock cylinder used in Test 11 was exposed to water for over 35 hr when being cut during sample preparation. It is assumed that this caused the saturation of the cylinder to be raised slightly from that of the oversized core from which the cylinder and the rock samples were taken. Additionally, the oversized core had been in storage in San Antonio, TX for about 4 yr at the time it was selected for use in this experiment. During this time, no precautions had been taken to maintain the rock core at its original saturation. It is conceivable that the outer portions of the core had become desaturated during the time of storage. This desaturation process could have given a misleading saturation value since the sample used for measurement of saturation was near the core surface and the cylinder was extracted from the core center. The value assigned to the saturation of the test medium in the numerical model was increased from 0.30 to 0.50 to accommodate for the apparent discrepancy. In summary, the numerical model configured for the basecase of Test 11 had well established values for permeability, porosity, and thermal conductivity. Values assigned to boundary thermal conductivity, heater power, the van Genuchten α, and saturation were less well known, but still had a reasonable sense of appropriateness.

Agreement between the predicted results from the numerical model and the experimental results was examined with respect to: (i) the time at which the gas pressure attained a maximum value, (ii) the maximum gas pressure attained, and (iii) the temperature recorded at the heater. Because the heater power was adjusted to ensure that the simulated heater temperature concurred with the measured heater temperature of 165 °C, the numerical model was judged based on the first two criteria—the time and amplitude of the gas pressure peak. The measured time and amplitude of the maximum gas pressure peak in Test 11 were 4.5 hr and 17 kPa, respectively. The resulting basecase numerical model for Test 11 predicted a maximum gas pressure of 57 kPa occurring at 5 hr (Figure 4-52).

The sensitivity of the numerical model to changes in several input parameters was evaluated by modifying the assigned values to one parameter while maintaining all other input parameters at their basecase values. Parameters modified in this exercise included heater power, permeability, porosity, saturation, thermal conductivity, and the van Genuchten α. Parameter values assigned to the Test 11 basecase used in the sensitivity analysis are listed in Table 4-3. The impact of changing the parameter values is evaluated relative to the maximum gas pressure of 17 kPa and the maximum temperature of 165 °C at 4.5 hr as measured in Test 11. The effect of modifying each of these values on the predicted time and amplitude of the maximum gas pressure is discussed in the following paragraphs.

The value of the van Genuchten parameter α was assumed to be 2.24×10^{-7} Pa^{-1} in the basecase simulation of Test 11. Increasing the value to 2.24×10^{-6} Pa^{-1} resulted in a predicted maximum gas pressure of 170 kPa at 1.0 hr after the initiation of the test. This predicted gas pressure was more than one order of magnitude higher than the measured value of 17 kPa. If the value of α was reduced to 2.24×10^{-8} Pa^{-1}, the corresponding predicted maximum gas pressure was 37 kPa. While this latter value is closer to the measured maximum gas pressure, reducing α an order of magnitude seemed excessive and difficult to justify. This decrease in maximum gas pressure in response to a decrease in α, the inverse of the air-entry value, is counter intuitive. It was assumed that a partially saturated medium exhibiting smaller equivalent pore sizes would tend to impede the movement of gas, thus resulting in

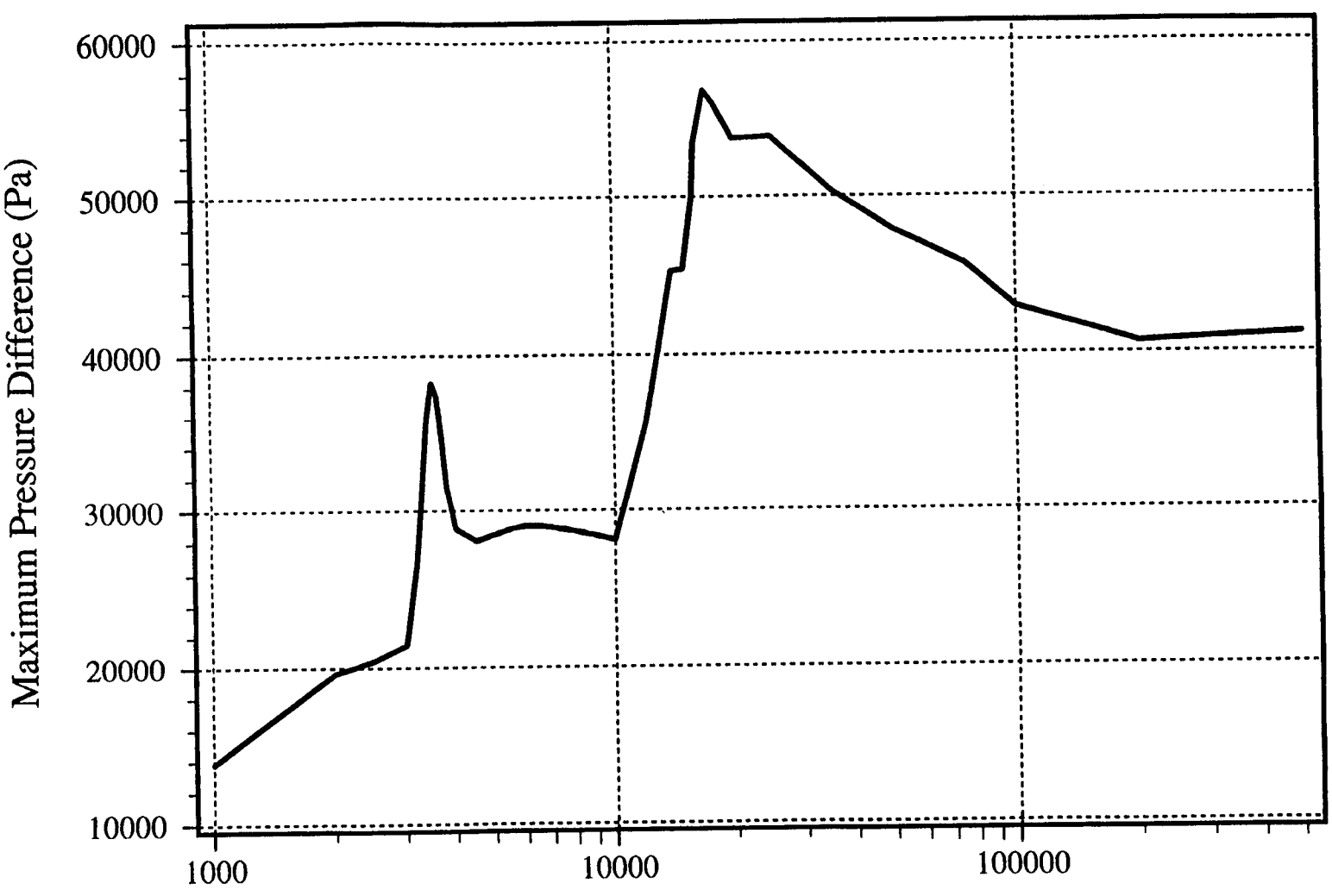

Figure 4-52. Numerically predicted gas pressure for Test 11 cylinder using basecase properties

Table 4-3. Summary of Test 11 basecase parameter values used in sensitivity analysis

Parameter	Value
Heater Power (W)	35.0
Permeability (m^2)	5.0×10^{-17}
Saturation	0.50
van Genuchten α (Pa^{-1})	2.24×10^{-7}
Tuff Thermal Conductivity-Dry (W/m-K)	1.74
Tuff Thermal Conductivity-Wet (W/m-K)	1.90
Boundary Thermal Conductivity-Dry (W/m-K)	0.4
Boundary Thermal Conductivity-Wet (W/m-K)	0.4

increased pressures. This reversal from the expected trend, however, was predicted by the numerical model.

Increasing the power to 38 W resulted in a maximum increase in gas pressure to 140 kPa and temperature to 182 °C. If heater power was increased to 64 W (i.e., no heat loss) the temperature increased to about 300 °C and pressure increased to 7000 kPa. The maximum gas pressure occurred sooner than the peak temperature, indicating that the modeled system was not dynamically similar to Test 11, in which case the maximum temperature and pressure occurred simultaneously. This calculation further supports the premise that there was an approximately 45 percent heat loss.

An increase in permeability by two orders of magnitude from 5.0×10^{-17} to 5.0×10^{-15} m^2 decreased the maximum pressure to 65 kPa and the temperature to 146 °C. The time at which these peaks occur was increased to 7.2 hr. An increase in porosity from 0.07 to 0.30 increased the peak pressure to 210 kPa. This change in porosity had no effect on temperature nor time to reach maximum pressure. The increase in saturation to 0.80 resulted in an increase in peak pressure to about 500 kPa, while the maximum temperature decreased to 162 °C. The time at which this occurred was increased to 22 hr.

Predicted maximum pressure values were sensitive to changes in the assigned value for the van Genuchten α parameter. An α value of 2.24×10^{-5} Pa^{-1} resulted in an increase in the peak gas pressure to 2900 kPa which occurred at 0.8 hr. An increase in α to 2.24×10^{-3} Pa^{-1} decreased pressure to 3700 kPa at 5 hr.

Numerical prediction of the maximum gas pressure observed in Test 11 has been evaluated by adjusting the model input parameters to include all feasible ranges of values. Prediction of a maximum pressure of 17 kPa at 4.5 hr was not accomplished. All reasonable model simulations predicted pressures in excess of that observed in Test 11. Sensitivity analysis identified the α parameter as the only input

parameter whose adjustment resulted in predicted maximum pressure values that approached the observed value. However, this meant reducing the value of α an order of magnitude. As was stated earlier, such a decrease in α may be excessive. Furthermore, a decrease in the value of α should have caused an increase, not a decrease, in the predicted maximum gas pressure. This rationale is based on the observation that an increase in the air-entry value (the inverse of α) should reduce the size of pores available for gas flow, thus resulting in greater pressure buildup.

An alternative source for the gas pressure inconsistency between predicted and observed gas pressures is the way gas permeability is calculated in the code used in these simulations. The relative permeabilities of gas and liquid are summed to 1.0 in the V-TOUGH (and C-TOUGH) codes. These values may not be appropriate for all media. Air and water permeability measurements on the ALTS tuff reported by Rasmussen et al. (1993) indicated that the measured relative permeabilities do not sum to a constant. Inappropriate characterization of gas flow permeabilities could have also been a source for the discrepancy between predicted and measured maximum gas pressures.

4.1.2.3 Conclusions

Conclusions from the gas pressure buildup experiment results are summarized as the following:

- Gas pressure buildup experiments were successfully conducted and monitored in two media types, a cement slurry mixture and a tuff sample from the ALTS. Gas pressure differences of 22 kPa and 17 kPa were measured.

- Low permeability rock was desaturated close to the heater during heating. The vapor condensed relatively uniformly in the rock matrix between the dryout zone and the outer boundary.

- After the initial gas pressure buildup was released, periodic gas pressure releases were observed.

- Times and rates of resaturation were measured in both cylinder experiments: Tests 9 and 11. Resaturation times of 100–200 days for the cement and 70–470 days for the tuff were measured. A resaturation rate of 3×10^{-7} m/s was measured for the cement. The resaturation rate could not be measured in the tuff.

- The maximum temperature and the time at which the maximum temperature and maximum pressure occurred were successfully predicted using C-TOUGH. The maximum pressure was reproduced within a factor of about three with the numerical models.

- Sensitivity analyses evaluated the effect of changes in model parameter values assigned to heater power, permeability, porosity, saturation, thermal conductivity and the van Genuchten α. Of these, model performance was determined to be most sensitive to the van Genuchten α parameter.

Results from the gas pressure buildup experiments provided the following conclusions that contribute to understanding the fundamental basis of thermally driven moisture redistribution through partially saturated porous media.

- Moisture vaporized at the heat source condensed relatively evenly through the tuff matrix between the dryout zone and the constant temperature outer boundary. The formation of a moisture buildup zone immediately past the dryout zone was not observed.

- The gas pressure buildup experiments support the conceptual model for thermally driven moisture redistribution through partially saturated porous media which states that water is transported primarily as vapor during the heating period and as liquid during the cooling period.

- Gas pressure buildup and release was observed at the heat source. This mechanism can potentially transport large amounts of liquid and vapor relatively long distances from the heat source.

4.2 ASSESSMENT OF SCALING LAWS

The scaling laws for the conceptual model developed in Section 2.2 to describe moisture transport in a locally heated, partially saturated porous medium were assessed by comparing predictions of time and pressure calculated with the scaling laws against: (i) experimental results at the laboratory scale; and (ii) numerical simulation predictions at the laboratory, field, and mountain scales. The assessments were used to establish the range of validity over which the conceptual model and scaling laws can be used to design field-scale experiments and to provide a method to interpret such experiments in terms of repository-scale analyses.

4.2.1 Thermal Evolution Model

As discussed in Chapter 2, the scaling laws are predicated on a thermal evolution model of the proposed geologic HLW repository that is characterized by three distinct periods: (i) an early heating period, (ii) an intermediate transitional period, and (iii) a late cooling period. One set of scaling laws was developed for the heating period and a separate set for the cooling period. The rate of temperature increase and decrease, the maximum temperature, the duration of the heating, and transitional and cooling periods depend on the specific thermal loading of the repository. This generalization of thermal periods and of the transport mechanisms during each period assumes that the strength of the repository heat source is sufficient to cause significant vaporization near the heat source; a smaller heat generation rate would not necessarily result in the formation of the three distinct thermal periods. The scaling laws, in fact, can be used to help determine whether the heating rate is sufficient to cause significant vaporization and a consequent large buildup of gas pressure. After a discussion of the database used in these evaluations, the heating and cooling periods scaling laws assessments are presented.

4.2.2 Laboratory Experiments and Numerical Simulations Used in the Scaling Law Assessments

4.2.2.1 Experiment Database

The primary experimental data available for assessing both sets of scaling laws were the results of the gas pressure buildup tests. The gas pressure buildup tests had a dual objective. The primary objective of these experiments was to provide the requisite data for testing the proposed scaling laws. The secondary objective was to use the results in the investigation of those mechanisms that contribute to

thermally driven moisture redistribution in partially saturated porous media. A description of the gas pressure buildup experiments is presented in Section 3.2. A discussion of the heat and mass transfer mechanisms evaluated using these tests can be found in Section 4.1.2.

Four experiments were conducted in this group of tests. Results of only two of these tests were suitable for analysis of the scaling laws, Tests 9 and 11. These tests were similar in geometry and heating, but a different medium was used for each; a cement slurry was used as the solid matrix for Test 9 while a sample of tuff from the ALTS was used for Test 11. The other cylinder tests also had the objective of investigating gas pressure buildup and moisture transport; however, media difficulties or failures were encountered during these tests. In one case, the permeability of the medium was too large to allow for a significant gas pressure buildup (Test 8); in the other, the integrity of the medium was compromised when the consolidated medium cracked (Test 10). Thus, data from these other tests did not qualify for use in assessing the scaling laws.

4.2.2.2 Numerical Simulations

Numerical simulations were conducted to evaluate the proposed conceptual model and the scaling laws over a wider range of parameters and geometric sizes than covered by the experimental results. Three general length scales were addressed in the evaluation: laboratory, field, and mountain. The approximate spatial dimensions of these three simulations are 0.1, 1, and 100 m; thus a spatial scale of three orders of magnitude was addressed. The test cases for each of the three scales were Test 11, the LBTs at Fran Ridge (Buscheck et al., 1994; Lin et al., 1994) near YM and the proposed HLW repository at YM, respectively. The test case for the laboratory scale, Test 11, was also simulated numerically to gain confidence that the heat and mass transfer mechanisms were appropriately represented in the numerical modeling approach. Five models representing the three spatial scales were simulated in this part of the analysis: the basecase for Test 11, the LBT at heat rates of 1,500 and 3,000 W and YM at heat loads of 57 and 114 kW/acre. All the numerical analyses used either V-TOUGH or C-TOUGH.

Laboratory Scale. The 1D radial gas pressure buildup experiments were characterized as a vertically oriented 2D system in cylindrical coordinates. These experiments were numerically simulated in 2D to accommodate heat lost through the top and bottom boundaries and other 2D features. This 2D representation does not preclude the fact that heat and mass transfer mechanisms in the cylinder experiments are essentially 1D in the radial direction. Only Test 11 was numerically simulated. Uncertainties regarding the assignment of representative property values to the cement medium used in Test 9 rendered accurate simulation of this experiment untenable. The numerical model for Test 11 used in the scaling laws analysis was the same as used for the investigation of heat and mass transfer mechanisms. The model and results from the analysis of the Test 11 model are discussed in Section 4.1.2.

Field Scale. The LBT at Fran Ridge was modeled as a vertically oriented 2D domain. Due to the symmetry of the system, only a vertical half phase was modeled. The actual block has cross-sectional dimensions of 3 m in both the x- and y-directions and a total height of 4.5 m above the excavated surface of the bedrock. The numerical model has a vertical dimension of 6 m (thus, extending an additional 1.5 m below ground surface in an attempt to diminish adverse boundary effects) and a horizontal dimension of 1.5 m, which takes advantage of the symmetry of the experiment. The vertical boundary above the ground surface was specified as no-fluid flow and adiabatic. This characterization was justified by the planned placement of an impervious layer and guard heaters on this surface. The top boundary, which is to remain open to the atmosphere, was assigned a high permeability (4.0×10^{-2} m^2), low thermal conductivity (0.2 W/m-K), and large elemental volumes to allow moisture movement and heat loss across

the top of the model. The bottom of the model and that part of the vertical boundary below the actual ground surface were assigned the same permeability as the block, low thermal conductivity (0.2 W/m-K), very low specific heat, and very large elemental volumes to allow for fluid flow and heat loss through the base of the model. The heat source was simulated as five horizontal cylinders (two and one-half in the half plane) perpendicular to the plane of the model. These heat sources were placed 1.5 m above the ground surface (3 m above the base of the model), similar to the design of the LBT. Each heater was capable of providing 300 W for a total heat rate of 1,500 W to the block. A second model of the LBT was simulated with the heat rate assigned to each of the five heaters doubled to 600 W, giving a total heat rate of 3,000 W. The second simulation was conducted to assess the effect of higher temperatures on fluid flow and gas pressure buildup. A schematic of the LBT model is presented in Figure 4-53.

The LBT medium was assumed to be a homogeneous composite block of fractures and rock matrix and was treated as an equivalent continuum (Wang and Narasimhan, 1986; Klavetter and Peters, 1986; Nitao, 1988). The relative permeability for the equivalent continuum is expressed as a volume average of the fracture and matrix relative permeabilities:

$$k_{rel,B} = \frac{\left[K_f\, k_{rel,f}\, \phi_f + K_m\, k_{rel,m}\, (1 - \phi_f)\right]}{K_B}\ , \qquad (4\text{-}2)$$

where the subscript B denotes bulk properties. The saturated bulk liquid hydraulic conductivity, K_B, is defined in this model by the relation:

$$K_B = K_f + K_m\, (1 - \phi_f)\ . \qquad (4\text{-}3)$$

According to this formulation, a medium with a matrix porosity of 0.10, fracture porosity of 0.00183, matrix permeability of 1.9×10^{-18} m^2, and fracture permeability of 1.0×10^{-11} m^2 has a composite permeability of 1.8×10^{-14} m^2. The property values for LBT were taken from Klavetter and Peters (1986).

Mountain Scale. A vertically oriented 1D numerical model was used to simulate mass and heat transfer in the YM repository-scale model. A 1D model was selected over a more representative geometric model to provide greater vertical resolution in the region closest to the heater horizon. The model extended from ground surface, which had an assigned saturation of 0.5 and temperature of 15 °C, to full saturation and a temperature of 30 °C at a depth of 600 m. The upper and lower boundaries were characterized as no-fluid flow and constant temperature boundaries. The model was assumed to be a uniform composite medium with the same properties as those assigned to the LBT model. Two cases representing different heat loads were simulated. In the first, a nominal heat load of 57 kW/acre was imposed at the repository horizon depth of 375 m. For the second case, the heat load was increased to 114 kW/acre to represent an extended dry repository scenario.

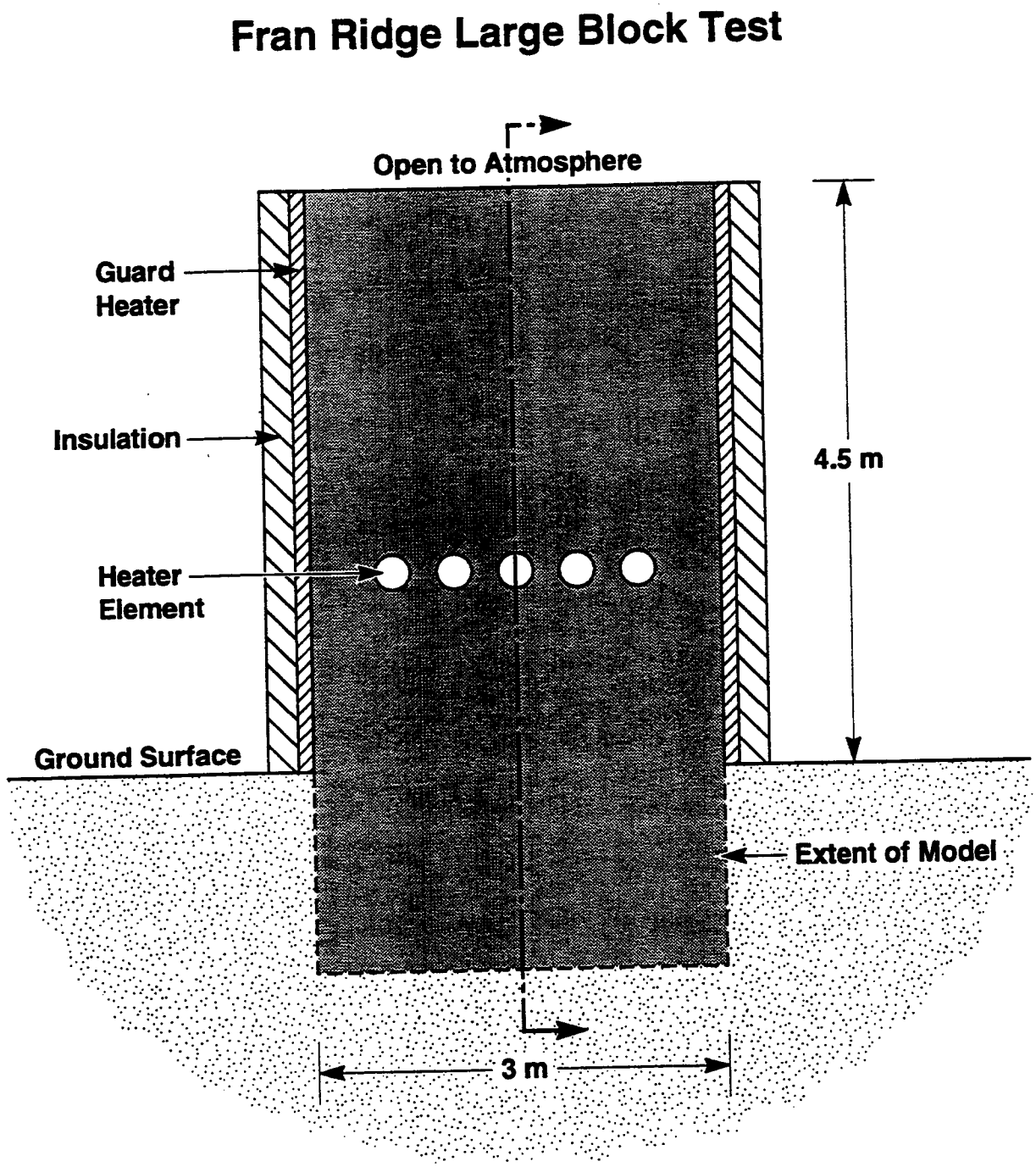

Figure 4-53. Schematic of the Lawrence Livermore National Laboratory large block test numerical model

Table 4-4. Summary of property values assigned to the laboratory-scale cylinder model, the field-scale large block test model, and the mountain-scale Yucca Mountain repository model

Parameter	Test 9 and Test 11 (Laboratory Scale)	Fran Ridge LBT (Field Scale)	YM Repository (Mountain Scale)
Liquid Saturation S_l	0.90 (Test 9) 0.50 (Test 11)	0.70	0.68
Matrix porosity ϕ	0.32 (Test 9) 0.07 (Test 11)	0.10	0.10
Matrix permeability k (m^2)	2.0×10^{-18} (Test 9) 5.0×10^{-17} (Test 11)	1.9×10^{-18}	1.9×10^{-18}
Matrix value of van Genuchten n	1.323 (Test 9) 1.26 (Test 11)	1.798	1.798
Matrix value of van Genuchten α (Pa^{-1})	6.36×10^{-7} (Test 9) 2.24×10^{-7} (Test 11)	5.8×10^{-7}	5.8×10^{-7}
Fracture Porosity ϕ	—	0.00183	0.00183
Fracture Permeability k (m^2)	—	1.0×10^{-11}	1.0×10^{-11}
Composite Permeability k (m^2)	—	1.8×10^{-14}	1.8×10^{-14}
Fracture value of van Genuchten n	—	4.23	4.23
Fracture value of van Genuchten α (Pa^{-1})	—	1.315×10^{-7}	1.315×10^{-4}

The intrinsic and hydraulic properties of the matrices in the simulations are summarized in Table 4-4. For Tests 9 and 11, many of these properties were measured directly (when such measurements were feasible). In the simulations, some of the properties were varied about the measured values to examine the sensitivity of the predictions to changes in the property values (Section 4.1.2). For Test 9, the properties changed with time during the test, so the values listed in the table are considered to be best estimates rather than exact measurements.

4.2.3 Assessment of the Conceptual Model Scaling Laws for the Heating Period

4.2.3.1 Criteria for Similarity During the Heating Period

To compare systems of different geometric scales requires that the systems are sufficiently similar. A quantifiable measure of similarity for the heating period has been identified. According to the similarity relations developed in Section 2.2, the magnitude and time duration of the gas pressure buildup and the advective and buoyancy-induced gas velocities will be the same at homologous locations and homologous elapsed time durations for porous media of different geometric sizes and hydrologic properties if the gas Advection Number has a similar magnitude. This gas Advection Number, as defined previously by Eq. (2.33), is:

$$Ad_g = \frac{\phi S_{vo} \alpha_s \mu_{go} Q}{k k_{rel,go} L \rho_{go} g \beta_{go} K_s T_{avg} \Delta T_o} \left(\frac{\rho_{vo}}{\rho_{go}}\right) \left(\frac{h_{fg,o}}{R_v T_{avg}}\right) \approx \frac{\phi S_{vo} \alpha_s \mu_{go}}{k k_{rel,go} L \rho_{go} g \beta_{go} K_s T_{avg}} \left(\frac{\rho_{vo}}{\rho_{go}}\right) \left(\frac{h_{fg,o}}{R_v T_{avg}}\right) . \quad (4\text{-}4)$$

Thus, systems at different scales are similar if their Ad_g numbers are similar.

The strength of the heat source, Q directly affects the magnitude of T_{avg} and ΔT_o in Eq. (4-4). There is considerable interest in designating the best value of Q for the repository and to understanding the impact of the choice on the response of the repository. Selection of waste package design and repository design will determine if the repository follows the Site Characterization Plan (SCP) design with relatively low areal thermal loading (and consequently, relatively low temperatures) or if an extended-dry repository design concept (with relatively high temperatures) is selected (Buscheck and Nitao, 1992, 1993, 1994). As will be demonstrated, differences in the thermal loading can affect the nature of the fluid flow regimes to be expected at both the LBT and the proposed YM repository. An indication of which flow regimes are to be expected is indicated by the magnitude of Ad_g, as discussed in Section 2.2. When $Ad_g >> 1$, large pressure gradients and advective gas flows will be created, and the heated region will tend to be of the extended-dry type.

To evaluate Ad_g for the various systems, representative values must be chosen for all the parameters, including those such as vapor density which may vary with time and location in the system. As an example of this selection, the range of vapor saturation S_{vo} can vary from approximately zero near the heat source to approximately full saturation in zones of condensation; hence, a representative average value for S_{vo} is 0.5, and this value is used in Eq. (4-4) in all the computations to assess the validity of the scaling laws. It was also necessary to have estimates of ΔT_o and ΔT_{avg} and of the characteristic length, L, for each system. The temperatures ΔT_o and T_{avg} for a given heating rate can be obtained by combining Eqs. (2-28) and (2-29) or from a separate heat conduction analysis. But here, for simplicity,

results of the numerical simulations were used to calculate these temperatures. Numerically predicted values for ΔT_0 for the five test cases are contained in Table 4-5.

The L values of the laboratory and LBT experiments were reasonably assumed to be the physical size of the respective experiments. The L value of the repository was not so evident. A heat conduction analysis could be used to estimate the size of the repository's affected volume, however, the numerical simulation results were again used for simplicity. In addition, the heating rate for the YM repository model was specified in terms of power released per unit area, rather than in terms of per unit heater length, which is the form assumed in the definition of Ad_g. A characteristic area of $L \times 1$ m^2 was assumed to use this areal specification of Q in Ad_g. The results of the Ad_g calculations are summarized as follows.

Laboratory Scale. The L value for the laboratory experiments is 0.145 m. The maximum ΔT_0 was 170 °C in Test 9 and 145 °C in Test 11. The computed value of Ad_g was about 170,000 for Test 9 and about 10,000 for Test 11, both at a heating rate of 35 W. Consequently, both of these tests were conducted for conditions that represent strongly pressure-driven advective gas flow. Incidentally, if the heating rate is increased, the value of Ad_g for these tests decreases slightly because of the change in the representative thermodynamic properties with temperature.

Field Scale. The L value for the LBT is 1.6 m. For a heat release rate of 1,500 W, the ΔT_0 is 134 °C. If the permeability of the block is characterized as a composite medium with a permeability of 1.8×10^{-14} m^2, the computed value of Ad_g is about 20. For a heat release rate of 3,000 W, the value of Ad_g is about 18. The gas flow regime for this characterization is predicted by the conceptual model to be pressure-driven, but not strongly so.

In the actual LBT, however, it is anticipated that significant gas pressures will build up. There is compelling evidence in the results from a field test conducted at G-Tunnel that gas pressure buildup will result from heat sources located in partially saturated fractured rock. This evidence is from the previous study by LLNL at a G-Tunnel heater test which measured gas pressure buildups as great as 33, 20, and 11 kPa at distances of 0.8, 2.0, and 1.0 m, respectively, from the middle of the heater (Ramirez et al., 1991). In fact, gas pressure buildup was observed at all three locations in which gas pressure was recorded during this test. The G-Tunnel heater experiment was conducted in the Grouse Canyon tuff, a fractured, welded tuff with properties believed to be similar to YM (Zimmerman and Finley, 1986) and Fran Ridge, the site of the LBT. Although the medium at the site of the G-Tunnel field test is fractured, pressures were obviously measured at locations not directly connected by an open gas pathway to the heat source. Apparently, the fracture component to the medium did not actively participate in the dissipation of gas pressure from the heater to the points of gas pressure measurement. Consequently, a more relevant value of Ad_g for the rock medium at the LBT is one based on the matrix permeability rather than composite block permeability. For this permeability, the computed Ad_g was about 200,000 for a heat rate of 1,500 W. Similarly, an Ad_g of 180,000 was computed for a heat rate of 3,000 W and the gas flow was predicted to be strongly pressure-driven.

Mountain Scale. The L value for YM at a 57 kW/acre heating load was inferred from the extent of significant thermal impact predicted in the numerical simulation to be about 100 m. The maximum

temperature difference was 80 °C. The value of Ad_g was computed to be about 0.4 based upon a composite permeability model. This low value indicated that gas flow would be dominated by buoyancy or diffusion effects rather than by pressure gradients. However, if the connectivity of fractures is not sufficient to dissipate gas pressures as demonstrated at the field scale in the G-Tunnel heater experiment, the composite permeability model may be inappropriate. This observation raises an important question of the representative elemental volume (REV) relevant to this scaling exercise (Bear, 1979), namely, will fractures contribute to gas flow at the repository or mountain scale even though fractures did not contribute to gas flow at the field scale? Additional site characterization may be required to address this question. Similar to the LBT analysis, characterizing gas flow through the mountain using a matrix permeability of 1.9×10^{-18} m^2 gave the Ad_g a value of 4,000, suggesting pressure-driven flow.

For the YM repository at a heat load of 114 kW/acre, an L value of 200 m was determined using the numerical simulation and the maximum ΔT_0 was 157 °C. For a model based on a composite permeability, the computed value of Ad_g was about 0.25. Again, the response of the repository was predicted to be controlled by buoyancy and vapor diffusion when the composite permeability model was assumed. But, if matrix permeability is used in the definition of Ad_g, the computed value is about 2,500. The characteristic values for these different representations at the three scales are summarized in Table 4-5. These calculations of Ad_g indicate that, if the medium is assigned the permeability of the matrix and not a composite matrix/fracture medium to estimate gas pressure buildup, the laboratory-, field-, and mountain-scale systems are all similar (i.e., $Ad_g >> 1$) with respect to heating period responses.

4.2.3.2 Similarity Criteria Values for Different Scale Experiments

The validity of the proposed heating period scaling laws to correlate the thermal responses of the various systems was first assessed by comparing the conceptual model to the experimental results for Tests 9 and 11 and the numerical predictions for Test 11. After assessing the validity of the heating period scaling laws using comparisons at the laboratory scale, numerical simulations of heat and mass transfer for the LBT and the YM repository were compared to the heating period scaling law predictions. The key indicator parameters for the heating period assessment were the magnitude of the gas pressure increase, Δp_g, and the time at which the maximum gas pressure occurs.

Laboratory Scale. The experimental results from Tests 9 and 11 are summarized as follows: Test 9—Δp_g of 20 kPa was measured at 8.5 hr after the start of heating and Test 11 a maximum Δp_g of 17 kPa was observed 4.5 hr after the onset of heating.

The maximum of Δp_g and time of the peak Δp_g were also numerically simulated for Test 11. For Test 11, the numerical simulation predicted a Δp_g of 57 kPa and time of 4.5 hr required to obtain the peak Δp_g (Figure 4-52), compared to the observed values in the experiment of 17 kPa, and a time of 4.5 hr to obtain the peak Δp_g. The simulated Δp_g response of Test 11 exhibited a feature not observed during the conduct of the experiment. This feature was the early spike in Δp_g predicted after about 5 min of heating. Because the predicted early spike occurred at 5 min into the simulation, it is not considered to be analogous to the periodic discharge of gas pressure that was observed at both the G-Tunnel and cylinder experiments. The early spike could be an artifact of the rapid increase in Q

Table 4-5. Summary of characteristic parameters assigned to scaling law model for test cases assessed

Experiment	L (m)	Q (W)	ΔT_0 (°C)	k (m^2)	Ad_g
Test 9	0.145	35	170	2.0×10^{-18}	170,000
Test 11	0.145	35	145	5.0×10^{-17}	10,000
LBT	1.6	1,500	134	1.8×10^{-14}	20
LBT	1.6	1,500	134	1.9×10^{-18}	200,000
LBT	1.6	3,000	180	1.8×10^{-14}	18
LBT	1.6	3,000	180	1.9×10^{-18}	180,000
YM	200	57*	80	1.8×10^{-14}	0.4
YM	200	57*	80	1.9×10^{-18}	4,000
YM	200	114*	157	1.8×10^{-14}	0.25
YM	200	114*	157	1.9×10^{-18}	2,500

*** denotes kW/acre**

coupled with a coarse numerical grid proximal to the heater elements used in the model. Sensitivity analysis indicated that the large predicted Δp_g values were mostly dependent on permeability and the van Genuchten α parameter. However, as discussed in Section 4.1.2, the values assigned to permeability and the van Genuchten α parameter for Test 11 are considered representative of the tuff sample. Differences between the predicted and observed responses for Test 11 may be attributable to the manner in which the relative gas permeability is determined in C-TOUGH. Because higher values for Δp_g are predicted than observed, the relative gas permeability of the Test 11 experiment appears to be greater than that predicted in the model. This observation suggests that calculation of Δp_g in the Test 11 model could be improved by incorporating a rock-specific gas/liquid relative permeability relationship into the numerical model.

This difference notwithstanding, the close agreement between predicted and observed time of peak Δp_g and agreement in Δp_g within a factor of about three indicated the numerical model adequately replicated heat and mass transfer in Test 11. Use of the numerical model to predict Δp_g and time to peak Δp_g in similar systems with different spatial scales is justified.

Scaling law values for the Δp_g buildup and the time duration over which high Δp_g persists as predicted by the conceptual model are given by Eqs. (2-29) and (2-30). Representative gas and vapor properties appropriate for the average ΔT_0 measured in the tests are used in these calculations. The characteristic values assigned to the laboratory scaling model are summarized in Table 4-5. The scaling law predictions of the Δp_g buildup experiment are as follows: Test 9—Δp_g was 90,000 Pa; and time required to obtain the Δp_g peak was 11.7 hr; Test 11—Δp_g was 12,000 Pa, and time required to obtain the Δp_g peak was 11.7 hr. The scaling law prediction for time to Δp_g peak was within a factor of about two for both tests. The results of the scaling law prediction for Δp_g and time to the Δp_g peak are summarized with the observed values and numerically simulated predictions for the laboratory-scale experiments in Table 4-6.

Field Scale. The numerical simulation for the LBT at a heating rate of 1,500 W gave a ΔT_o of 132 °C, a Δp_g of 20 kPa and time required to obtain the peak Δp_g of about 115 days. For a heating rate of 3,000 W, the simulation predictions were: ΔT_o of 180 °C; a Δp_g of 35.5 kPa, and the time required to obtain the peak Δp_g of about 50 days. The numerical predictions are illustrated in Figures 4-54 and 4-55.

The magnitude and the time of the peak Δp_g were predicted for the LBT using the heating period scaling laws. The maximum ΔT_0 used in these analyses was at the time of the maximum Δp_0 from the numerical simulation. The scaling law prediction for the field-scale LBT was a value of 150 kPa for Δp_g at a time of 75 days at a heating rate of 1,500 W and 190 kPa for Δp_g at a time of 75 days at a heating rate of 3,000 W. The medium was assigned a permeability value representative of the matrix (1.9×10^{-18} m^2), not of a composite medium (1.8×10^{-14} m^2). The maximum Δp_g predicted for the LBT with the larger composite permeability would only be about 5 kPa. Results from the G-Tunnel heater test, with a characteristic size comparable to the proposed LBT, indicate that a value for Δp_g of 100 to 300 kPa is reasonable.

Mountain Scale. The numerical simulation for the YM model with a heat load of 114 kW/acre predicted for a ΔT_o of 157 °C that there would be a maximum Δp_g of 42 kPa occurring at 160 yr. For the lower heat load of 57 kW/acre and a ΔT_0 of 80 °C, the results were a Δp_g of 5.5 kPa occurring at 63 yr. These numerical predictions are illustrated in Figures 4-56 and 4-57.

The magnitude and the time of the peak Δp_g were predicted for the YM repository using the heating period scaling laws. The maximum ΔT_0 used in these analyses was at the time of the maximum Δp_0 from the numerical simulation. The scaling law prediction for the field-scale YM was a value of 160 kPa for Δp_g at a time of 350 yr at a heating load of 57 kW/acre and 290 kPa for Δp_g at a time of 800 yr at a heating load of 114 kW/acre. The medium was assigned a permeability value representative of the matrix (1.9×10^{-18} m^2), not of a composite medium (1.8×10^{-14} m^2). Justification for using the lower permeability was based on a comparison of predicted and observed gas pressures at the field scale. Although mountain-scale measurements of a maximum Δp_g are not available, there is no evidence to suggest that this justification is not valid. A comparison of the numerical and heating period scaling law predictions is summarized in Table 4-7.

Table 4-6. Summary of measured, numerically predicted, and scaling law predicted gas pressure peaks and time at which the peak occurred

Experiment	Observed Δp_g Peak (kPa)	Observed Time of Δp_g Peak (hr)	Numerical Δp_g Peak (kPa)	Numerical Time of Δp_g Peak (hr)	Scaling Law of Δp_g Peak (kPa)	Scaling Law Time Δp_g Peak (hr)
Test 9	22	8.5	n/a	n/a	90	11.7
Test 11	17	4.5	57	5	12	11.7

4.2.3.3 Summary of Heating Period Scaling Law Assessment

The experimental Δp_g buildup and duration are predicted by the conceptual model to be within about a factor of four of the measured results for Test 9, whose assigned property values were questionable, and within a factor of 1.5 for Test 11. These comparisons show sufficient agreement to conclude that the conceptual model adequately predicts the gas flow regime (i.e., pressure driven), the magnitude of the Δp_g buildup, and the time duration of the Δp_g buildup for the laboratory experiments.

Comparisons between the observed and numerically predicted results and the scaling law predictions indicate that the conceptual model is in agreement with the laboratory-scale cylinder tests. The comparisons also demonstrate that the conceptual model agrees well with the numerical simulations of the LBT and the YM repository when a matrix permeability is assigned to the scaling model. There was poor agreement when a composite permeability was assigned to the LBT and YM numerical models.

The reason for these inconsistent predictions of the conceptual model is its assumption that the Δp_g buildup is primarily caused by the confining effect of the porous medium on the flow vapor generated by evaporation near the heater. Consequently, the model is likely not to represent the Δp_g buildup in a porous medium that has a relatively large permeability (i.e., little confinement) but that is heated to temperatures significantly above the boiling point of the liquid (so that vapor pressures are generated independently of the influence of medium confinement). For those kinds of systems, the Δp_g buildup is roughly equal to the vapor pressure of the liquid, and the confining effect of the medium is of little importance. Put more succinctly, the model does not represent the Δp_g response during the heating period for media and heating rates when Ad_g is roughly of magnitude unity or less and $\Delta T_o > 150$ °C. Actual fractured, but otherwise tight, porous media, however, are likely to exhibit high gas pressure caused by confinement, as demonstrated by the G-Tunnel heater test results.

Lack of connectivity among fractures has also been observed during gas flow tests at the ALTS (Bassett et al., 1994). The previous discussion indicated the reasons why a composite permeability model of such media may not adequately simulate Δp_g responses since the composite model assumes

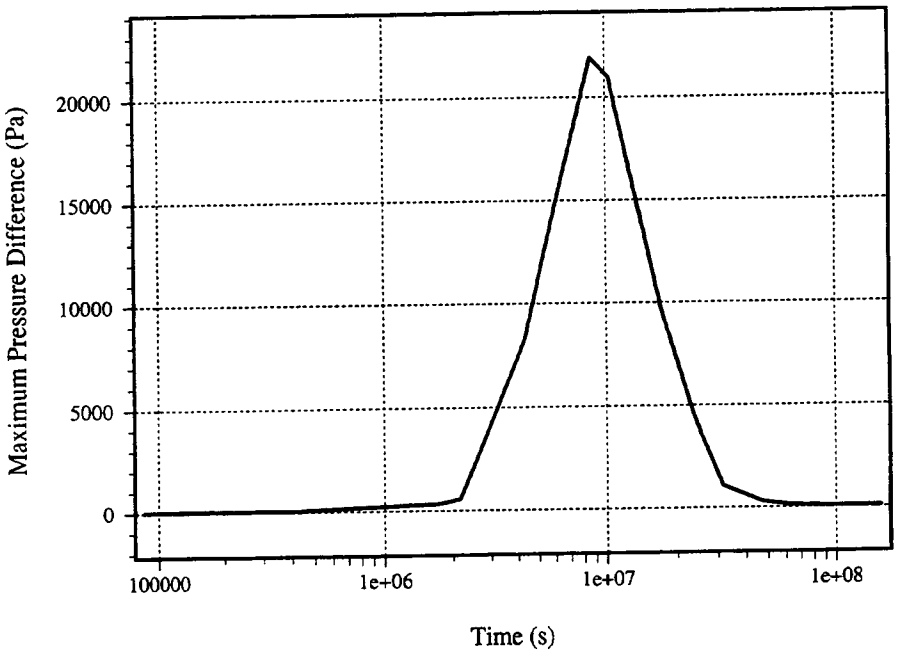

Figure 4-54. Numerically predicted maximum gas pressure differences for the large block test at 1,500 W

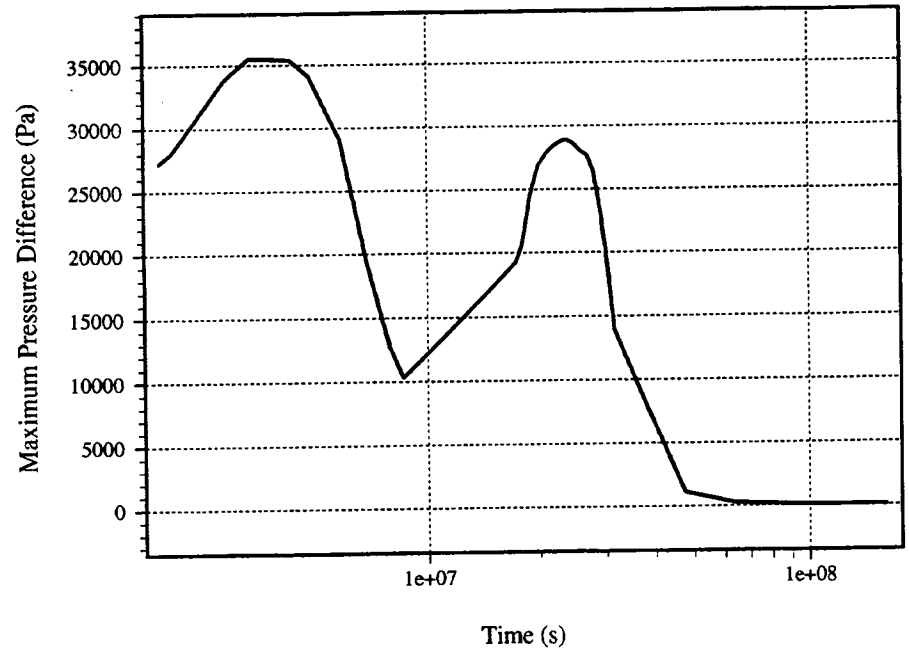

Figure 4-55. Numerically predicted maximum gas pressure differences for the large block test at 3,000 W

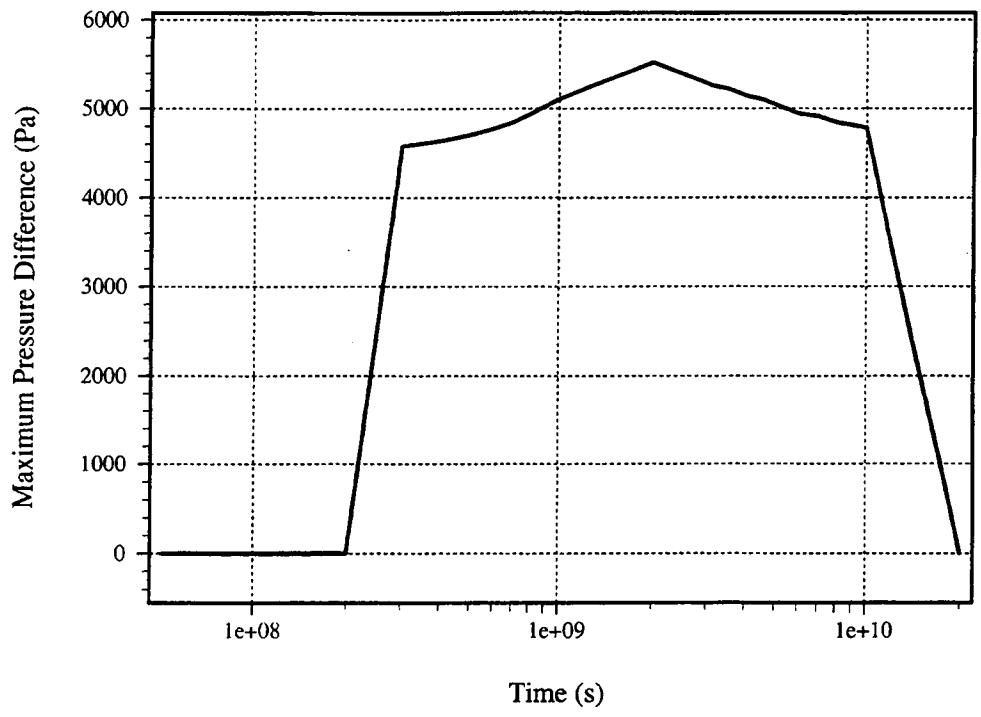

Figure 4-56. Maximum gas pressure differences for the Yucca Mountain repository at 57 kW/acre

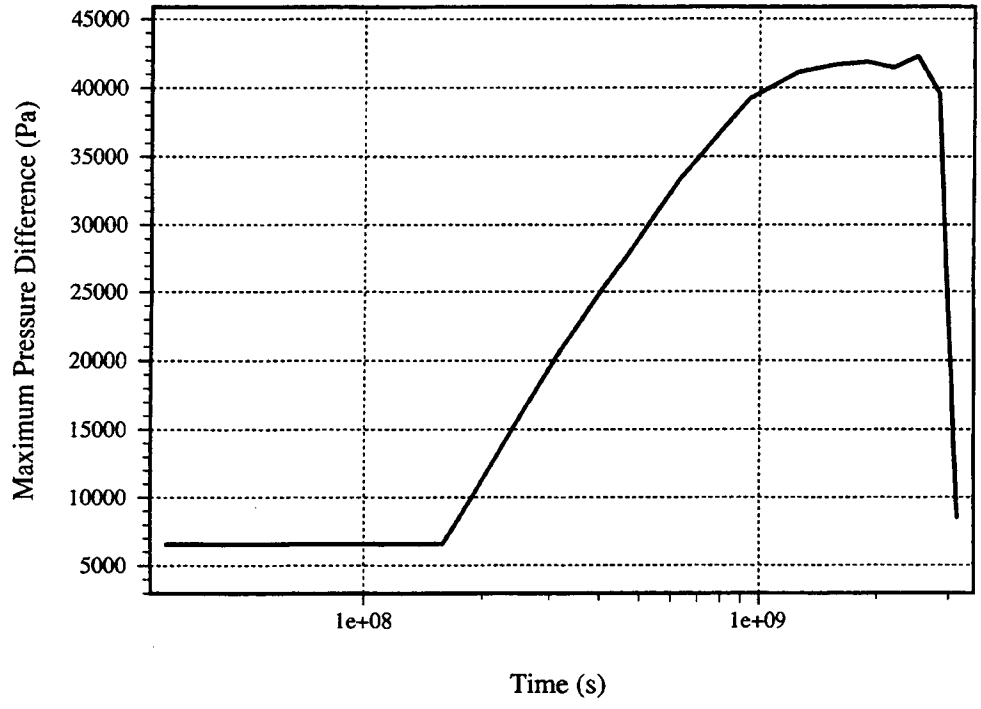

Figure 4-57. Maximum gas pressure differences for the Yucca Mountain repository at 114 kW/acre

Table 4-7. Comparison of numerical and heating period scaling law predictions of magnitude and time of maximum gas pressure

Experiment	Q	Numerical Prediction			Scaling Law Prediction		
		ΔT_0 (°C)	Time of Δp_g Peak	Δp_g (kPa)	ΔT_0 (°C)	Time of Δp_g Peak	Δp_g (kPa)
Test 11	35 W	145	5 hr	57	145	11.7 hr	12
LBT	1,500 W	132*	115 days	22	134	75 days	150
LBT	3,000 W	209*	50 days	35	209	75 days	190
YM	57 kW/acre	80	63 yr	5	80	350 yr	160
YM	114 kW/acre	157	160 yr	42	157	800 yr	290

* **denotes temperature at time of maximum gas pressure**

connectivity. Hence, the good agreement of the conceptual model to the cylinder experiments indicates that the scaling law model should provide a good representation of the heating period for the media of interest.

Numerical simulations of the LBT by Green and Dodge (1994) illustrate the implication of the relative value of Ad_g to the predicted gas and liquid flow regimes. In essence, this study illustrated that in a system with a low Ad_g (i.e., high permeability, low heat load), upward buoyancy-driven flow is predicted throughout the entire block. This premise is supported by Manteufel (1994) whose low Ad_g thermosyphon model also predicted buoyancy-driven gas flow. Conversely, for a system with a high Ad_g (i.e., low permeability, high heat load), Green and Dodge demonstrated that gas flow is advection-driven and away from the heat source. This indicates how flow of gas (i.e., water vapor) below the heater in a system with a high Ad_g, as compared to a system with a low Ad_g, could exhibit drastically different saturation levels and subsequent liquid flow.

The presence of high gas pressures at three measurement locations near the G-Tunnel heater raised important questions regarding the connectivity of fractures. At a minimum, it can be stated that the high gas pressures were an indication that the fractures were not adequately connected to dissipate gas pressure buildup at a field scale of 1 to 2 m. Additional questions raised by this observation are: (i) does this imply that this lack of fracture connectivity will also inhibit the flow of liquid through the same rock, and (ii) are these the mechanisms that inhibit fluid flow through connected fractures at the field scale expected to occur at the mountain scale. Although neither question is easily answered,

mountain scale measurements of both gas and liquid flow are prohibitively difficult. Future field-scale experiments similar to the G-Tunnel heater test that are conducted to closely monitor redistribution of moisture can contribute to resolving the question of fracture connectivity at least at the field scale.

4.2.4 Assessment of the Conceptual Model Scaling Laws for the Cooling Period

The critical response during the cooling period in the thermal evolution of a repository is the time required to rewet previously dried media at the point of the heat source. The performance of a repository will be strongly affected by rewetting and the time at which rewetting occurs. As discussed in Section 2, rewetting can occur by liquid transport due to capillary pressure gradients and by mass diffusion due to relative humidity gradients. This analysis considers only rewetting that occurs through the matrix. Gravity-driven refluxing down fractures is not addressed. As will be argued, this assumption does not significantly limit the relevance of this analysis. After the peak temperature has dissipated, the activity of the vaporization/condensation mechanism will significantly decrease. This could, in turn, significantly reduce the prospect of vertically oriented fractures draining and rewetting the dryout zone at the location of the heat source. It is important to realize that, in the absence of this fracture flow mechanism, the rewetting liquid is transported through the matrix, not through the fractures or, in numerical simulations, through a composite medium, because the capillary pressure gradients exist primarily in the matrix. Therefore, the permeability of the matrix is the primary controlling factor of rewetting due to liquid transport during the cooling period, even for fractured media.

As a result of the dominant influence of the matrix permeability on liquid rewetting, the conceptual model of rewetting developed in Section 2 should be valid even for systems for which the conceptual model of the dryout during the heating period was not (i.e., media highly permeated with open fractures and high heating rates). Experimentally measured rewetting times for the laboratory experiments are compared to predicted times using numerical simulations and the cooling period scaling laws. After assessing the numerical simulations and scaling laws predictions at the laboratory scale, rewetting is predicted for the field and mountain scale.

4.2.4.1 Criteria for Similarity During the Cooling Period

Similarity among the responses of the gas pressure buildup experiments, the LBT model, and the YM repository model, as was explained in Section 2.2.4, depend on the liquid Advection Number Ad_l. The liquid Advection Number is defined by Eq. (2-44) in terms of the gas Advection Number: $\Delta d_l = (\rho_{go}/\rho_{lo})\,(\beta_{go}/\beta_{lo})\,Ad_g$. For reasons just discussed, the gas Advection Number in Eq. (2-44) should be based on the matrix permeability of the media.

The computed values of Ad_l for the various systems are shown in Table 4-8. With the exception of Test 9 (cement slurry), all the systems have values of Ad_l of the same order of magnitude (i.e., they range from 2 to 14) and, therefore, according to the conceptual model, are all reasonably good analogues of each other during the rewetting period. For these systems, the liquid rewetting flow is predicted to be somewhat more controlled by capillary pressure gradients than by buoyancy effects; the model incorporates both effects.

Table 4-8. Gas and liquid advection numbers for different scales

Experiment	Q (W)	k (m^2)	Ad_g	Ad_l
Test 9	35	2×10^{-18}	170,000	110
Test 11	35	5×10^{-17}	10,000	7
LBT	1,500	1.9×10^{-18}	200,000	14
LBT	3,000	1.9×10^{-18}	180,000	13
YM	57*	1.9×10^{-18}	2,500	2
YM	114*	1.9×10^{-18}	4,000	5

* Denotes kW/acre

4.2.4.2 Similarity Criteria Values for Different Scales

Laboratory Scale Results. The durations of both Tests 9 and Test 11 were sufficiently long after cessation of heating to allow estimates of rewetting rates and times during the cooling period. These estimates were made using relative measurements of saturation from Figures 4-48 and 4-51. In both cases, a transition period of about 2 days or so after the heater was turned off was followed by cooling of the medium and eventual rewetting. Estimates of rewetting were not made until after the transition period.

Measurements of rewetting through the cement slurry mixture in Test 9 were made within the 5-cm dryout zone near the heater. At a location near the heater where the liquid saturation had approached zero at the end of the heating period, the region appeared to rewet at a little less than 1 percent per day. From this measurement, it is estimated that complete rewetting at the heater would require about 120 days. An assumption of a linear rate of rewetting is contained in this estimate. This estimate near the heater compares to a rewetting duration of 85 days at a distance of about 3 cm from the heater, where the liquid saturation had decreased only to 0.5. A representative average for complete rewetting of the cement was about 100 days after a heating period that lasted 11 days.

Estimates for rewetting of the ALTS tuff sample used in Test 11 were calculated by the same procedure as was done in Test 9. Slower water flux rates resulted in saturation changes extending to a distance of only about 3 cm from the heater in Test 11. The rewetting estimates at a distance of 1 to 2 cm from the heater in this test varied from about 70 days to 450 days, depending on the location examined. A representative average value for complete rewetting of the tuff is about 150 days after a heating period that lasted 7 days. Therefore, slower flux rates in the tuff as compared to the cement produced a smaller de-watered zone during the heating period and a correspondingly longer rewetting period during the cooling period.

Rewetting of Test 11 was numerically simulated with the same model used to simulate the heating period. Numerically predicted rewetting for Test 11 is illustrated in Figure 4-58. The Test 11 numerical model was assigned basecase properties in this simulation. As illustrated, complete resaturation of the tuff was predicted in the simulations to occur within about 10 days, under-predicting the time to rewetting by over an order of magnitude compared to laboratory results. Thus, numerical simulations for rewetting in Test 11 were not used as part of the database in the conceptual model assessment.

The medium in the numerical simulations for rewetting at the LBT and YM was characterized as uniform with matrix properties. This characterization was possible because liquid transport during rewetting occurs exclusively in the matrix. Characterizing the LBT and YM with the relatively large permeability of a composite media was deemed inappropriate. As stated earlier, episodic or catastrophic rewetting through fractures was not considered in this analysis.

Field Scale. Rewetting in the LBT was numerically simulated with the same model used in the heating period analysis. The rewetting simulation results are illustrated along a vertical line through the middle of the LBT for a heating rate of 1,500 W in Figure 4-59 and for a heating rate of 3,000 W in Figure 4-60. Saturations for only the model region from the heater horizon to the top of the block are illustrated in these figures. Although the block was desaturated to a much greater degree at the higher heating rate, the rates and times of rewetting for the two heating scenarios are very similar. This similarity is attributed to the observation that temperatures in the block returned to ambient relatively quickly in both cases and that the source of water for a large portion of the rewetting experienced at the heater horizon originated from below.

Prediction of complete rewetting of the block in the LBT was not realized within the 20-yr simulation period illustrated in Figures 4-59 and 4-60. Calculation of a rewetting rate from either of the figures provided an estimate of time for complete resaturation at the heater horizon of about 190 yr. A linear extrapolation of the rewetting rate at 20 yr was also used in these calculations.

Mountain Scale. The rewetting simulations for the YM repository model were conducted using the same numerical models used in the heating period analyses. These simulations were conducted at heat loads of both 57 Kw/acre and 114 kW/acre. Numerically predicted saturations for YM along a 1D profile from ground surface to the water table at a depth of 600 m are illustrated in Figure 4-61 for a heat load of 57 kW/acre and in Figure 4-62 for a heat load of 114 kW/acre. The main physical difference between the simulated saturation at the two heating loads is the degree of drying out that occurred during the heating period and the magnitude of the Δp_g buildup.

The saturation contours predicted for YM at the 57-kW/acre heating load are at times of 285, 635, 1,585, and 100,000 yr. Rewetting to the preheating ambient saturation of 0.80 was completed between the simulation times of 1,585 and 100,000 yr. The rate of rewetting inferred from these data gives a time to complete rewetting of about 4,750 yr.

Similarly predicted saturation contours for the 114-kW/acre case are at times of 1,585, 2,220, 63,400, and 98,300 yr. For this higher heat load, the medium dried out to a much greater extent during the heating period. Consequently, the rewetting duration was much longer than for the lower heat load. In fact, the rewetting had not been completed within the 98,000-yr simulation. Linear extrapolation from this rate of rewetting implies a time for complete rewetting to pre-heating saturation levels of at least 127,000 yr.

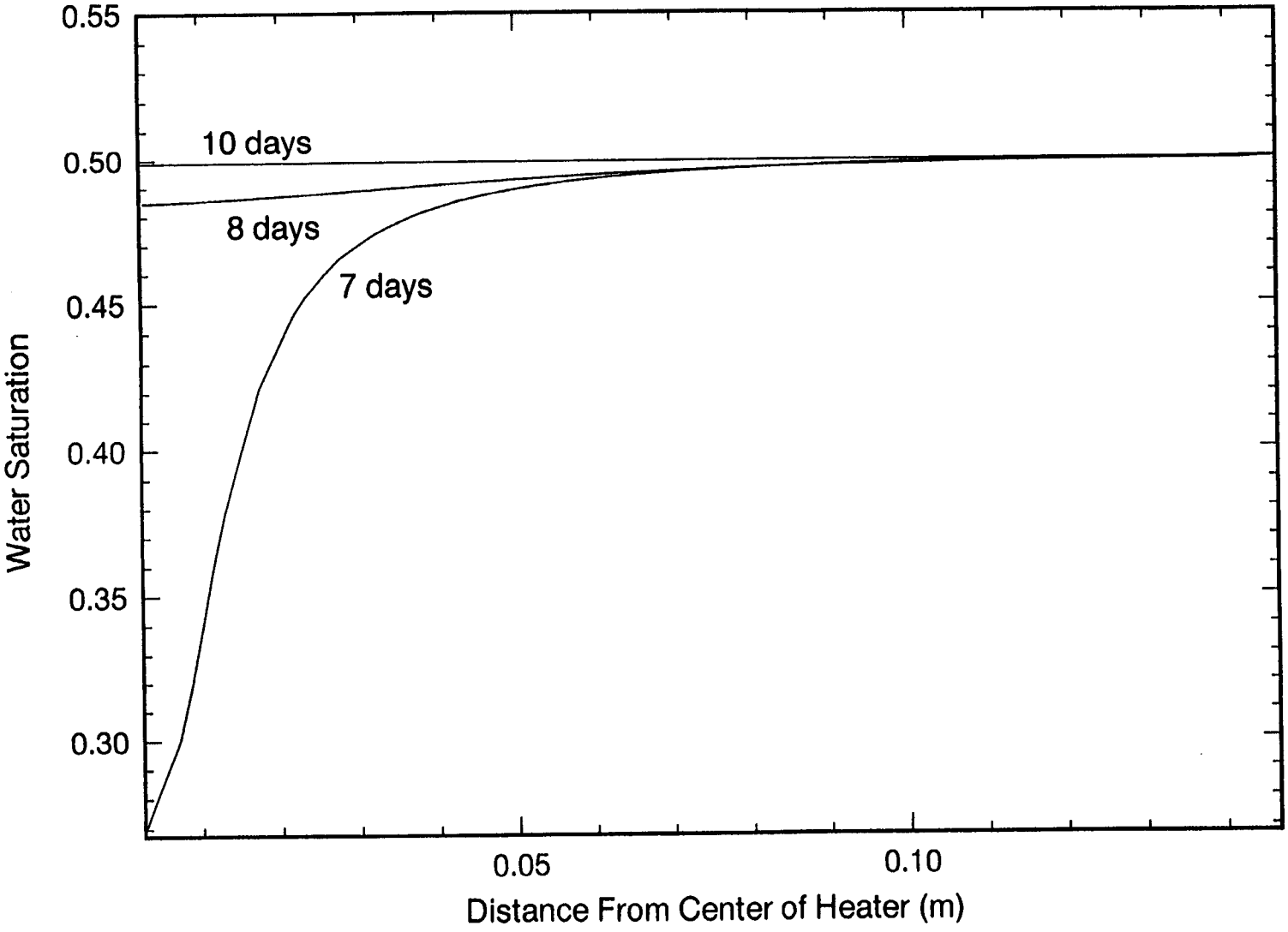

Figure 4-58. Numerically predicted rewetting of Test 11 at 7, 8, and 10 days after heating was discontinued

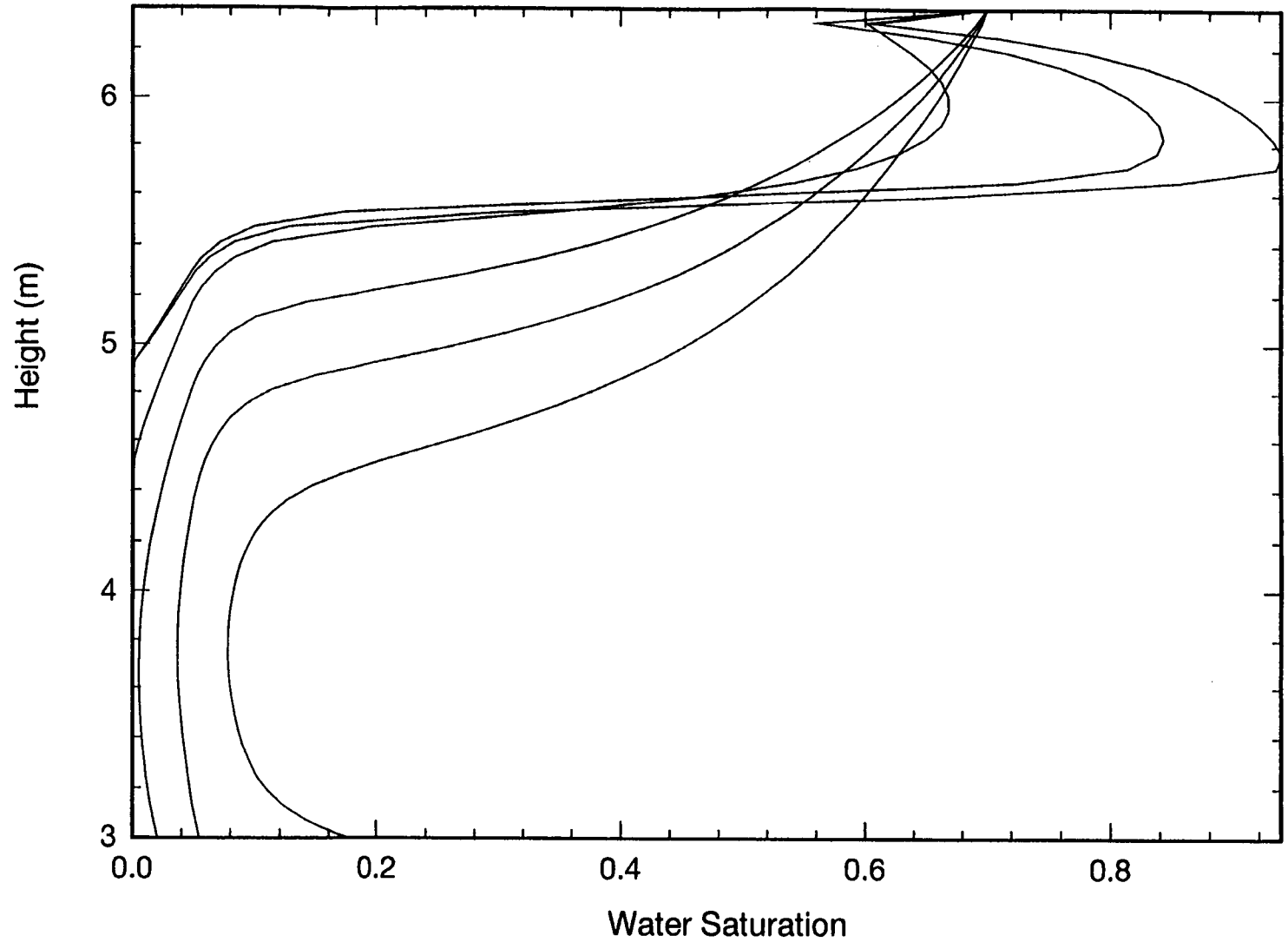

Figure 4-59. Numerically predicted rewetting at the large block test for a heat load of 1,500 W. Curves are, from right to left, at 270, 300, 365, 1,459, 3,650, and 7,300 days after start of heating. Heat was linearly ramped to zero from 300 to 365 days.

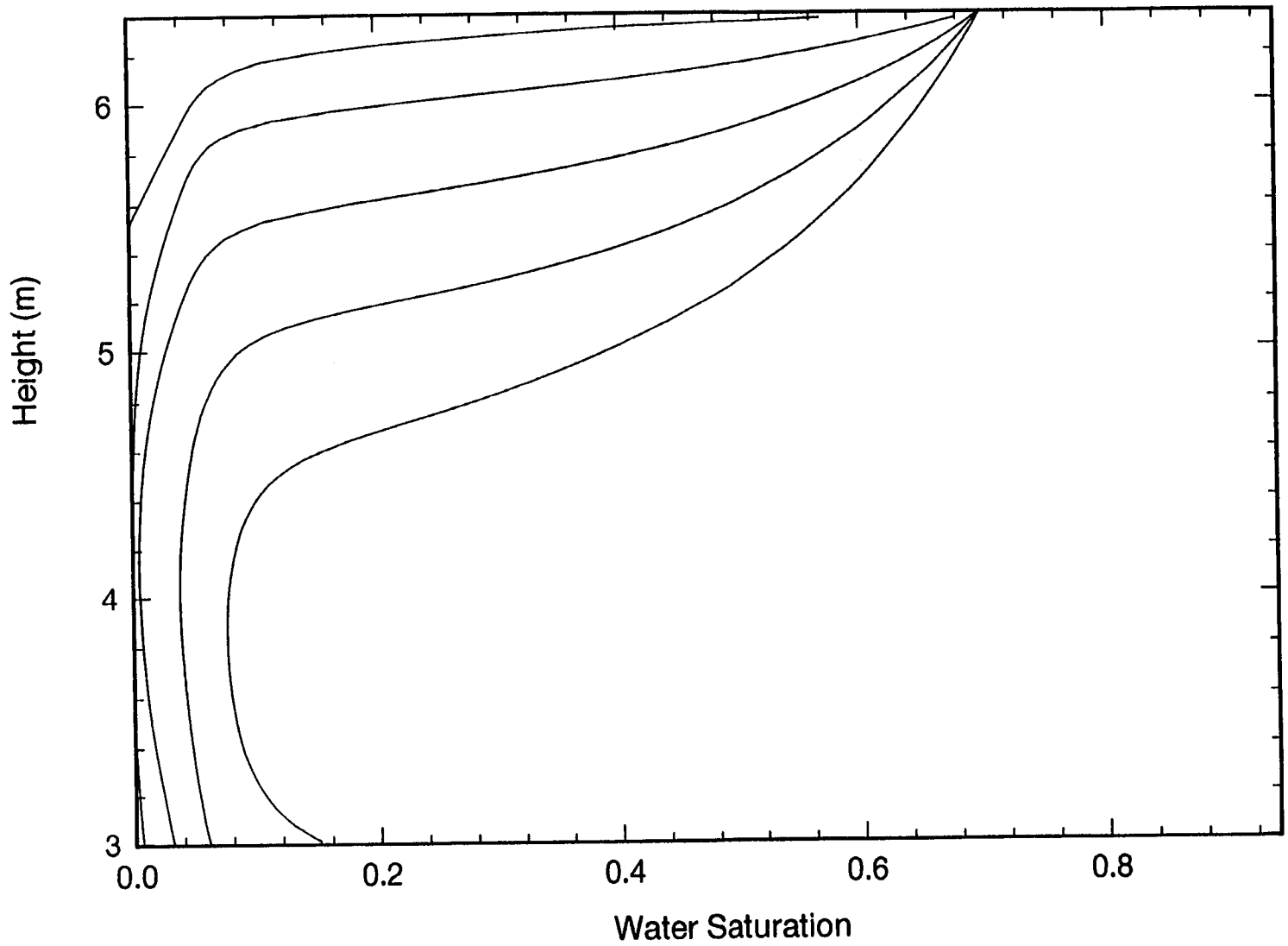

Figure 4-60. Numerically predicted rewetting at the large block test for a heat load of 3,000 W. curves are, from right to left, at 365, 547, 1,459, 3,650, and 7,300 days after start of heating. Heat was linearly ramped to zero from 300 to 365 days.

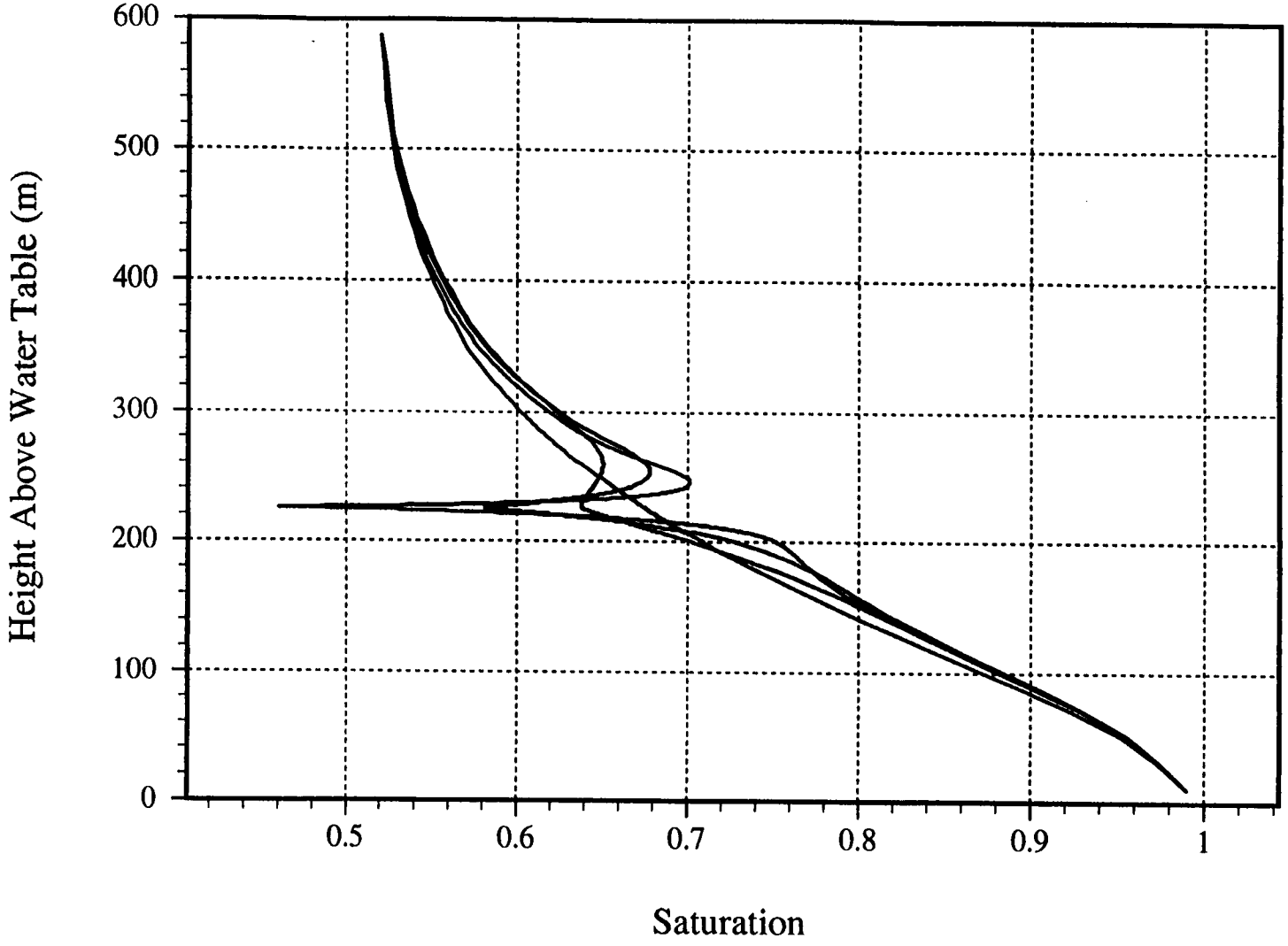

Figure 4-61. Numerically predicted rewetting at the Yucca Mountain repository for 57 kW/acre. Curves are, from left to right at repository horizon (220 m), 285, 634, 1,585, and 100,000 yr after start of heating.

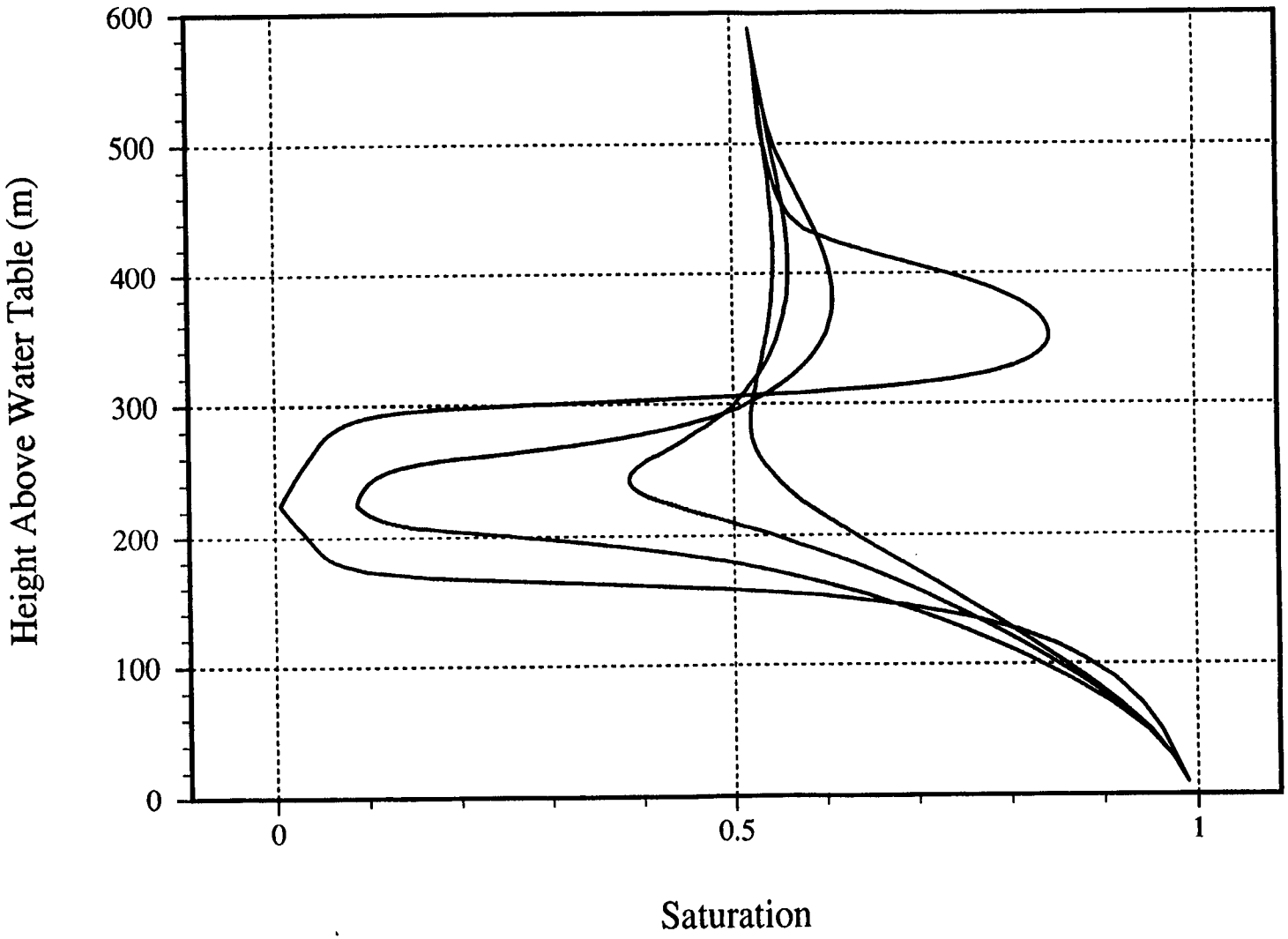

Figure 4-62. Numerically predicted rewetting at the Yucca Mountain repository for 114 kW/acre. Curves are, from left to right at repository horizon (220 m), at 1,585, 2,220, 63,420, and 98,300 yr after start of heating.

4.2.4.3 Summary of Cooling Period Scaling Laws Assessment

The conceptual model recognizes two possible mechanisms for rewetting during the cooling period. These two mechanisms are rewetting as liquid and as water vapor. Rewetting as liquid is driven by capillary forces. The driving mechanism for rewetting by water vapor is mass diffusion. The relative contributions of these two rewetting mechanisms were assessed. The rewetting times predicted by the conceptual model are given by Eq. (2-45) for liquid transport alone, and by Eq. (2-50) for vapor diffusion alone. These time estimates were compared to the Tests 9 and 11 results and the numerical simulations of the LBT and the YM repository to assess the validity of the conceptual model.

Laboratory Scale. The time to rewet dried out media by liquid transport was expressed in Eq. (2-45) as follows:

$$t_l = \left[\frac{(\mu_{lo}/\mu_{go})(k_{rel,go}/k_{rel,lo})(\rho_{lo}/\rho_{go})(R_v T_{avg}/h_{fg})(T_{avg}/\Delta T_o)}{S_{vo}(\Delta \hat{p}_c/\Delta S_l)}\right]\left(\frac{L^2}{\alpha_s}\right). \qquad (4\text{-}5)$$

A representative value of $k_{rel,lo}$ and the dimensionless capillary pressure derivative must be computed to use Eq. (4-5) to estimate the time required for rewetting solely by liquid transport. At any location, both these quantities change significantly during rewetting. Here, they were evaluated for an average liquid saturation value between the initial saturation and total dryout. For Test 9 (cement slurry), the initial saturation was 0.8 to 0.9, so the representative value is 0.4; for Test 11 (tuff sample), the initial saturation was 0.5, so the representative value is 0.25.

For these values of representative saturation and the assigned values of the van Genuchten parameters, the liquid relative permeability was computed from Eq. (2-9) to be 0.0024 for Test 9, and 0.000054 for Test 11. The (dimensional) capillary pressure derivative with saturation was computed from Eq. (2-11) to be 3.30×10^5 Pa for Test 9, and 1.470×10^5 Pa for Test 11. Therefore, the dimensionless pressure changes (capillary pressure divided by the predicted gas pressure increase) needed for Eq. (4-5) are about 3,300 for Test 9 and about 395,000 for Test 11.

With these estimates of input parameter values, the rewetting times predicted by the conceptual model were calculated to be 105 days for Test 11 (compared to about 150 days in the experimental results) and 240 days for Test 9 (compared to about 100 days). These predictions are well within the accuracy range anticipated for the conceptual model.

It has been anticipated in the conceptual model that the vapor diffusion contribution to rewetting will be small during the cooling period. Neither the experiments nor the simulations can show this conclusion explicitly, but the conceptual model is capable of estimating the time required for rewetting to occur solely by vapor diffusion. If this time is significantly longer than the time required for rewetting solely by liquid transport, then diffusion is a negligible effect.

The time to rewet dried out media by vapor diffusion was expressed in Eq. (2-50) as follows:

$$t_g \approx 0.03\left(\frac{\rho_{lo}}{\rho_{vo}}\right)\left(\frac{\Delta S_l}{\tau S_v}\right)\left(\frac{p_v}{\Delta p_v}\right)\frac{L^2}{\alpha_s}. \qquad (4\text{-}6)$$

To use Eq. (4-6) to estimate the diffusion rewetting duration, a representative estimate is needed of the partial pressure difference of the vapor Δp_v caused by vapor pressure lowering. Here, Δp_v is estimated to be about 0.2 times the average vapor pressure p_v over the heated region. With these estimates, the predicted rewetting time from Eq. (4-6) due solely to mass diffusion is $48/\tau$ days. A representative value of the tortuosity τ for these media is not known. Lichtner and Walton (1994) state that representative values for tuff range from about 0.01 to about 0.025 for a medium with a porosity of 0.1. For an average τ value τ of 0.017, the predicted time for rewetting by mass diffusion solely is in excess of 2,500 days, or about an order of magnitude longer than that predicted for rewetting solely by liquid transport. Hence, it is concluded that rewetting by vapor diffusion driven by a relative humidity gradient during the cooling period can be neglected for these media.

For media with larger values of τ (which would make diffusion more prominent) or significantly larger values of matrix permeability (which would decrease the capillary pressure gradient driving liquid rewetting), vapor mass diffusion could be a more significant contributor to rewetting.

Field and Mountain Scale. Initial saturation for both the LBT and YM simulations was estimated at about 0.7. Thus, the representative average saturation for use in Eq. (4-5) was about 0.35. Estimates were also needed of the gas pressure buildup during the heating period to evaluate the dimensionless capillary derivative in Eq. (2-45). As discussed earlier, the conceptual model of the heating period was not a good predictor of gas pressure buildup for systems that have both a relatively large permeability such as the composite block media and a heat load that causes significant boiling. Thus, the values of the gas pressure buildup predicted by the numerical simulation were used to compute the dimensionless capillary derivative in Eq. (4-5). Furthermore, two estimates of the liquid rewetting time were computed for each case: (i) an estimate based on the thermal diffusion time L^2/α_s (the conceptual model estimate of the time required to obtain the maximum gas pressure buildup), and (ii) an estimate in which L^2/α_s was replaced in Eq. (4-5) by the time to obtain the maximum gas pressure buildup predicted by the numerical simulation.

The time for rewetting the block at the LBT by liquid flow was predicted using the conceptual model for heating rates of 1,500 and 3,000 W. At the lower heating rate, the time to rewetting is equal to approximately $364L^2/\alpha_s$. This equates to about 75 yr. When the L^2/α_s thermal diffusion time scale is replaced by the time of maximum gas pressure buildup predicted by the numerical simulation, the predicted time becomes 115 yr. The conceptual model range of predicted times of rewetting for the LBT is in order-of-magnitude agreement with the numerical simulation predicted time of 190 yr. Similar calculations for the LBT at a heating rate of 3,000 W using the cooling period scaling laws of the conceptual model provide predicted rewetting times of 85 and 130 yr. The conceptual model predictions of rewetting times were relatively insensitive to the change in heating rate. Again, these compare favorably with the numerically predicted time of 190 yr.

The time of rewetting predicted using the cooling period scaling laws of the conceptual model for the YM repository at a 57 kW/acre heat load was equal to $91L^2/\alpha_s$. This predicted a rewetting time of 22,000 yr. When the thermal diffusion time scale L^2/α_s was replaced by the gas pressure buildup time predicted from the numerical simulation, the predicted time was 5,750 yr. Both estimates are in approximate agreement with the numerical prediction of 4,750 yr. For the 114 kW/acre heat load, the conceptual model predicted a rewetting duration of $729L^2/\alpha$ or about 650,000 yr. The predicted rewetting time was 116,000 yr with the thermal diffusion time scale replaced with the numerical prediction for the time of maximum gas pressure buildup. Again, both predictions are in agreement with the numerical prediction of 127,000 yr.

The results of the numerically predicted times of rewetting compared to the rewetting times predicted using the cooling period scaling laws of the conceptual model are summarized in Table 4-9. Scaling law times were predicted using a thermal diffusion time scale (Scaling Law A) and numerically predicted times for maximum gas pressure (Scaling Law B).

4.2.5 Conclusions of the Scaling Laws Assessment

Comparisons of the conceptual model to the laboratory experiments and the LBT and YM simulations for both the heating and cooling period have demonstrated the usefulness and the range of validity of the model. Conclusions from the heating period scaling law assessment can be summarized as follows.

The conceptual model is a valid representation of systems that have:

- $Ad_g \approx 1$ and $\Delta T_o < 100$ °C (open media, low heating rates)
- $Ad_g > 1$ and either $\Delta T_o > 125$ °C or $\Delta T_o > 100$ °C (tight media, low/high heating rates)

It is not a valid representation for systems that have:

- $Ad_g \approx 1$ and $\Delta T_o > 125$ °C (open media, high heating rates)
- Gas pressure buildup observed in the laboratory-scale cylinder test and the field-scale G-Tunnel heater experiment raised questions about the connectivity of fractures in partially saturated fractured porous media. Gas pressure buildup during the heating period at the G-Tunnel experiment indicates that a high density of fractures does not necessarily ensure fracture connectivity.

For all the systems, the conceptual model is an adequate representation of the time duration over which large gas pressures can be anticipated. However, this is merely a consequence of the fact that thermal conduction sets the time duration, not the confining effect of the media.

Conclusions from the cooling period scaling laws assessment can be summarized as follows:

- A set of cooling period scaling laws have been formulated to predict the time of rewetting for systems of different scales.
- The relative importance of rewetting by vapor diffusion and rewetting by liquid flow has been assessed. For the particular systems evaluated here, rewetting is dominated by liquid flow and rewetting by vapor diffusion from relative humidity gradients can be neglected.
- Rewetting times predicted with the cooling period scaling laws were in agreement with rewetting times of two laboratory-scale experiments. The numerically predicted rewetting trend did not agree with either the cooling period scaling law prediction or the laboratory results.

Table 4-9. Comparison of rewetting times numerically predicted, predicted with the cooling period scaling laws and a thermal diffusion time scale (Scaling Law A), and predicted with the cooling period scaling laws and a numerically predicted time of maximum gas pressure (Scaling Law B)

System	Numerical Prediction (yr)	Scaling Law A (yr)	Scaling Law B (yr)
LBT at 1,500 W	190	75	115
LBT at 3,000 W	190	85	130
YM at 57 kW/acre	4,750	22,000	5,750
YM at 114 kW/acre	127,000	650,000	116,000

- Cooling period scaling law rewetting times were predicted using two characteristic times: (i) the thermal diffusion time scale, and (ii) the numerically predicted time of maximum gas pressure. Rewetting times for the LBT at heating rates of 1,500 and 3,000 W and for YM at heating loads of 57 and 114 kW/acre predicted using either of the two characteristic times were in agreement.

- Both scaling law rewetting time predictions were in agreement with numerically predicted rewetting times for the LBT at heating rates of 1,500 and 3,000 W and for YM at heating loads of 57 and 114 kW/acre.

- Rewetting times for the LBT are predicted to range from 75 to 190 yr for the LBT with a heating rate of either 1,500 or 3,000 W. Rewetting times for YM are predicted to range from 4,750 to 22,000 yr for a heat load of 57 kW/acre and from 116,000 to 650,000 yr for a heat load of 114 kW/acre. Rewetting exceeds the initial drying times by a factor of about 10^2 for both the LBT and YM at any of the heating rates or loads.

Results from the formulation of analyses conducted with a set of scaling laws for the cooling period of the thermal evolution of the HLW repository have contributed to resolving the fundamental basis of moisture redistribution through partially saturated porous media.

To the extent that the comparisons discussed in this section validate the conceptual models of the response of a porous medium during heating and cooling periods, the model can be used to design laboratory or field experiments to achieve specified objectives. In particular, the gas Advection Number Ad_g provides a dimensionless parameter that allows an experiment to be designed to investigate either pressure-driven gas flow during heating or to ensure that pressure-driven gas flow does not occur. In general, pressure-driven gas flow would tend to dry out a heated region much more extensively and rapidly than flows induced by buoyancy or vapor diffusion.

The conceptual model of the cooling period of the system's response makes evident the parameters that control the time duration required for rewetting of the previously dried out region. This model, for example, could be used to design an experiment that would allow rewetting to be investigated in the laboratory or field for a time duration of practical length.

The conceptual models can also be used to make predictions of the response of larger systems from the measured responses obtained in experiments of smaller systems. The various pressure, velocity, and time duration expressions of the model are, in effect, the recommended methods of scaling up the smaller system responses.

5 CONCLUSIONS AND RECOMMENDATIONS

The central objective of the Thermohydrology Research Project was to develop a technical understanding of thermally driven redistribution of moisture in partially saturated porous media, as it applies to a geologic repository. A series of laboratory-scale thermohydrology experiments were conducted to provide data to help identify and evaluate individual driving forces that control water (liquid and vapor phases) movement from and to a heat source. Scaling theories were derived from similarity analyses to relate the thermohydrologic phenomena observed at the laboratory scale to that of field and full repository-scale. Computer simulations of two-phase flow were performed to provide a basis for evaluating the scaling theories.

The Thermohydrology Research Project began with the intent of addressing a broad spectrum of generic questions regarding thermohydrologic phenomena. While some of these questions were answered in the conduct of the study, other new and challenging ones were encountered. Initial progress made in addressing those technical questions was documented in an interim progress report (Green et al., 1993). Subsequent to that report, the laboratory-scale experiments were designed to address four fundamental questions regarding thermohydrologic phenomena:

(i) What are the principal mechanisms controlling the redistribution of moisture?

(ii) Under what hydrothermal conditions and time frames do individual mechanisms predominate?

(iii) What hydrothermal regimes are associated with each driving mechanism?

(iv) What is the temporal and spatial scale of each hydrothermal regime?

In essence, these questions identify the need to understand the factors, conditions, and processes that control the rates of dryout and rewetting of the repository. The findings and mathematical theories developed to address these questions are summarized below. Technical recommendations for a field-scale thermohydrology experiment are also presented.

5.1 FINDINGS OF LABORATORY-SCALE EXPERIMENTS

Eleven laboratory-scale thermohydrology experiments were conducted which are categorized according to: (i) the fluid phase (i.e., liquid or gas) considered, (ii) hydrothermal regime (i.e., boiling or sub-boiling), (iii) test cell geometry (i.e., rectangular or radial), and (iv) test medium (i.e., consolidated or unconsolidated). Two groups of experiments were designed to address the four basic technical questions regarding two-phase flow processes. In addition, they were designed to provide the data necessary for testing various scaling theories proposed in Section 2. The first group, referred to as the liquid flow experiments, was designed to study the flow patterns in the liquid phase. The second group, designated as the gas flow experiments, focused on the dynamics of the gas phase and the build up of gas pressure. The analysis of experimental results attempted to relate the fluid-flow regimes to system variables. Of particular interest are the rates and directions of liquid and vapor flow and their time histories during the heating and cooling periods.

The results of the laboratory-scale experiments were interpreted and extended using numerical simulations of two-phase flow. The major observations, inferences, and conclusions drawn from the experimental results and computer modeling are:

- Two condensation models have been identified: (i) media with low permeability and small air-entry pressure will be more likely to experience a relatively narrow moisture buildup zone on the cool side of a dryout zone near a heat source; (ii) media with a low permeability and large air-entry pressure will tend to exhibit condensation over a broad area beyond the zone of dryout.

- Temperatures much above boiling may not be sufficient to completely dry out media with low permeability (for example, temperatures greater than 170 °C did not appear to completely dry out ceramic with a permeability of 1×10^{-13} m^2 or less).

- Fluid flow patterns near a heat source may be more complex than predicted by numerical simulation. In particular, complex flow of liquid near the heat source in a laboratory-scale experiment, including the downward flow of water from above the heat source, was not well replicated in the numerical model.

- Experimental measurements confirmed the occurrence of gas pressure buildup and subsequent pressure driven vapor flow in media with low saturated liquid permeability.

- Intermittent gas pressure buildup and release near the heat source can potentially transport large amounts of liquid and vapor relatively long distances from the heat source.

- Measured rewetting rates were one to two orders of magnitude smaller than the drying rates.

Based on these observations, it is inferred that the extent of the repository dryout zone will be a strong function of the bulk liquid permeability of the matrix. Media with lower permeabilities will dry out more slowly, but will rewet at significantly lower rates than high permeability media. The nature of condensation, that is, will moisture condense near the dryout zone or at a distance from the heat source, is also dependent on the hydraulic properties of the medium.

5.2 FINDINGS OF SIMILARITY ANALYSIS

Using similarity theory, scaling laws were formulated for use in predicting the rates of dry out and rewetting at the field and mountain scales using results from laboratory-scale models. Because the driving mechanisms were different for the heating and cooling periods, a separate set of scaling laws was developed for each period. The conceptual models associated with each set of scaling laws are based on the general mathematical theory of two-component, two-phase flow in heated, partially saturated porous medium. The scaling laws were specialized and simplified to apply to: (i) the buildup of gas pressure during the initial period of large heating rates, and the attendant drying out of the media; and (ii) the rewetting of the dried out region during the later cooling phase. The two conceptual models were characterized in terms of dimensionless parameters.

Heating Period Model. The conceptual model of the heating period demonstrated that the requirements for similarity among systems of various geometric sizes and thermohydrologic properties are summarized in a new dimensionless number called the gas Advection Number, Ad_g. Like other dimensionless numbers, Ad_g is the ratio of two physical effects, in this case the ratio of (i) gas pressure gradients created by the confining effect of the medium to (ii) buoyancy-induced body forces. Ad_g is formally expressed in terms of thermohydrologic parameters such as permeability and porosity, fluid parameters such as density, viscosity, and coefficient of thermal expansion, and heating rate parameters such as the temperature increase of the media near the heater.

For cases where $Ad_g >> 1$, the heating is sufficient to cause the creation of large pressure gradients and high advective gas flows. Under these conditions, the region near the heat source is likely to experience a significant degree of drying out. The model also predicts the magnitude of the peak gas pressure gradient that will be produced. The time at which the peak gas pressure occurs is predicted to be the same as the characteristic thermal diffusion time. For cases where $Ad_g \leq 1$, heating is expected to produce only small gas flows away from the heat source and buoyancy has a dominant role in setting the characteristics of fluid flow. For these conditions, less drying of the repository is expected.

The heating period model was compared to the results and numerical simulations of laboratory-scale experiments and to numerical simulations of the LBT and of the YM repository. The value of Ad_g for the laboratory-scale tests was computed to be more than 10^4, and so the model predicted that large pressure gradients and a significant degree of drying out should be observed in the experiments. This assessment was, in fact, confirmed by the results of the experiments. Further, conceptual model predictions of the magnitude of the peak pressure and the time required to obtained the peak compared well with experimental results. A similarly close comparison was found for the numerical simulation of the laboratory-scale experiments.

Evaluations of these inferences and trends were made using computer model representations of the LBT scale and YM scale systems. Differences in the LBT and YM conceptual models were associated with assignment of media permeability. The two approaches were used: (i) a model with a permeability equivalent to the matrix, and (ii) a model with a composite matrix/fracture permeability. The matrix permeability was about four orders of magnitude less than that for the composite model. For the composite model, the computed value of Ad_g for LBT was of order 10 and that for YM was of order unity. Hence, the composite permeability conceptual model predicted that little pressure buildup should occur.

Values of Ad_g for the LBT and YM based on a matrix permeability assumption were relatively large (i.e., $> 10^3$) thereby predicting high gas pressure buildup and velocities. The numerical simulations predicted that the peak pressure for both cases was at least 10 kPa, thus substantiating the matrix permeability model. High gas pressures (i.e., 300 kPa) observed during a heater test conducted in highly fractured tuff at G-Tunnel (Ramirez, 1991) indicated that high gas pressures will occur even in highly fractured tuff. Thus, the matrix permeability model is more appropriate than the composite permeability for use in the conceptual scaling model. However, numerical simulations based on the composite model were in agreement with experimental results from both the laboratory and field scales and with the heating period scaling law predictions.

Cooling Period Model. The most important aspect of moisture redistribution during the cooling period is the time required to rewet the region dried out during the heating period. Rewetting time is important because it is a measure of when water comes back into contact with the canister environment after it had been dried out. This rewetting aspect of the cooling period was investigated using the conceptual model. Analogous to the heating period, a liquid Advection Number Ad_l was developed. The rewetting response of various systems is expected to be similar when the values of Ad_l are of a similar order of magnitude for the systems. The computed value of Ad_l for the laboratory-scale experiments and for the LBT and YM models were all of the same magnitude (about 10), thus indicating that all three systems are good analogues of each other for the cooling period.

The conceptual model considered rewetting both by liquid transport and by vapor phase diffusion. In all cases studied, the conceptual model predicted that rewetting due to vapor diffusion was negligibly small. The liquid transport rewetting always occurs in the matrix even for fractured media, because of the large capillary pressure gradients created in the matrix by the drying out during the heating phase. Hence, the conceptual model of the cooling period should apply equally to fractured or nonfractured media.

The cooling period conceptual model scaling predictions were compared to laboratory-scale experiments and numerical simulations. For the reasons given for the heating period, the numerical simulations of rewetting were based on the permeability of the matrix rather than that of the composite media. The times predicted by the conceptual model for liquid transport rewetting compared very well to the measured values for the laboratory-scale experiments (100 to 150 days) and the simulated rewetting times for the LBT (75 to 190 yr) and YM (116,000 to 650,000 yr). The comparisons of the conceptual model predictions to laboratory test data and to numerical simulations show that the model is capable of determining and assessing the hydrologic and heating rate conditions required for drying out and rewetting of heated, partially saturated porous media. Measured times for rewetting exceeded the time for drying at the laboratory scale by a factor of 10^1 to 10^2. The times to rewet the LBT and YM predicted numerically and substantiated with the conceptual models exceeded the dryout times by a factor of about 10^2.

Scaling Implications of the Conceptual Model. The scaling law conceptual models can be used with confidence to evaluate laboratory- and field-scale experiments as analogues of repository responses to heating. The pressure, velocity, and time scaling laws that arise in the conceptual model can also be used to interpret, or scale up, the responses measured in laboratory- and field-scale experiments in terms of repository responses, when the thermohydrologic and heating rate conditions of the experiments are considered to be sufficiently similar to the repository. Likewise, the conceptual model can be used to guide numerical simulations of these responses. However, similarity approaches have limited use for the canister scale because flow in individual discrete features such as fractures cannot be appropriately scaled.

5.3 RECOMMENDATIONS

The overall results of this project suggest that similarity analyses can provide reasonable predictions of the spatial and temporal scales of heat and mass transfer mechanisms active at a repository scale. However, they do not appear to be a viable analytical tool to assess canister-scale moisture redistribution mechanisms where the physics of flow many depend on discrete features of the geologic media. Understanding and predicting moisture redistribution in fractured rock near a heat-generating canister is of critical importance since the performance of a HLW repository is dependent on the rate at

which the canister environment dries out during the heating period, stays dry, and eventually rewets during the cooling period. Few field-scale experiments have been conducted to answer this information need. The G-Tunnel heater experiment (Ramirez, 1991; Buscheck et al., 1991) and the spent fuel test at Climax (Patrick, 1986) did fulfill, in part, the requirements of such tests. Only one field-scale experiment is currently active that would provide information toward these information needs, the Fran Ridge LBT (Lin et al., 1994; Buscheck et al., 1993). The scales (characteristic lengths) of these three field-scale experiments are all about 1 to 3 m. Not all information needs were met or will be met by these field-scale experiments.

An additional field-scale experiment is proposed that would contribute to the investigation of thermally driven moisture redistribution in partially saturated fractured, porous media. The scale of the proposed field-scale experiment is 8 to 10 m and the medium is a fractured, welded tuff. The proposed field-scale experiment would be conducted at the Peña Blanca Natural Analog site near Chihuahua, Mexico (Pearcy, 1994; Green et al., 1994). The Peña Blanca Natural Analog field site currently offers a physical setting highly conducive to the conduct of a field-scale heater experiment. Peña Blanca, as a natural analog of YM, offers unique opportunities to measure the hydraulic properties and observe thermally driven moisture redistribution at a field scale that is large enough to permit investigation of the composite effect of fractures and matrix, but sufficiently limited that scales of time and distance are not prohibitively large that measurements cannot be made in reasonable times and at reasonable distances. The physical and geometric attributes providing surface and subsurface exposure of the site are not known to be available at any other site.

The analog site exhibits a high degree of exposure provided through the removal of a large amount of the overlying host rock and debris conducted as part of prior activities associated with a Uranium mine that operated at the site. The deposit has been exposed through the excavation of the mine. Enhancing the accessibility of the site is the presence of 80 m of horizontal adits located 8 to 10 m below the most extensive level surface of exposed rock and a series of 10 m deep vertical boreholes located near the adit. The proposed heater test would actually consist of a number of separate heater tests throughout the adit in which individual heaters would be emplaced 1 to 3 m above the top of the adit. Because the adit transects a wide range of permeabilities and differing fracture sets, each heater test would be conducted under widely differing hydrogeologic conditions. A vertical cross-sectional schematic of the proposed heater test is illustrated in Figure 5-1.

Results gained from the field-scale heater tests would be compared to moisture redistribution predicted using conceptual and mathematical models to assess their ability to predict flow and transport for a field-scale application. The models would be constructed using information gained in the laboratory-scale experiments and field characterization measurements, but not using the actual field-scale test results. Controlled blind comparison of model predictions based on site-specific property values and observed field-scale thermally driven moisture redistribution experiments would provide independent assessment of conceptual and mathematical models.

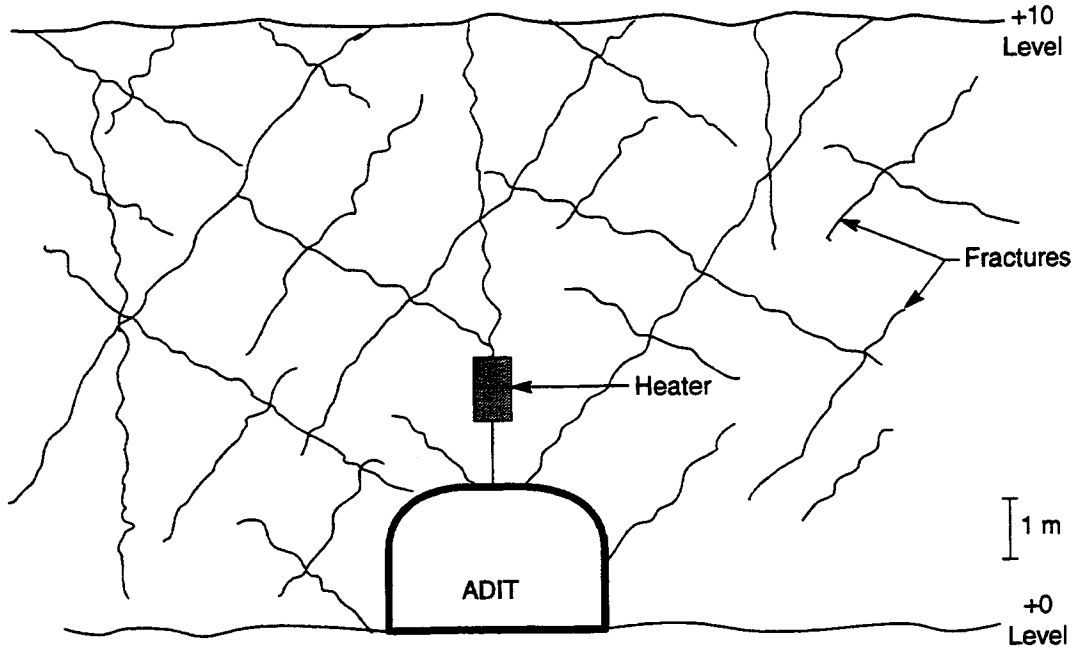

Figure 5-1. Schematic of proposed Peña Blanca field-scale heater test

6 REFERENCES

ALCOA Chemical. 1969. *Hydrated Calcined, Tabular Aluminas, and Calcium Aluminate Cement.* Alcoa Products Data Sheet. Pittsburgh, PA: Aluminum Company of America.

American Society for Testing and Materials. 1977. *Capillary Moisture Relationships for Coarse- and Medium-Textured Soils by Porous-Plate Apparatus.* ASTM D 2325. Philadelphia, PA: American Society for Testing and Materials.

Andrews, R.W., T.F. Dale, and J.A. McNeish. 1994. *Total System Performance Assessment-1993: An Evaluation of the Potential Yucca Mountain Repository.* Las Vegas, NV: INTERA, Inc.

Ashworth, E. 1992. The variation of the thermal conductivity of tuff with moisture experimental results and proposed model. *Proceedings of the 33rd U.S. Symposium on Rock Mechanics, Sante Fe, NM.* Rotterdam, The Netherlands: A.A. Balkema: 859–868.

Baker, W.E., P.S. Westine, and F.T. Dodge. 1973. *Similarity Methods in Engineering Dynamics.* Rochelle Park, NJ: Hayden Book Co.

Bassett, R.L., S.P. Neuman, T.C. Rasmussen, A. Guzman, G.R. Davidson, and C.F. Lohrstorfer. 1994. *Validation Studies for Assessing Unsaturated Flow and Transport Through Fractured Rock.* NUREG/CR-6203. Washington, DC: Nuclear Regulatory Commission.

Batchelor, G.K. 1967. *An Introduction to Fluid Dynamics.* London, United Kingdom: Cambridge University Press.

Bear, J. 1972. *Dynamics of Fluids in Porous Media.* New York, NY: Dover Publications.

Bear, J. 1979. *Hydraulics of Groundwater.* New York, NY: McGraw-Hill Inc.

Blackwell, D.D., and R.E. Spafford. 1987. Experimental methods in continental heat flow. *Methods of Experimental Physics* 24(B): 189–226.

Bonano, E.J., and E.J. Davis. *Numerical Simulation of Longitudinal Roll Vortices in a Heated Flowing Liquid Film.* 80-HT-70. New York, NY: American Society of Mechanical Engineers: 1–9.

Buckingham, E. 1914. Model experiments and the forms of empirical equations. *Physical Review* 4: 345.

Buscheck, T.A., and J.J. Nitao. 1992. The impact of thermal loading on repository performance at Yucca Mountain. *Proceedings of the Third Annual International Conference on High-Level Radioactive Waste Management.* La Grange Park, IL: American Nuclear Society: 1,003–1,017.

Buscheck, T.A., and J.J. Nitao. 1993. The analysis of repository-heat-driven hydrothermal flow at Yucca Mountain. *Proceedings of the Fourth Annual International High-Level Radioactive Waste Management Conference.* La Grange Park, IL: American Nuclear Society: 846–867.

Buscheck, T.A., and J.J. Nitao. 1994. The impact of buoyant, gas-phase flow and heterogeneity on thermo-hydrological behavior at Yucca Mountain. *Proceedings of the Fifth Annual International High-Level Radioactive Waste Management Conference*. La Grange Park, IL: American Nuclear Society: 27–74.

Buscheck, T.A., R. Carlson, W. Daily, K. Lee, W. Lin, N. Mao, A. Ramirez, T. Ueng, H. Wang, and D. Watwood. 1991. *Prototype Engineered Barrier System Field Test (PEBSFT) Final Report*. UCRL-ID-106159. Livermore, CA: Lawrence Livermore National Laboratory.

Buscheck, T.A., D.G. Wilder, and J.J. Nitao. 1993. Large-scale *in situ* heater tests for hydrothermal characterization at Yucca Mountain. *Proceedings of the Fourth Annual International Conference on High-Level Radioactive Waste Management*. La Grange Park, IL: American Nuclear Society: 1,854–1,872.

Corey, A.T. 1986. *Mechanics of Immiscible Fluids in Porous Media*. Littleton, CO: Water Resources Publications.

Dodge, F.T., and R.T. Green. 1994. Pressure-driven gas flow in heated, partially-saturated porous media. *Proceedings of the Fifth Annual International Conference on High-Level Radioactive Waste Management*. La Grange Park, IL: American Nuclear Society: 2,217–2,227.

Domenico, P.A., and F.W. Schwartz. 1990. *Physical and Chemical Hydrogeology*. New York: John Wiley and Sons.

Flint, L.E., and A.L. Flint. 1990. *Preliminary Permeability and Water Retention Data for Nonwelded and Bedded Tuff Samples, Yucca Mountain, Area, Nye County, Nevada*. U.S. Geological Survey Open File Report 90-569. Denver, CO: U.S. Geological Survey.

Fox, R.W., and A.T. McDonald. 1978. *Introduction to Fluid Mechanics*. New York, NY: McGraw-Hill Publishing Co.

Freeze, R.A., and J.A. Cherry. 1979. *Groundwater*. Englewood Cliffs, New Jersey: Prentice-Hall.

Gardner, W.H. 1986. *Water Content. Methods of Soil Analysis Part 1—Physical and Mineralogical Methods*. A. Klute, ed. Madison, WI: Soil Science Society of America, Inc.: 493–544.

Gee, G.W., M.D. Campbell, G.S. Campbell, and J.H. Campbell. 1992. Rapid measurements of low soil water potentials using a water activity meter. *Soil Science of America Journal* 56: 1,068–1,072.

Gilboy, W.B. 1984. γ- and X-Ray tomography in NDE applications in nuclear instruments and methods. *Physics Research V* (1221): 193–200.

Glass, R.J., J.Y. Parlange, and T.S. Steenhuis. 1989a. Wetting front instability 1. Theoretical discussion and dimensional analysis. *Water Resources Research* 25(6): 1,187–1,194.

Glass, R.J., J.Y. Parlange, and T.S. Steenhuis. 1989b. Wetting front instability. 2. Experimental determination of relationships between system parameters and two-dimensional unstable flow field behavior in initially dry porous media. *Water Resources Research* 25(6): 1,195–1,207.

Green, R.T., R.D. Manteufel, F.T. Dodge, and S.J. Svedeman. 1993. *Theoretical and Experimental Investigation of Thermohydrologic Processes in a Partially Saturated, Fractured Porous Medium.* NUREG/CR-6026. Washington, DC: Nuclear Regulatory Commission.

Green, R.T., K.A. Meyer, and G. Rice. 1994. *Hydraulic Characterization of Hydrothermally-Altered Nopal Tuff.* CNWRA 94-027. San Antonio, TX: Center for Nuclear Waste Regulatory Analyses.

Hirschfelder, J.O., C.F. Curtiss, and R.B. Bird. 1954. *Molecular Theory of Gases and Liquids.* New York, NY: John Wiley and Sons.

Hsiung, S.M., D.D. Kana, M.P. Ahola, A.H. Chowdhury, and A. Ghosh. 1994. *Laboratory Characterization of Rock Joints.* NUREG/CR-6178. Washington, DC: Nuclear Regulatory Commission.

Keyhani, M., F.A. Kulacki, and R.N. Christensen. 1981. *Convective Heat Transfer Within Spent Fuel Canisters: An Experimental Laboratory Study.* BMI/ONWI-229. Columbus, OH: Battelle Memorial Institute.

Klavetter, E.A., and R.R. Peters. 1986. *Estimation of Hydrologic Properties of an Unsaturated, Fractured Rock Mass.* SAND84-2642. Albuquerque, NM: Sandia National Laboratories.

Kulacki, F.A., and A.A. Emara. 1975. *High Rayleigh Number Convection in Enclosed Fluid Layers with Internal Heat Sources.* NUREG-75/065. Washington, DC: Nuclear Regulatory Commission.

Lichtner, P.C. 1994. *Multi-Phase Reactive Transport Theory.* CNWRA 94-018. San Antonio, TX: Center for Nuclear Waste Regulatory Analyses.

Lichtner, P.C., and J. Walton. 1994. *Near-Field Liquid-Vapor Transport in a Partially Saturated High-Level Nuclear Waste Repository.* CNWRA 94-022. San Antonio, TX: Center for Nuclear Waste Regulatory Analyses.

Lin, W., D.G. Wilder, J.A. Blink, S.C. Blair, T.A. Buscheck, D.A. Chesnut, W.E. Glassley, K. Lee, and J.J. Roberts. 1994. The testing of thermal-mechanical-hydrological-chemical processes using a large block. *Proceedings of the Fifth Annual International Conference on High-Level Radioactive Waste Management.* La Grange Park, IL: American Nuclear Society: 1,938–1,945.

Manteufel, R.D. 1994. *Large-Scale Buoyant Flow at an Unsaturated HLW Repository.* 94-WA/HT-39. New York, NY: American Society of Mechanical Engineers.

Manteufel, R.D., and R.T. Green. 1993. Observations of thermally-driven liquid redistribution in a partially saturated porous medium. *Multiphase Transport in Porous Media.* FED-173/HTD-265. New York, NY: American Society of Mechanical Engineers: 93–107.

Manteufel, R.D., R.T. Green, F.T. Dodge, and S.J. Svedeman. 1992. An experimental investigation of two-phase, two-component nonisothermal flow in a porous medium with a simulated fracture. HTD-216. *Heat and Mass Transfer in Porous Media*. New York, NY: American Society of Mechanical Engineers: 9–18.

Manteufel, R.D., M.P. Ahola, D.R. Turner, and A.H. Chowdhury. 1993. *A Literature Review of Coupled Thermal-Hydrologic-Mechanical-Chemical Processes Pertinent to the Proposed High-Level Nuclear Waste Repository*. NUREG/CR-6021. Washington, DC: Nuclear Regulatory Commission.

Miller, E.E. 1980. Similitude and scaling of soil-water phenomena. *Applications of Soil Physics*. D. Hillel, ed. New York, NY: Academic Press: 300–318.

Miller, D.E., and W.H. Gardner. 1962. Water infiltration into stratified soil. *Soil Science Society of America Proceedings* 26: 115–119.

Moore, W.J. 1963. *Physical Chemistry*. Englewood Cliffs, NJ: Prentice-Hall.

Narasimhan, T.N. 1982. Physics of saturated-unsaturated subsurface flow. *Geological Society of America*. Special Paper 189.

Nichols, C.I., and J. Heaviside. 1988. Gamma-ray-absorption techniques improve analysis of core displacement tests. *SPE Formation Evaluation*. SPE Paper 14421. Richardson, TX: Society of Petroleum Engineers: 69–75.

Nitao, J.J. 1988. *Numerical Modeling of the Thermal and Hydrological Environment Around a Nuclear Waste Package Using the Equivalent Continuum Approximation: Horizontal Emplacement.* UCID-21444. Livermore, CA: Lawrence Livermore National Laboratory.

Nitao, J.J. 1990. *V-TOUGH—An Enhanced Version of the TOUGH Code for the Thermal and Hydrologic Simulation of Large-Scale Problems in Nuclear Waste Isolation.* UCID-21954. Livermore, CA: Lawrence Livermore National Laboratory.

Nuclear Regulatory Commission. 1994. *License Application Review Plan for a Geologic Repository for Spent Nuclear Fuel and High-Level Radioactive Waste*. NUREG-1323, Rev. 0. Washington, DC: Nuclear Regulatory Commission.

Patrick, W.C., ed. 1986. *Spent Fuel Test—Climax: An Evaluation of the Technical Feasibility of Geologic Storage of Spent Nuclear Fuel in Granite*. UCRL-53702. Livermore, CA: Lawrence Livermore National Laboratory.

Pearcy, E.C. 1994. *Fracture Transport of Uranium at the Nopal I Natural Analog Site.* CNWRA 94-011. San Antonio, TX: Center for Nuclear Waste Regulatory Analyses.

Persoff, P., K. Pruess, and L. Myer. 1992. Two-phase flow visualization and relative permeability measurement in transparent replicas of rough-walled rock fractures. *Proceedings of the Sixteenth Workshop on Geothermal Reservoir Engineering*. Stanford, CA: Stanford University: 203–210.

Pruess, K. 1985. *A Quantitative Model of Vapor Dominated Geothermal Reservoirs as Heat Pipes in Fractured Porous Rock.* LBL-19366. Berkeley, CA: Lawrence Berkeley Laboratory.

Pruess, K. 1987. *TOUGH User's Guide.* NUREG/CR-4645. Berkeley, California: Lawrence Berkeley Laboratory.

Ramirez, A.L., ed. 1991. *Prototype Engineered Barrier System Field Test (PEBSFT) Final Report.* UCRL-ID-106159. Livermore, CA: Lawrence Livermore National Laboratory.

Ramirez, A.L., R.C. Carlson, and T.A. Buscheck. 1991. In Situ *Changes in the Moisture Content of Heated, Welded Tuff Based on Thermal Neutron Measurements.* UCRL-ID-104715. Livermore, CA: Lawrence Livermore National Laboratory.

Ramspott, L.D. 1991. The constructive use of heat in an unsaturated tuff repository. *Proceedings of the Second Annual High-Level Radioactive Waste Management Conference.* La Grange Park, IL: American Nuclear Society: 1,602–1,607.

Ransohoff, T.C., and C.J. Radke. 1988. Mechanisms of foam generation in glass-bead packs. *SPE Reservoir Engineering*: 573–585.

Rasmussen, T.C., and D.D. Evans. 1989. *Fluid Flow and Solute Transport Modeling Through Three-Dimensional Networks of Variably Saturated Discrete Fractures.* NUREG/CR-5239. Washington, DC: Nuclear Regulatory Commission.

Rasmussen, T.C., D.D. Evans, P.J. Sheets, and J.H. Blanford. 1990. *Unsaturated Fractured Rock Characterization Methods and Data Sets at the Apache Leap Test Site.* NUREG/CR-5596. Washington, DC: Nuclear Regulatory Commission.

Rasmussen, T.C., D.D. Evans, P.J. Sheets, and J.H. Blanford. 1993. Permeability of Apache Leap tuff: Borehole and core measurements using water and tuff. *Water Resources Research* 29(7): 1,997–2,006.

Slattery, J.C. 1972. *Momentum, Energy, and Mass Transfer in Continua.* New York, NY: McGraw-Hill.

Somerton, W.H., J.A. Keese, and S.L. Chu. 1973. Thermal behavior of unconsolidated oil sands. SPE-4506. *Presented at the 48th Annual Fall Meeting of the Society of Petroleum Engineers, Las Vegas, NV.* Richardson, TX: Society of Petroleum Engineers.

Somerton, W.H., A.H. El-Shaarani, and S.M. Mobarak. 1974. High temperature behavior of rocks associated with geothermal type reservoirs. SPE-4897. *Presented at the 44th Annual California Regional Meeting of the Society of Petroleum Engineers, San Francisco, CA.* Richardson, TX: Society of Petroleum Engineers.

U.S. Department of Energy. 1994. *Yucca Mountain Site Characterization Project Five Year Plan, Fiscal Years 1996-2000.* Predecisional Draft. Washington, DC: U.S. Department of Energy.

van Genuchten, R. 1978. *Calculating the Unsaturated Hydraulic Conductivity with a New, Closed-Form Analytical Model*. Research Report 78-WR-08. Princeton, NJ: Princeton University: Department of Civil Engineering.

van Genuchten, M.Th., F.J. Leij, and S.R. Yates. 1991. *The RETC Code for Quantifying the Hydraulic Functions of Unsaturated Soils*. IAG-DW12933934. Riverside, CA: U.S. Department of Agriculture: U.S. Salinity Laboratory.

van Wylen, G.J., and R.E. Sonntag. 1968. *Fundamentals of Classical Thermodynamics*. New York, NY: John Wiley and Sons, Inc.

Wang, J.S.Y. 1992. Variations of hydrological parameters of tuff and soil. *Proceedings of the Third International High-Level Waste Management Conference*. La Grange Park, IL: American Nuclear Society: 727–731.

Wang, J.S.Y., and T.N. Narasimhan. 1986. *Hydrologic Mechanisms Governing Partially Saturated Fluid Flow in Fractured Welded Units and Porous Nonwelded Units at Yucca Mountain*. LBL-21022. Berkeley, CA: Lawrence Berkeley Laboratory.

Wooding, R.A. 1956. Steady state free thermal convection of liquid in a saturated permeable medium. *Journal of Fluid Mechanics* 2(3): 273–285.

Woodside, W., and J.H. Messmer. 1961. Thermal conductivity of porous media. I. Unconsolidated Sands. *Journal of Applied Physics* 32(9): 1,688–1,706.

Zimmerman, R.M., and R.E. Finley. 1986. *Summary of Geomechanical Measurements Taken In and Around the G-Tunnel Underground Facility, NTS*. SAND86-1015. Albuquerque, NM: Sandia National Laboratories.

Zimmerman, R.M., R.L. Schuch, D.S. Mason, M.L. Wilson, M.E. Hall, M.P. Board, R.P. Bellman, and M.P. Blanford. 1986. *Final Report: G-Tunnel Heated Block Experiment*. SAND84-2620. Albuquerque, NM: Sandia National Laboratories.